

Multimodal-Nonlinear-Optical- Microspectroscopy for Biological and Diagnostic Applications

Kumulative Dissertation

zur Erlangung des akademischen Grades

Doctor rerum naturalium (Dr. rer. nat.)



FRIEDRICH-SCHILLER- UNIVERSITÄT JENA

VORGELEGT DEM RAT DER CHEMISCH-GEOWISSENSCHAFTLICHEN
FAKULTÄT DER
FRIEDRICH-SCHILLER-UNIVERSITÄT JENA

von M.Sc. Fisseha Bekele Legesse

geboren am 22.11.1988 in Addis Ababa, Äthiopien

Gutachter:

1. Prof. Dr. Jürgen Popp

Institut für Physikalische Chemie, Friedrich-Schiller-Universität Jena

2. Prof. Dr. Benjamin Dietzek

Institut für Physikalische Chemie, Friedrich-Schiller-Universität Jena

Tag der Verteidigung: 11.07.2018

Contents

1	Introduction	1
1.1	Motivation	1
1.2	Nonlinear Multimodal Micro-spectroscopy	4
1.2.1	Coherent Anti-Stokes Raman Scattering (CARS)	4
1.2.2	Two-Photon Excited Fluorescence (TPEF)	10
1.2.3	Second Harmonic Generation (SHG)	11
1.2.4	Multi-modal Imaging Scheme	12
2	Discussion	14
2.1	Multimodal Microscope [FBL1]	14
2.1.1	HNSCC and Multimodal Image Analysis	17
2.2	CARS imaging in the Fingerprint Region ([FBL2], [FBL3])	18
2.2.1	Hepatic Retinol Content Investigation	23
2.2.2	Pigment Accumulation in Microalgae	27
2.3	Optimizing Image Acquisition [FBL4], [FBL5], [FBL6]	31
2.3.1	Image Acquisition Rate	32
2.3.2	Spatial Resolution	37
3	Summary	40
4	Outlook	44
5	Zusammenfassung	46
	Bibliography	49
6	Publications and conference contributions	57
6.1	Multimodal nonlinear microscopy of head and neck carcinoma - toward intraoperative diagnostics	58
6.2	Hepatic vitamin A content investigation using CARS microscopy	81

6.3	Investigation of microalgal carotenoid content using CARS microscopy and spontaneous Raman spectroscopy	94
6.3.1	Investigation of microalgal carotenoid content using CARS microscopy and spontaneous Raman spectroscopy (print version)	105
6.4	Fiber-based dual-focus time-demultiplexed SHG microscopy	114
6.5	Dual-focus CARS microscopy using a compact two-beam fiber laser source	119
6.6	Bessel beam CARS microscopy	124
	Curriculum Vitae	135
	Acknowledgement	136
	Erklärung	137
	Selbstständigkeitserklärung	141

List of Abbreviations

IR	infrared
NIR	near-infrared
OCT	optical coherence tomography
MRI	magnetic resonance imaging
US	ultrasonography
CARS	coherent anti-Stokes Raman scattering
NR	non-resonant
SHG	second harmonic generation
TPEF	two photon excited fluorescence
MPEF	multi-photon excited autofluorescence
SVEA	slowly varying envelope approximation
NA	numerical aperture
H&E	hematoxylin and eosine
OPO	optical parametric oscillator
PMT	photomultiplier tube
fs	femto-seconds
ps	pico-seconds
ns	nano-seconds
μs	micro-seconds
SD	standard deviation
TCC	TPEF to CARS contrast
SAAID	second harmonic to autofluorescence ageing index of dermis
PCF	photonic crystal fiber
SESAM	saturable absorber mirror
FBG	fiber Bragg grating
LDA	linear discriminant analysis
GVD	group velocity dispersion

1 | Introduction

1.1 Motivation

To meet the ever-increasing demands in biomedicine and life sciences, optical visualization tools have consistently been developed and improved upon ever since the invention of the first crude light microscopes. Different aspects of the interaction between electromagnetic radiation and biological specimens have been exploited for creating a contrast. Bright-field light microscopy, that allows the discrimination of different structures in cells and tissues based on the absorption of white light in the sample, has been prominently used in biological investigations and conventional pathology. The contrast obtained from light microscopy has been enhanced by using different techniques such as phase [1], differential interference contrast [2] among others. The information obtained from such techniques is limited to morphology which is just one aspect of the samples being investigated. Considering the particular example of pathological examination, diseases also affect the biomedical composition of tissue thereby necessitating chemical contrast to be obtained from the techniques used. This precludes staining procedures that have elevated light microscopy into becoming the state of the art for histo-pathological investigations and biological imaging in general [3, 4]. However, typically, only few structures in the sample can be stained and thus the contrast obtained is limited. Staining is also a time-consuming and cumbersome process that causes perturbation of the sample.

Fluorescence microscopy, initially utilizing the native, weak, single photon excited auto-fluorescence of molecules in the sample, is another milestone in the development of light microscopy techniques with regards to obtaining chemical contrast. This approach has subsequently been greatly advanced with the introduction of fluorescence labels [5]. Although fluorescent labels improve chemical sensitivity, the inherent invasiveness of the process leads to perturbation of the sample with possible photo-toxicity and image acquisition times are sometimes limited due to fluorophore photobleaching.

Spectroscopic techniques based on infrared (IR) absorption [6] and Raman scattering [7] have augmented the myriad of chemical information that could be extracted from samples to a great extent. These techniques have, consequently, been integrated into microscopic setups for use in the assessment of biological samples as they are capable of probing the unique spectral signature of biomolecules. IR spectroscopy is based on the net absorption of light in the IR region of the electromagnetic spectrum. The spatial resolution achievable with IR spectroscopy is limited and imaging in aqueous environments is problematic due to the large background signal from water [8]. Raman spectroscopy, on the other hand, is based on the inelastic scattering of light by the characteristic vibrational and rotational modes of molecules [9, 10]. Accordingly, molecular signatures that could serve as markers for disease-related abnormalities have been probed using Raman spectroscopy in a diagnostic framework [11]. Generally, potential utilization of information from Raman spectroscopy has been hindered by the weakness of signals from biomolecules resulting in long integration times and overwhelming single-photon fluorescence background. The shortcomings of the techniques elucidated so far indicate the need for the development of novel optical technologies to visualize biological samples.

The various qualities needed from such visualization tools hinted at in the aforementioned discussion could be summarized by analysing the typical work flow of histo-pathological investigations. The process begins with the inspection of suspected lesions on the human body followed by the excision of the affected tissue for examination under a light microscope. This process is usually aided by staining procedures. The first important aspect is the acquisition of chemical contrast to complement visualizations of morphology. This is relevant because diseases affect the biomedical content of cells or tissue and these changes are usually precursors to morphological alterations. What naturally follows from this requirement is the capability to detect small amounts and changes in molecules and discern between different molecular sub-species in the sample. Augmenting on the information collected will allow one to make more informed decisions and hopefully improve objectivity. This, however, should not be achieved at a cost of invasiveness, a major shortcoming of staining and labelling approaches whereby the sample being investigated is perturbed by the technique. This factor also affects the suitability of the method for *in vivo* investigations.

Another aspect is spatial resolution which is inherently intertwined with the ability to identify small, sub-cellular structures within the sample. In light microscopy, spatial resolution is dependent on excitation wavelength, as formulated in Abbe's diffraction limit equation. The wavelength of the excitation light also affects the

depth of penetration in tissue. There has to be a compromise between this competing requirements in general. This is particularly an issue in diagnostic tools such as optical coherence tomography (OCT) [12], magnetic resonance imaging (MRI) [13] and ultrasonography (US) [14] that allow deep tissue investigations and even whole body imaging but do not offer cellular resolution that is critical in diagnostic applications.

The speed of image acquisition is another critical parameter in the practicality of a diagnostic imaging tool. There are many facets intrinsically associated with image acquisition rate. One is the capability to track dynamic processes that could serve to highlight the mechanism of pathological change. Faster imaging also translates to shorter diagnostic cycle and the investigation of larger volume of samples which in turn means more robust results. There of course has to be a compromise between all these qualities and the need for affordable, compact and easy to use imaging tools. The later attributes are the usual culprits for ineffective translation of different photonic technologies developed throughout the years into clinics and everyday use.

Non-linear optical microspectroscopic techniques can fulfil the elucidated requirements by allowing a fast, non-invasive, *in vivo* investigation of cells and tissue with high resolution. Information regarding the morphology and chemical composition of samples can be extracted from these non-linear methods without the need for additional stains. These techniques also have inherent optical sectioning capabilities allowing three dimensional imaging of thick tissue samples. Here, particularly, non-linear multimodal microscopy combining the modalities coherent anti-Stokes Raman scattering (CARS), second harmonic generation (SHG), and two-photon excited fluorescence (TPEF) microscopy has been employed to image and characterize biological samples. First the non-linear multimodal imaging of histological slides for disease diagnostics is presented. Then the focus of the CARS modality is shifted from the usually exploited CH group of stretching vibrations to the C=C stretching vibration in the fingerprint region. In that respect, the utilization of multimodal imaging for visualizing vitamin A in hepatic tissue and carotenoids in microalga is discussed. Lastly efforts for improving the image acquisition rate and lateral resolution of the CARS microscopic setups are presented. Basic theoretical concepts necessary to understand the non-linear techniques are modularly presented in the following subsections.

1.2 Nonlinear Multimodal Micro-spectroscopy

All classical optical phenomena are described by Maxwell's equations. The response of matter to applied fields is encompassed in the constitutive relations that supplement the basic Maxwell's equations. In particular, the effect of electric field on matter is formulated as:

$$\vec{D} = \epsilon_o \vec{E} + \vec{P} \quad (1.1)$$

where \vec{D} is the electric flux density or the electric displacement, ϵ_o is the permittivity of free space, \vec{E} is the electric field intensity and \vec{P} is the Polarization [15]. \vec{P} is a macroscopic term that embodies the properties of the material's charges and molecules in the presence of an electric field.

When the intensity of the applied field is weak the material responds linearly and thus the induced Polarization can be described by:

$$\vec{P} = \epsilon_o \chi^{(1)} \vec{E} \quad (1.2)$$

Here, the constant $\chi^{(1)}$ is the linear susceptibility. Typical optical phenomena observed in materials such as absorption and reflection can be expressed using this linear constant of proportionality. However as the applied electric field becomes stronger the response of the material is no longer linearly proportional to the strength of the field. The expression for the induced polarization could subsequently be represented in a power series that includes higher order terms as:

$$\vec{P} = \epsilon_o \left(\chi^{(1)} \cdot \vec{E} + \chi^{(2)} \cdot \vec{E} \cdot \vec{E} + \chi^{(3)} \cdot \vec{E} \cdot \vec{E} \cdot \vec{E} + \dots \right) \quad (1.3)$$

Where, $\chi^{(2)}$ and $\chi^{(3)}$ are the second order and third order non-linear susceptibilities, respectively. The second order non-linear polarization $\vec{P}^{(2)} = \epsilon_o \chi^{(2)} \vec{E} \cdot \vec{E}$ is related to physical processes such as SHG. On the other hand, the third order non-linear polarization $\vec{P}^{(3)} = \epsilon_o \chi^{(3)} \vec{E} \cdot \vec{E} \cdot \vec{E}$ describes two-photon absorption and CARS. Typically the higher the order of the non-linear susceptibility the smaller it's magnitude and therefore intense pulses from ultrafast laser sources are needed to produce noticeable non-linear polarizations [16].

Coherent Anti-Stokes Raman Scattering (CARS)

Molecules vibrate at characteristic frequencies depending on, among other things, the specific type and strength of chemical bonds they contain. Vibrational spectroscopy refers to the ensemble of techniques that probe these molecular vibrations

Introduction

to extract information about the molecular composition and structure of samples. One of the most frequently used vibrational spectroscopic techniques is Raman spectroscopy [9] which is based on the inelastic scattering of a photon from a sample. Some incident photons can give energy to the molecular vibration resulting in a scattered photon with lower energy thereby constituting a Stokes radiation. If the molecule is a vibrationally excited state some scattered photons will gain energy from the molecule and will contribute to an anti-Stokes radiation. Although the Raman spectra of molecules serve as chemical fingerprints in a multitude of applications ([17, 18, 19, 20]), the Raman scattering efficiency of most molecules is quite low. This necessitates long acquisition times that limit the applicability of the technique especially for imaging purposes.

CARS is a non-linear variant of Raman scattering that produces coherent vibrations and much stronger signals than spontaneous Raman scattering that consequently enable faster image acquisition. CARS is a four-wave mixing process in which a pump (ω_p) and a Stokes (ω_s) beam applied on a sample coherently drive Raman active vibrations at their difference frequency ($\omega_p - \omega_s$). A probe beam (ω_{pr}) is then inelastically scattered off these vibrations to produce an anti-Stokes signal $\omega_{as} = \omega_{pr} + \omega_p - \omega_s$. For experimental simplicity the same source is used to generate the pump and probe beams resulting in an anti-Stokes signal at $\omega_{as} = 2\omega_p - \omega_s$. This process is depicted in the energy level diagram in figure 1.1(a).

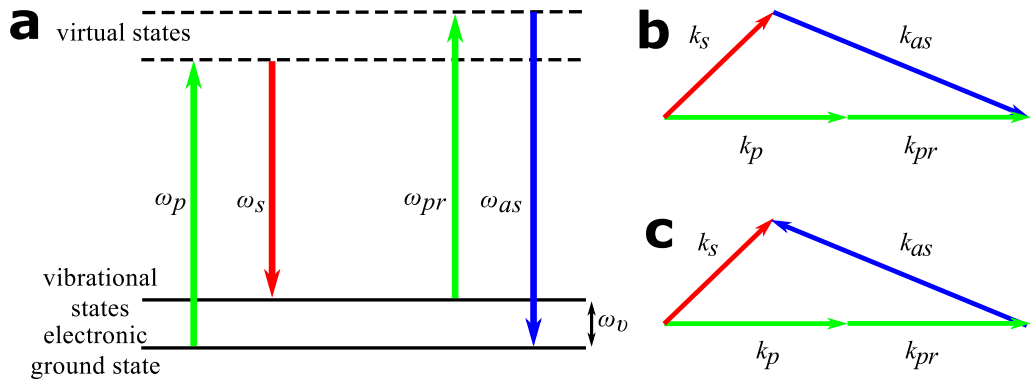


Figure 1.1: (a) Energy level diagram of the CARS process. When the beat frequency of the pump and Stokes beam $\omega_p - \omega_s$ is equal to the molecular vibrational frequency ω_v an anti-Stokes signal is generated at $\omega_{as} = 2\omega_p - \omega_s$. (b) Phase matching condition for forward-generated CARS signal. (c) Phase matching condition for epi-CARS signal, where $k = n\omega/c$ is the wavevector and k_s , k_p , k_{pr} , and k_{as} are the Stokes, pump, probe, and anti-Stokes wavevectors, respectively.

The classical description of the Raman and CARS processes is presented in brief below. Applied electric fields set the electrons of a molecule in oscillatory motion. This effect is embodied by the expression that relates the induced electric dipole

Introduction

moment $\mu(t)$ to the polarizability $\alpha(t)$ as:

$$\mu(t) = \alpha(t)E(t) \quad (1.4)$$

For an incident field $E(t) = Ae^{-i\omega t} + c.c$ with an amplitude A and frequency ω . The motion of the electrons is affected by the motion of the nuclei to which they are attached. This perturbation of the polarizability by the presence of nuclear modes is introduced by applying a Taylor series expansion.

$$\alpha(t) = \alpha_0 + \left(\frac{\delta\alpha}{\delta Q} \right)_0 Q(t) + \dots \quad (1.5)$$

where Q is the nuclear coordinate and $\delta\alpha/\delta Q$ embodies the effect of the nuclear motion on the polarizability. Assuming a classic harmonic oscillatory motion with the frequency ω_v for the nuclei along the nuclear coordinated Q , an incoming field at ω will result in a Stokes Raman signal with the intensity $I(\omega_s)$ give by:

$$I(\omega_s) = \frac{\omega_s^4}{12\pi\epsilon_0 c^3} Q_0^2 I_0 \left(\frac{\delta\alpha}{\delta Q} \right)_0^2 \quad (1.6)$$

where $\omega_s = \omega - \omega_v$ is the Stokes frequency, Q_0 is the amplitude of the nuclear motion, and $I_0 = |A|^2$ is the incident beam intensity. As each of these molecular vibrations from different molecules have their own phase the radiation generated is incoherent and the total Raman signal intensity scales linearly with the number of scatterers N . In the case of the CARS processes, the pump ($E_p(t) = A_p e^{-i\omega_p t} + c.c$) and Stokes ($E_s(t) = A_s e^{-i\omega_s t} + c.c$) beams applied on the sample cause the cloud of electrons around the nuclei to oscillate at the difference frequency $\Omega = \omega_p - \omega_s$. This electron cloud motion will exert a force on the nuclear modes of the molecule resulting in a damped oscillatory motion with amplitude given by:

$$Q(\omega_v) = \frac{1}{m} \left(\frac{\delta\alpha}{\delta Q} \right)_0 \frac{A_p A_s^*}{\omega_v^2 - \Omega^2 - 2i\Omega\gamma} \quad (1.7)$$

where γ is the damping constant, A_p and A_s are the amplitudes of the pump and Stokes beam respectively, and ω_v is the resonance frequency of the nuclear mode. This in turn translates into alteration of the electronic polarizability. The propagating incoming fields will then experience this perturbation. The coherent superposition of these microscopic induced dipoles generates a macroscopic polarization that contains contributions at different frequencies. The amplitude of the third order macroscopic polarization at the anti-Stokes frequency is $|P^{(3)}|^2 \propto |\chi^{(3)}|^2 I_p^2 I_s^*$, where

Introduction

the intensity of the pump and Stokes beam given by $I_p = |A_p|^2$ and $I_s = |A_s|^2$ respectively. Herein the third order non-linear susceptibility is related to the microscopic parameters as:

$$\chi^{(3)} = \frac{N}{m} \left(\frac{\delta\alpha}{\delta Q} \right)_0 \frac{1}{\omega_v^2 - \Omega^2 - 2i\Omega\gamma} \quad (1.8)$$

Because the nuclear motions of all N molecules driven by the external fields have a well-defined phase relationship the resulting signal builds up due to the coherent superposition of the fields.

The generation and propagation of waves from the third order non-linear polarization can be determined from the non-linear wave equation of the form:

$$\nabla^2 \vec{E} - \frac{n^2}{c^2} \frac{\partial^2}{\partial t^2} \vec{E} = \frac{1}{\epsilon_0 c^2} \frac{\partial^2}{\partial t^2} \vec{P}^{(3)} \quad (1.9)$$

In a plane wave approximation, the Stokes and pump beam can be assumed to propagate co-linearly through a homogeneous $\chi^{(3)}$ sample of thickness L . Solving the scalar wave equation with the use of the slowly varying envelope approximation (SVEA) results an intensity of the CARS signal given by:

$$I_{AS} \propto |\chi^{(3)}|^2 I_p^2 I_s \cdot L^2 \text{sinc}^2 \left(\frac{\Delta k L}{2} \right) \quad (1.10)$$

where $k = n\omega/c$ is the wavevector, Δk is the wavevector mismatch computed as $\Delta k = k_{as} - (2k_p - k_s)$ for the case $k_{pr} = k_p$, and L is the interaction length.

A number of observations can be made about the evolution of the CARS intensity from this formula. The intensity of the CARS signal is quadratically dependent on $\chi^{(3)}$ which in turn scales with the number of scatterers in the sample N . Equation 1.10 also introduces another important parameter, the wavevector mis-match Δk which has to be minimized for getting strong CARS signals. This condition is termed as phase matching condition and is visualized in figures 1.1(b) and (c) for forward and backward propagating CARS signals, respectively.

In the early experimental implementation of CARS the incident fields were weakly focused. This necessitates the adoption of bulky non-collinear beam geometries such as in Box-CARS in order to satisfy the phase matching condition [21, 22]. This has historically constrained CARS to spectroscopic applications such as for the inspection of gases in flames. Tight focusing of the beams has relaxed this phase matching condition because of the shortening of the interaction length which minimizes the sinc^2 term in equation 1.10 [23]. This has made CARS microscopic imaging accessible by allowing the raster scanning of the beams.

Introduction

Although the classical formulation of $\chi^{(3)}$ in equation 1.8 provides an intuitive insight into non-linear interaction of light and matter it merely provides a qualitative picture. Quantum descriptions of the CARS process provide a quantitative description by taking into account the quantized nature of both the field and the matter. This considerations result in expressions that fit into the observed characteristics of the third-order non-linear susceptibility such as the presence of both resonant and non-resonant (NR) contributions created by coherent four wave mixing [24]. The energy level diagram for such four photon non resonant component of the third order susceptibility is depicted in figure 1.2(a).

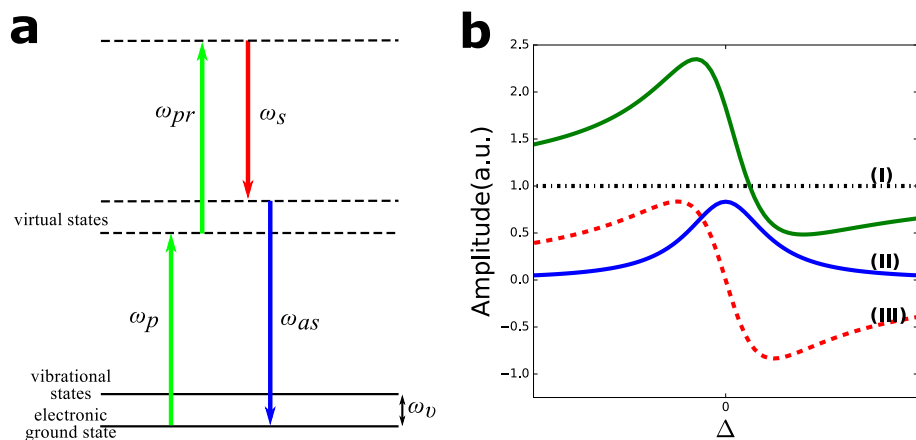


Figure 1.2: (a) Energy level diagram showing the non-resonant contributions to the CARS process. (b) The total CARS spectrum (solid green line) with individual contributions: (I) non-resonant contribution (dotted black line). (II) Raman resonant contribution (solid blue line). (III) mixing term (dashed red line).

This four-wave mixing, non-resonant component is incorporated in the expression for the $\chi^{(3)}$ as:

$$\chi^{(3)} = \chi_{NR}^{(3)} + \chi_R^{(3)}. \quad (1.11)$$

while the Raman-resonant contribution to the susceptibility $\chi_R^{(3)}$ is given by :

$$\chi_R^{(3)} = \frac{A_R}{\Delta - i\gamma} \quad (1.12)$$

where A_R is the normalized vibrational mode strength, Δ is the detuning frequency given by $\Delta = \omega_p - \omega_s - \omega_v$ in which ω_v is the vibrational frequency, and γ corresponds to the bandwidth of the Raman line. The magnitude of $\chi_R^{(3)}$ is enhanced when the difference frequency of the pump and the Stokes matches the frequency of a Raman active vibration of the target molecule. It is a Lorentzian function

approximation of the solution to a damped harmonic oscillator formulation of the frequency dependence [25]. Inserting equation 1.11 into equation 1.10 results in:

$$I_{AS}(\Delta) \propto |\chi_{NR}^{(3)}|^2 + |\chi_R^{(3)}(\Delta)|^2 + 2\chi_{NR}^{(3)}\text{Re}\{\chi_R^{(3)}(\Delta)\}. \quad (1.13)$$

The first term on the right side of the equation is purely frequency independent and manifests in CARS images as a constant offset term. The second term is the actual relevant contribution to the CARS imaging process. The last interference term couples the resonant and non-resonant components and is the major drawback for CARS imaging as it cannot be simply subtracted from the total acquired signal. The responses of each of these terms and their total sum to the detuning Δ is shown in figure 1.2(b). A number of approaches, such as frequency modulation (FM) CARS [26], polarization sensitive detection CARS [27], time-resolved CARS [28] have been proposed to remove the background or detect only the resonant contribution and have been reasonably successful but do so at an overhead complexity of detection modules.

Different vibrational modes have been investigated using CARS including the OH stretching vibration mode in water molecules [29] and the phosphate stretch vibration in DNA [30]. Nonetheless, most investigations have focused on probing the limited number of strong Raman modes in the high wavenumber (2500–3500 cm^{-1}) region of the vibrational spectrum. In particular, the CH_2 symmetric stretching vibration at 2845 cm^{-1} typically found in abundance in lipids has been exploited for investigating the fat content in tissue [31, 32, 33].

In comparison, there have been far less CARS investigations in the information-rich fingerprint region (800–1800 cm^{-1}) region. One reason for this the lack of strong resonances, in comparison with the non-resonant background, in the fingerprint region making it difficult to isolate the spectral signature of a molecule from the CARS spectra acquired. This problem is illustrated in figure 1.3(a) in which the total CARS spectrum is plotted for different Raman-resonant to non-resonant CARS ratios. The more the non-resonant contribution overwhelms the resonant part, the less the CARS spectrum resembles the spontaneous Raman resonance (which is proportional to the imaginary part of the third-order susceptibility χ^3). Another complication in the fingerprint region is the presence of multiple, overlapping peaks from different molecular groups in biological tissue within the fingerprint region. This congestion of the spectra makes it difficult to extract individual molecular contributions to the CARS spectrum. This particular issue is elaborated in figure 1.3(b) wherein CARS spectra of two neighbouring resonances under two different

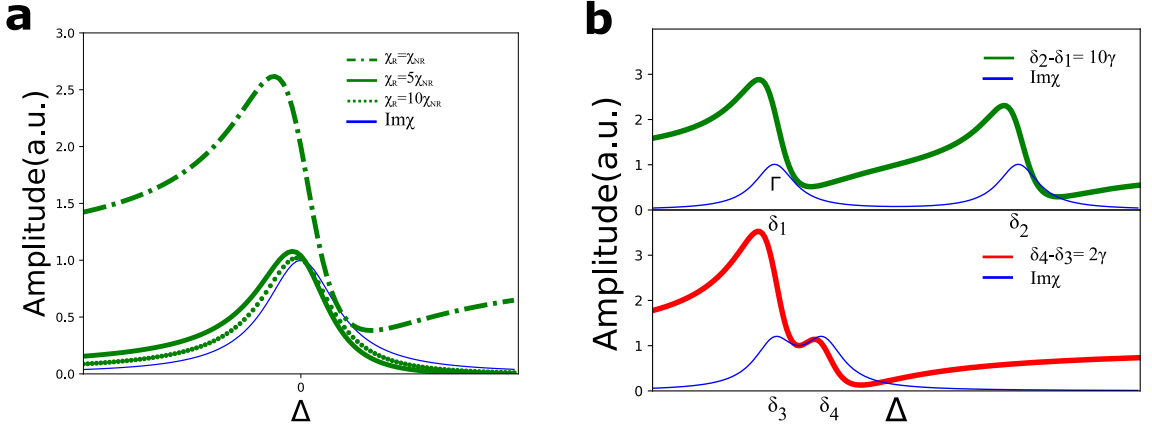


Figure 1.3: *Complications arising from the dispersive shape of the CARS spectrum in the fingerprint region. (a) Shape of CARS spectra from varying ratios of Raman-resonant to non-resonant background. Raman spectrum (blue), $\chi_R^{(3)} = 10\chi_{NR}^{(3)}$ (green dots), $\chi_R^{(3)} = 5\chi_{NR}^{(3)}$ (green solid), $\chi_R^{(3)} = \chi_{NR}^{(3)}$ (green dashes). (b) Effect of CARS spectrum on two neighbouring peaks. Well separated Raman resonances (top). Overlapping peaks (bottom).*

conditions are displayed. When the two resonances are well separated (top plot) the CARS spectrum agrees reasonably well with the spontaneous Raman resonance. For very close resonances (bottom plot) the dispersive nature of the non-resonant CARS background obscures individual components.

Two-Photon Excited Fluorescence (TPEF)

TPEF is a non-linear fluorescence technique that can be used to image autofluorophores in tissue samples as in case of single fluorescence. In the latter, a single photon is absorbed by a chromophore resulting in an electronic excitation from the ground state into an electronically excited state. From the excited state the electron undergoes fast radiation-less de-excitation steps and eventually relaxes back to the electronic ground state by emitting a fluorescence photon. This incoherent process is depicted in figure 1.4(a). In the case of TPEF the excitation mechanism is changed and two photons are simultaneously absorbed to excite the electron [34]. The first photon excites the electron to a virtual level and the second photon excites to an excited electron state as in figure 1.4(b). The de-excitation path then proceeds as in the case of one-photon fluorescence.

With paraxial approximation considerations, the intensity of TPEF I_f can be formulated as:

$$\langle I_f \rangle \cong \sigma_{TPEF} \cdot I_o^2. \quad (1.14)$$

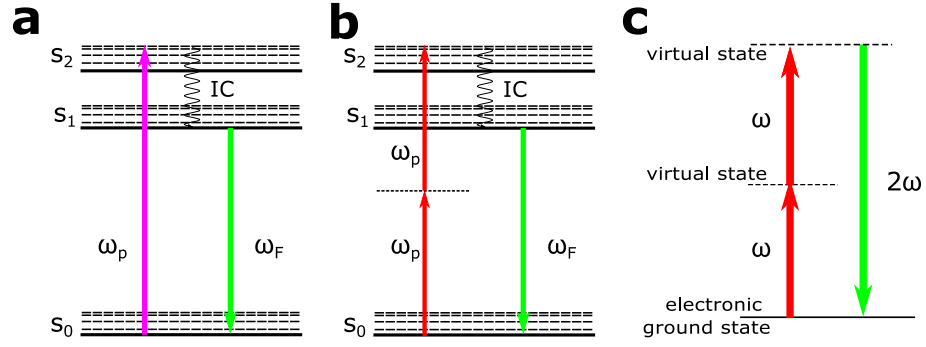


Figure 1.4: *Jablonski diagram for (a) single photon excited fluorescence. (b) TPEF. (c) Energy level diagram for SHG.*

where I_o is the intensity of the incident field and σ_{TPEF} is the TPEF cross-section which encapsulates the two photon absorption cross-section σ_{TPA} and the fluorescence quantum yield η as $\sigma_{TPEF} = \sigma_{TPA} \cdot \eta$.

In contrast to one photon fluorescence, in TPEF microscopy the signal generated is spectrally remote from the excitation wavelength allowing easier collection of the generated signal. The non-linearity of TPEF is observable from equation 1.14 as the intensity of the generated signal depends quadratically on the intensity of the incident field [35]. Though typical intrinsic TPEF cross-sections are lower than that of exogenous labels, there are a number of endogenous fluorophores in mammalian tissue that have been investigated using TPEF. Among such autofluorophores include porphyrins, aminoacids, macromolecular proteins like collagen and elastin, enzymes such as NADH and flavines [36]. Similarly, the absorption of more than two low-energy photons simultaneously could result in the excitation of an electron from the ground state to an electronic excited state. The non-linearity in the dependence of fluorescence intensity on the incident fields correspondingly scales with the number of photons involved. Fluorescence arising from such non-linear absorption of photons, including TPEF, is in general termed as multi-photon excited autofluorescence (MPEF).

Second Harmonic Generation (SHG)

SHG is a second order, non-linear, coherent scattering optical process. In terms of photon exchange, in SHG, two photons of frequency ω are consumed to form a photon with twice the frequency 2ω of each incident photon. Figure 1.4(c) shows the energy level diagram of this process.

SHG is the result of the second-order non-linear contribution to the polarization $\vec{P}^{(2)} = \epsilon_o \chi^{(2)} \vec{E} \cdot \vec{E}$. The second order non-linear susceptibility $\chi^{(2)}$ vanishes for

a centrosymmetric medium. As such, SHG occurs only in non-centrosymmetric materials. Proceeding as in the CARS case, the intensity of the SHG signal can be determined starting from the non-linear wave equation. Accordingly, the intensity of the SHG signal after traversing a $\chi^{(2)}$ material of thickness L is given by:

$$I(2\omega) \propto (\chi^{(2)})^2 \cdot I_w^2 \cdot L^2 \cdot \text{sinc}^2\left(\frac{|\Delta k|L}{2}\right). \quad (1.15)$$

The intensity of the SHG signal scales quadratically with the incident field intensity. The wave-vector mismatch here is formulated as $\Delta k = 2k_\omega - k_{2\omega}$ in which the k_ω , $k_{2\omega}$ are the wave-vectors for the excitation and the SHG fields respectively. SHG microscopy collects morphological information about the distribution of anisotropic structures in biological tissue [37]. Typically in mammalian tissue SHG arises from collagen, a highly-ordered, non-centrosymmetric structure that has large hyperpolarizability [38]. Consequently, the structural organization of collagen at different levels has been investigated using SHG microscopy [39]. Other structural proteins that are SHG active include actin-myosin, tubulin and cholesterol crystals.

Multi-modal Imaging Scheme

Combining CARS, SHG and TPEF into a single multi-modal microscope allows one to obtain complimentary information from endogenous indicators in the sample. Accordingly, mammalian tissue samples can be characterized with regards to the distribution of different molecular groups, collagen and endogenous autofluorophores. Such high resolution morpho-chemical information about cells and tissue enables the assessment of physiological as well as pathological states.

These techniques are non-linear and as such there are some inherent advantages gained when imaging biological samples. First, because the signal generation is constrained to a tight focal volume in non-linear imaging, there is an intrinsic optical sectioning capability. This allows three-dimensional imaging of thick tissue samples and whole cell volumes. In contrast to optical sectioning provided by pinholes in confocal microscopy, here the efficiency of signal detection is not compromised and no de-scanning is required. Second, during imaging, photodamage and photobleaching of the sample are constrained to the focal volume (wherein the excitation intensities are high enough). Moreover, when compared to the ultraviolet-visible beams used for single photon fluorescence, the longer excitation wavelength of non-linear imaging incur less photodamage to the tissue. The near-infrared (NIR) excitation wavelengths also allow for better depth of penetration in tissue due to lower absorption, by water and hemoglobin, and lower scattering [40, 41, 42]. Another

Introduction

contributing factor for an improved penetration depth in non-linear imaging is the fact that rather than just the ballistic photons as in confocal microscopy, all of the scattered photons from the tissue contribute to the detected signal from a single scan position. Non-linear multimodal frameworks that exploit these merits have found diverse application in biological and diagnostic research areas [43, 44, 45].

2 | Discussion

2.1 Multimodal Microscope [FBL1]

The basic features of microscopic platforms that combine the non-linear modalities CARS, SHG and TPEF are discussed using the setup shown in figure 2.1(a) as a reference.

The first critical aspect of such setups is the excitation laser source. High photon fluxes are required for non-linear excitation. This necessitates the use of ultrafast laser sources that keep the average power low but result in intense peak powers at the focal spot. Historically the first among the modalities to be incorporated into laser scanning microscopes, TPEF has been implemented using laser sources that generate pulses of duration ranging from 100 femto-seconds (fs) to few pico-seconds (ps) [35]. SHG modality has been incorporated to such setups by making small modifications to the detection system with regards to the detection filters used and the placement of the detector. In these implementations, fs pulses are preferred as they keep the average power (P_{avg}) minimum thereby limiting tissue photodamage without compromising on the high peak power (P_p) needed to generate the non-linear effect (as apparent in the equation $P_p \propto P_{avg}/(f_p \cdot \tau_p)$ where τ_p is the pulse duration and f_p is the pulse repetition rate). The more stringent constraints in the multi-modal framework in terms of the laser source are placed by the CARS modality as it requires two excitation wavelengths that need to be overlapped both spatially and temporally in the sample. In conventional CARS systems based on bulk sources, the outputs of a mode-locked laser and a synchronously pumped optical parametric oscillator (OPO) are the sources of the Stokes and pump beams for the CARS excitation, respectively. For CARS microscopy, the ps mode of operation is preferred over the fs as it increases the resonant signal to non-resonant background ratio and reduces photodamage to the tissue. This is because typical Raman line width's are smaller than the bandwidth of fs pulses leading to inefficient use of the

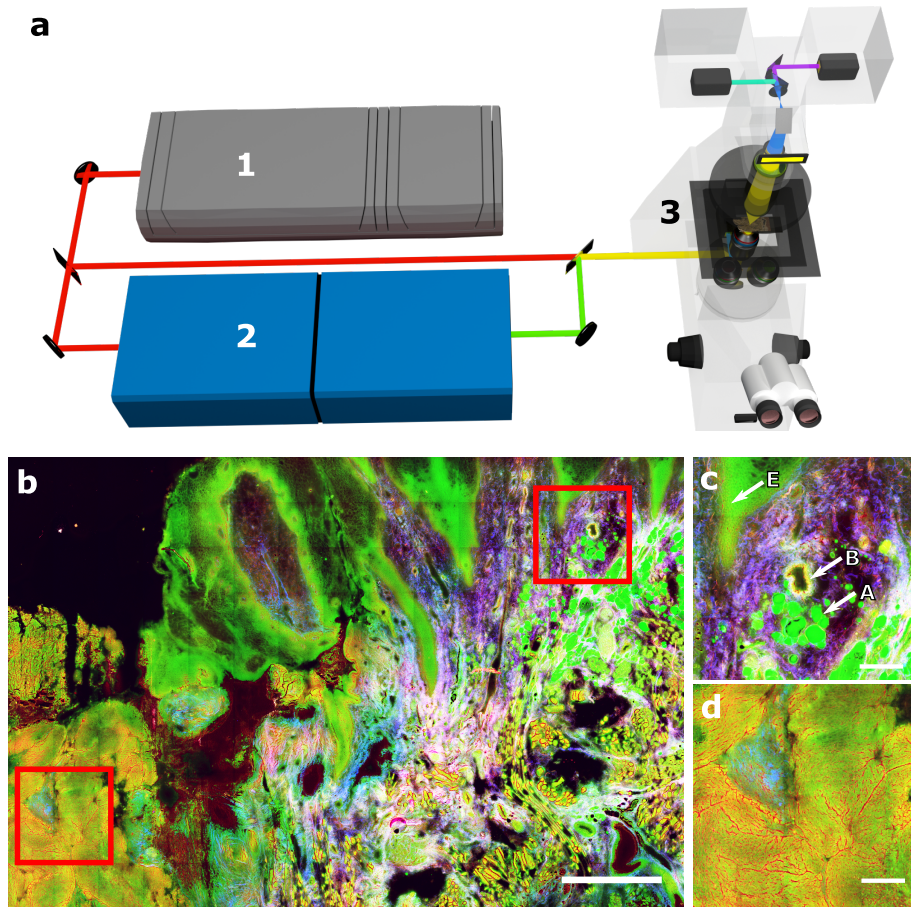


Figure 2.1: *Non-linear multimodal imaging for disease diagnosis. (a) Experimental setup for multimodal imaging. (1) Ti:sapphire laser (2) OPO (3) Laser scanning microscope (LSM Zeiss 510 Meta). (b) Multimodal image of a head and neck squamous cell carcinoma. Scale bar: 500 μm (c) Inset pictures showing, elastin fibers surrounding a blood vessel (B), adipocytes containing lipids (A), collagen in blue, and healthy squamous epithelial tissue(E). Scale bar : 100 μm (d) cancerous squamous epithelial tissue. green: CARS, Red: TPEF, blue: SHG. Scale bar : 100 μm*

laser power available, high NR background and in case other resonances are nearby reduced spectral resolution.

In the particular case presented in figure 2.1(a) a Ti:sapphire laser (1) generates 2 ps laser pulses at pulse repetition rate of 76 MHz. A beam splitter divides the beam into two and part of the beam serves to pump a tunable OPO (A.P.E, Germany) (2) wherein parametric process in a $\chi^{(2)}$ PPLN crystal generates a NIR signal (1000-1600 nm) and an IR idler beam (1600-3200 nm). Wavelength tuning in the OPO is possible by cavity length detuning exploiting the intrinsic group velocity dispersion (GVD) of an additional 48 mm glass block. An SHG crystal in the path of the signal beam doubles the frequency of the output to provide a beam in the

visible range between 500 to 800 nm. As the cavity length of the OPO is matched with the pump the pulses generated are synchronous. Different combination of the beam from the Ti:sapphire laser and the signal and idler from the OPO can be used for the CARS process. To illustrate, for probing the Raman-active vibrational peak of the CH₂ stretching vibration centred at 2845 cm⁻¹ the fundamental output from Ti:sapphire laser tuned to 831 nm is used as CARS Stokes beam and the OPO signal set to 671 nm serves as the CARS pump beam. The two beams are then combined using a dichroic mirror and overlapped temporally and spatially before being sent to a laser scanning microscope. Temporal overlap is ensured by adjusting a mechanical delay stage equipped with a retro-reflector, a reasonably manageable task when ps pulses are involved. Spatial overlap can be ensured by making use of two pinholes placed at a certain distance before the microscope.

For the multiphoton imaging experiments performed a commercial inverted laser scanning microscope (LSM 510 Meta, Zeiss, Jena, Germany) is repurposed (3). In the microscope a tightly focused laser spot is raster scanned over the sample and signal intensities are recorded point by point. Here, beam scanning, made possible with non-resonant galvanometric scanners, is selected over sample scanning because it is faster and a large field of view can be covered. The forward generated CARS and SHG signals are collected by a condenser placed after the sample. The anti-Stokes signal generated from the CARS process and the SHG signal produced from the fundamental Ti:sapphire beam are then separated using a beam splitter and further filtered by band pass filters before being detected by photomultiplier tubes (PMTs). The TPEF signals are collected in the backward direction by the focusing objective and filtered by a dichroic mirror, a shortpass filter, and a bandpass filter before being detected by a PMT placed at the base of the microscope.

When the sample to be imaged is bigger than the field of view of the objective, tile scans, which are then stitched into larger mosaics, are acquired. These measurements are performed stepwise by translating the sample in lateral direction with the motorized stage (Märzhäuser Wetzlar, Wetzlar, Germany, accuracy $\pm 3 \mu\text{m}$ in lateral direction). These mosaics are usually affected by visible edge artefacts due to grey-level differences across tile boundaries. A technique was previously introduced for seamlessly stitching the tiles into an artefact-free mosaic [46]. The algorithm first corrects for the uneven illumination that appears in each of the tiles with a multiplicative average brightness tile. Then neighbouring tile edges are compared and the brightness at each corner is forced to a single common value. The correction at the edges is then broadcast to the rest of each tile using a mask that takes the values of each tile corner into consideration. This stitching algorithm has been

successfully applied to the non-linear images acquired using the microscopic setup shown in figure 2.1(a).

The described non-linear multimodal imaging platform has been integrated into the work flow of diseases diagnosis in case studies involving a number of patients and tissue samples. In the standard clinical procedure, suspected tissue lesions are inspected and tissue excisions are made. Histopathological slides are then prepared from these excisions. Typically these slides are examined under bright field microscopes. From these observations, mostly morphological information is extracted because the chemical contrast provided by the methods is limited. For instance in the commonly used hematoxylin and eosine (H&E) staining protocol, structures in a cell that can be stained with a basic dye(hematoxylin) such as DNA in the nuclei are discriminated against the components mostly found in the cytoplasm that are stained with the acidic dye(eosin). Such staining procedures are time consuming and destructive. This is where non-linear multimodal imaging fits into the picture by allowing the examination of the unstained slides. It also provides the necessary morpho-chemical contrast at diffraction limited resolution.

HNSCC and Multimodal Image Analysis

The multimodal imaging approach introduced above together with state of the art image analysis procedures has for instance been used to discern between healthy and cancerous tissue in the case of head and neck squamous cell carcinoma [FBL1] as shown in figure 2.1(b) on page 15. In the tissue samples imaged, different structures are discernible with the complementary morphological and chemical contrast provided by the combination of the CARS, TPEF and SHG modalities. In particular, the CARS modality tuned to match CH_2 stretching vibration allows the imaging of lipids. Similarly, elastin, NAD(P)H, and keratin produce strong TPEF signals. The main contribution in the SHG channel arises from collagen in the tissue. The recognition of functional tissue subunits based on this complementary morpho-chemical contrast is exemplified in figure 2.1(c) wherein lipid rich adipose tissue, a blood vessel with high elastin fiber content and collagen tissue are apparent from the CARS, TPEF and SHG modalities respectively. Similar to visual inspection of stained tissue samples, characteristic morphological changes affiliated with malignant transformation, such as altered cytoplasm to nuclei ratio, are observable from these multi-modal images 2.1(d).

Moreover, the relative intensity of the modalities provides additional information that can be used in the discrimination of cancerous and healthy tissue areas. In this

regard multidimensional histograms, typically employed in co-localization analysis, are suitable ways to present the information contained in multiple channels. From such analysis, it is evident that healthy and cancerous areas form separate clusters in the scattergrams. Quantitatively such information can be formulated as a Michelson contrast to establish the discriminatory parameters TPEF to CARS contrast (TCC) and TPEF to SHG contrast (SAAID). Consequently, TCC is for example higher in cancerous tissue compared to healthy tissue albeit with significant inter-patient variance that prevents automatic prediction.

Another set of image attributes that correlate well with the morphological information in the images are texture features. A previous study ([47]) has examined the viability of using texture features extracted from CARS images in the automatic prediction of healthy and cancerous tissue. The performance of various texture descriptors has been analysed in an automatic feature selection framework to select the ones optimal for classification. Analogously, in [FBL1], the statistical texture properties, mean, standard deviation (SD), smoothness, third moment, uniformity, entropy were computed for all the three modalities and a Fisher's discriminant ratio was used to rank their performance in discriminating healthy and cancerous tissue. Accordingly, the 20 top-performing parameters were employed in a linear discriminant analysis (LDA) model with four classes ('healthy', 'cancerous', 'other' and 'background'). The resulting LDA predictions compared well with the pathologist's diagnosis. For the majority of the subsequently presented work in this thesis the focus of CARS imaging is shifted from the highly investigated, CH group of stretching vibrations to the vibrational peaks in the relatively unexplored fingerprint region.

2.2 CARS imaging in the Fingerprint Region ([FBL2], [FBL3])

The abundance of spectral signatures from various molecules found in cells and tissue make the spectral fingerprint region ($800\text{--}1800\text{ cm}^{-1}$) the most biologically relevant. CARS micro-spectroscopy in this region is challenging for that same reason as elaborated in section 1.2.1. Specifically, the congestion of the spectral peaks and their interference with each other and non-resonant background complicates the isolation of individual contributions in the CARS spectra acquired. However, there are organelles and compartments in cells and tissue that serve as repository to relatively high concentrations of certain molecules that have strong Raman signatures in the fingerprint region. For instance, as much as 80 % of the vitamin A in

the liver is enclosed in lipid droplets of hepatic stellate cells [48]. The high-density localization of such molecules within discernible repositories could be utilized as a means of contrast in CARS microscopy.

The influence of the non-resonant CARS background is reduced when using NIR excitation wavelengths for both the pump and Stokes. This is mainly owing to the fact that two photon absorption responsible for the non-resonant background is reduced as there are fewer two photon electronic resonances in tissue that can be excited by NIR wavelengths. However, the setup introduced above (shown in figure 2.1 on page 15) is not suited for working with NIR excitation wavelengths as the pump beam is selected to be in the visible range. This is because the optical components in the microscope reduce the overall throughput to as low as ($< 10\%$) for wavelengths above 850 nm. For the experiments in the NIR wavelength region an in-house built microscopic setup depicted in figure 2.2(a) is employed instead. The depth of penetration that is achievable with optical microscopic methods is also dependent on the wavelengths of the excitation beams. The NIR photons utilized in this setup travel deep into tissue as they lie within the biological window of the electromagnetic radiation. There is less scattering by mammalian tissue (scattering scales with λ^{-4}) and less absorption by water and hemoglobin within this window as can be seen in figure 2.2(b).

The laser source for this microscope is an Nd:vanadate picosecond laser (High-Q picoTrain, High-Q laser, Austria)(1) that generates a 1064 nm, 7.5 ps long pulses at 80 MHz repetition rate. An in-cavity crystal in the pico-train frequency doubles this fundamental beam to produce an output that pumps a tunable OPO (Levante Emerald, A.P.E, Berlin, Germany)(2). The parametric process in the OPO occurs in a temperature tunable LBO crystal. The signal from the OPO is tunable from 660 to 960 nm while the respective idler tuning range is 1120 - 2030 nm. The signal from the OPO can be directly used for the CARS process without further conversion resulting in a stable system. The two excitation beams are overlapped, spatially and temporally, and coupled into the in-house built microscope (3). Assembling such a custom microscope enables easy access to the optical components so that efficient signal generation and collection can be optimized for each modality. This is particularly relevant to non-linear microscopy because the generated signals are weak compared to the excitation beams and proper collection of the signals and rejection of the interfering signals than what is provided from commercial systems is needed. The galvo-scanners of the microscope (4) direct the beams to the back focal plane of the objectives using NIR optimized scan and tube lenses. Depending on the objective used different relay lenses can be fitted on the microscope. Here,

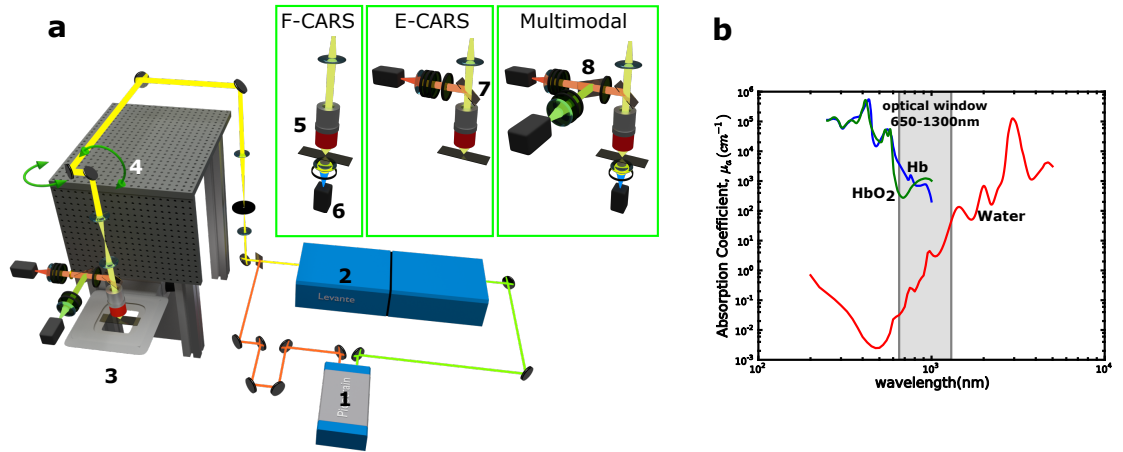


Figure 2.2: (a) *Experimental setup for non-linear multi-modal imaging with NIR excitation wavelengths and an in-house built laser scanning microscope. One output of a Nd:vanadate picosecond laser (High Q picoTrain) (1) is used as Stokes beam for the CARS process while a frequency doubled output pumps an OPO (Levante Emerald) (2) which is used as CARS pump. The two beams are combined and sent directly to a laser scanning microscope (3). The combined beams are directed by the galvo-scanners (4) of the microscope onto the back focal plane of a focusing objective lens (5). Forward generated CARS is detected by a PMT (6) placed after a condenser lens. The backward generated CARS signal can be separated from the excitation beams and redirected to another PMT with beam splitter (7). In the multimodal detection configuration a dichroic mirror (8) separates the CARS from MPEF and/or SHG signals.* (b) *Absorption spectra of water and blood by mammalian tissue, elucidating the clear optical window for tissue imaging (adapted from [42]).*

when working with a $20\times$, 0.4 numerical aperture (NA) NIR objective (M Plan Apo NIR $20\times$, Mitutoyo, Japan) (5) four NIR achromatic doublets that keep the 4 mm diameter of the beam incident on the scan mirrors are used to fill the relatively small back aperture of the objective. For studies with a larger back aperture, $25\times$, 1.1 NA water immersion objective (CFI Apo LWD 25XW, Nikon Inc., U.S.A) a more compatible NIR tube scan lens combination (MPM-SL, Thorlabs, originally designed for Thorlabs multiphoton imaging systems) is fitted onto the microscope.

The different detection configurations possible with this setup are depicted in the inset pictures of figure 2.2(a). The forward generated CARS and SHG signals can be collected in the forward direction using a condenser or a simple focusing lens with aperture comparable to the focusing objective as shown in the F-CARS configuration. The signals are ultimately detected by a PMT (H10721-20, Hamamatsu, Japan) (6) after passing through band pass filters appropriate for the modality. For the backward generated CARS and TPEF signals the collection in the epi direc-

tion with the E-CARS configuration is possible. Here a beam splitter (7) is needed to separate and redirect the generated signal from the excitation beams. For the CARS modality additional series of band pass filters are placed before the PMT to selectively detect the anti-Stokes signal. Analogously, for the TPEF modality corresponding band pass filters can be employed to detect the non-linear fluorescence excited by the fundamental beam of the Ti:sapphire. To detect the three non-linear modalities at the same time the multi-modal configuration is used. In this case, an additional dichroic mirror (8) in the backward beam path is needed to separate the CARS signal from SHG and fluorescence signals.

Initial experiments with this setup in the fingerprint region involved pure Retinoid molecular species (retinol synthetic, retinyl palmitate, retinoic acid and trans-Retinal) (Sigma – Aldrich Chemie GmbH, Germany). These molecules feature intense vibrational peaks in their Raman spectrum in the vicinity of 1590 cm^{-1} . This arises from the conjugated carbon double bonds (C=C) in their elongated polyene structure. The functional groups specific to each species result in various shifts in the position of the peak. The estimated spectral resolution of the CARS setup ($\approx 5\text{ cm}^{-1}$), in principle, allows the discrimination of the different retinoid species. This has consequences in liver imaging because the retinoid metabolite composition of healthy and pathological liver is different [49]. To test the capability of the setup, CARS images were acquired from diluted (1:10 in ethanol) (figure 2.3(a-c)) and pure (figure 2.3(d-f)) forms of retinol and trans-Retinal placed alongside each other on a microscopic slide. CARS spectra were extracted from a series of images that are acquired by varying the pump wavelength. The OPO output tuned to 909 nm combined with the fundamental beam from Nd:vanadate allows probing of the Raman-active vibrational peak of retinol at 1595 cm^{-1} and results in an anti-Stokes signal at 795 nm. Trans-Retinal has a shifted vibrational peak at 1572 cm^{-1} which can be probed by tuning the OPO beam to 911 nm leading to an anti-Stokes signal at 797 nm [50]. In these experiments a 775 nm dichroic mirror (FF775-Di01-25x36, Semrock, U.S.A) is used to separate the anti-Stokes signal from the excitation beams. The series of band pass filters (FF01-785/62-25, FF01-794/160-25, FF01-731/137-25, Semrock, U.S.A) placed in the detection path work well for both vibrational peaks probed.

The normalized mean intensity of regions in the acquired CARS images were then presented in box-plots as a function of the pump wavelength. The spectra obtained are also fitted to examine the influence of the non-resonant background in the acquisitions. This entails the reformulation of equation 1.13, that summarizes the frequency dependence of the anti-Stokes signal intensity by inserting the Lorentzian expression for just the Raman resonant part in equation 1.12 resulting in:

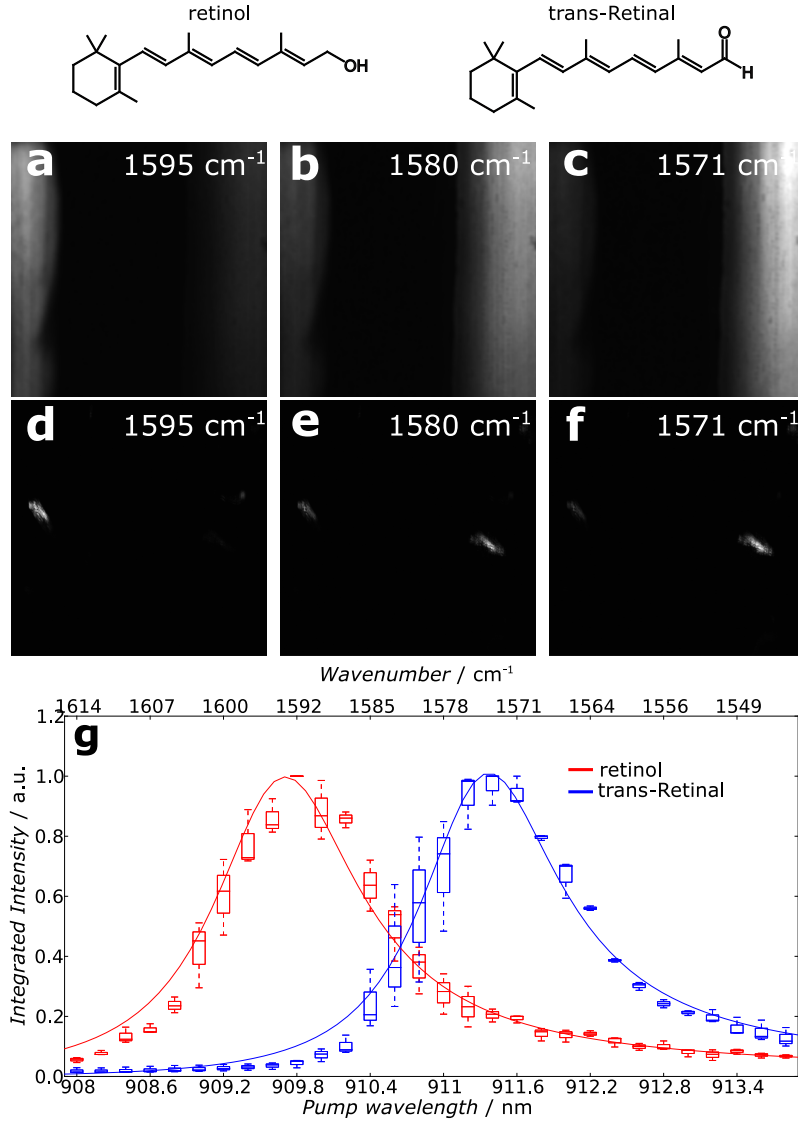


Figure 2.3: CARS spectral properties of pure Retinoid molecular species. A spectral series CARS images of retinol and trans-Retinal diluted (1:10 in ethanol) (a-c) and in pure solid form (d-f). The images with the CARS setup tuned to match 1595 cm^{-1} (a,d) show just the retinol. In the spectral position between the two resonance peaks (1580 cm^{-1}) (b,e) both retinol and trans-retinal are visible with reduced contrast. When the CARS setup is tuned to match 1571 cm^{-1} (c,f) the trans-retinal forms a stronger contrast than the retinol in the images. (g) CARS spectra from the series of images show two distinct peaks for the two molecular species.

$$I_{AS}(\Delta) \propto \chi_{NR}^{(3)2} + \frac{A_R^2}{\Delta^2 + \Gamma^2} + \frac{2\chi_{NR}^{(3)}A_R\Delta}{\Delta^2 + \Gamma^2}. \quad (2.1)$$

The fitting then utilized this model to determine the unknown parameters, ω_{vib} , Γ , A_R and $\chi_{NR}^{(3)}$ using a least square model in Python (Python Software Foundation, U.S.A).

From such CARS spectral acquisitions, depicted in figure 2.3(g), it is evident that the peak of retinol can be clearly discriminated from that of trans-Retinal. The two observed resonances resemble Lorentzians indicating the major contribution in the CARS spectrum arises from the Raman-resonant components that is proportional to the imaginary part of $\chi^{(3)}$. Similar results are obtained for the other Retinoid molecular sub-species envisaging the potential of the microscopic setup for investigating retinoid metabolism. The subsequently presented sections demonstrate the application of the finger-print CARS contrast in tissue (hepatic) and cellular (diatoms) environments.

Hepatic Retinol Content Investigation

Vitamin A is instrumental in vision, immune system, growth and development in general [51, 52, 53]. Most of the vitamin A in the body is stored in the liver, particularly in the Hepatic stellate cells (HSCs) encapsulated in the lipid droplets within the cytoplasm [48]. Pathological states of the liver manifest alterations in the metabolism of vitamin A early on [49] and the loss of retinol content by the HSCs is characteristic of an injured or diseased liver [54]. This prompts the investigation of hepatic tissue retinol content for understanding liver diseases.

Single photon fluorescence of vitamin A in fresh liver cryosections when excited by UV light has helped to image its distribution in a label-free manner in contrast to the invasive gold-standard technique of gold chloride impregnation [55, 56]. However, rapid photobleaching and tissue photodamage by UV light has long prevented fluorescence from being a practical approach for long duration investigation of hepatic tissue [48]. These problems are circumvented when using CARS microscopy which also enables thick tissue imaging because of its optical sectioning capability. Particularly with the use of NIR excitation wavelengths better penetration depths can be achieved and the photobleaching of the specimen is avoided.

These factors prompted the study in [FBL2] wherein CARS microscopy is employed to assess the vitamin A content of thick liver tissue by probing the characteristic retinol vibrational peak in the Raman spectra. Consequently, freshly sampled tissue from mouse and pig livers were studied with the NIR CARS microscopic setup. Sample preparation was kept to a minimum and only entailed the excision of tissue blocks and hydration before a cover-slip is placed. A representative CARS image of the mouse liver is depicted in figure 2.4(a). In the image, Raman resonant contribution from the bright spots form a strong contrast with the relatively darker uniform tissue background. Similar contrast is also obtained from the pig liver sample. The

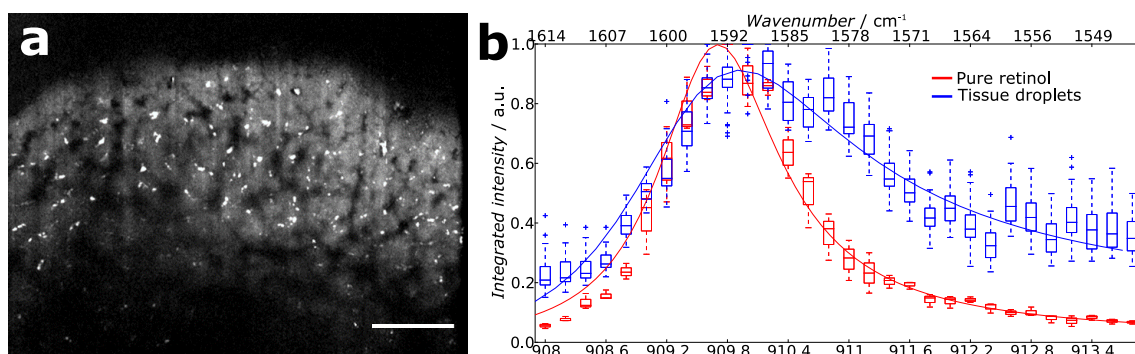


Figure 2.4: *Imaging Retinol in liver tissue samples. (a) Representative CARS image of a freshly excised mouse liver tissue with the CARS modality tuned to probe the retinol peak at 1595 cm^{-1} . The bright spot that form a strong contrast with the rest of the tissue background correspond to retinol containing droplets. Scale bar: $50\ \mu\text{m}$ (b) CARS spectra of pure retinol (red) and droplets in pig liver tissue (blue) computed from a series of images obtained by varying the pump wavelength. The characteristic peak of retinol is observable in the CARS spectra from the tissue droplets, though it features a small red shift of the peak (in wavenumber) and an asymmetry in the peak indicating a minor contribution of the non-resonant background.*

extracted CARS spectrum from these spots is compared to that of pure retinol with its characteristic vibrational peak at 1595 cm^{-1} due to the C=C stretching vibration in its conjugated polyene structure. Although, the spectrum from the tissue droplets has a slight dispersive shape because of the non-resonant contributions the peaks do correspond indicating that the bright spots are indeed deposits of vitamin A. These CARS spectra correspond very well, in terms of peak position and width, with the SRS/CARS spectra of pure retinol recorded by Freudiger *et al.* [57].

Although the CARS signal from the vitamin A sample is strong, information about its distribution in the bulk sample is lacking as there is no information from the rest of the tissue. Particularly, considering the architecture of the liver depicted in figure 2.5; the liver is comprised of roughly hexagonal structures termed hepatic lobules containing a central vein in the middle and portal triads consisting of hepatic veins and arteries at the corners. The liver sinusoids are enlarged capillaries that run from the central vein to the hepatic arteries and veins of the portal triads. The major cells of the liver, the hepatocytes, occupy the hepatic lobule space between the sinusoids. The vitamin A containing hepatic stellate cells are situated in the space of Disse between the liver sinusoids and the hepatocytes. Imaging the lobular structure of the hepatic tissue would provide the missing contextual information.

For these purposes, the modalities SHG and MPEF can be utilized to provide complementary morpho-chemical information. The collagen in the connective tissue that surrounds the hepatic lobules provides decent SHG signal because it is a non-

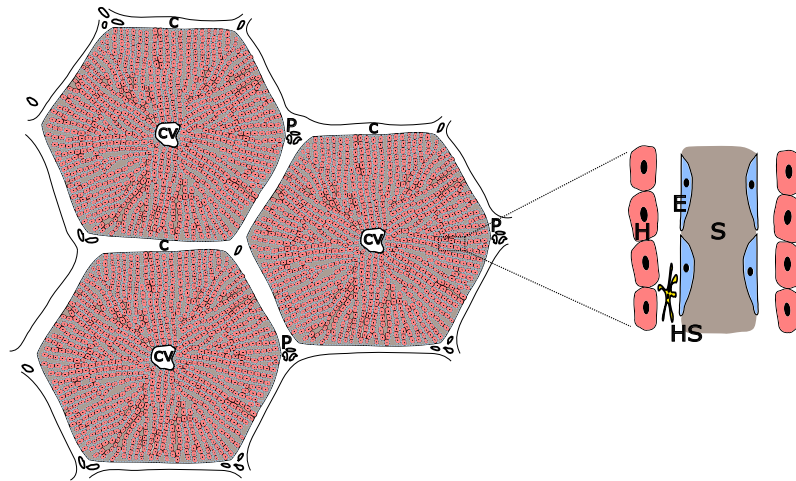


Figure 2.5: A schematic showing the architecture of the liver. The hexagonally shaped hepatic lobules contain the blood filled sinusoids (*S*) that run from the central vein (*CV*) to the portal tracts (*P*). The rest of the hepatic lobule space is lined with the major cells of the liver, the hepatocytes (*H*). The hepatic stellate cells (*HS*) that encapsulate the retinol-containing lipid droplets are situated in the space of Disse between the liver sinusoid and the hepatocytes.

centrosymmetric structure (see figure 2.6(a)). Collecting fluorescence from a broad spectral window allows to image other structures in the hepatic tissue. In particular the bright plates of hepatocytes form a contrast with the dark blood filled sinusoids due to the NADH autofluorescence. Such a multimodal image of a bulk liver tissue is depicted in figure 2.6(b). A corresponding image of the tissue area with the CARS modality tuned to retinol detection is presented in figure 2.6(c). The composite image in figure 2.6(d) better illustrates the merit of using multiple modalities.

The fact that vitamin A is stored in lipid droplets in liver presents another approach to confirm the contrast observed in the CARS images. The image of the lipid droplets in the tissue acquired with the CARS modality reconfigured for detecting the CH_2 stretching vibration at 2845 cm^{-1} results in bright spots that co-localize with those of the retinol (see figures 2.6(e-h)). The extended structure of the liver tissue can be imaged at high resolution by stitching multiple tiles together (with the technique described in section 2.1). Representative stitched MPEF images depicted in figure 2.7(a,c), show the complete structure of a liver louble as introduced above. Independently acquired CARS images from the respective tissue areas presented figure 2.7(b,d) show the distribution of retinol within the elucidated structure. Simultaneous acquisition of the modalities that is made possible by compromising some of the image quality ensures an error-free co-registration of the modalities.

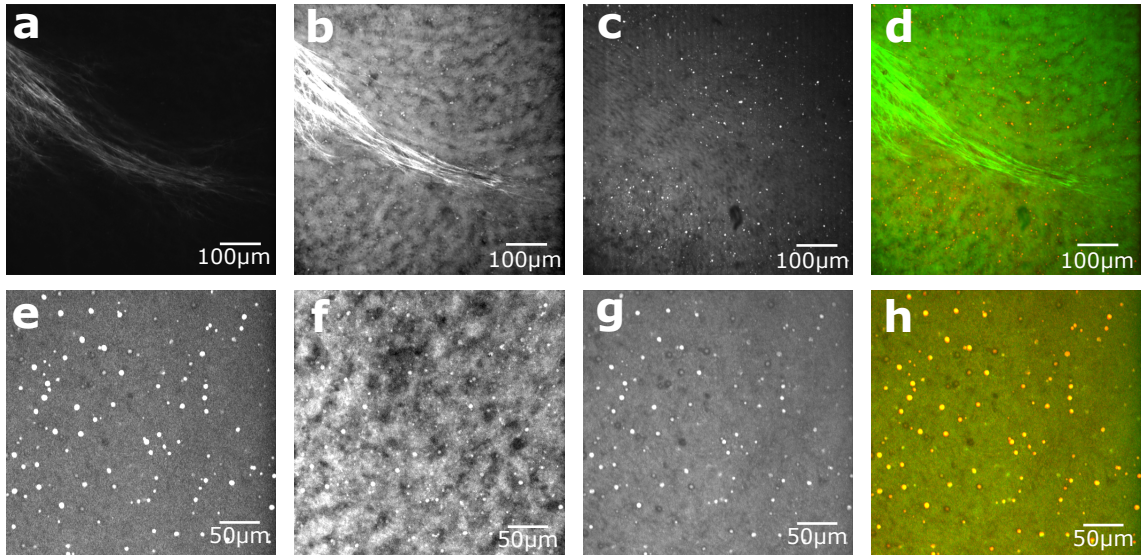


Figure 2.6: Multimodal imaging of hepatic tissue is illustrated (a-d). (a) Connective tissue surrounding hepatic lobules visualized using SHG imaging of a pig liver tissue ($\approx 15 \mu\text{m}$ below the surface). (b) Visualization of hepatocytes and liver sinusoids using MPEF. (c) Vitamin A droplets imaged with the CARS modality. (d) An overlaid image of the modalities showing complementary contrast (red: retinol CARS, green: MPEF plus SHG). The encapsulation of vitamin A in lipid droplets is demonstrated in (e-f). (e) and (f) show pig liver tissue ($\approx 20 \mu\text{m}$ below the surface) imaged using CARS (tuned for vitamin A detection) and MPEF respectively. (g) lipid droplets in the hepatic tissue imaged by re-configuring the CARS setup for probing the CH_2 stretching vibration. (h) overlaid composite image (retinol-CARS: red, multi-photon fluorescence: green, lipid-CARS: blue, lipid-CARS: green) shows the co-localization of the bright spots from both modalities.

Such simultaneously acquired multimodal images are presented in figures 2.7(e) and (f).

The presented approach of hepatic retinol imaging with CARS microscopy does not lead to photobleaching of the signal or tissue photodamage as confirmed by the inspection of a time series of images taken from a single tissue area. A comparative TPEF image of the retinol in hepatic tissue using the setup in figure 2.1(a) with comparable average power leads to the bleaching of the signal and an observable photodamage to the tissue with the multiple scanning.

Such bulk tissue CARS imaging in the fingerprint region is potentially instrumental in the *in vivo* assessment of abnormalities in vitamin A metabolism. The introduced setup could also be applied in nonperturbative investigation of living cells as elaborated in the following section.

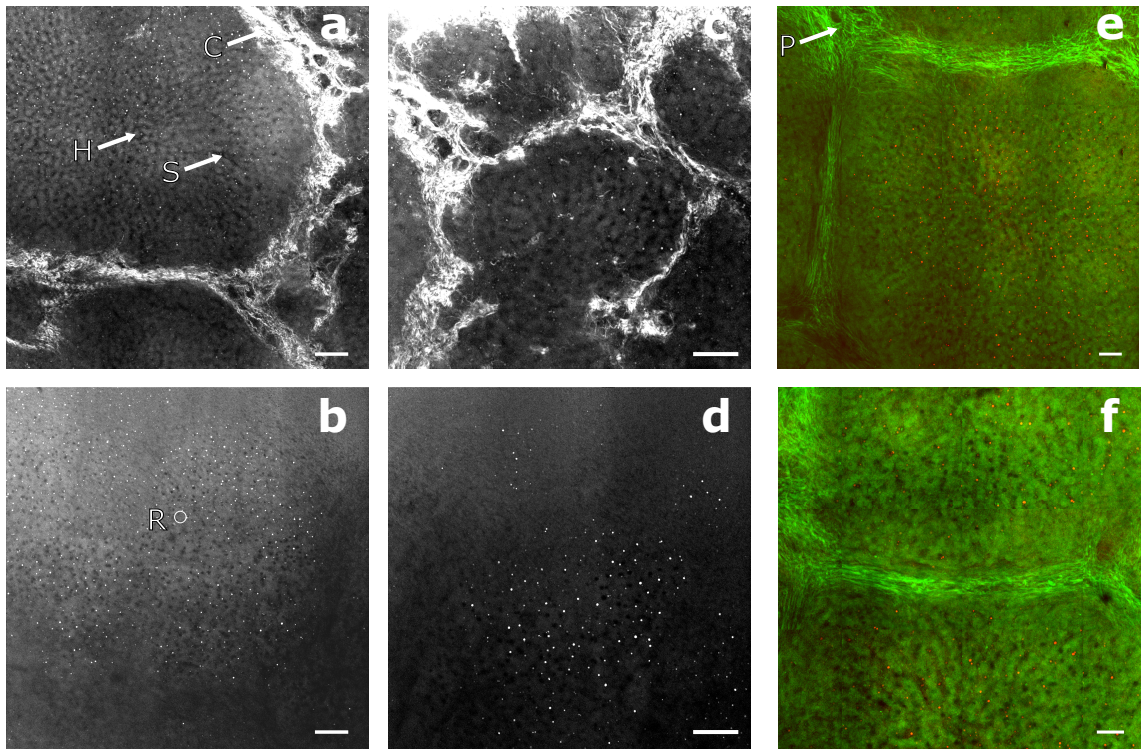


Figure 2.7: Representative large mosaic multimodal images of hepatic tissue. (a) The SHG signal from the connective tissue (C) outlines the partial boundary of a hepatic lobule. The MPEF from the hepatocytes (H) forms a contrast with the dark sinusoids (S). The subsequently acquired image of the same tissue area using the CARS modality tuned to retinol detection shows how the vitamin A droplets scatter throughout the lobular structure. Similar, sequentially acquired multimodal images in (c) and (d) show a more complete structure of a smaller hepatic lobule. Overlaid images from simultaneous acquisition of the MPEF (green) and CARS modalities (red) in (e) and (f) better demonstrate the intra-lobular distribution of vitamin A droplets in a classical liver lobule and a liver acinus (the functional unit of the liver), respectively. Scale bars: 100 μm

Pigment Accumulation in Microalgae

In addition to the principal aim of bio-fuel production, the extraction of value added co-products from microalgae is an active field of research [58]. A number of biomolecules and pigments extracted from microalgae have found various applications in the pharmaceutical, food and cosmetic industries [59]. Particularly, carotenoids extracted from diatoms such as fucoxanthin (Fx) have anti-oxidative and anti-inflammatory properties [60]. The extraction efficiency of pigments from microalgae is influenced by different environmental factors such as light regimen and nutrient composition. With substantial sample preparation involved, the metabolic response of microalgae to these factors, in bulk volumes, can be monitored by

high pressure liquid chromatography (HPLC) and mass spectrometry. Raman spectroscopy has helped bring the assessment of microalgal pigment content to single cell levels and native aqueous environments [61, 62]. The typical Raman scattering efficiency of pigments found in microalgae is low thereby necessitating longer acquisition times that are impractical when large numbers of cells are involved.

CARS presents itself as a viable alternative for these purposes as it provides stronger signals. CARS allows fast, label-free investigation of a large number of cells. In addition, strong single photon fluorescence from chlorophyll is avoided as the anti-Stokes signal detected is blue-shifted from the excitation beams. Accordingly, CARS microscopy was utilized to first map the distribution of pigments, carotenoids in particular, in the uni-cellular autotrophs *Ditylum brightwellii* and *Stephanopyxis turris* and subsequently monitor the effect of different light cycles on the accumulation of these pigments ([FBL3]). From band assignments of Raman spectra from these diatoms [63] there is a prominent peak in the molecular fingerprint region around 1528 cm^{-1} that is attributed to the carotenoid pigments in the diatoms. The single band CARS microscopy experiments focused on these particular bands. The NIR setup described in section 2.2 was used for these studies with the OPO signal tuned to 915 nm as the CARS pump beam and the fundamental output of the pico-train at 1064 nm as the CARS Stokes excitation beam. In these studies the microscope was configured for detection in the epi-direction with simultaneous acquisition of a complementary TPEF.

Typical multimodal microscopic images of *D. brightwellii* and *S. turris* are presented in figure 2.8(a) and (b), respectively. In these images, the red channel corresponds to the CARS modality and the green represents TPEF. The stretching vibration of the conjugated double bonds (C=C) in the carotenoids contained in the chloroplasts of the diatoms form strong resonant CARS contrast to the rest of the cell. In parallel, fluorescence from chlorophyll found throughout the cell forms a complementary contrast in the TPEF channel. To confirm the carotenoid contrast in the CARS images, the spectral properties of the observed high-intensity areas are co-plotted with corresponding measurements of pure fucoxanthin (Fx) and β -carotene in figure 2.8(c). These plots portray the mean intensity from the regions in an image series taken as the pump wavelength is varied. The CARS spectra extracted from the diatoms have a Lorentzian shape signifying a major contribution from the Raman-resonant component. Although various pigments with peaks near this spectral region are found in the diatoms in varying concentrations, the dominating contribution here is apparently from the Fx which has a peak at 1531 cm^{-1} .

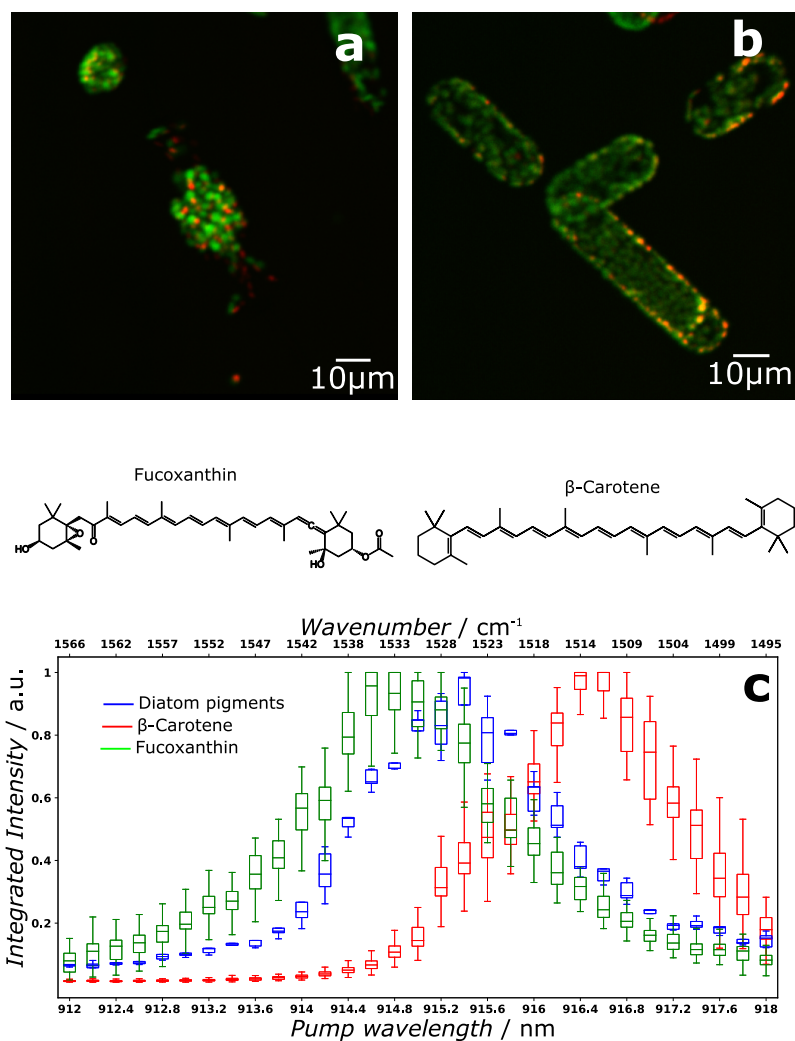


Figure 2.8: Non-linear microscopic images of diatoms. Composite images of the diatom *D. brightwellii* (a) and *S. turris* (b) with the modalities epi-collected CARS at 1528 cm^{-1} (red) and TPEF from chlorophyll (green). (c) CARS spectra computed from series of images of *D. brightwellii* (in blue), pure fucoxanthin (in green) and β -carotene (in red). The peaks of *D. brightwellii*, and pure fucoxanthin (in green) agree well indicating the later to be the major carotenoid contribution in the diatom.

Discussion

This carotenoid imaging potential of the CARS modality helps map its spatial distribution in the entirety of the diatom cell at diffraction limited resolution.

The effect of varying the light regimen on the amount of carotenoid accumulated in the diatoms can thus be investigated with CARS microscopy by imaging the carotenoid distribution in a large number of cells. Sample CARS images of *D. brightwellii* kept under different light-dark cycles are presented in figure 2.9(a) and (b). Evidently, cells kept under longer dark cycles (20:4) display stronger CARS signal intensities. As the CARS signal intensity is quadratically proportional to the pigment concentration, this differences in the images imply that longer dark cycles lead to accumulation of pigments.

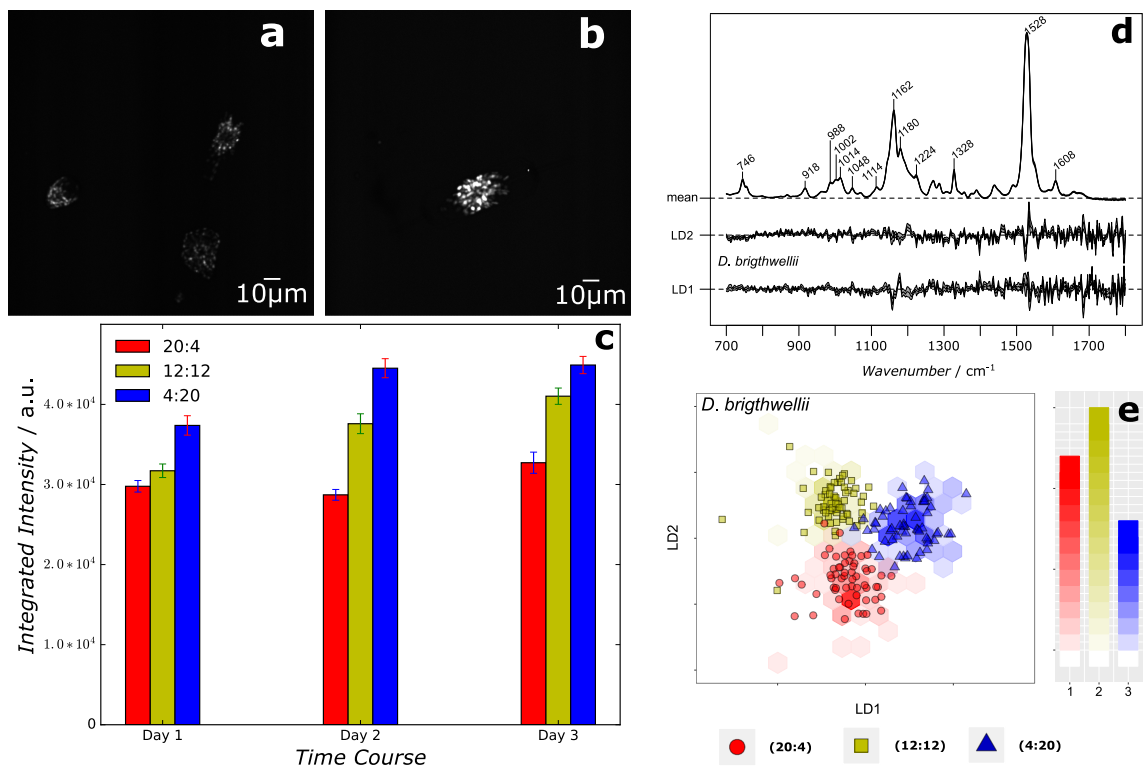


Figure 2.9: Investigating the effect of different light intensities on pigment accumulation in *D. brightwellii*. The diatom under 20:4 light:dark cycle (a) under 4:20 light:dark cycle (b). (c) Mean CARS intensity of *D. brightwellii* for three different light cycles for three consecutive days of experiments showing increased carotenoid accumulation for longer dark periods. (d) Spontaneous Raman spectra of the diatom *D. brightwellii* displayed along with linear discriminant (LD) coefficients (mean and standard deviation). (e) Score plots for a randomly chosen iteration step containing two different layers. One layer with 2-dimensional histogram (hexagons) for the distribution of projected training data into LD and another layer for projections of the corresponding test data that was left out from modelling.

Comprehensive studies involving large number of *D. brightwellii* cells were carried out to assert the above claim. To analyse the large volume of images acquired automatically, a marker based watershed algorithm developed in MATLAB (The MathWorks, MA, USA) was utilized. The algorithm segments the chloroplasts that encapsulate the carotenoids in the diatom images which are then used as masks for computing the mean intensity of the carotenoid areas. The results of the analysis summarized in figure 2.9(c) are concurrent with the observation on the sample images. The observed pigment accumulation for longer dark cycles, consistent over days of experiments, is repeated for studies with *Stephanopyxis turris* as well.

To reveal possible relative pigment contribution changes that might occur simultaneously, spontaneous Raman spectroscopic measurements of limited sample points within the diatoms were performed concurrently (results displayed in figure 2.9(d)). PLS-LDA classification of the Raman results identified changes with contributions solely coming from carotenoid molecules as the light regimen is varied (see figure 2.9(e)). A reallocation in pigment composition favouring the accumulation of photoprotective pigments diatoxanthin (Dtx) and diadinoxanthin (Ddx) is uncovered with these studies. In conclusion, CARS microscopic imaging allowed the incorporation of spatial carotenoid distribution information from a large number of diatoms for analysing the effect of light-dark cycles on pigment accumulation.

2.3 Optimizing Image Acquisition [FBL4], [FBL5], [FBL6]

The experimental setups discussed so far are based on bulk laser sources that have a large footprint and are costly. In addition they are very sensitive to environmental condition such as the temperature in the room, mechanical vibrations and skilled personnel are usually needed to configure and handle the systems. For eventually transitioning the technology to the end user compact, robust, easy to use, turn key systems are needed. This motivated the research for employing fiber-laser sources in non-linear microscopy. Consequently, fiber laser sources that employ four wave mixing inside photonic crystal fibers (PCF) to generate excitation beams needed for CARS microscopy have been developed [64, 65]. Such a laser source, together with a variant of the home-built laser scanning microscope described above have been integrated into a compact, portable platform that is robust, easy to handle and thus suitable for end users [66].

Image Acquisition Rate

Related to the aforementioned development, the discussion in section 2.1.1 highlighted the demonstratively viable use of multi-modal imaging in providing molecular as well as morphological contrast useful for life sciences. However, the studies only highlighted potential use of multimodal imaging because they involved only limited number of tissue samples. For making automatic diagnostic predictions, the image analysis and classification models need to incorporate a large volume of samples. This will also allow incorporation of information from complete biopsies.

However, considering the image acquisition parameters in the clinical studies performed with the multi-modal setup in [FBL1], pixel dwell time of $1.6 \mu\text{s}$ and averaging twice requires half a minute for acquiring a single tile that corresponds to a tissue area of $450 \times 450 \mu\text{m}^2$. This easily scales to hours when imaging typical cryo-sections. Consequently the time needed for imaging a large number of samples would be impractical in a medically meaningful setting. This motivates the need for an improvement in the image acquisition rate of multimodal setups. Such a progress would also have impact on other multimodal imaging application areas. Particularly, the imaging of dynamic processes that is often essential in unraveling intricate molecular processes occurring in living cells that would benefit if video-rate multimodal image acquisition is easily manageable.

A number of ideas have been put forth for improving the image acquisition rate of laser scanning microscopes. Single-focus approaches increase the image acquisition rate by increasing the scanning speed of the scan mirrors. This can be performed by using polygonal mirrors or resonant scanners [67, 68]. The speed of scanning in laser scanning microscopes is constrained by, among other factors, the pixel dwell times needed for imaging which is inherently intertwined with the imaging modality involved. As such, if the signal obtained from the contrast forming mechanism is weak increasing the scanning speed beyond a certain specified limit will only lead to reduced signal to noise ratio. This is usually counter-acted by increasing the excitation powers used for imaging which leads to tissue damage. Another consequence of faster scanning is thermal (linear) damage to the tissue as the sample does not have enough time to cool down between successive scans. These issues are compounded by the complexity of implementing such faster scanning modules to begin with. Particularly, polygonal mirrors are very sensitive to beam fluctuations and the optical design of the entire setup is complicated when dealing with the subsequent artefacts caused. The fixed speed with which resonant scanners are

driven, needed for constant frame grab rates, leads to variation in the pixel dwell times across the field angle of the mirrors.

The other subset of techniques for speeding the image acquisition process parallelize the whole process using multiple beams. These methods split the excitation beam into a number of small beamlets, using different approaches, and apply multiple well separated foci onto the sample [69, 70, 71]. The eventual detection of the signals is then of course carried out using area detectors such as CCD cameras which are less suitable for non-linear imaging when compared to PMTs. Collecting signals from multiple spots at the same time leads to coherence artifacts wherein interference of the multiple signals degrades the images quality. Time multiplexing in which the excitation beamlets are temporally delayed from one another, *e.g* using thick glass plates, solves this particular problem and allows single point detection as the signals obtained can be temporally de-multiplexed [72]. The generation of the multiple excitation beamlets, typically using microlens arrays, presents its own challenges such as in-homogeneities of illumination across the different arms and the inefficient use of the laser excitation light. Another variant of multi-focus approaches circumvents this beam splitting problems by starting with a multi-beam output laser source [73]. This method is based on bulk laser sources with cumbersome oscillator designs that are difficult to scale up in terms of the number of beams to be generated.

In a novel approach to increase the image acquisition speed, some of the elements just discussed were taken and transferred to the compact fiber laser designs introduced in the previous section. In the first step, the concepts of time multiplexed multi-beam excitation and de-multiplexed detection were tested on dual-focus SHG microscopy as it requires only a single excitation beam ([FBL4]). Accordingly, the output of the fiber laser source is divided 10:1 into two parts using a beam splitter and one part is delayed by half the repetition rate of the oscillator by passing through a single mode fiber. 100 m of a single mode fiber (SM800, Thorlabs) is required for the 1 MHz repetition rate fiber laser. The power of the minor part is reduced after transmission through the delay fiber, consequently, an amplification in an additionally spliced 1.5 m of Ytterbium (Yb) fiber (LAS-YB-07-01, CorActive) that is core-pumped at 976 nm is needed to result in power levels similar to the other arm. Sending the two beams at different angles to the galvo-mirrors of the laser scanning microscope results in two laterally separated focal spots at the sample. The signal from these two spots is then sequentially detected (demultiplexed) to record two images within one cycle of the laser oscillator. For demultiplexing the SHG signal, 80 ns long voltage pulses generated by the fiber laser internal photodiode

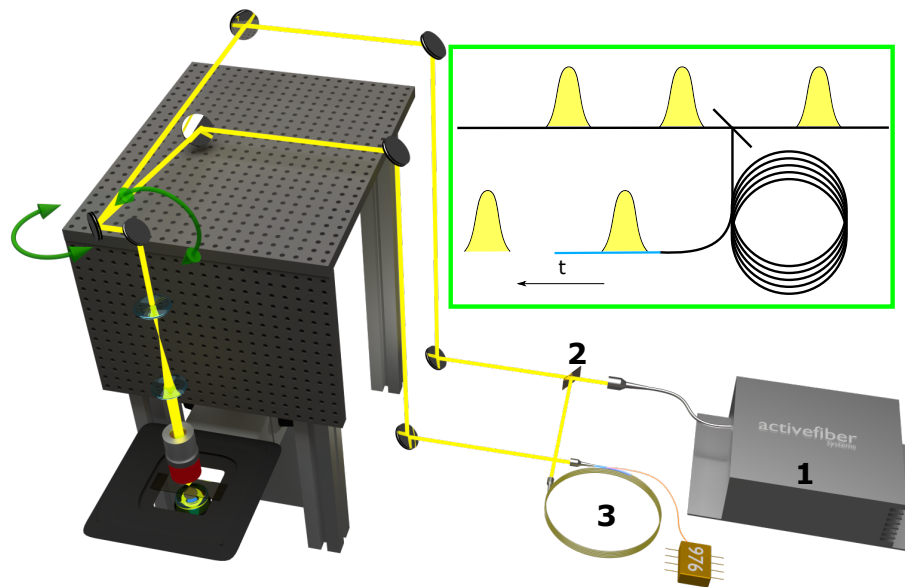


Figure 2.10: *Experimental setup for dual focus SHG microscopy. The fiber laser (1) output is split 10:1 by a reflective filter (2) and the minor part is coupled into a 100m single mode fiber (3) that delays the pulses by half the repetition rate of the laser. The amplified delayed beam and the un-altered beam are coupled onto the galvo-scanners of the microscope at different angles forming two distinct laterally displaced foci in the sample. Demultiplexing by a triggered PMT separates the responses of the signals from the beams. The time multiplexing principle is illustrated in the inset.*

are temporally delayed (9520 Digital Delay Pulse Generator, Quantum Composers) for gating the PMT readout. This whole approach is graphically depicted in figure 2.10.

The two laterally displaced focal spots cover two separate fields of view in essence speeding up the image acquisition process by a factor of two. Another benefit of the dual focus setup can be exploited by varying the divergence of the incoming beams so that two different focal planes can be acquired simultaneously. This is particularly useful when imaging thick tissue samples. These two applications of the dual focus setup are depicted in figure 2.11.

The next milestone in the development of the dual focus concept was to realize it for CARS microscopy ([FBL5]) The fiber-delaying and amplification steps performed on the output of the laser source for the single color in SHG microscopy are impractical to perform for both colors needed for CARS microscopy simultaneously. Therefore, the fiber laser itself was redesigned to provide two outputs each containing two colors. To help illustrate the changes made the schematics of the dual focus CARS fiber laser source is presented in figure 2.12. The original design of the fiber laser introduced in the previous section is highlighted in grey. The laser is

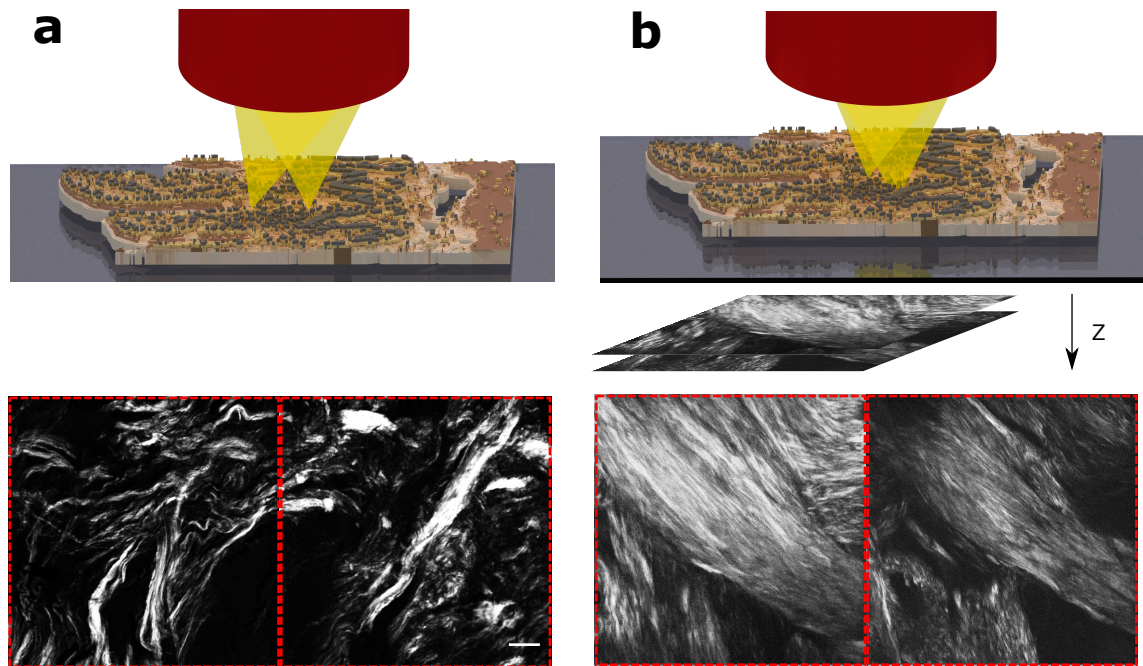


Figure 2.11: *Dual-focus SHG microscopy of human skin tissue. (a) In-plane laterally separated focal spots resulting in an extended horizontal field of view. (b) focal spots at different depths, achieved by varying the divergence of one beam, enabling the acquisition of two focal planes within the same laser pulse cycle. Scale bars: 50 μm .*

based on a Yb fiber oscillator that generates 1032 nm laser pulses at repetition rate of 1 MHz. The oscillator output is amplified in two steps in Yb fibers followed by four wave mixing inside a PCF fiber wherein signal and idler beams are generated. The dispersion characteristics of the PCF are adjusted to generate a signal output at 797 nm so that it can be used as a pump for the CARS process together with the fundamental output of the oscillator to probe the CH_2 stretching vibration at 2850 cm^{-1} . In the redesign for dual focus CARS the oscillator output is first split using a beam splitter placed before the main amplification step and one part (shaded in yellow) is fiber delayed by half the repetition rate of the oscillator and two paths proceed with further amplification and four wave mixing in a PCF as in the original laser design. The result is a dual output laser source with each output containing both colours needed for CARS microscopy.

The two outputs can be utilized as in the case of dual focus SHG microscopy, to result in two laterally displaced fields of view by controlling the angle with which they hit they scan mirrors. CARS images of human artery tissue acquired with such displaced but overlapping fields of view are presented in figures 2.13(a-b). Manipulating the distance between the fiber ends and achromatic doublets that

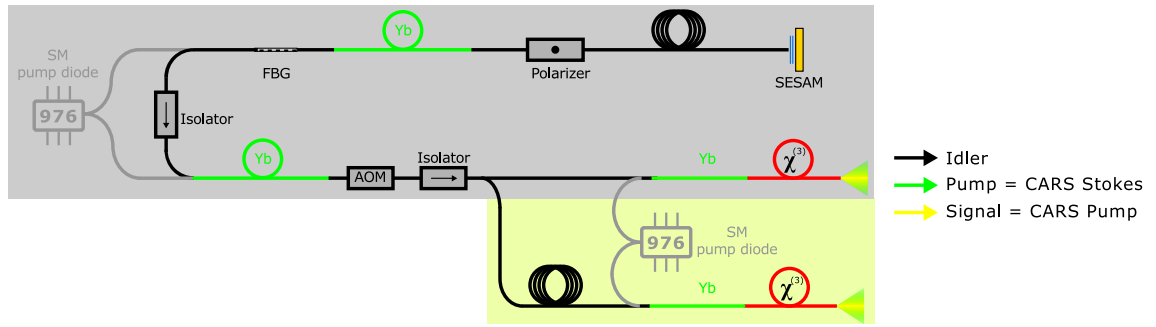


Figure 2.12: Schematic of a dual focus CARS laser source. An oscillator, bounded by a semi-conductor saturable absorber mirror (SESAM) at one side and a fiber Bragg grating (FBG) at the other produces an output that is split into two paths after being amplified. A fiber delay in one path allows time multiplexed outputs. This is succeeded by further amplification in a Yb fiber and second color generation using four-wave mixing in a PCF in both arms of the laser. The modification to the original laser layout, presented first in [64] (grey-shaded), is highlighted in yellow.

collimate the beams enables one to modify the divergence of the beams. This can be used to acquire two laterally displaced focal planes within one cycle of the fiber oscillator as shown in figure 2.13(c-d). The focus of the second beam in this case is placed on the border between the thin tissue slice and the sample holder made of quartz glass to emphasize the lateral separation of the two focal planes.

The characteristics of the beams obtained from the redesigned laser source configuration are comparable to the single focus laser designs and consequently the quality and contrast on the CARS images obtained are maintained. There appear to be no coherence artefacts and interfocus cross talk indicating the effectiveness of the time multiplexing and demultiplexing modules. Although the results demonstrated here are for the CARS modality, this approach might as well be used for the other non-linear modalities, TPEF and SHG with the placement of proper filters in the detection path. In general, the proof of principle experiments carried out demonstrate the potential of multiple focus non-linear microscopy based on compact fiber laser sources. Increasing the number of foci points is also possible by adding similar beam paths of varying delay fiber lengths. The theoretical constraint is the number of pulses that can be accommodated within the temporal window of the detector. In practice, other factors also hinder the relay of multiple beams onto the scan mirrors of the laser scanning microscope. The current mechanism of coupling multiple beams onto the small surface area of the scan mirrors using just steering mirrors is not a practical approach when a large number of beams are involved. For these purpose, dedicated beam scanning module design that involve multiple scan mirrors could be a solution. Alternatively, the twice-fold increase in

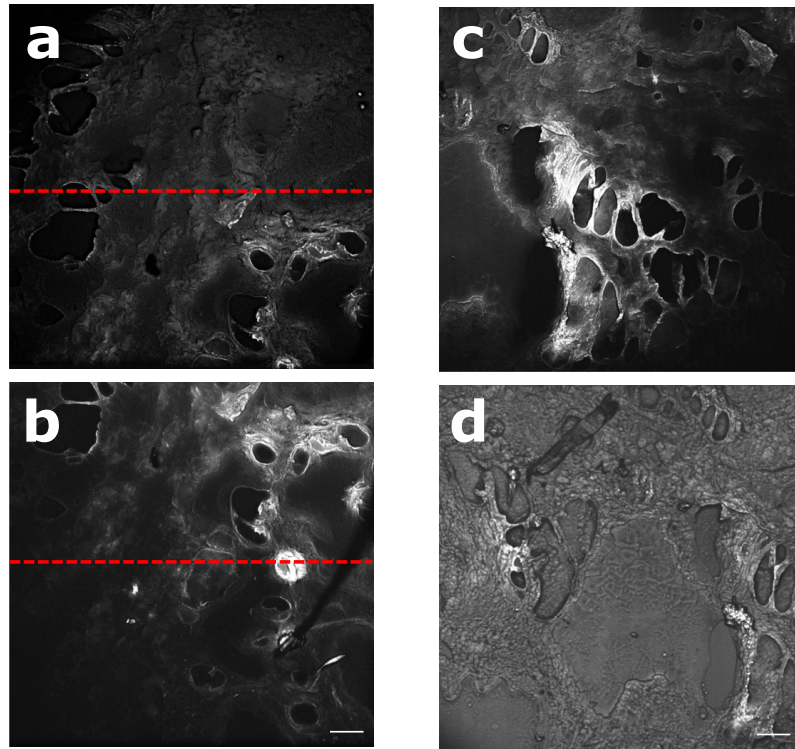


Figure 2.13: *Dual-focus CARS microscopy of human artery tissue. (a) and (b) show two laterally displaced fields of view acquired simultaneously with overlapping parts emphasized with red dashed lines. (c) and (d) show two axially shifted images with one being out of focus. Scale bars: 50 μm .*

the image acquisition rate can be sacrificed for an improvement in the signal to noise ratio by simultaneously increasing the pixel dwell time. The setup also presents an opportunity to accommodate different non-linear modalities on a single detection module.

Spatial Resolution

Collinear beam geometries for the CARS excitation beams allow the prospective use of alternative excitation beam profiles. Resolution enhancement is an area that is usually explored when employing beam profiles other than the standard Gaussian. Consequently a comparison is made between the focal intensity distribution of a typically employed Gaussian beam with that of a Bessel beam ([FBL6]).

When examining the resulting two beam profiles it became evident that, although it features side lobes, the Bessel beam has a thinner lateral dimension than the Gaussian at the focus. Since the induced anti-Stokes polarization in CARS is given by $|P_{as}^{(3)}|^2 \propto I_p^2 I_s$ choosing a Gaussian profile for the Stokes beam would multiplicatively remove the side lobes and preserve the narrow lateral profile. This is

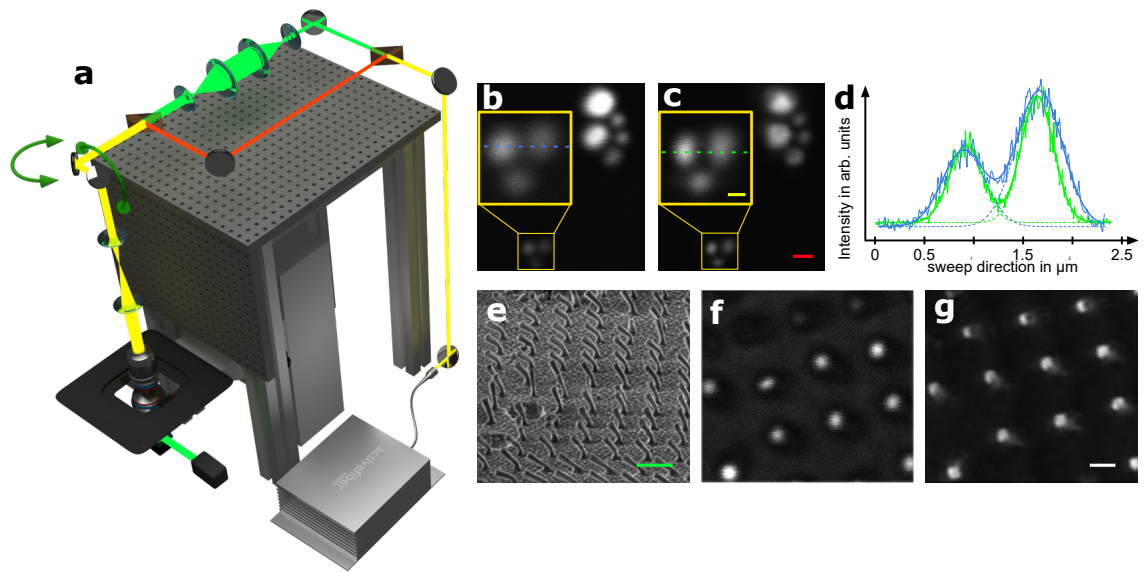


Figure 2.14: *Bessel Beam experimental setup (a) and measurement results (b-g). (a) The pump and Stokes beam in the fiber laser source output are separated by a beam splitter. Four lenses reshape the pump into a ring-shaped beam. The two beams are then recombined before being sent to the galvo-scanners of the microscope. The generated anti-Stokes radiation is collected in forward direction and detected by a PMT. (b) and (c) present CARS images of polyethylene beads under Gaussian and Bessel illumination, respectively. (d) plots the profile of bead at the position of the green dotted line. The blue graphs show the profile and Gaussian fits of the Bessel illuminated sample while the green graphs plot corresponding data for the Gaussian illumination. (e) displays a scanning electron microscope (SEM) image of the a micro-structured cyclic-olefin copolymer (COC) sample. (f) and (g) show CARS images of a the COC sample under Gaussian and illumination, respectively. The yellow, red, green and white scale bars correspond to $0.5 \mu\text{m}$, $1 \mu\text{m}$, $5 \mu\text{m}$ and $2 \mu\text{m}$ respectively.*

expected to result in higher resolution in the lateral direction when a Bessel pump beam is used instead of a Gaussian in CARS microscopy. For an ideal Bessel beam the improvement in lateral resolution would be a factor of 1.33. In an experimentally realizable Bessel like focal intensity profile, achieved by focusing a thin laser ring, an enhancement by a factor of 1.25 is expected.

To experimentally demonstrate this resolution improvement the microscopic setup in figure 2.14(a) was used. For lossless generation of the laser ring in the pump arm of the excitation path two axicons were used. A keplerian telescope is then used to reduce the beam to a size small enough to fit the scan mirrors of the microscope. A collection objective with an NA larger than the focusing objective was chosen based

on the numerical analysis of the anti-Stokes beam far field radiation that highlighted the strength of the signal at angles higher than the excitation beam.

The experimental results obtained for these parameters are presented in figures 2.14(b-g) wherein polyethylene (PE) beads are imaged with Gaussian (figure 2.14(b)) and Bessel (figure 2.14(c)) pump beams. The resulting differences are better illustrated in the single line profile extracted and the respective Gaussian fits in figure 2.14(d). Similar experiments with cyclic-olefin copolymer (COC) samples demonstrate that small structures are more pronounced in the Bessel images when compared to Gaussian CARS images figure 2.14(e-g).

3 | Summary

Innovative visualization techniques are needed to meet the increasing demands in life sciences and biomedicine. For instance, the escalating burden on healthcare systems due to the ageing of the world population and the subsequent prevalence of cardiovascular diseases and cancer necessitates the development of novel means to screen and diagnose diseases in a manner that reduces costs and inflicts minimal inconvenience on patients. Such techniques need to provide morphological as well as chemical information about the sample being investigated at high resolution. They also have to be fast and label-free to allow the sample to be examined in its native environment.

Multimodal non-linear imaging techniques can fulfil this role because they provide non-invasive and potentially *in vivo* means to investigate tissue with cellular resolution. A particularly promising approach that has garnered attention as of late is the combination of coherent anti-Stokes Raman scattering (CARS), second harmonic generation (SHG) and two photon excited autofluorescence (TPEF) microscopy. CARS microscopy, a non-linear variant of Raman, provides a contrast based on intrinsic molecular vibrations in the sample. SHG microscopy images non-centrosymmetric structures in the tissue such as collagen. TPEF is a non-linear fluorescence imaging technique that is used to image autofluorophores in a tissue sample. Therefore a multimodal approach integrating these modalities permits the detailed characterization of tissue samples with regards to the distribution of different molecular groups (*e.g.*, CH₂, CH₃), anisotropic biological structures, and endogenous autofluorophores. Laser scanning microscopic setups that incorporate these modalities have been developed by accommodating the different requirements of each technique and the resulting complementary contrast has been employed for various applications. Analysis of images acquired by such microscopes has to be preceded by preprocessing steps. In this respect, stitching algorithms incorporating uneven illumination correction procedures have been developed and applied to mitigate visible edge artifacts that arise when tile scans are used to image extended biological specimens that exceed the field of view provided by the microscope. Sub-

sequent image analysis of the non-linear multimodal images have augmented the typical morphological information obtained from such images.

In the first section of this thesis, the diagnostic potential of multimodal non-linear imaging has been demonstrated in the case of head and neck squamous cell carcinoma ([FBL1]). In the preliminary intensity analysis of the images obtained, cancerous areas featured an increased median TPEF to CARS contrast (TCC) values when compared to healthy squamous epithelium. Succeeding linear discriminant analysis (LDA) predication of healthy and cancerous areas based on intensity and texture features leads to results that are in good agreement with the pathologist's diagnosis.

Typically, as in the study just described, CARS microscopy has focused on lipid imaging due to the strong contrast afforded by the abundance of the CH_2 symmetric stretching vibration at 2845 cm^{-1} . In contrast, the second part of this thesis investigates the feasibility of CARS microscopy for imaging intense bands in the fingerprint region ($800\text{-}1800\text{ cm}^{-1}$) wherein the presence of multiple overlapping peaks and interference with non-resonant background present challenges. Specifically, the emphasis is on imaging the prominent peaks arising from conjugated $\text{C}=\text{C}$ double bonds in retinol, tretinoin, β -carotene, and various microalgal pigments. To alleviate the effects of the non-resonant CARS background, a setup with near-infrared (NIR) wavelengths for both pump and Stokes beam and a corresponding high-throughput in-house built microscope are used in these studies.

The first CARS fingerprint imaging application in the thesis is concerned with the vitamin A content of liver tissue ([FBL2]). As the standard techniques for liver vitamin A imaging either require staining or lead to photobleaching, CARS microscopy presents itself as a potentially better alternative. Capitalizing on the label-free, non-disruptive merits of CARS microscopy, bulk liver tissue samples under physiological conditions have been imaged. Vitamin A forms a strong CARS contrast in the pig and mouse liver tissues investigated. Morphological information of about the lobular structure of the hepatic tissue missing from the CARS images was provided by simultaneously acquired SHG and multi-photon excited autofluorescence (MPEF) modalities. Subsequently, the intra-lobular distribution of vitamin A has been mapped in a multi-modal framework incorporating the three modalities. The results foresee prospective application of CARS for *in vivo* assessment of heterogeneity in vitamin A distribution in pathological hepatic tissue abnormalities. The study has also reiterated the significance of combining the CARS with SHG and MPEF modalities to obtain complementary contrast.

Summary

Analogously, in a uni-cellular application, CARS has been employed to image carotenoids in the diatoms *D. brightwellii* and *S. turris* ([FBL3]). Various environmental factors affect the extraction yield of these pigments from the microalgae. CARS microscopy is suited for monitoring the effects of these factors because it is fast and disruption-free thereby allowing the whole-cell imaging of a large number of diatoms within limited time scale. The strong contrast obtained from CARS microscopy has been utilized to effectively investigate the accumulation of microalgal pigments in response to photoperiod variations. Accordingly, using a marker based watershed analysis of the acquired images, it is observed that carotenoids amass when the diatoms are kept in extended dark-light regimens.

For ultimately transferring multimodal microscopic technologies to the end-user compact fiber laser sources have been developed to replace the bulky sources used in the applications presented above. Concurrent to this progress an improvement in image acquisition speed is also required. This will enable processing of large number tissue sample within a limited time and allow imaging of dynamic processes.

As part of this effort, the third part of the thesis examines two beam excitation and demultiplexed detection as a means of doubling the speed of laser scanning microscopes based on compact fiber laser sources. The practicality of this basic approach was first demonstrated for SHG microscopy ([FBL4]). This entailed fiber-delaying part of the fiber laser output and coupling both beams (the delayed and the undelayed one) into the microscope at different angles or divergences to result in two laterally or axially displaced fields of view within one laser cycle. This in-effect translates to the doubling of the image acquisition rate. In a subsequent project, the concept was realized for the CARS modality using a more involved implementation that necessitated the re-design of a fiber laser source to produce two time multiplexed outputs each containing two colours ([FBL5]). Other non-linear modalities can also be accommodated in the setup by using the proper detection filters. The highlight of the technique, as compared to bulk laser sources with multiple outputs, is its scalability which can be achieved by adding similar extensions of varying fiber length.

Another area of improvement explored is the resolution of the CARS microscopic setup. Herein, based on results from numerical studies, a Bessel like beam was employed as one of the excitation arms in the setup to enhance lateral resolution ([FBL6]). A factor of 1.25 improvement in the lateral resolution was experimentally demonstrated for polyethylene (PE) and cyclic-olefin copolymer (COC) samples using a double axion construction for lossless generation of a laser ring on the pump arm of the CARS setup.

Summary

In summary, this dissertation makes an important contribution to pushing the boundaries of multimodal imaging with regards to both, the development of new fields of application (by assessing relatively less pursued wavenumbers) and the improvement of implementation techniques (with respect to the image acquisition rate and lateral resolution).

4 | Outlook

The capability to obtain strong CARS contrast in the fingerprint region in thick sample tissues is potentially instrumental in drug delivery studies. Typically, confocal spontaneous Raman microspectroscopy has been employed to obtain longitudinal penetration profiles of drugs. Stimulated Raman Scattering (SRS) microscopy has in addition allowed lateral mapping of retinoic acid distribution applied on fresh mouse skin [57]. Analogously, in preliminary investigations, the microscopic setup introduced above was used to visualize the penetration of tretinoin on pig skin samples. First, cryo-sections excised from thick skin tissue samples that have been incubated with tretinoin were imaged. The corresponding on and off resonance images acquired with the CARS modality, presented in figures 4.1(a-b), indicate penetration through the stratum corneum of the epidermis.

These investigations are underpinned by label-free visualization of the skin layering by the complementary multimodal contrast as in previous studies [45](figure 4.1(c)). Such clearly imaged skin structures provide contextual background in the label-free investigation of drug penetration. Corresponding bulk tissue imaging experiments shown in 4.1(d) illustrate non-invasive investigation of drug penetration. Further studies with different metabolites applied at the same time would provide insightful information about possible different penetration pathways. Although CARS fingerprint imaging in this thesis is discussed in the framework of life science applications, it could potentially be used in other areas such as material sciences as well. In regards to the latter, the setup introduced has, for example, been employed in understanding molecular self healing processes [74].

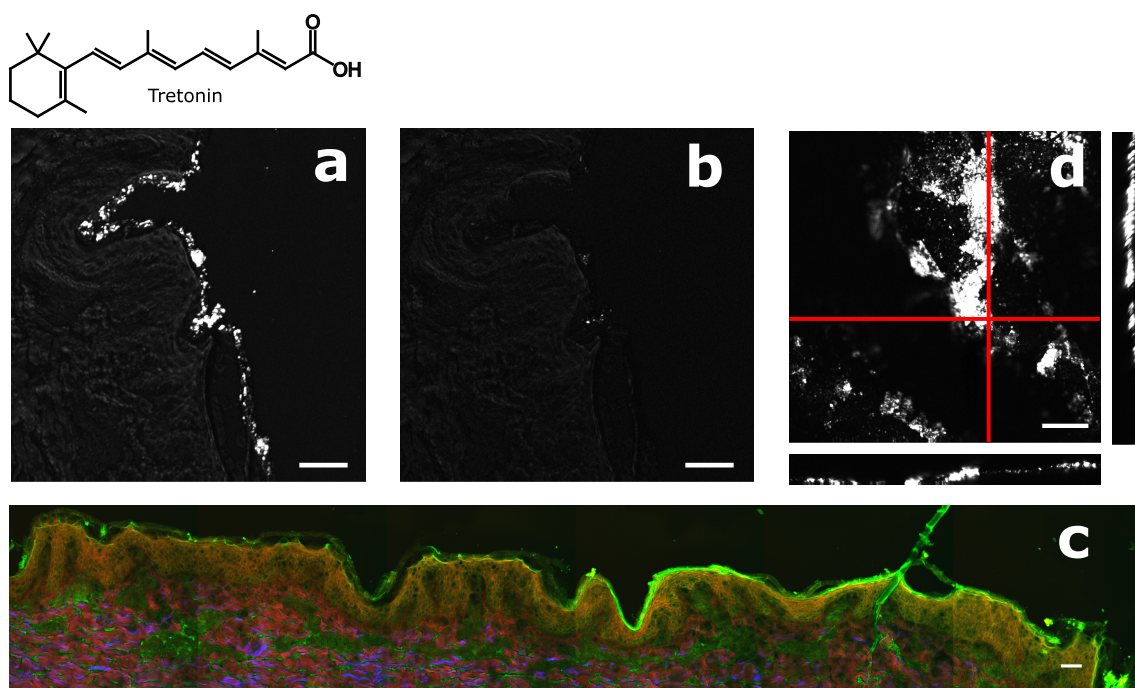


Figure 4.1: Monitoring the delivery of tretonin on pig skin using CARS microscopy. (a) A skin tissue cryo-section imaged with the CARS modality tuned to detect the vibrational peak of tretonin at 1572 cm^{-1} . The penetration of tretonin throughout the stratum corneum layer of the skin is observable. (b) A corresponding off-resonance CARS image of the cryo-section at 1600 cm^{-1} . (c) A multimodal image of the skin sample (CARS: red, TPEF: green, SHG: blue) shows the architectural organization of the liver sample. (d) A depth series of images from a thick skin sample treated with tretonin (with top and side views). Scale bars: $50\text{ }\mu\text{m}$

5 | Zusammenfassung

Innovative Visualisierungstechniken werden benötigt, um den steigenden Anforderungen in den Biowissenschaften und Biomedizin gerecht zu werden. Zum Beispiel erfordert die zunehmende Belastung der Gesundheitssysteme, aufgrund der Alterung der Weltbevölkerung und der nachfolgenden Prävalenz von Herz-Kreislauf-Erkrankungen bzw. Krebs, die Entwicklung neuer Mittel zur Diagnose von Krankheiten. Hierbei sollten idealerweise die Kosten der Untersuchungen gesenkt werden und den Patienten nur minimale Unannehmlichkeiten bereitet werden. Solche Visualisierungstechniken müssen sowohl morphologische als auch chemische Informationen mit einer hohen Auflösung über die zu untersuchende Probe liefern. Des Weiteren müssen sie schnell durchführbar und markierungsfrei sein, damit die Probe in ihrer natürlichen Umgebung untersucht werden kann.

Diese notwendigen Bedingungen können durch multimodale nichtlineare Bildgebungsverfahren erfüllt werden, da sie nicht-invasive und potentielle *in vivo*-Mittel zur Untersuchung von Gewebe mit zellulärer Auflösung darstellen. Ein vielversprechender Ansatz, der in den letzten Jahren Beachtung gefunden hat, ist die Kombination von kohärenter anti-Stokes-Raman-Streuung (CARS)-, Frequenzverdopplungs- (SHG) und Zwei-Photonen angeregter Fluoreszenz (TPEF)-Mikroskopie. Die CARS-Mikroskopie, eine nichtlineare Variante von Raman, liefert einen Kontrast, der auf intrinsischen Molekülschwingungen in der Probe beruht. Die SHG Mikroskopie bildet nicht-zentrosymmetrische Strukturen im Gewebe wie Kollagen ab. TPEF ist eine nicht-lineare Fluoreszenz-Bildgebungstechnik, die zur Abbildung von Autofluorophoren in einer Gewebeprobe verwendet wird. Daher erlaubt der multimodale Ansatz, der diese Modalitäten miteinander verknüpft, eine detaillierte Charakterisierung von Gewebeproben in Bezug auf die Verteilung der verschiedenen Molekülgruppen (z.B. CH_2 , CH_3), anisotropen biologische Strukturen, sowie endogener Autofluorophore zu erzielen. Laser-Scanning-Mikroskop-Setups, die diese Modalitäten beinhalten, wurden entwickelt, indem die unterschiedlichen Anforderungen jeder Technik berücksichtigt wurden und der resultierende Komplementärkontrast für verschiedene Anwendungen verwendet wurde. Der Analyse von Bildern, die mit solchen

Mikroskopen aufgenommen werden, müssen Bearbeitungsschritte vorausgehen. In dieser Hinsicht wurden Näherungsalgorithmen entwickelt, um ungleiche Beleuchtung zu korrigieren und sichtbare Kantenartefakte zu mindern, die durch Kachelscans entstehen, wenn ausgedehnte biologische Proben abgebildet werden, die das Sichtfeld des Mikroskops überschreiten. Bildanalysen basierend auf Intensitätsniveaus und Texturmerkmalen, die aus den nichtlinearen multimodalen Bildern extrahiert wurden, haben die typische morphologische Information erhöht.

Im ersten Teil dieser Arbeit wurde das diagnostische Potenzial der multimodalen nichtlinearen Bildgebung beim Kopf-Hals-Plattenepithelkarzinom ([FBL1]) aufgezeigt. In der vorläufigen Intensitätsanalyse der erhaltenen Bilder wiesen die Krebsbereiche im Vergleich zu gesundem Plattenepithel einen erhöhten mittleren TPEF-zu-CARS-Kontrast (TCC)-Wert auf. Eine nachgelagerte Identifikation von gesunden und kanzerösen Arealen mittels Lineare Diskriminante Analyse (LDA), basierend auf Intensitäts- und Texturmerkmalen, führt zu Ergebnissen, die eine gute Übereinstimmung mit der Diagnose des Pathologen zeigen.

Wie auch im obigen Fall konzentriert sich die CARS-Mikroskopie typischerweise auf die Lipidbildgebung, die aufgrund des starken Kontrastes, der durch die Häufigkeit der symmetrischen CH_2 -Streckschwingung bei 2845 cm^{-1} erzielt wird. Im Gegensatz dazu untersucht der zweite Teil dieser Arbeit die Durchführbarkeit der CARS-Mikroskopie für die Abbildung intensiver Banden in der Fingerprint-Region ($800\text{-}1800\text{ cm}^{-1}$), in denen das Vorhandensein mehrerer überlappender Peaks und Interferenzen mit nicht-resonantem Hintergrund eine Herausforderung darstellt. Insbesondere liegt der Schwerpunkt auf der Abbildung der hervorstechenden Peaks, die sich aus konjugierten $\text{C}=\text{C}$ -Doppelbindungen in Retinol, Tretinoin, *Beta*-Carotin und verschiedenen Mikroalgenpigmenten ergeben. Um die Auswirkungen des nicht-resonanten CARS-Hintergrunds zu mindern, wird in diesen Studien ein Aufbau mit nahinfraroten (NIR)-Wellenlängen, sowohl für den Pump-, als auch für den Stokes-Strahl mit entsprechend hoher Lichtausbeute im selbstgebautem Mikroskop verwendet.

Die erste Anwendung des CARS-Fingerprint-Imagings in dieser Arbeit beschäftigt sich mit dem Vitamin-A-Gehalt von Lebergewebe ([FBL2]). Da die Standardtechniken für die Leber-Vitamin-A-Bildgebung entweder eine Färbung erfordern oder zu einer Photobleichung führen, bietet sich die CARS-Mikroskopie als vielversprechende Alternative an. Unter Ausnutzung der Vorteile der CARS-Mikroskopie (markierungsfrei, zerstörungsfrei) wurden Bulk-Lebergewebeproben unter physiologischen Bedingungen untersucht. Vitamin A bildet in den untersuchten Lebergeweben von Schweinen und Mäusen einen starken CARS-Kontrast. Morphologische Infor-

mationen über die lobuläre Struktur des Lebergewebes, die in den CARS-Bildern fehlen, wurden durch simultane Messung der SHG- und MPEF-Modalitäten erhalten. Anschließend wurde die intra-lobuläre Verteilung von Vitamin A in einem multimodalen Rahmen mit den drei Modalitäten abgebildet. Die Ergebnisse weisen auf eine prospektive Anwendung von CARS für die *in vivo*-Bewertung der Heterogenität der Vitamin-A-Verteilung bei pathologischen hepatischen Gewebeanomalien hin. Die Studie hat das Potenzial der Kombination von CARS mit SHG- und TPEF-Modalitäten erneut aufgezeigt, da ein komplementärer Kontrast erhalten wird.

Analog dazu wurde CARS in einer uni-zellulären Anwendung verwendet, um Carotinoide in den Diatomeen *D. brightwellii* and *S. turris* ([FBL3]) abzubilden. Verschiedene Umweltfaktoren beeinflussen die Extraktionsausbeute dieser Pigmente aus den Mikroalgen. Die CARS-Mikroskopie ist geeignet, um die Auswirkungen dieser Faktoren zu überwachen, da sie schnell und störungsfrei ist und dadurch die Ganzzell-Bildgebung einer großen Anzahl von Kieselalgen in einem begrenzten Zeitbereich ermöglicht. Der starke, aus der CARS-Mikroskopie erhaltene Kontrast wurde verwendet, um die Akkumulation von Mikroalgenpigmenten als Reaktion auf Schwankungen der Photoperiode wirksam zu untersuchen. Unter Verwendung einer markerbasierten Wasserscheideanalyse der aufgenommenen Bilder wird daher beobachtet, dass sich Carotinoide ansammeln, wenn die Kieselalgen in ausgedehnten Dunkellicht-Regimen gehalten werden.

Für eine erfolgreiche Anwendung multimodaler mikroskopischer Technologien in einem medizinischen Umfeld wurde eine kompakte Faserlaserquelle entwickelt, um die bisher verwendeten sperrigen Lasersetzungen zu ersetzen. Zusätzlich ist eine Verbesserung der Bilderfassungsgeschwindigkeit erforderlich. Dies wird die Verarbeitung einer großen Anzahl von Gewebeproben innerhalb einer begrenzten Zeit, sowie die Abbildung dynamischer Prozesse ermöglichen.

Als Teil dieser Bemühungen werden im dritten Teil der Arbeit Zweistrahlanregungs- und Demultiplexdetektion untersucht, um die Geschwindigkeit von Laser-Scanning-Mikroskopen auf der Basis von kompakten Faserlaserquellen zu verdoppeln. Die Praxistauglichkeit dieses grundlegenden Ansatzes wurde erstmals für die SHG-Mikroskopie demonstriert ([FBL4]). Die verwendete Faser verzögerte einen Teil des Faserlaserausgangs, bevor beide Strahlen (der verzögerte und der nicht verzögerte) unter verschiedenen Winkeln oder Divergenzen in das Mikroskop eingekoppelt wurden. Dies führt zu zwei seitlich oder axial verschobenen Sichtfeldern innerhalb eines Laserzyklus führte, was sich in der Verdopplung der Bilderfassungsrate niederschlägt. In einem weiteren Projekt wurde das Konzept für die CARS-Modalität unter Verwendung einer komplizierteren Implementierung realisiert, die das Re-

Design einer Faserlaserquelle erforderte, um zwei zeitgemultiplexte Ausgänge zu erzeugen, die jeweils zwei Farben enthielten ([FBL5]). Andere nichtlineare Modalitäten können ebenfalls in dem Setup unter Verwendung der geeigneten Detektionsfilter untergebracht werden. Im Vergleich zu Bulk-Laserquellen mit mehreren Ausgängen zeichnet sich diese Technik insbesondere durch ihre Skalierbarkeit aus, die durch das Hinzufügen ähnlicher Erweiterungen variabler Faserlänge erreicht werden kann.

Ein weiteres Gebiet, in dem im Rahmen dieser Arbeit Fortschritte erzielt werden konnten, ist die Auflösung der CARS-Mikroskopie. Hier wurde, basierend auf Ergebnissen von numerischen Studien, ein Bessel-ähnlicher Strahl als einer der Anregungsarme im Aufbau verwendet, um die laterale Auflösung zu verbessern ([FBL6]). Ein um den Faktor von 1.25 verbesserte laterale Auflösung wurde experimentell für Polyethylen (PE)- und Cycloolefincopolymer (COC)-Proben unter Verwendung einer Doppelaxionkonstruktion zur verlustfreien Erzeugung eines Laserrings an dem Pumpenarm des CARS-Aufbaus gezeigt.

Die vorliegende Dissertation leistet einen wichtigen Beitrag zur Erweiterung der Möglichkeiten multimodaler Bildgebung, sowohl in Hinblick auf die Erschließung neuer Anwendungsfelder (durch Nutzung bisher selten verwendeter Wellenzahlen), als auch auf verbesserte Implementierungstechniken (Bildwiederholrate und laterale Auflösung).

Bibliography

- [1] F. Zernike, “Phase contrast, a new method for the microscopic observation of transparent objects,” *Physica* **9**, 686–698 (1942).
- [2] D. G. Allen, R.D. and G. Nomarski, “The zeiss-nomarski differential interference equipment for transmitted-light microscopy,” *Zeitschrift für wissenschaftliche Mikroskopie und mikroskopische Technik* **69**, 193–221 (1969).
- [3] F. Böhmer, “Zur pathologischen anatomie der meningitis cerebromedularis epidemica,” *Ärztliches Intelligenzblatt* **12**, 539–50 (1865).
- [4] E. Fischer, “Eosin als tinctionsmittel für mikroskopische präparate,” *Archiv für mikroskopische Anatomie* **12**, 349–352 (1876).
- [5] A. H. Coons and M. H. Kaplan, “Localization of antigen in tissue cells: II. improvements in a method for the detection of antigen by means of fluorescent antibody,” *Journal of Experimental Medicine* **91**, 1–13 (1950).
- [6] B. Stuart, *Infrared spectroscopy* (Wiley Online Library, 2005).
- [7] G. Turrell and J. Corset, *Raman microscopy: developments and applications* (Access Online via Elsevier, 1996).
- [8] H. J. Humecki, *Practical guide to infrared microspectroscopy*, vol. 19 (CRC Press, 1995).
- [9] C. V. Raman and K. S. Krishnan, “A new type of secondary radiation,” *Nature* **121**, 501–502 (1928).
- [10] C. V. Raman, “A change of wave-length in light scattering,” *Nature* **121**, 619 (1928).
- [11] C. Krafft, B. Dietzek, and J. Popp, “Raman and CARS microspectroscopy of cells and tissues,” *Analyst* **134**, 1046–1057 (2009).

BIBLIOGRAPHY

- [12] A. F. Low, G. J. Tearney, B. E. Bouma, and I.-K. Jang, “Technology insight: optical coherence tomography—current status and future development,” *Nature Clinical Practice Cardiovascular Medicine* **3**, 154–162 (2006).
- [13] N. Sans, M. Faruch, H. Chiavassa-Gandois, C. L. C. de Ribes, C. Paul, and J.-J. Railhac, “High-resolution magnetic resonance imaging in study of the skin: normal patterns,” *European journal of radiology* **80**, e176–e181 (2011).
- [14] K. König, M. Speicher, M. J. Köhler, R. Scharenberg, and M. Kaatz, “Clinical application of multiphoton tomography in combination with high-frequency ultrasound for evaluation of skin diseases,” *Journal of biophotonics* **3**, 759–773 (2010).
- [15] R. W. Boyd, *Nonlinear optics* (Academic press, 2003).
- [16] J.-X. Cheng and X. S. Xie, *Coherent Raman scattering microscopy* (CRC press, 2016).
- [17] A. Downes and A. Elfick, “Raman spectroscopy and related techniques in biomedicine,” *Sensors* **10**, 1871–1889 (2010).
- [18] M. Schmitt and J. Popp, “Raman spectroscopy at the beginning of the twenty-first century,” *Journal of Raman Spectroscopy* **37**, 20–28 (2006).
- [19] C. Krafft, D. Codrich, G. Pelizzo, and V. Sergo, “Raman and FTIR microscopic imaging of colon tissue: a comparative study,” *Journal of Biophotonics* **1**, 154–169 (2008).
- [20] A. Walter, S. Erdmann, T. Bocklitz, E. Jung, N. Vogler, D. Akimov, B. Dietzek, P. Rösch, E. Kothe, and J. Popp, “Analysis of the cytochrome distribution via linear and nonlinear Raman spectroscopy,” *Analyst* **135**, 908–917 (2010).
- [21] M. D. Duncan, J. Reintjes, and T. Manuccia, “Scanning coherent anti-Stokes Raman microscope,” *Optics letters* **7**, 350–352 (1982).
- [22] M. Muller, J. Squier, C. De Lange, and G. Brakenhoff, “Cars microscopy with folded boxcars phasematching,” *Journal of Microscopy* **197**, 150–158 (2000).
- [23] A. Zumbusch, G. R. Holtom, and X. S. Xie, “Three-dimensional vibrational imaging by coherent anti-Stokes Raman scattering,” *Physical Review Letters* **82**, 4142–4145 (1999).
- [24] G. L. Eesley, *Coherent Raman Spectroscopy* (Elsevier, 2013).

BIBLIOGRAPHY

- [25] C. L. Evans and X. S. Xie, “Coherent anti-Stokes Raman scattering microscopy: chemical imaging for biology and medicine,” *Annu. Rev. Anal. Chem.* **1**, 883–909 (2008).
- [26] F. Ganikhanov, C. L. Evans, B. G. Saar, and X. S. Xie, “High-sensitivity vibrational imaging with frequency modulation coherent anti-Stokes Raman scattering (FM CARS) microscopy,” *Optics letters* **31**, 1872–1874 (2006).
- [27] J.-X. Cheng, L. D. Book, and X. S. Xie, “Polarization coherent anti-Stokes Raman scattering microscopy,” *Optics letters* **26**, 1341–1343 (2001).
- [28] A. Volkmer, L. D. Book, and X. S. Xie, “Time-resolved coherent anti-stokes raman scattering microscopy: Imaging based on raman free induction decay,” *Applied Physics Letters* **80**, 1505–1507 (2002).
- [29] E. Dufresne, D. Stark, N. Greenblatt, J. Cheng, J. Hutchinson, L. Mahadevan, and D. Weitz, “Dynamics of fracture in drying suspensions,” *Langmuir* **22**, 7144–7147 (2006).
- [30] J. Cheng, Y. Jia, G. Zheng, and X. Xie, “Laser-scanning coherent anti-Stokes Raman scattering microscopy and applications to cell biology,” *Biophysical Journal* **83**, 502–509 (2002).
- [31] X. Nan, W. Y. Yang, and X. S. Xie, “CARS microscopy lights up lipids in living cells,” *Biophotonics International* **11**, 44–47 (2004).
- [32] X. Nan, J.-X. Cheng, and X. S. Xie, “Vibrational imaging of lipid droplets in live fibroblast cells with coherent anti-Stokes Raman scattering microscopy,” *Journal of lipid research* **44**, 2202–2208 (2003).
- [33] C. Evans, X. Xu, S. Kesari, X. Xie, S. Wong, and G. Young, “Chemically-selective imaging of brain structures with CARS microscopy,” *Optics Express* **15**, 12076–12087 (2007).
- [34] M. Oheim, D. J. Michael, M. Geisbauer, D. Madsen, and R. H. Chow, “Principles of two-photon excitation fluorescence microscopy and other nonlinear imaging approaches,” *Advanced drug delivery reviews* **58**, 788–808 (2006).
- [35] W. Denk, J. H. Strickler, and W. W. Webb, “Two-photon laser scanning fluorescence microscopy,” *Science* **248**, 73–76 (1990).

BIBLIOGRAPHY

- [36] W. R. Zipfel, R. M. Williams, R. Christie, A. Y. Nikitin, B. T. Hyman, and W. W. Webb, “Live tissue intrinsic emission microscopy using multiphoton-excited native fluorescence and second harmonic generation,” *Proceedings of the National Academy of Sciences* **100**, 7075–7080 (2003).
- [37] S. Fine and W. Hansen, “Optical second harmonic generation in biological systems,” *Applied Optics* **10**, 2350–2353 (1971).
- [38] W. Mohler, A. C. Millard, and P. J. Campagnola, “Second harmonic generation imaging of endogenous structural proteins,” *Methods* **29**, 97–109 (2003).
- [39] R. Cicchi, N. Vogler, D. Kapsokalyvas, B. Dietzek, J. Popp, and F. S. Pavone, “From molecular structure to tissue architecture: collagen organization probed by SHG microscopy,” *Journal of Biophotonics* **6**, 129–142 (2013).
- [40] D. A. Boas, C. Pitris, and N. Ramanujam, *Handbook of biomedical optics* (CRC press, 2016).
- [41] F. Helmchen and W. Denk, “Deep tissue two-photon microscopy,” *Nature methods* **2**, 932 (2005).
- [42] G. M. Hale and M. R. Querry, “Optical constants of water in the 200-nm to 200- μ m wavelength region,” *Applied optics* **12**, 555–563 (1973).
- [43] N. Vogler, T. Meyer, D. Akimov, I. Latka, C. Krafft, N. Bendsoe, K. Svanberg, B. Dietzek, and J. Popp, “Multimodal imaging to study the morphochemistry of basal cell carcinoma,” *Journal of Biophotonics* **3**, 728–736 (2010).
- [44] T. Meyer, O. Guntinas-Lichius, F. von Eggeling, G. Ernst, D. Akimov, M. Schmitt, B. Dietzek, and J. Popp, “Multimodal nonlinear microscopic investigations on head and neck squamous cell carcinoma: Toward intraoperative imaging,” *Head & neck* **35**, E280–E287 (2013).
- [45] S. Heuke, N. Vogler, T. Meyer, D. Akimov, F. Kluschke, H. R wert-Huber, J. Lademann, B. Dietzek, and J. Popp, “Multimodal mapping of human skin,” *Br J Dermatol.* (2013).
- [46] F. B. Legesse, O. Chernavskaiia, S. Heuke, T. Bocklitz, T. Meyer, J. Popp, and R. Heintzmann, “Seamless stitching of tile scan microscope images,” *Journal of microscopy* **258**, 223–232 (2015).

BIBLIOGRAPHY

- [47] F. B. Legesse, A. Medyukhina, S. Heuke, and J. Popp, "Texture analysis and classification in coherent anti-Stokes Raman scattering (cars) microscopy images for automated detection of skin cancer," *Computerized Medical Imaging and Graphics* **43**, 36–43 (2015).
- [48] M. Suematsu, M. Oda, H. Suzuki, H. Kaneko, N. Watanabe, T. Furusho, S. Masushige, and M. Tsuchiya, "Intravital and electron microscopic observation of ito cells in rat hepatic microcirculation," *Microvascular research* **46**, 28–42 (1993).
- [49] S. L. Friedman, "Molecular regulation of hepatic fibrosis, an integrated cellular response to tissue injury," *Journal of Biological Chemistry* **275**, 2247–2250 (2000).
- [50] K. Kochan, K. Marzec, E. Maslak, S. Chlopicki, and M. Baranska, "Raman spectroscopic studies of vitamin A content in the liver: a biomarker of healthy liver," *Analyst* **140**, 2074–2079 (2015).
- [51] S. A. Ross, P. J. McCaffery, U. C. Drager, and L. M. De Luca, "Retinoids in embryonal development," *Physiological reviews* **80**, 1021–1054 (2000).
- [52] X.-H. Tang and L. J. Gudas, "Retinoids, retinoic acid receptors, and cancer," *Annual Review of Pathology: Mechanisms of Disease* **6**, 345–364 (2011).
- [53] W. S. Blaner, S. M. O'Byrne, N. Wongsiriroj, J. Kluwe, D. M. D'Ambrosio, H. Jiang, R. F. Schwabe, E. M. Hillman, R. Piantedosi, and J. Libien, "Hepatic stellate cell lipid droplets: a specialized lipid droplet for retinoid storage," *Biochimica et Biophysica Acta (BBA)-Molecular and Cell Biology of Lipids* **1791**, 467–473 (2009).
- [54] H. Senoo, K. Yoshikawa, M. Morii, M. Miura, K. Imai, and Y. Mezaki, "Hepatic stellate cell (vitamin A-storing cell) and its relative—past, present and future," *Cell biology international* **34**, 1247–1272 (2010).
- [55] N. Higashi and H. Senoo, "Distribution of vitamin A-storing lipid droplets in hepatic stellate cells in liver lobules—a comparative study," *The Anatomical Record Part A: Discoveries in Molecular, Cellular, and Evolutionary Biology* **271**, 240–248 (2003).
- [56] B. Vollmar, S. Siegmund, and M. D. Menger, "An intravital fluorescence microscopic study of hepatic microvascular and cellular derangements in developing cirrhosis in rats," *Hepatology* **27**, 1544–1553 (1998).

BIBLIOGRAPHY

- [57] C. W. Freudiger, W. Min, B. G. Saar, S. Lu, G. R. Holtom, C. He, J. C. Tsai, J. X. Kang, and X. S. Xie, “Label-free biomedical imaging with high sensitivity by stimulated Raman scattering microscopy,” *Science* **322**, 1857–1861 (2008).
- [58] P. M. Foley, E. S. Beach, and J. B. Zimmerman, “Algae as a source of renewable chemicals: opportunities and challenges,” *Green Chemistry* **13**, 1399–1405 (2011).
- [59] A. C. Guedes, H. M. Amaro, and F. X. Malcata, “Microalgae as sources of carotenoids,” *Marine drugs* **9**, 625–644 (2011).
- [60] J. Peng, J.-P. Yuan, C.-F. Wu, and J.-H. Wang, “Fucoxanthin, a marine carotenoid present in brown seaweeds and diatoms: metabolism and bioactivities relevant to human health,” *Marine drugs* **9**, 1806–1828 (2011).
- [61] N. D. Parab and V. Tomar, “Raman spectroscopy of algae: a review,” *J. Nanomed. Nanotechnol* **3**, 24 (2012).
- [62] P. Heraud, J. Beardall, D. McNaughton, and B. R. Wood, “In vivo prediction of the nutrient status of individual microalgal cells using raman microspectroscopy,” *FEMS microbiology letters* **275**, 24–30 (2007).
- [63] J. Rüger, N. Unger, I. W. Schie, E. Brunner, J. Popp, and C. Krafft, “Assessment of growth phases of the diatom *ditylum brightwellii* by FT-IR and Raman spectroscopy,” *Algal Research* **19**, 246–252 (2016).
- [64] M. Baumgartl, T. Gottschall, J. Abreu-Afonso, A. Díez, T. Meyer, B. Dietzek, M. Rothhardt, J. Popp, J. Limpert, and A. Tünnermann, “Alignment-free, all-spliced fiber laser source for cars microscopy based on four-wave-mixing,” *Optics express* **20**, 21010–21018 (2012).
- [65] T. Gottschall, M. Baumgartl, A. Sagnier, J. Rothhardt, C. Jauregui, J. Limpert, and A. Tünnermann, “Fiber-based source for multiplex-cars microscopy based on degenerate four-wave mixing,” *Optics express* **20**, 12004–12013 (2012).
- [66] T. Meyer, M. Baumgartl, T. Gottschall, T. Pascher, A. Wuttig, C. Matthäus, B. F. Romeike, B. R. Brehm, J. Limpert, A. Tünnermann *et al.*, “A compact microscope setup for multimodal nonlinear imaging in clinics and its application to disease diagnostics,” *Analyst* **138**, 4048–4057 (2013).
- [67] C. Evans, E. Potma, M. Puoris’ haag, D. Côté, C. Lin, and X. Xie, “Chemical imaging of tissue in vivo with video-rate coherent anti-Stokes Raman scattering

BIBLIOGRAPHY

- microscopy,” Proceedings of the National Academy of Sciences of the United States of America **102**, 16807 (2005).
- [68] F. S. Pavone and P. J. Campagnola, *Second harmonic generation imaging* (CRC Press, 2013).
- [69] J. Bewersdorf, R. Pick, and S. W. Hell, “Multifocal multiphoton microscopy,” Optics letters **23**, 655–657 (1998).
- [70] A. Buist, M. Muller, J. Squier, and G. Brakenhoff, “Real time two-photon absorption microscopy using multi point excitation,” Journal of microscopy **192**, 217 (1998).
- [71] T. Minamikawa, M. Hashimoto, K. Fujita, S. Kawata, and T. Araki, “Multi-focus excitation coherent anti-Stokes Raman scattering (CARS) microscopy and its applications for real-time imaging,” Optics express **17**, 9526–9536 (2009).
- [72] V. Andresen, A. Egner, and S. W. Hell, “Time-multiplexed multifocal multiphoton microscope,” Optics letters **26**, 75–77 (2001).
- [73] K. E. Sheetz, E. E. Hoover, R. Carriles, D. Kleinfeld, and J. A. Squier, “Advancing multifocal nonlinear microscopy: development and application of a novel multibeam yb: Kgd (wo 4) 2 oscillator,” Optics express **16**, 17574–17584 (2008).
- [74] J. Popp, R. Geitner, F.-B. Legesse, N. Kuhl, T. Meyer, T. Bocklitz, S. Zechel, J. Vitz, M. Hager, U. S. Schubert *et al.*, “Do you get what you see? understanding molecular self-healing,” Chemistry-A European Journal (2017).

6 | Publications and conference contributions

6.1 Multimodal nonlinear microscopy of head and neck carcinoma - toward intraoperative diagnostics

Documentation of Authorship

Sandro Heuke*	Acquisition and analysis of multimodal images, preparation of the manuscript
Olga Chernavskaia*	Development of algorithms, image analysis, preparation of the manuscript
Thomas Bocklitz	Development of algorithms, Analysis of multimodal images, Project coordination and supervision
Fisseha Bekele Legesse	Analysis of multimodal images
Tobias Meyer	Discussion of results
Denis Akimov	Setting up the multimodal experiment
Olaf Dirsch	Procuration biopsy specimen, Preparation of the tissue specimen, staining histopathology
Günther Ernst	Procuration biopsy specimen, Preparation of the tissue specimen, staining histopathology
Ferdinand von Eggeling	Project coordination and supervision, discussion of results
Iver Petersen	Project coordination and supervision, discussion of results
Orlando Guntinas-Lichius	Project coordination and supervision, discussion of results
Michael Schmitt	Project coordination and supervision, discussion of results
Jürgen Popp	Project coordination and supervision, discussion of results

All authors revised, edited and proof read the final manuscript.

*Both authors share first authorship of this manuscript.

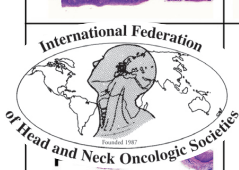
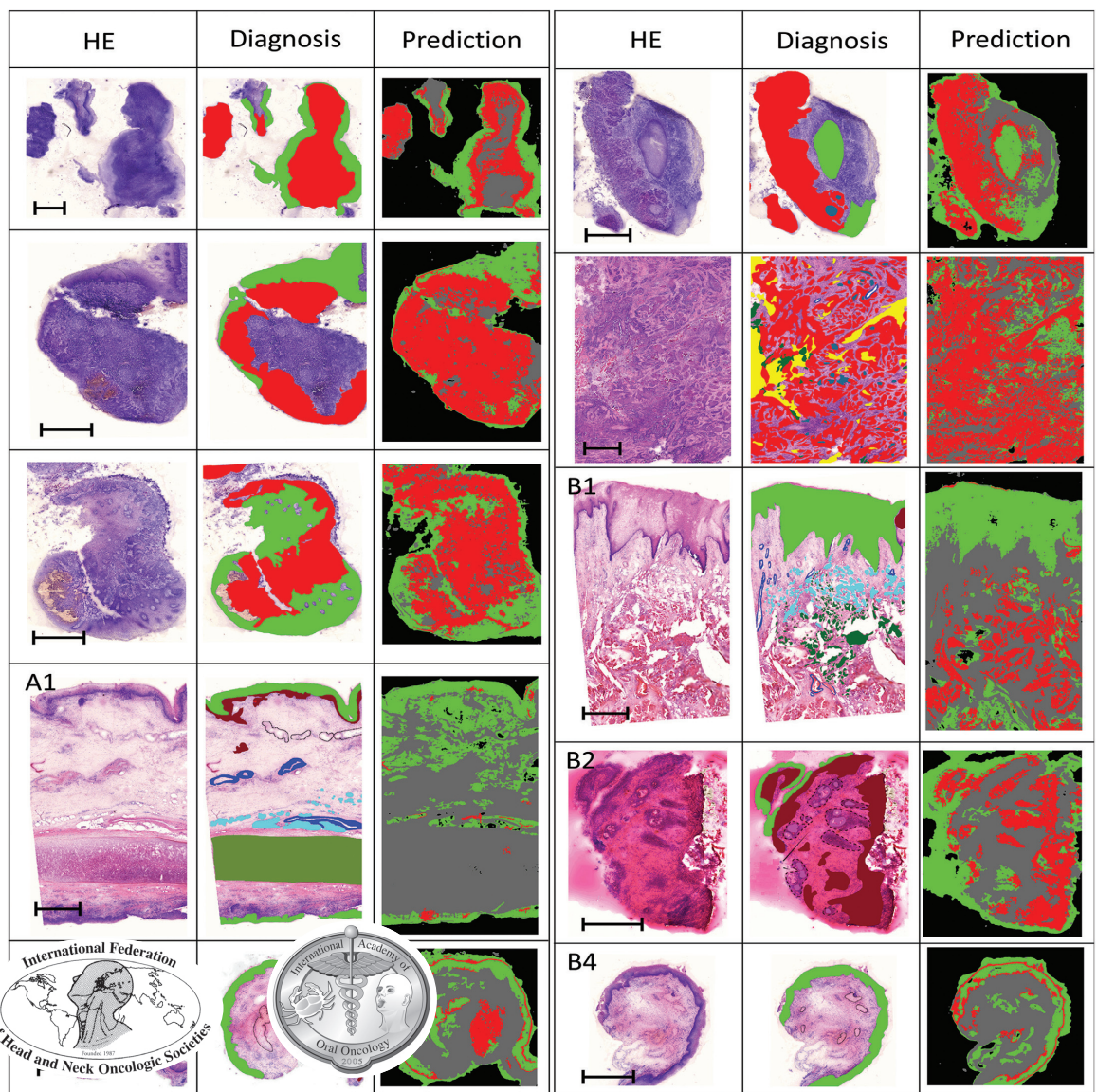
Reprinted with kind permission from the Wiley publishing house.

[FBL1] S. Heuke, O. Chernavskaia, T. Bocklitz, F. B. Legesse, T. Meyer, D. Akimov, O. Dirsch, G. Ernst, F. von Eggeling, I. Petersen, M. Schmitt, and J. Popp, “Multimodal nonlinear microscopy of head and neck carcinoma – toward surgery assisting frozen section analysis,” *Head & neck* **38**, 1545–1552 (2016).

Author	S. Heuke	Fisseha Bekele Legesse
Suggested equivalent of publications	1.0	0.5

HEAD & NECK

JOURNAL FOR THE SCIENCES AND SPECIALTIES OF THE HEAD AND NECK



The official journal of the INTERNATIONAL FEDERATION OF HEAD AND NECK ONCOLOGIC SOCIETIES and INTERNATIONAL ACADEMY OF ORAL ONCOLOGY

WILEY Blackwell

Multimodal nonlinear microscopy of head and neck carcinoma — toward surgery assisting frozen section analysis

Sandro Heuke, Dipl Chem,^{1,2} Olga Chernavskaia, PhD,^{1,2} Thomas Bocklitz, PhD,² Fisseha Bekele Legesse, M. Sci.,^{1,2} Tobias Meyer, PhD,^{1,2} Denis Akimov, PhD,¹ Olaf Dirsch, MD,³ Günther Ernst, MD,^{1,4} Ferdinand von Eggeling, PhD,^{1,2,4} Iver Petersen, MD,⁵ Orlando Guntinas-Lichius, MD,⁴ Michael Schmitt, PhD,² Jürgen Popp, PhD^{1,2*}

¹Leibniz Institute of Photonic Technology, Jena, Germany, ²Institute of Physical Chemistry and Abbe Center of Photonics, Friedrich-Schiller University, Jena, Germany, ³Institute of Pathology, Klinikum Chemnitz, Chemnitz, Germany, ⁴Department of Otorhinolaryngology, Jena University Hospital, Jena, Germany, ⁵Institute of Pathology, Jena University Hospital, Jena, Germany.

Accepted 16 March 2016

Published online 21 April 2016 in Wiley Online Library (wileyonlinelibrary.com). DOI 10.1002/hed.24477

ABSTRACT: *Background.* Treatment of early cancer stages is deeply connected to a good prognosis, a moderate reduction of the quality of life, and comparably low treatment costs.

Methods. Head and neck squamous cell carcinomas were investigated using the multimodal combination of coherent anti-Stokes Raman scattering (CARS), two-photon excited fluorescence (TPEF), and second-harmonic generation (SHG) microscopy.

Results. An increased median TPEF to CARS contrast was found comparing cancerous and healthy squamous epithelium with a *p* value of $1.8 \cdot 10^{-10}$. A following comprehensive image analysis was able to predict the diagnosis of imaged tissue sections with an overall accuracy of 90% for a 4-class model.

Conclusion. Nonlinear multimodal imaging is verified objectively as a valuable diagnostic tool that complements conventional staining protocols and can serve as filter in future clinical routine reducing the pathologist's workload. © 2016 Wiley Periodicals, Inc. *Head Neck* 38: 1545–1552, 2016

KEY WORDS: nonlinear microscopy, spectral histopathology, head and neck cancer imaging, coherent anti-Stokes Raman scattering (CARS), second-harmonic generation (SHG), two-photon excited fluorescence (TPEF), image analysis

INTRODUCTION

Head and neck cancer is ranked the sixth most common cancer¹ with 13.4 age-adjusted incidences and a mortality rate of 2.6 among 100,000 individuals in the United States estimated for the year 2014.² Among head and neck cancer, the squamous cell carcinoma is, with a proportion of 95%, the most frequently occurring laryngeal malignant neoplasm. Fortunately, the mortality rate of head and neck cancer decreased over the past 2 decades in western European countries,³ which may be attributed to the high accuracy of 87% to 94% of the available diagnostic tools and an effective multimodality treatment

combining chemotherapy and radiotherapy. Still, the adverse impact of head and neck cancer treatment is high for affected individuals and the society. Invasive and non-invasive treatment side-effects derogates the patient's quality of life, including pain, physical and emotional dysfunctioning, or xerostomia.⁴ Furthermore, high economic burden is connected to head and neck cancer (eg, attributable costs were estimated to range between \$5000 and \$15,000 per case per year in the United States).⁵ To minimize the overall burden, early diagnosis seems to be one of the most apparent solutions, because low-stage tumors are often curable with function-preserving treatments, improved prognosis, and reduced follow-up care.⁶ Early diagnosis⁷ or potential preventive medical examination programs inevitably rely on the availability of suitable imaging techniques. An exclusive visual examination is not suited for such purpose because it lacks sufficient spatial resolution. For small localized and therefore early tissue alterations, the ideal imaging modality combines cellular resolution, short acquisition times to enable the investigation of large areas in the range of millimeter to centimeter, and meaningful contrast. The latter is required to provide information about the tumor's location as well as prognosis. Established imaging modalities, such as positron emission tomography, CT, or MRI, fail in particular to provide cellular resolution with current spatial

*Corresponding author: J. Popp, Leibniz-Institut für Photonische Technologien e.V., Postfach 100239, 07702 Jena, Germany. E-mail: Juergen.Popp@ipht-jena.de

Contract grant sponsor: Financial support of the European Union, the "Thüringer Kultusministerium," the "Thüringer Aufbaubank," the Federal Ministry of Education and Research, Germany (BMBF) within the research project FiberHealthProbe (FKZ 13N12525, 13N12526), the German Science Foundation, the Fonds der Chemische Industrie, and the Carl-Zeiss Foundation are greatly acknowledged.

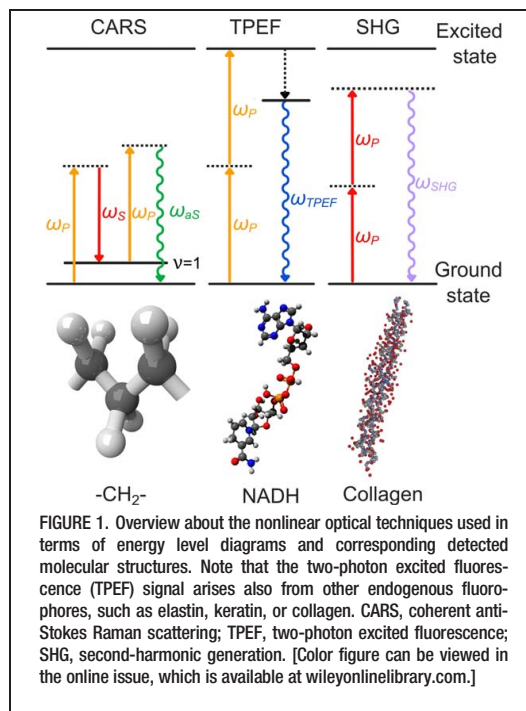
Sandro Heuke and Olga Chernavskaia contributed equally to this work.

Additional Supporting Information may be found in the online version of this article.

HEUKE ET AL.

resolving capabilities in the order of millimeters^{8,9}; although it should be noted that higher accessibility of spatial resolution in the order of micrometers was demonstrated in the laboratory.¹⁰

In contrast with positron emission tomography, CT, and MRI, optical microscopy inherently provides spatial resolution in range of the detection wavelength. The application of linear optical microscopy, such as linear Raman, fluorescence microscopy, or optical coherence tomography, is connected to other major drawbacks (e.g., lack of sufficient imaging speed, tissue penetration, or meaningful contrast).¹¹ Nonlinear optical imaging techniques, however, allow for intrinsic confocal high-speed imaging with pixel dwell times of microseconds, deep tissue penetration up to 1.2 mm,¹² and yield molecular contrast. Providing information about the lipid, autofluorophore, and collagen distribution, the multimodal combination of coherent anti-Stokes Raman scattering (CARS), two-photon excited fluorescence (TPEF), and second harmonic generation (SHG) is suited in particular to investigate the local tumor spread, metabolic activity, vascularization, and the tumor stroma interaction.^{13,14} Today, no *in vivo* multimodal system is commercially available enabling imaging in the spatially confined laryngopharyngeal locality. Nonetheless, the development of inexpensive and compact fiber lasers¹⁵ combined with recent innovations of miniaturized fiber optical probes¹⁶ for nonlinear imaging render the advent of commercially available multimodal imaging systems a question of time. To boost such technology advances, the purpose of this article was to demonstrate the match between clinical requirements and the performance of the nonlinear CARS/TPEF/SHG multimodal imaging approach by thoroughly examining *ex vivo* 10 samples from different patients with a total of 30 tissue sections. It shall be noted that earlier studies of ours already demonstrated the diagnostic potential of a CARS/TPEF/SHG imaging approach for diagnosing brain cancer,¹⁷ colon carcinoma, nonmelanoma skin cancer,¹³ and, recently, also laryngeal carcinoma.¹⁴ The present study, however, significantly extends and exceeds our earlier work with respect to the quantity of size and number of the samples investigated. However, more importantly, a rigorous image analysis procedure was developed and added aiming for an automatic objective diagnosis to guide pathologists and surgeons in future applications. Until today, image analysis applied to nonlinear microscopy was performed mostly using only 1 or 2 modalities. Analyzing SHG images by means of the gray level co-occurrence matrix,¹⁸ fast Fourier transform¹⁹ methods, or extraction of tumor-associated collagen signatures (TACS),²⁰ determines cancer-related morphology alteration of collagen fiber bundles. Based on absolute intensity values, colocalization was applied to TPEF or CARS images discriminating transplanted neural precursor cells and damaged axons²¹ or tissues of distinct lipid to protein levels,²² respectively. For the 2 modalities, SHG and autofluorescence an aging index of dermis (SAAID) was derived²³ by determining the ratio between collagen to elastin fibers that can be readily linked to aging or prolonged sun exposure (i.e., solar elastosis). However, a common analysis procedure for CARS, TPEF, and SHG images extracting morphology and intensity related

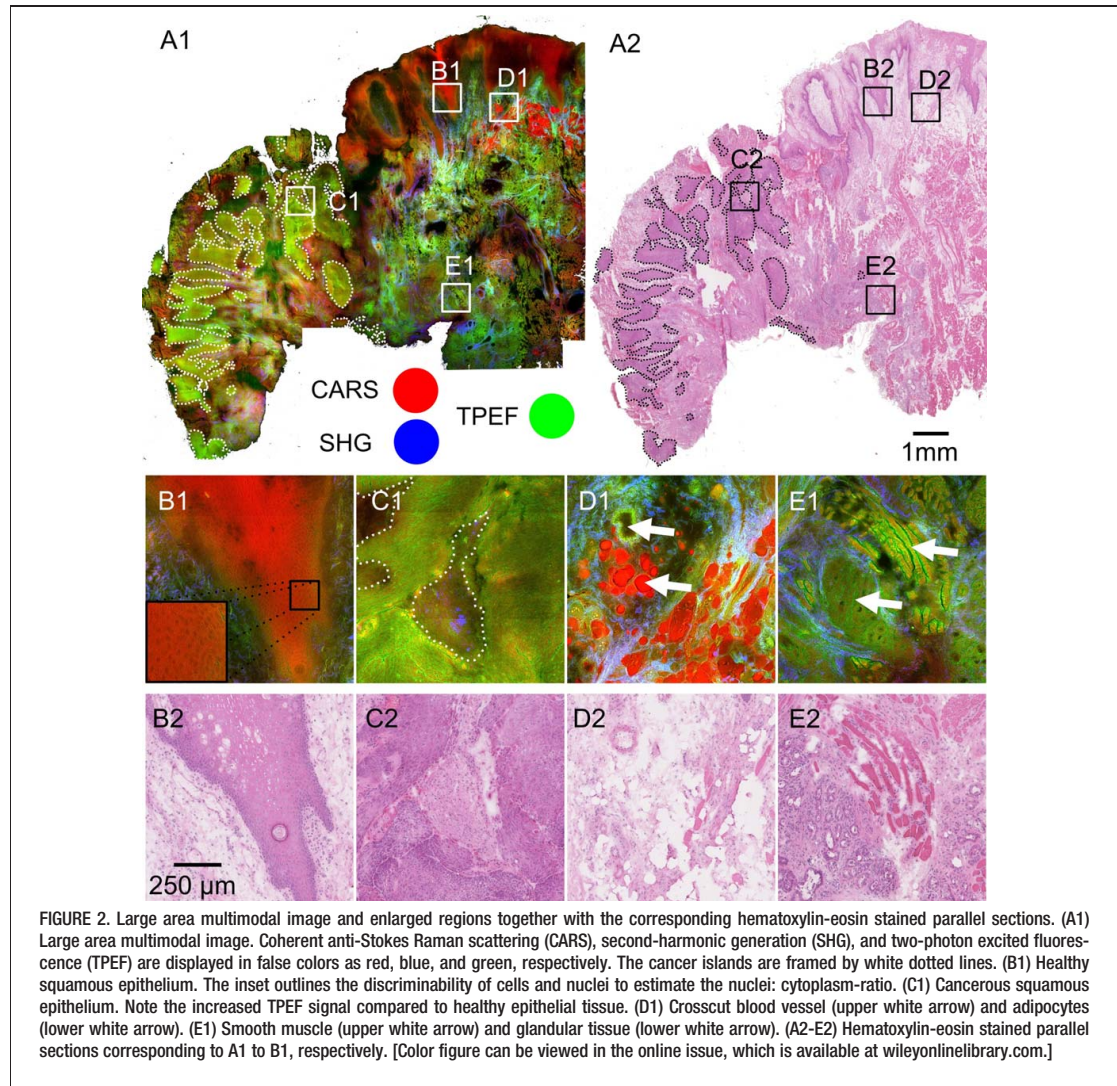


features, is missing. In this study, we present, to the best of our knowledge, the first extensive and quantitative CARS/TPEF/SHG image analysis approach allowing for the discrimination between healthy from cancerous squamous epithelium. After this approach, often proposed merely qualitative statements resulting from visual analysis of multimodal images can be quantified and utilized for a prediction of diagnosis. Further, future related studies can be compared on the grounds of numbers serving for the improvement of prediction algorithms.

Thus, the presented results pave the way for *ex corpore in vivo* multimodal imaging applications regarding diagnosis, guided surgery, or monitoring of the therapeutic outcome of any (neo)adjuvant radiotherapy or chemotherapy of head and neck cancer.

RESULTS AND DISCUSSION

Within this study, 30 tissue sections were investigated using nonlinear multimodal microscopy. Approximately 3 sections each originate from 10 patients aged between 39 to 85 years (9 men and 1 woman) with a diagnosis of head and neck cancer located at the hypopharynx, nasopharynx, and oropharynx. The diagnosis of head and neck cancer was confirmed by histopathology of tumor biopsies of 10 patients corresponding to 17 sections with squamous cell cancer. Additionally, control biopsies of normal mucosa in the same patients were taken corresponding to 13 sections with histopathologically confirmed normal mucosa. Note that the diagnostic assignment was performed only on the grounds of the



hematoxylin-eosin stained tissue section. The pathologist had no access to the multimodal images rendering the present report to a “blinded” study. All sections were investigated native (i.e., without prior washing or staining procedure), using the joint combination of CARS, SHG, and TPEF. Details about the experimental configurations and imaging parameters concerning the applied laser sources, image size, and acquisition time can be found in the Supplementary Figure S1, online only. The CARS excitation wavelengths were tuned to match the CH₂ symmetrical stretching vibration. Thus, mainly CH₂-rich lipids and comparatively weaker proteins yield a pronounced CARS signal. TPEF signal is collected in the spectral window between 426 and 490 nm arising from strong autofluorophores of the tissue,

such as elastin, NAD(P)H, keratin, and comparatively weaker collagen. The distinction of fluorophores is partially achieved if the signal strength and morphological information are combined (eg, NAD(P)H is the strongest native fluorophore of epithelial cells and smooth muscle cells),^{24,25} whereas elastin provides the strongest TPEF signal and displays a fibrous texture that is thicker than collagen. In addition, the latter is mapped by SHG so that a misinterpretation is excluded. Thus, combining CARS, TPEF, and SHG — referred to as multimodal imaging — yields complementary molecular contrast that provides information about different orders of tissue organization ranging from supramolecular structures (SHG), molecules (TPEF of NAD(P)H), and molecular groups (CARS). An overview based on

HEUKE ET AL.

energy level diagrams about the nonlinear optical techniques applied can be found in Figure 1.

For conciseness reasons, only multimodal images of 1 head and neck cancer sample are displayed in detail in Figure 2 as a representative of all 17 cancer samples investigated. Figure 2(A1) shows a stitched scan of a head and neck cancer arising from the oropharynx with a sample diameter of approximately 1.6 cm imaged with a step size of 220 nm. Analyzing Figure 2(A1), the major tissue layers and important functional subunits of the oropharynx can be readily retrieved. To accustom with multimodal contrast, Figure 2(D1) demonstrates the appearance of lipid-rich adipocytes and a crosscut blood vessel with high elastin fiber content in multimodal imaging. Note the potential to monitor elastin-containing arteries and veins, but not capillaries as part of the tissues' vascularization. Further, Figure 2(E1) highlights the appearance of smooth muscle and glandular tissue. Thus, the multimodal contrast in combination with morphological information allows for the localization of potential head and neck cancer areas, namely squamous epithelial tissue.

Although the localization of squamous epithelial tissue in hematoxylin-eosin-stained images is performed by a trained pathologist at first glance, the distinction of cancerous and benign epithelial tissue is challenging and performed mostly by evaluation of morphological findings. Similar morphological information can also be retrieved by multimodal imaging, such as the nuclei to cytoplasm ratio (see Figure 2[B1]). For an overview summarizing morphological findings, we refer the interested reader to earlier work.¹⁴ Here, it shall be focused on statistic measures, such as texture properties and intensity ratios of the modalities.

Highlighting the intensity differences Figures 2(B1) and 2(C1) display benign and cancerous squamous epithelial tissue, respectively. The major difference between healthy and malignant transformed epithelium can be attributed by an increased TPEF signal for the cancerous area arising most likely from an increased concentration of NAD(P)H (note: NAD(P)⁺ appears dark in TPEF). This finding and justification is in agreement with earlier observations reported for other cancers located at various body sides^{13,14} and can be further connected to an increased metabolic activity that forms the basis for a fast cancer growth. Note that the NAD(P)H concentration within excised tissue decreases after resection within the first 4 hours. Thus, the difference of the TPEF signal strength between cancerous and healthy epithelial tissue is expected to be higher for living cells facilitating the image analysis in potential *in vivo* applications.

Aiming for quantification, a relative intensity (i.e., the ratio of 2 modalities), is to be favored over the pure TPEF, as reported earlier in biomedical tissue studies by correlation of the SHG and TPEF signal strength. In this study, the previously introduced Michelson contrast (SAID = $[I_{SHG} - I_{TPEF}] / [I_{TPEF} + I_{SHG}]$) designed to measure the aging of the dermis²³ was applied for discrimination of healthy dermis from stroma in proximity to basal cell carcinoma.²⁶

Adopting the ratio of TPEF to SHG to head and neck cancer permits for distinction of epithelial and connective tissue. Unfortunately, it is not suited to differentiate

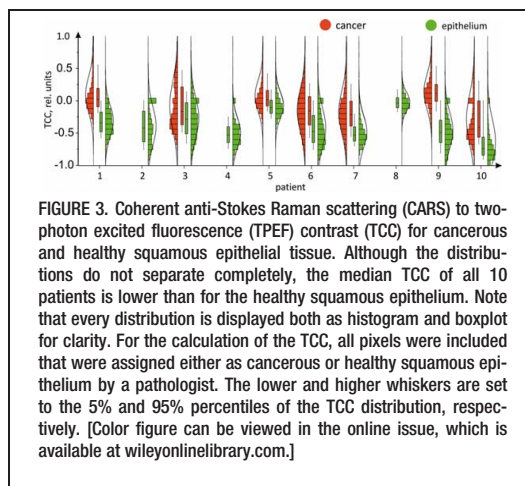
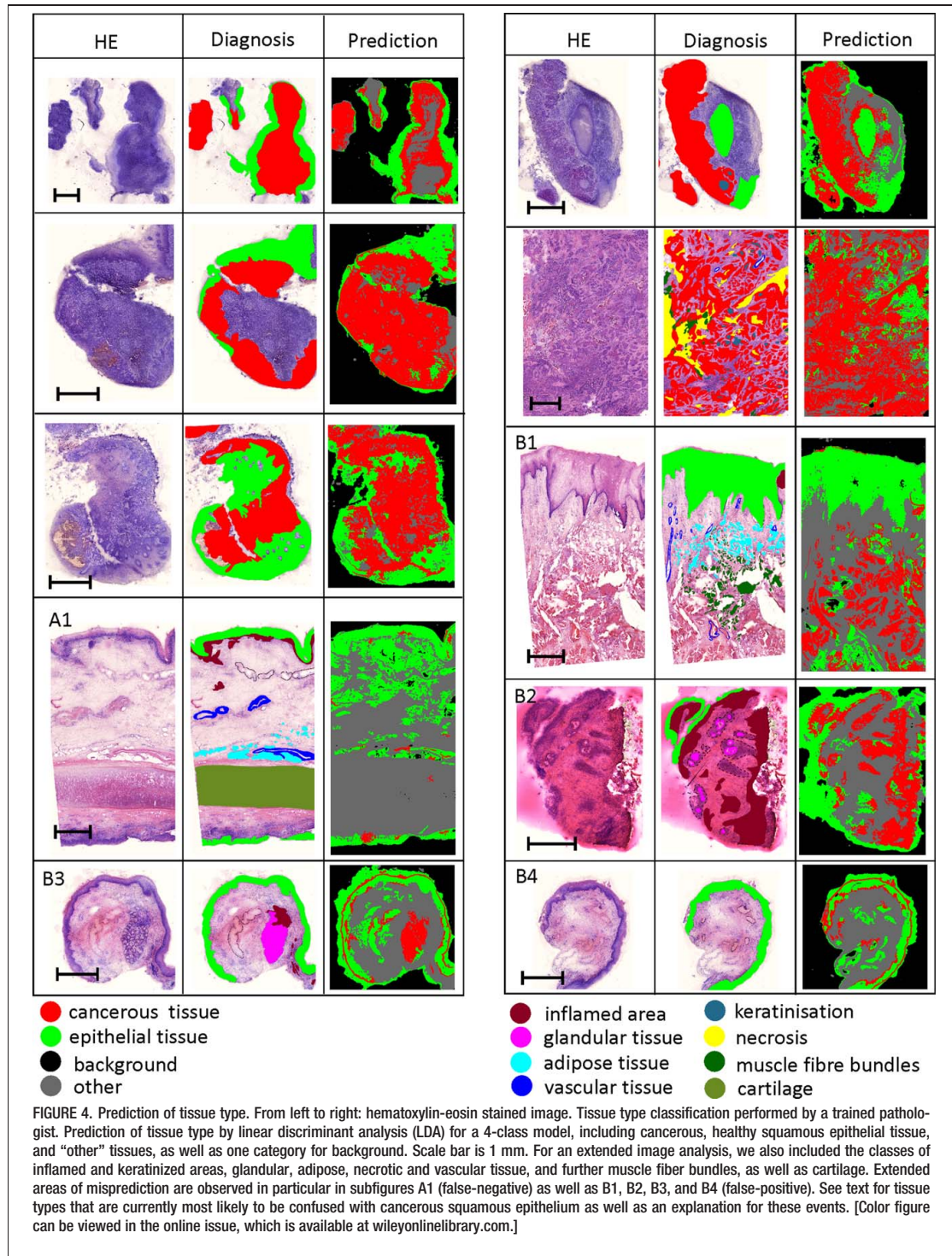


FIGURE 3. Coherent anti-Stokes Raman scattering (CARS) to two-photon excited fluorescence (TPEF) contrast (TCC) for cancerous and healthy squamous epithelial tissue. Although the distributions do not separate completely, the median TCC of all 10 patients is lower than for the healthy squamous epithelium. Note that every distribution is displayed both as histogram and boxplot for clarity. For the calculation of the TCC, all pixels were included that were assigned either as cancerous or healthy squamous epithelium by a pathologist. The lower and higher whiskers are set to the 5% and 95% percentiles of the TCC distribution, respectively. [Color figure can be viewed in the online issue, which is available at wileyonlinelibrary.com.]

cancerous from benign epithelial tissue directly, because both do not express collagen themselves, although head and neck cancer is known to rebuild the extracellular matrix by remote controlling of the surrounding fibroblasts.^{27,28} Thus, forming the ratio with an empty channel (SHG) would decrease the information content. Consequently, we selected the TPEF to CARS contrast ($TCC = [I_{TPEF} - I_{CARS}] / [I_{TPEF} + I_{CARS}]$) for visualization of the qualitative differences between healthy and cancerous squamous epithelial tissue. As apparent from Figure 3, cancerous squamous epithelium is characterized by an increased TCC value as compared to healthy squamous epithelium. However, the universality of such a simple approach suffers from considerably high intrapatient and interpatient variance (see Figure 3; ie, the median as well as the width of the TCC distributions feature large variations). Nevertheless, Figure 3 supports 3 important statements. (1) On median, the TCC level of cancerous squamous epithelium exceeds that of healthy squamous epithelium, as supported by a Wilcoxon Mann-Whitney test resulting with a p value of $1.8 \cdot 10^{-10}$. (2) The interpatient and intrapatient variance as well as the lack of separation of the TCC distributions for healthy and malignant transformed tissue forbids an automated prediction solely based on a single TCC value of potential cancerous areas and an accurate delineation of the malignant transformed regions. (3) For an improved accuracy of cancer prediction, features beyond the TCC level need to be extracted utilizing all 3 imaging modalities. Because pathologists mostly base their diagnosis on morphology, it seems obvious to include texture features apart from the pixel-wise absolute or relative intensity values. In fact, texture features were extensively used for cancer prediction evaluating stained tissue section in the past.²⁹⁻³²

For bedside use, the texture analysis of multimodal images – composed of up to several gigapixels of image data – should be computationally inexpensive to result in reliable predictions within seconds or few minutes. Further, biomedical specimens are generally nonsymmetric



limiting the useful parameter set to those that are rotationally invariant. Otherwise, the orientation of the sample on the sample holder or the direction along which the tissue was sliced would influence the prediction results. After these considerations, we selected simple statistical properties of the intensity histogram of the multimodal images, such as mean, standard deviation (SD), smoothness, third moment, uniformity, and entropy for our analysis.³³ An overview of all features evaluated, including their definition, is provided in the Supplementary Table S1, online only. For each feature utilized, we calculated the Fisher's discriminant ratio to rank their significance for the discrimination between cancerous and healthy squamous epithelium as well as cancerous and nonsquamous epithelial tissue. A summary of the Fisher's discriminant ratio computation results can be found in Supplementary Table S2, online only. As a result of the texture analysis, it was found that texture measures, such as the SD, smoothness, and entropy of the TPEF and CARS channel, as well as the mean TPEF and the TCC value, are of utmost importance for the discrimination between cancerous and healthy squamous epithelium. To distinguish between cancerous and other types of tissue, excluding healthy squamous epithelium, in particular, the uniformity and entropy of SHG as well as the SD, smoothness, and third moment of the CARS channel are of major significance.

The total 18 texture features as well as the SAAID and TCC values were utilized for prediction of all 30 multimodal images applying a linear discriminant analysis (LDA). As a reference for machine learning and prediction quality, a trained pathologist outlined distinct tissue types as visualized in Figure 4 and Supplementary Figure S2, online only. Here, the pathologist distinguished up to 8 different classes of tissue (ie, benign squamous epithelial tissue, cancer squamous epithelial tissue, inflamed area, glandular tissue, adipose tissue, vascular tissue, muscle fiber bundles, and keratinization).

The results for the nontrivial distinction between healthy squamous and cancerous squamous epithelium adding only 2 further classes (i.e., "other" tissues and background), are shown in Figure 4. For this simplest model, the predictions of healthy epithelium are in great visual agreement with the initial diagnosis. Further, Figure 4 illustrates a good compliance between true cancerous and predicted cancerous tissue. In relative numbers, the pixelwise true-positive rate for cancer is 63.0%, for healthy epithelium is 74.2%, whereas the mean and SD of the ratio of diagnosed and predicted cancerous area is 0.78 and 0.27, respectively (see also Supplementary Table S3, and Figure S3, online only). Epithelium is mispredicted as cancer with 17.3%. The true-positive prediction values for background and nonsquamous epithelial tissue are 89% and 68%, respectively, resulting in an overall pixel weighted accuracy of 74%.

For an appropriate clinical treatment, however, the finding of absence or presence of cancer is the ultimate goal rather than the ability of a pixelwise classification. For further diagnostic applications, the prediction may be reduced to a simple "cancerous specimen" or "noncancerous specimen" statement for an individual sample section. To provide such a statement for all tissue sections investigated, it was decided to set the threshold

TABLE 1. Confusion matrix for a linear discriminant analysis-based cancer diagnosis for all 30 multimodal images.

		Automatic predicted class	
		Cancer yes	Cancer no
Pathologist's diagnosis	Cancer yes	88% (15/17)	12% (2/17)
	Cancer no	30% (4/13)	70% (9/13)

The rate of the correct diagnosis can be found on the main diagonal. Although the prediction of true-positive cancer is good, a comparably high false-positive result is obtained. False-positive diagnosis results in particular from tissues with high metabolic activities, which are smooth muscle, glandular, and inflamed tissue, as well as the highly proliferating basal layer. False-negative diagnoses arise from samples with cancerous areas much smaller than the selected image area threshold of 5%.

to 5% of the overall number of pixels that needed to be grouped as cancerous squamous epithelium by LDA. The resulting prediction quality of this approach is summarized in Table 1 as confusion matrix.

Table 1 displays high rates of 88% and 70% for true-positive and true-negative cancer diagnoses based on multimodal images, respectively. The major challenge, however, remains in a high rate of false-positive diagnoses. Although, false-positive decisions in medical diagnosis is less critical than false-negative diagnosis — with the argument that all machine cancer predictions will force particular attention of a trained pathologist and are therefore controlled — further efforts are required to improve the accuracy of the automated prediction and diagnosis.

For a better understanding of the current challenges, the false-positive diagnosed samples outlined in Figure 4 by the subscript B1 to B4 shall be considered in more detail. Samples B1 to B3 possess extended areas of smooth muscle, glandular, and inflamed tissue, respectively, which are falsely diagnosed as "cancer." Like cancerous tissue, smooth muscle, glandular, and inflamed tissue share a high metabolic activity in order to fulfill their functionalities, which are physical contraction, secretion, and immune defense, respectively. An increased metabolic activity requires high NAD(P)H concentrations that result in comparably high TPEF signal strength. As neither the CARS nor the SHG signal strength differ significantly for cancerous, glandular, and inflamed tissue, confusion of tissue types may result. For sample B4, in particular, the fast-growing and dividing basal layer between squamous epithelium and dermis is mispredicted to a high extend. Again, confusion is caused most likely by the high metabolic NAD(P)H uptake and an increased cell density that is also frequently encountered for head and neck cancer.

Less likely than a false-positive result, 2 of 17 samples were diagnosed as healthy, although they were classified as cancer (eg, the sample with subscript A1 in Figure 4). The simple reason for this false-negative result can be attributed to the prediction threshold of 5% cancerous tissue of a whole multimodal image to be grouped into the category "cancer." In both cases, the LDA was able to predict the cancerous areas correctly, but the predicted areas were too small to force a positive diagnosis — see also the prediction result of the sample with subscript A1 in Figure 4.

Because the presented LDA model is likely to confuse cancerous squamous epithelium with the growing basal

TABLE 2. Confusion matrix for a linear discriminant analysis-based cancer diagnosis including the linear discriminant analysis postprocessing for all 30 multimodal images.

		Automatic predicted class	
		Cancer yes	Cancer no
Pathologist's diagnosis	Cancer yes	94% (16/17)	6% (1/17)
	Cancer no	15% (2/13)	85% (11/13)

Compared to Table 1, the additional LDA reduces significantly the confusion of cancerous epithelium with smooth muscle, glandular and inflamed tissue and, thereby, the false-negative and false-positive rate.

layer of the epithelium, glandular tissue, as well as with smooth muscles and inflamed areas, it seems imperative to add more classes for a better distinction of tissue types. Thus, we applied the LDA to a 10 class model, including the tissue types: cancer, epithelium, inflamed area, adipose tissue, glandular tissue, keratinization, smooth muscle, vascular tissue, background, and "other" (see also Figure 4 and Supplementary Figure S2, online only). The prediction results are summarized in Supplementary Table S4. Although the confusion between cancer and inflamed areas significantly dropped, new mispredictions as "cancer" appeared mostly for glandular tissue, smooth muscle, and keratinization. Different than desired, the overall cancer prediction quality reduced for the more complicated model demanding more information or improved features involved for decision-making.

In order to overcome these difficulties, we introduce in our study a second classifier, which is used for automatic postprocessing. Such a procedure allows significantly reduced false-positive rates because of using additional information about the most difficult classes (ie, tissue types), which are falsely predicted as cancer. Thus, the overall workflow to derive an optimal diagnosis consists of the following steps. First, we use the LDA that classifies the images into the 4 classes, namely cancerous tissue, healthy squamous epithelial tissue, "other" tissues, and a category for background (see Figure 4). For each sample, connected regions are grouped that are predicted as cancer. The additional classifier constructs for each cancer group 3 binary decisions for the 3 following pairs of classes: cancer, glandular tissue; cancer, inflamed area; and cancer, smooth muscle. For the construction of each of these 3 binary classifiers, selected features are used that are optimal for the particular decision. Cancer is predicted if at least one connected region exists, whereas all 3 binary decisions are positive in terms of cancerous tissue prediction.

Table 2 shows the final results of the diagnostic 2-step procedure. Note the improvements in quality of diagnostics compare to the LDA classifier alone (Table 1). The reduction of false-positive rates is done by incorporating additional information about the tissue, which was wrongly predicted as cancer, namely glandular tissue, inflamed area, and smooth muscle. At the same time, the true-positive rate is increased, because for the presented diagnostic model the size of the cancer area is not important anymore. The decision of "cancer tissue" is made only if cancer is confirmed at least in one connected

region. Regardless, the described advantages in prediction quality feature a drawback: the 2-step diagnostic model is computationally more complex and, thus, requires more time to make a final decision. Currently, the image acquisition time is about 160 s/mm², whereas the complete image analysis requires 13 minutes (preprocessing = 5 minutes; feature extraction = 3 minutes; classification, step 1 = 2.5 minutes; and classification, step 2 = 2.5 minutes) for the largest multimodal images on an Intel Xeon processor E5-2643v2 (6 Cores, 3.50 GHz, 25 MB). We would like to point out that the system was not yet optimized for speed. Multifocus approaches as well as the implementation of resonant or polygonal laser scanning mirrors can increase the image acquisition speed by a multifold, whereas additional computational power is just a matter of time or funds.

CONCLUSION

We have shown that multimodal nonlinear microscopy provides diagnostically relevant information. This information content may be split into morphological features, such as the nuclei to cytoplasm ratio and intensity findings. For the latter, it was demonstrated that the TPEF to CARS contrast (TCC) is enhanced for cancerous squamous epithelium as compared to healthy squamous epithelium on median with a p value of $1.8 \cdot 10^{-10}$ resulting from a Wilcoxon Mann-Whitney test.³⁴ The large inpatient and interpatient variances, however, prevent a direct classification based on such simple measures. Aiming for an automated classification, we extracted texture features in addition to the TPEF to SHG contrast (SAAID) and TCC. Using a total of 20 parameters, we performed, we believe for the first time, a supervised prediction of cancerous tissue based on multimodal images applying an LDA. The pixel-weighted average accuracy of prediction for a 4 class model (cancer, healthy squamous epithelium, other tissue types, and background) was found to be 74%, and the LDA prediction is in good agreement with the pathologist's diagnosis. In particular, the SD, smoothness, and entropy of the TPEF and CARS channel, as well as the TCC and the mean TPEF value are of largest significance for the discrimination between cancerous and healthy squamous epithelium. The presented LDA model is suited for a visualization of different tissue areas. Another classification model was trained, which converts the visualization of the tissue into a diagnosis if a cancer region is present or not. This fully automatic procedure features a 90% accuracy compared to gold standard diagnosis of a blinded pathologist. In addition, the false-negative rate is 6%, which is quite low.

The presented methodology may be regarded as a starting point for further studies elucidating the origin of the observed biological variations. To verify whether the variation originates from the area of resection, a future study has to comprise a larger pool of samples that arise only from one or a very few head and neck areas. Still, our results clearly demonstrate the usefulness of automatic prediction approaches evaluating multimodal images and, therefore, will boost the development of objective diagnostic tools based on nonlinear optical microscopy. The model reported in this contribution can be applied as a filter that allows for the reduction of the pathologist's

workload and thereby increase overall quality of diagnostics.

REFERENCES

1. Jemal A, Bray F, Center MM, Ferlay J, Ward E, Forman D. Global cancer statistics. *CA Cancer J Clin* 2011;61:69–90.
2. Howlader N, Noone AM, Krapcho M, et al. SEER cancer statistics review (CSR) 1975–2011. 2014. Available at: http://seer.cancer.gov/csr/1975_2011/. Accessed August 1, 2015.
3. Garavello W, Bertuccio P, Levi F, et al. The oral cancer epidemic in central and eastern Europe. *Int J Cancer* 2010;127:160–171.
4. So WK, Chan RJ, Chan DN, et al. Quality-of-life among head and neck cancer survivors at one year after treatment – a systematic review. *Eur J Cancer* 2012;48:2391–2408.
5. Wissinger E, Griebisch I, Lungershausen J, Foster T, Pashos CL. The economic burden of head and neck cancer: a systematic literature review. *Pharmacoeconomics* 2014;32:865–882.
6. Marioni G, Marchese-Ragona R, Cartei G, Marchese F, Staffieri A. Current opinion in diagnosis and treatment of laryngeal carcinoma. *Cancer Treat Rev* 2006;32:504–515.
7. Seoane J, Takkouche B, Varela-Centelles P, Tomás I, Seoane-Romero JM. Impact of delay in diagnosis on survival to head and neck carcinomas: a systematic review with meta-analysis. *Clin Otolaryngol* 2012;37:99–106.
8. Platzek I, Beuthien-Baumann B, Schneider M, et al. PET/MRI in head and neck cancer: initial experience. *Eur J Nucl Med Mol Imaging* 2013;40:6–11.
9. Haerle SK, Fischer DR, Schmid DT, Ahmad N, Huber GF, Buck A. 18F-FET PET/CT in advanced head and neck squamous cell carcinoma: an intra-individual comparison with 18F-FDG PET/CT. *Mol Imaging Biol* 2011;13:1036–1042.
10. Al Faraj A, Luciani N, Kolosnjaj-Tabi J, et al. Real-time high-resolution magnetic resonance tracking of macrophage subpopulations in a murine inflammation model: a pilot study with a commercially available cryogenic probe. *Contrast Media Mol Imaging* 2013;8:193–203.
11. Smith L, Macneil S. State of the art in non-invasive imaging of cutaneous melanoma. *Skin Res Technol* 2011;17:257–269.
12. Horton NG, Wang K, Kobat D, et al. In vivo three-photon microscopy of subcortical structures within an intact mouse brain. *Nat Photonics* 2013;7:205–209.
13. Heuke S, Vogler N, Meyer T, et al. Detection and discrimination of non-melanoma skin cancer by multimodal imaging. *Healthcare* 2013;1:64–83.
14. Meyer T, Guntinas-Lichius O, von Eggeling F, et al. Multimodal nonlinear microscopic investigations on head and neck squamous cell carcinoma: toward intraoperative imaging. *Head Neck* 2013;35:E280–E287.
15. Baumgartl M, Gottschall T, Abreu-Afonso J, et al. Alignment-free, all-spliced fiber laser source for CARS microscopy based on four-wave-mixing. *Opt Express* 2012;20:21010–21018.
16. Balu M, Liu G, Chen Z, Tromberg BJ, Potma EO. Fiber delivered probe for efficient CARS imaging of tissues. *Opt Express* 2010;18:2380–2388.
17. Meyer T, Bergner N, Bielecki C, et al. Nonlinear microscopy, infrared, and Raman microspectroscopy for brain tumor analysis. *J Biomed Opt* 2011;16:021113.
18. Hu W, Li H, Wang C, Gou S, Fu L. Characterization of collagen fibers by means of texture analysis of second harmonic generation images using orientation-dependent gray level co-occurrence matrix method. *J Biomed Opt* 2012;17:026007.
19. Medyukhina A, Vogler N, Latka I, et al. Automated classification of healthy and keloidal collagen patterns based on processing of SHG images of human skin. *J Biophotonics* 2011;4:627–636.
20. Provenzano PP, Eliceiri KW, Campbell JM, Inman DR, White JG, Keely PJ. Collagen reorganization at the tumor-stromal interface facilitates local invasion. *BMC Med* 2006;4:38.
21. Greenberg ML, Weinger JG, Matheu MP, et al. Two-photon imaging of remyelination of spinal cord axons by engrafted neural precursor cells in a viral model of multiple sclerosis. *Proc Natl Acad Sci U S A* 2014;111:E2349–E2355.
22. Meyer T, Chemnitz M, Baumgartl M, et al. Expanding multimodal microscopy by high spectral resolution coherent anti-Stokes Raman scattering imaging for clinical disease diagnostics. *Anal Chem* 2013;85:6703–6715.
23. Lin SJ, Wu R Jr, Tan HY, et al. Evaluating cutaneous photoaging by use of multiphoton fluorescence and second-harmonic generation microscopy. *Opt Lett* 2005;30:2275–2277.
24. Schilders SP, Gu M. Three-dimensional autofluorescence spectroscopy of rat skeletal muscle tissue under two-photon excitation. *Appl Opt* 1999;38:720–723.
25. Zoumi A, Lu X, Kassab GS, Tromberg BJ. Imaging coronary artery microstructure using second-harmonic and two-photon fluorescence microscopy. *Biophys J* 2004;87:2778–2786.
26. Lin SJ, Jee SH, Kuo CJ, et al. Discrimination of basal cell carcinoma from normal dermal stroma by quantitative multiphoton imaging. *Opt Lett* 2006;31:2756–2758.
27. Sok JC, Lee JA, Dasari S, et al. Collagen type XI $\alpha 1$ facilitates head and neck squamous cell cancer growth and invasion. *Br J Cancer* 2013;109:3049–3056.
28. Rosenthal EL, Zhang W, Talbert M, Raisch KP, Peters GE. Extracellular matrix metalloprotease inducer-expressing head and neck squamous cell carcinoma cells promote fibroblast-mediated type I collagen degradation in vitro. *Mol Cancer Res* 2005;3:195–202.
29. Pires A, Rusinek H, Suh J, Naidich DP, Pass H, Ko JP. Clustering of lung adenocarcinomas classes using automated texture analysis on CT images. *Proc SPIE* 2013;8669:866925.
30. George J, Claes P, Vunckx K, et al. A textural feature based tumor therapy response prediction model for longitudinal evaluation with PET imaging. Proceedings/IEEE International Symposium on Biomedical Imaging: from nano to macro. 2012 9th IEEE International Symposium; 2012. pp 1048–1051.
31. Hamilton PW, Bartels PH, Thompson D, Anderson NH, Montironi R, Sloan JM. Automated location of dysplastic fields in colorectal histology using image texture analysis. *J Pathol* 1997;182:68–75.
32. Smolle J. Computer recognition of skin structures using discriminant and cluster analysis. *Skin Res Technol* 2000;6:58–63.
33. Gonzales RC, Woods RE. Digital image processing, 3rd edition. Upper Saddle River, NJ: Prentice Hall; 2007.
34. Bronshtein IN, Semendyayev KA, Musiol G, Muehlig H. Handbook of Mathematics. Deutsch Harri GmbH; 1985.

Supplementary information to: [Multimodal nonlinear microscopy of head and neck carcinoma – towards surgery assisting frozen section analysis](#)

Authors: Sandro Heuke^{1,2,†}, Dipl.-Chem., Olga Chernavskaia^{1,2,†}, PhD, Thomas Bocklitz², PhD, Fisseha Bekele Legesse^{1,2}, M. Sci., Tobias Meyer^{1,2}, PhD, Denis Akimov¹, PhD, Olaf Dirsch³, MD, Günther Ernst^{1,4}, MD, Ferdinand von Eggeling^{1,2,4}, PhD, Iver Petersen⁵, MD, Orlando Guntinas-Lichius⁴, MD Michael Schmitt², PhD, Jürgen Popp^{1,2*}, PhD.

Affiliations:

¹Leibniz Institute of Photonic Technology, Jena, Germany.

²Institute of Physical Chemistry and Abbe Center of Photonics, Friedrich-Schiller-University, Jena, Germany.

³Department of Pathology, Hospital, Chemnitz, Germany.

⁴Department of Otorhinolaryngology, University Hospital, Jena, Germany.

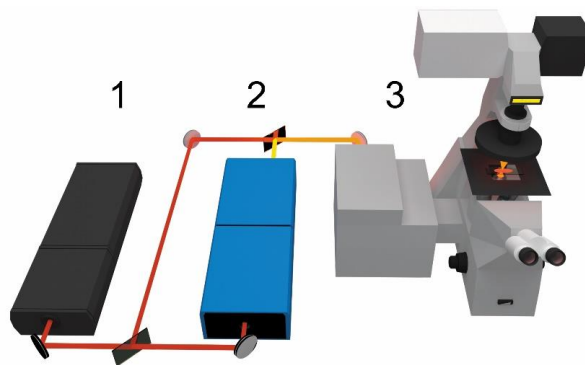
⁵Institute of Pathology, Jena University Hospital, 07743 Jena, Germany.

[†]Both authors contributed equally.

Supplementary information - Materials and Methods: experimental Setup

A detailed presentation of the experimental setup can be found elsewhere [35]. A schematic of the experimental setup is displayed in supplementary figure 1. Briefly, a Coherent Mira HP Titanium-Sapphire (Ti:Sa) laser (Coherent, USA) is pumped by a continuous wave Neodymium-Vanadate laser with an average power of 18 W operating at 532 nm. The Ti:Sa-laser generates 2-3 ps pulses (FWHM) at 830 nm with a repetition rate of 76 MHz. The 3.5 W averaged output power of the Ti:Sa-laser is split into two parts. The first part is used directly, i.e., without frequency conversion, as the Stokes beam. The second part is coupled into an optical parametric oscillator (OPO, APE, Berlin) that allows to adjust the pump wavelength in the range from 500 to 1600 nm. To match the CH₂ symmetrical stretching vibration at 2850 cm⁻¹ for the CARS measurements, the OPO is tuned to 671 nm. Both beams, pump and Stokes, are temporally and spatially overlapped and coupled into a laser scanning microscope (LSM 510 Meta, Zeiss, Jena, Germany) and focused onto the sample with a 20× (NA 0.8) achromatic objective (Zeiss). The optical non-linear response of the sample is wavelength filtered by means of various dielectric filters and detected by photomultiplier tubes (PMT, Hamamatsu Photonics, Hamamatsu, Japan). Large area scans of the samples of up to 12×15 tiles, each having a size of 450 μm × 450 μm, were recorded. Every tile was

acquired with a resolution of $2,048 \times 2,048$ pixels and a pixel dwell time of $1.6 \mu\text{s}$. By averaging twice the total acquisition time for per tile does not exceed 32 s for all three modalities, i.e. CARS, TPEF and SHG. The average power at sample was 25 mW and 50 mW for the pump and Stokes beam, respectively. A discussion about the applied power and potential linear as well as non-linear tissue photodamage can be found elsewhere [36].



Supplementary figure S1: Schematic of the experimental setup used for non-linear multimodal microscopy. 1 Ti:Sa-laser; 2 Optical parametric oscillator (OPO); 3 Laser scanning microscope.

Materials and Methods: sample preparation

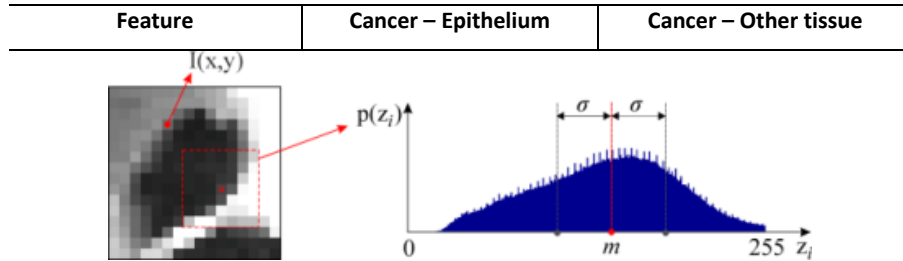
Head and Neck samples of 10 patients with primary diagnosis of head and neck squamous cell carcinoma (HNC) were collected at the Jena University Hospital, Jena. Institutional review board approval was obtained prior to study initiation by the Ethics Committee of the Jena University Hospital, Thuringia, Germany (No. 4158-07/14). The patients gave written informed consent to use tumor material for the presented investigations. The excised tissue blocks were frozen in distilled water and further sliced into $20 \mu\text{m}$ thin sections. For each section under investigation several adjacent parallel section of $5 \mu\text{m}$ thickness were obtained and subject to various staining protocols including H&E- and immunohistochemistry. The $20 \mu\text{m}$ thick sections were placed on quartz object holders (Ted Pella, USA) and investigated by non-linear multimodal microscopy without further washing or staining steps.

Materials and Methods: image processing

Prior to prediction all multimodal images were filtered, resampled 4x4, corrected for uneven illumination and contrast adjusted. Details about the preprocessing can be found elsewhere [37].

Various tissue types were labeled with distinct colors in H&E stained images by a trained pathologist. The areas marked were extracted and utilized for supervised classification - see fig. 4. A co-registration procedure between H&E stained and multimodal images was performed based on rigid transformation, since they were acquired with different microscopes [38]. The co-registration corrects shifts, rotation and zoom of H&E stained images relative to the corresponding multimodal images.

For classification 20 features were extracted, i.e., SAAID, TCC and 6 texture features for each modality. Details concerning the definition and meaning of texture features can be found in reference [33] and sup. Table S4. All features were normalized to [0 ... 1]. The equality of TCC median value for cancerous and healthy epithelium was estimated using a Wilcoxon-Mann-Whitney test [34]. The test results a p -value of $1.8 \cdot 10^{-10}$ supporting the rejection of the null hypothesis of equal medians. Fisher's discriminant ratio (FDR) was used to rank the significance of each individual feature for the discrimination between cancerous and healthy squamous epithelium as well as cancerous and non-squamous epithelial tissue [39]. The FDRs were calculated for a two-class model. Each feature was evaluated separately.



Mean	$m = \sum_{i=0}^{L-1} z_i p(z_i)$	Average intensity level of an image area.
Standard deviation	$\sigma = \sqrt{\sum_{i=0}^{L-1} (z_i - m)^2 p(z_i)}$	Average contrast.
Smoothness	$R = 1 - \frac{1}{1 + \sigma^2}$	Relative smoothness of the intensity levels. It is 0 for areas of constant intensity and returns a value of 1 for regions with large excursions of its intensity values.
Third moment	$\mu_3 = \sqrt{\sum_{i=0}^{L-1} (z_i - m)^3 p(z_i)}$	Skewness of intensity histogram. It returns a value of 0, a positive or negative value for histograms that are symmetric, skewed to the right or skewed to the left, respectively.
Uniformity	$U = \sum_{i=0}^{L-1} p^2(z_i)$	U is maximal when all intensity values are equal and decreases from there.
Entropy	$e = - \sum_{i=0}^{L-1} p(z_i) \log_2 p(z_i)$	Variability of intensity levels. The entropy becomes 0 for a constant image.

Supplementary table S1: Texture feature calculation based on statistical properties of the intensity histogram. Note that L denotes the number of bins that are specified by the image type, e.g. an 8-bit image possesses 256 bins.

Publications and conference contributions

	Mean of FDA	Std of FDA	Mean of FDA	Std of FDA
Std TPEF	0.889	0.149	0.009	0.009
Std CARS	0.688	0.048	0.341	0.062
Entropy TPEF	0.581	0.067	0.008	0.006
Smoothness CARS	0.507	0.046	0.243	0.050
Smoothness TPEF	0.431	0.074	0.030	0.014
(TPEF-CARS)/(TPEF+CARS)	0.414	0.070	0.009	0.007
Mean TPEF	0.395	0.125	0.065	0.029
Entropy CARS	0.394	0.051	0.251	0.038
Std SHG	0.160	0.029	0.144	0.062
3rd moment CARS	0.146	0.032	0.197	0.037
3rd moment SHG	0.098	0.018	0.026	0.018
Smoothness SHG	0.090	0.020	0.078	0.040
Uniformity TPEF	0.081	0.013	0.016	0.006
Entropy SHG	0.076	0.025	0.339	0.122
Mean SHG	0.064	0.018	0.138	0.047
Uniformity SHG	0.061	0.023	0.359	0.138
3rd moment TPEF	0.041	0.009	0.004	0.002
Uniformity CARS	0.029	0.009	0.047	0.006
(TPEF-SHG)/(TPEF+SHG)	0.020	0.006	0.111	0.020
Mean CARS	0.011	0.011	0.193	0.048

Supplementary table S2: Calculation of class separability using Fisher's discriminant ratio (FRD). All features are ranked in the order of descending values of FDR for the two classes cancerous squamous cell carcinoma and healthy squamous epithelium. For discrimination between cancerous and healthy squamous epithelium in particular the standard deviation, smoothness and entropy of TPEF and CARS, as well as the TCC and the mean TPEF value are of significance. To distinguish between cancerous and other types of tissue excluding healthy epithelium, the Uniformity of SHG, the standard deviation of CARS, the entropy of SHG and CARS as well as the smoothness and 3rd moment of CARS are of importance. Note that $FDR_i = (\mu_{1,i} - \mu_{2,i})^2 / (\sigma_{1,i}^2 + \sigma_{2,i}^2)$, where $\mu_{1,i}$, $\sigma_{1,i}^2$ and $\mu_{2,i}$, $\sigma_{2,i}^2$ are the mean and dispersion values of class 1 and class 2, respectively. The index $i = 1, 2, \dots, m$ corresponds to the selected feature. The mean FDR and its standard deviation were obtained by "leave one patient out" cross validation.

The supervised classification of the samples was performed using a linear discriminant analysis method (LDA) [40]. Additionally, the classification results were filtered as follows: for each class connected areas were identified [33]. If a particular area were smaller than 50x50 pixel corresponding to 44x44 μm^2 it was reclassified as “other type of tissue”.

Evaluation of the observed prediction quality was performed by leave one patient out cross validation meaning that the whole dataset was divided into a testing dataset, i.e. images of 3 sections originating from one patient, and a training dataset, i.e. samples from rest of the patients. The individual classifier was trained on the basis of one training dataset following the prediction of all images of testing dataset. This procedure was repeated for each patient and averaged to calculate the overall performance of prediction.

The prediction was executed for different 4 and 10 distinct classes. Pixelwise calculated classification results for 4 classes are presented as confusion matrix in sup. table S2. On the diagonal, true positive rates can be found for a particular class whereas non-diagonal elements present false negative or false positive rates for the corresponding class.

The decision about cancer presence in the whole scan was stated if the number of cancer predicted pixels is more than 5% of overall number of specimen (sample) pixels. The confusion matrix of this procedure is presented in table 1. However this procedure results in high false positive rate that is caused by glandular and inflamed tissues and smooth muscle. To overcome this challenge we construct three additional LDA classifiers that are specially adjusted to detect the difference between these problematic classes and cancerous regions. These three classifiers are binary, work independent of each other, and are supposed to separate cancerous areas from glandular tissue, inflamed tissue and smooth muscle tissue, respectively. Since these classes are not well separated, the three additional classification models utilize the best feature selection based on FDR value. Entropy and uniformity of SHG as well as TPEF-SHG and CARS-SHG correlation (new feature) are most important for the discrimination between cancer and glandular tissue. Entropy and uniformity of SHG, standard deviation and smoothness of CARS allow for a good separation between cancer and inflamed tissue. The separation of smooth muscle and cancer regions could be distinguished by SHG and TPEF texture features.

Now the decision about cancer presence in the whole image is performed according to the following steps:

The multimodal image is classified by the LDA model into 4 classes: cancer, benign epithelium, other type of tissue and background.

All cancer classified pixels are divided into isolated regions based on 8-connectivity property [34].

Publications and conference contributions

Each isolated region is decided to be cancer if the three binary classifiers predict cancer tissue in more than 70% of region pixels.

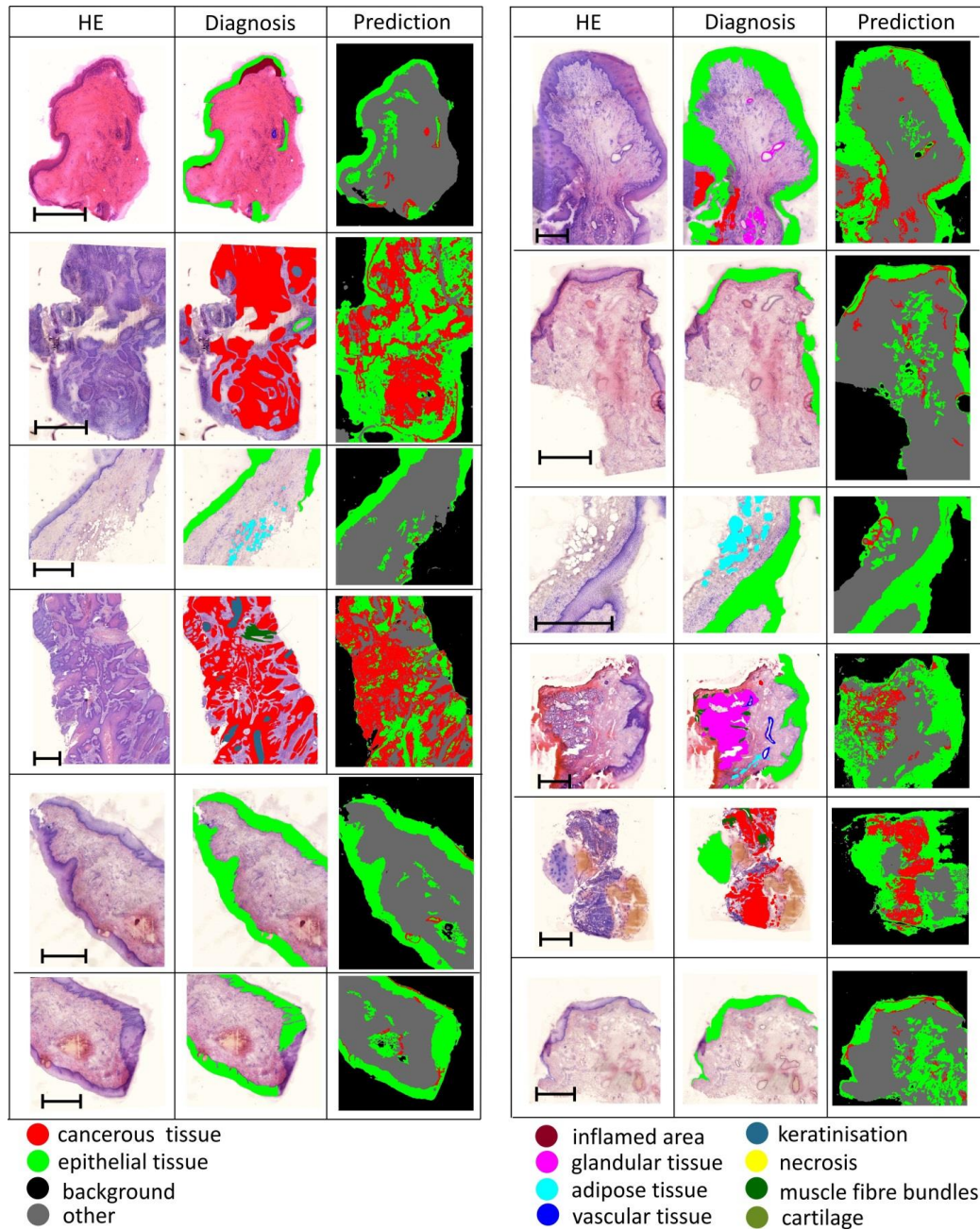
The presence of cancer in the whole sample is stated if at least one isolated region is predicted as cancer.

4 class model		Predicted class			
		cancer	epithelium	background	Other
Actual class	cancer	63.0	19.1	0.5	17.4
	epithelium	17.3	74.2	2.1	6.4
	background	0.2	4.6	88.7	6.5
	Other	18.8	10.7	2.6	67.9

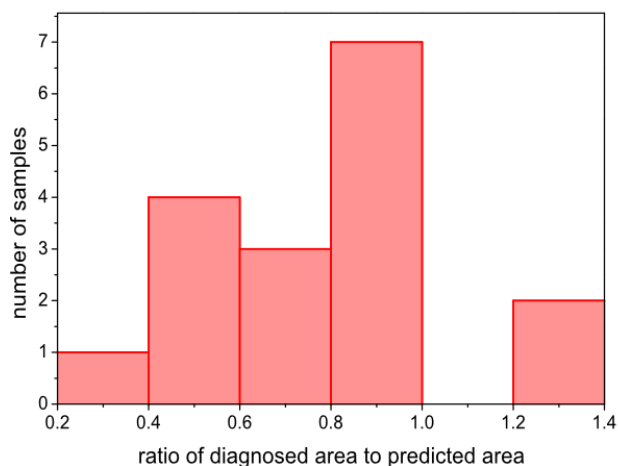
Supplementary table S3: Cancer prediction confusion matrix. The rates of the correct prediction can be found on the main diagonal. Though the prediction of true positive cancer is good a comparably high false negative result is obtained. See text for an explanation why and which tissue types are currently confused with cancerous tissue. All numbers are given in percent.

10 class model		Predicted class									
		cancer	epithelium	inflamed area	adipose tissue	glandular tissue	keratinization	smooth muscle	vascular tissue	background	other
Actual class	cancer	22.0	14.5	1.1	0.7	11.5	33.6	4.8	10.0	0.6	1.3
	epithelium	3.6	73.2	2.0	0.8	1.0	15.8	0.7	0.5	2.1	0.5
	inflamed area	1.4	10.8	45.0	0.6	16.6	4.0	3.1	10.8	0.7	7.0
	adipose tissue	1.9	21.7	6.5	35.6	3.0	4.4	10.1	11.5	1.6	3.7
	glandular tissue	13.3	16.9	15.2	0.8	18.0	9.2	8.9	11.4	0.1	6.2
	keratinization	7.4	16.9	0.1	7.2	5.2	45.6	15.5	2.0	0.0	0.2
	smooth muscle	23.4	8.4	6.2	0.7	11.4	4.9	30.4	8.6	0.9	5.1
	vascular tissue	6.4	19.5	38.7	2.4	3.8	4.8	5.4	14.1	0.0	5.1
	background	0.1	8.0	1.4	0.1	0.0	0.0	0.3	0.6	88.7	0.6
	other	10.5	20.0	25.2	1.8	4.1	3.3	9.1	11.9	2.4	11.8

Supplementary table S4: Result of classification into 10 classes is also presented in table 3. As it can be seen such as Inflamed areas and adipose tissue do not influence the prediction of cancer, but glandular tissue, vascular tissue, muscle fiber bundles and keratinization is often predicted as cancer and cause a high false negative rate for cancer in addition. All numbers are given in percent.



Supplementary figure S2: Prediction of tissue type (fig. 4) continued.



Supplementary figure S3: Area ratios of predicted and diagnosed cancerous tissue. The histogram was calculated for 17 samples with diagnosis of HNC. To estimate the variation of predicted cancer sizes in comparison to the pathologist's classifications the ratio of the pixel number of the predicted and corresponding diagnosed cancerous area was computed.

References

- [1] Jemal A, Bray F, Center MM, Ferlay J, Ward E, Forman D. Global Cancer Statistics. *CA Cancer J Clin.* 2011;61:69–90.
- [2] Howlader N, Noone AM, Krapcho M, Garshell J, Miller D, Altekruse SF, et al. SEER Cancer Statistics Review (CSR) 1975-2011. 2014;p. 25. Available from: http://seer.cancer.gov/csr/-1975_2011/.
- [3] Garavello W, Bertuccio P, Levi F, Lucchini F, Bosetti C, Malvezzi M, et al. The oral cancer epidemic in central and eastern Europe. *Int J Cancer.* 2010;127:160–171.
- [4] So WKW, Chan RJ, Chan DNS, Hughes BGM, Chair SY, Choi KC, et al. Quality-of-life among head and neck cancer survivors at one year after treatment – A systematic review. *Eur J Cancer.* 2012;48:2391–2408.
- [5] Wissinger E, Griebisch I, Lungershausen J, Foster T, Pashos CL. The Economic Burden of Head and Neck Cancer: A Systematic Literature Review. *Pharmacoeconomics.* 2014;32(9):865–82.

- [6] Marioni G, Marchese-Ragona R, Cartei G, Marchese F, Staffieri A. Current opinion in diagnosis and treatment of laryngeal carcinoma. *Cancer Treat Rev.* 2006;32:504–515.
- [7] Seoane J, b Takkouche, Varela-Centelles P, Tomás I, Seoane-Romero JM. Impact of delay in diagnosis on survival to head and neck carcinomas: a systematic review with meta-analysis. *Clin Otolaryngol.* 2012;37:99–107.
- [8] Platzek I, Beuthien-Baumann B, Schneider M, Gudziol V, Langner J, Schramm G, et al. *Eur J Nucl Med Mol Imaging.* 2013;40:6–11.
- [9] Haerle SK, Fischer DR, Schmid DT, Ahmad N, Huber GF, Buck A. 18F-FET PET/CT in Advanced Head and Neck Squamous Cell Carcinoma: an Intra-individual Comparison with 18F-FDG PET/CT. *Mol Imaging Biol.* 2011;13:1036–1042.
- [10] Faraj AA, Luciani N, Kolosnjaj-Tabi J, Mattarb E, Clement O, Wilhelm C, et al. Real-time high-resolution magnetic resonance tracking of macrophage subpopulations in a murine inflammation model: a pilot study with a commercially available cryogenic probe. *Contrast Media Mol Imaging.* 2013;8:193–203.
- [11] Smith L, MacNeil S. State of the art in non-invasive imaging of cutaneous melanoma. *Skin Res Technol.* 2011;17:257–269.
- [12] Horton NG, Wang K, Kobat D, Clark CG, Wise FW, Schaffer CB, et al. In vivo three-photon microscopy of subcortical structures within an intact mouse brain. *Nat Photonics.* 2013;7:205–209.
- [13] Heuke S, Vogler N, Meyer T, Akimov D, Kluschke F, Röwert-Huber HJ, et al. Detection and Discrimination of Non-Melanoma Skin Cancer by Multimodal Imaging. *Healthcare.* 2013;1:64–83.
- [14] Meyer T, Guntinas-Lichius O, von Eggeling F, Ernst G, Akimov D, Schmitt M, et al. Multimodal nonlinear microscopic investigations on head and neck squamous cell carcinoma: Toward intraoperative imaging. *Head & Neck.* 2012;35(9):280–287.
- [15] Baumgartl M, Gottschall T, Abreu-Afonso J, Díez A, Meyer T, Dietzek B, et al. Alignment-free, all-spliced fiber laser source for CARS microscopy based on four-wave-mixing. *Opt Express.* 2012;20:21010–21018.
- [16] Balu M, Liu G, Chen Z, Tromberg BJ, Potma EO. Fiber delivered probe for efficient CARS imaging of tissues. *Opt Express.* 2010;18:2380–2388.
- [17] Meyer T, Bergner N, Bielecki C, Krafft C, Akimov D, Romeike BFM, et al. Nonlinear microscopy, infrared, and Raman microspectroscopy for brain tumor analysis. *J Biomed Opt.* 2011;16:1–7.

- [18] Hu W, Li H, Wang C, Gou S, Fu L. Characterization of collagen fibers by means of texture analysis of second harmonic generation images using orientation-dependent gray level cooccurrence matrix method. *J Biomed Opt.* 2012;17(2):026007.
- [19] Medyukhina A, Vogler N, Latka I, Kemper S, Böhm M, Dietzek B, et al. Automated classification of healthy and keloidal collagen patterns based on processing of SHG images of human skin. *J Biophotonics.* 2011;4:627–636.
- [20] Provenzano PP, Eliceiri KW, Campbell JM, Inman DR, White JG, Keely PJ. Collagen reorganization at the tumor-stromal interface facilitates local invasion. *BMC Med.* 2006;4:38–52.
- [21] Greenberg ML, Weinger JG, Matheu MP, Carbajal KS, Parker I, Macklin WB, et al. Two-photon imaging of remyelination of spinal cord axons by engrafted neural precursor cells in a viral model of multiple sclerosis. *Proc Natl Acad Sci U S A.* 2014;111:E2349–E2355.
- [22] Meyer T, Chemnitz M, Baumgartl M, Gottschall T, Pascher T, Matthaeus C, et al. Expanding Multimodal Microscopy by High Spectral Resolution Coherent Anti-Stokes Raman Scattering Imaging for Clinical Disease Diagnostics. *Anal Chem.* 2013;85:703–6715.
- [23] Lin SJ, Wu RJ, Tan HY, Lo W, Lin WC, Young TH, et al. Evaluating cutaneous photoaging by use of multiphoton fluorescence and second-harmonic generation microscopy. *Opt Lett.* 2005;30:2275–2277.
- [24] Schilders SP, Gu M. Three-dimensional autofluorescence spectroscopy of rat skeletal muscle tissue under two-photon excitation. *Appl Opt.* 1999;38(4):720–723.
- [25] Zoumi A, Lu X, Kassab GS, Tromberg BJ. Imaging Coronary Artery Microstructure Using Second-Harmonic and Two-Photon Fluorescence Microscopy. *Biophys J.* 2004;87:2778–86.
- [26] Lin SJ, Jee SH, Kuo CJ, Wu RJ, Lin WC, Chen JS, et al. Discrimination of basal cell carcinoma from normal dermal stroma by quantitative multiphoton imaging. *Opt Lett.* 2006;31:2756–2758.
- [27] Sok JC, Lee JA, Dasari S, Joyce S, Contrucci SC, Egloff AM, et al. Collagen type XI a1 facilitates head and neck squamous cell cancer growth and invasion. *Br J Cancer.* 2013;109:3049–3056.
- [28] Rosenthal EL, Zhang W, Talbert M, Raisch KP, Peters GE. Extracellular matrix metalloprotease inducer-expressing head and neck squamous cell carcinoma cells promote fibroblast-mediated type I collagen degradation in vitro. *Mol Cancer Res.* 2005;3(4):195–202.
- [29] Pires A, Rusinek H, Suh J, Naidich DP, Pass H, Ko JP. Clustering of lung adenocarcinomas classes using automated texture analysis on CT images. *Proc SPIE.* 2013;8669:866925.
- [30] George J, Claes P, Vunckx K, Tejpar S, Deroose CM, Nuyts J, et al. A textural feature based tumor therapy response prediction model for longitudinal evaluation with PET imaging. In: *Biomedical Imaging (ISBI), 2012 9th IEEE International Symposium on; 2012.* p. 1048–1051.

- [31] Hamilton PW, Bartels PH, Thompson D, Anderson NH, Montironi R, Sloan JM. Automated location of dysplastic fields in colorectal histology using image texture analysis. *J Pathol.* 1997;182:68–75.
- [32] Smolle J. Computer recognition of skin structures using discriminant and cluster analysis. *Skin Research and Technology.* 2000;6(2):58–63. Available from: <http://dx.doi.org/10.1034/j.1600-0846.2000.006002058.x>.
- [33] Gonzales RC, Woods RE. *Digital image processing.* Prentice Hall; 2007.
- [34] Bronstein IN, Semendiyayev KA, Musiol G, Muehlig H. *Handbook of Mathematics.* Deutsch Harri GmbH; 1985.
- [35] Meyer T, Akimov D, Tarcea T, Chatzipapadopoulos S, Muschiolok G, Kobow J, et al. Three-Dimensional Molecular Mapping of a Multiple Emulsion by Means of CARS Microscopy. *J Phys Chem B.* 2008;112:1420–1426.
- [36] Heuke S, Vogler N, Meyer T, Akimov D, Kluschke F, R wert-Huber HJ, et al. Multimodal mapping of human skin. *Br J Dermatol.* 2013;4:794–803.
- [37] Legesse FB, Chernavskaia O, Heuke S, Bocklitz TW, Meyer T, Popp J, et al. Seamless stitching of tile scan microscope images. *J Microsc.* 2015;.
- [38] Fitzpatrick JM, Hill DL, Maurer Jr CR. Image registration. *Handbook of medical imaging.* 2000;2:447–513.
- [39] Theodoridis S, Koutroumbas K. *Pattern Recognition, 4th Edition.* Academic Press; 2008.
- [40] Hastie T, Tibshirani R, Friedman J. *The Elements of Statistical Learning – Data Mining, Inference, and Prediction.* Springer; 2008.
- [41] Gupta PK, Majumder SK, Uppal A. Breast cancer diagnosis using N2 laser excited autofluorescence spectroscopy. *Lasers Surg. Med.* 1997; 21:417–422.

6.2 Hepatic vitamin A content investigation using coherent anti-Stokes Raman scattering microscopy

Documentation of Authorship

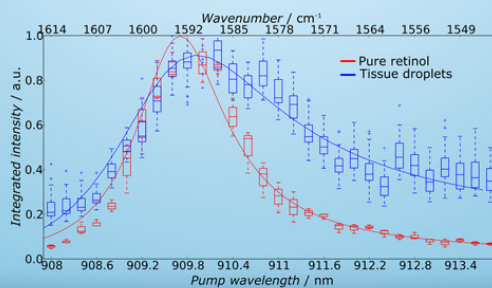
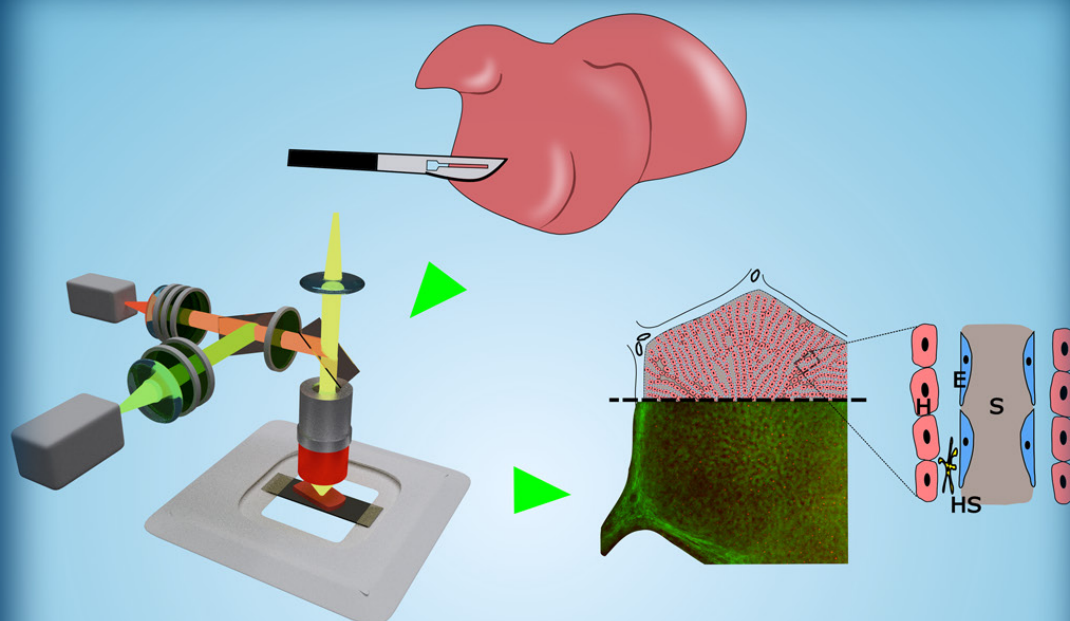
Fisseha Bekele Legesse	Acquisition and analysis of images, preparation of the manuscript
Sandro Heuke	Acquisition of images, Discussion of results
Kerstin Galler	Procuration of samples, Discussion of results
Patrick Hoffmann	Procuration of samples
Michael Schmitt	Project coordination and supervision, discussion of results
Ute Neugebauer	Project coordination and supervision, discussion of results
Michael Bauer	Project coordination and supervision, discussion of results
Jürgen Popp	Project coordination and supervision, discussion of results

All authors revised, edited and proof read the final manuscript.
Reprinted with kind permission from the Wiley publishing house.

[FBL2] F. B. Legesse, S. Heuke, K. Galler, P. Hoffmann, M. Schmitt, U. Neugebauer, M. Bauer, and J. Popp, "Hepatic Vitamin A Content Investigation Using Coherent Anti-Stokes Raman Scattering Microscopy," *ChemPhysChem* **17**, 4043–4051 (2016).

Author	Fisseha Bekele Legesse
Suggested equivalent of publications	1.0

A EUROPEAN JOURNAL
CHEMPHYSICHEM
OF CHEMICAL PHYSICS AND PHYSICAL CHEMISTRY



24/2016

Front Cover:
J. Popp and co-workers
Hepatic Vitamin A Content Investigation Using Coherent
Anti-Stokes Raman Scattering Microscopy

WILEY-VCH

www.chemphyschem.org

A Journal of





Hepatic Vitamin A Content Investigation Using Coherent Anti-Stokes Raman Scattering Microscopy

Fisseha Bekele Legesse,^[a, b] Sandro Heuke,^[a, b] Kerstin Galler,^[b, c] Patrick Hoffmann,^[b, c] Michael Schmitt,^[a] Ute Neugebauer,^[a, b, c] Michael Bauer,^[c, d] and Jürgen Popp^{*,[a, b, c]}

Standard techniques for examining the distribution of vitamin A in liver either require staining or lead to rapid photobleaching of the molecule. A potentially better alternative approach is to use coherent anti-Stokes Raman scattering (CARS) microscopy; a fast, label-free, non-disruptive imaging method that provides contrast based on molecular vibrations. This contribution evaluates the viability of CARS microscopy for imaging vitamin A within thick hepatic tissue under physiological conditions by tuning into its characteristic vibrational band in the fingerprint region. Additional information about the morphology and architecture of the tissue was acquired using second

harmonic generation (SHG) and multi-photon excited fluorescence (MPEF) to help mapping the intra-lobular positions of the vitamin A droplets. We demonstrate the capability of our multimodal imaging framework to selectively image lipid-soluble vitamin A droplets deep in bulk liver tissue with a high contrast while co-registering a complementary morphological background that clearly visualizes hepatic lobules. The results obtained envisage the good prospect of the technique for in vivo studies assessing vitamin A distribution heterogeneity and how it is affected by the progression of hepatic diseases.

1. Introduction

One of the multitude of varied functions performed by the liver is vitamin A storage and processing. Vitamin A (collective term for retinol and its derivatives) plays an essential role in growth and development, immune systems, and vision.^[1–3] As much as 80% of the vitamin A in the liver is encapsulated by the lipid droplets residing within the cytoplasm of quiescent hepatic stellate cells (HSCs)^[4] which are non-parenchyma cells of the liver situated between hepatocytes and liver sinusoids. HSCs are particularly pertinent during liver injury or disease wherein they become activated, lose their retinol content and deposit extracellular matrix molecules within the perisinusoidal space.^[5] The metabolism of vitamin A as a whole is affected in

the early stages of hepatic diseases.^[6] Therefore the investigation of the hepatic vitamin A content is of paramount significance in understanding the physiological functions of the liver as well as the onset and progression of hepatic diseases.

The vitamin A storing HSCs were discovered using gold chloride impregnation of sectioned liver tissue; a procedure which is still prevalently employed in anatomical studies addressing intra-lobular heterogeneity.^[7,8,5,9] This inherently invasive method requires time consuming and delicate preparation of the sample by expert anatomists. This calls for a technique that potentially allows in vivo investigation of vitamin A in liver tissue with minimal sample handling involved.

Vitamin A in fresh liver cryo-sections and thin tissue slices could be identified in label-free manner due to its rapidly fading, single-photon auto-fluorescence when excited by ultraviolet light.^[10] Microscopy that harnesses this fluorescence contrast has been used to demonstrate the distribution of HSCs in liver lobules.^[8,11] However, ultraviolet illumination leads to photobleaching of vitamin A,^[4] preventing its systematic study for an extended period of time within a tissue.

Raman microspectroscopy, in contrast, is not susceptible to photobleaching and enables high-resolution in vivo imaging of tissue by allowing the visualization of its molecular composition.^[12–15] The characteristic vibrational frequency of retinol has been utilized to detect^[16] and quantify^[17] quiescent HSCs in fresh liver tissue slices with Raman microspectroscopy alluding to its role as an intrinsic marker for healthy liver.^[18] Nonetheless, the incoherent and weak nature of spontaneous Raman signals necessitates long acquisition times for imaging tissue. In general, linear microscopic methods based on spontaneous Raman scattering and one-photon autofluorescence provide

[a] F. B. Legesse, Dr. S. Heuke, Prof. Dr. M. Schmitt, Prof. Dr. U. Neugebauer, Prof. Dr. J. Popp
Institute of Physical Chemistry and Abbe Center of Photonics
Friedrich Schiller University Jena
Helmholtzweg 4, 07743 Jena (Germany)

[b] F. B. Legesse, Dr. S. Heuke, Dr. K. Galler, P. Hoffmann,
Prof. Dr. U. Neugebauer, Prof. Dr. J. Popp
Leibniz Institute of Photonic Technology (IPHT) Jena e.V.
Albert-Einstein-Str. 9, 07745 Jena (Germany)
E-mail: juergen.popp@ipht-jena.de

[c] Dr. K. Galler, P. Hoffmann, Prof. Dr. U. Neugebauer, Prof. Dr. M. Bauer,
Prof. Dr. J. Popp
Center for Sepsis Control and Care
Jena University Hospital
Erlanger Allee 101, 07747 Jena (Germany)

[d] Prof. Dr. M. Bauer
Department of Anesthesiology and Intensive Care Medicine
Jena University Hospital
Am Klinikum 1, 07747 Jena (Germany)

Supporting Information for this article can be found under:
<http://dx.doi.org/10.1002/cphc.201600929>.

limited penetration depths and do not offer inherent optical sectioning.

Microscopy exploiting non-linear variants of these methods, two-photon excited fluorescence (TPEF)^[19] and coherent *anti*-Stokes Raman scattering (CARS),^[20,21] circumvents these problems because the signal generation is limited to a tight focal volume, providing an intrinsic three-dimensional sectioning capability. Furthermore, with these techniques there is a possibility to use sources operating in the NIR optical window which allows better penetration depths because there is less absorption and scattering of the excitation wavelengths by the tissue. Identification of HSCs in liver tissue employing TPEF microscopy of vitamin A has been reported.^[22] Although the illumination of a single focal plane at a time reduces the overall tissue damage and photo-bleaching in TPEF microscopy,^[23] these problems still persist due to higher-order photon interactions in the focal volume.^[24]

CARS microscopy, on the other hand, provides contrast based on intrinsic molecular vibrations in the sample as in spontaneous Raman microscopy but utilizes signals that are stronger by orders of magnitude. CARS is a four-wave mixing process involving the interaction of a pump (ω_p) and a Stokes (ω_s) beam in the sample. Molecules with Raman resonances matching the beat frequency of the excitation beams ($\omega_p - \omega_s$) are forced into coherent vibrations. A photon from a probe beam, which is usually chosen to have the same frequency as the pump beam for experimental simplicity, is then inelastically scattered off these coherent vibrations generating an *anti*-Stokes signal at $\omega_{as} = 2\omega_p - \omega_s$. The strength of the CARS signal, arising from its coherent nature, allows fast vibrational imaging of tissue because of the small acquisition times needed.^[25]

Most tissue investigations with CARS have, so far, focused on probing limited number of strong Raman modes in the high-wavenumber (2500–3500 cm^{-1}) region of the vibrational spectrum. In particular, the strong CARS signal in lipids, arising from the high concentration of the CH_2 symmetric stretching vibration at 2845 cm^{-1} , has prompted its prevalent use in assessing the fat content of tissue.^[26–28] In this regard, CARS has been employed to detect the excessive accumulation of lipid droplets in the hepatocytes of the liver tissue (hepatic steatosis) which is a precursor for hepatic diseases such as cirrhosis.^[29,30] CARS has also been demonstrated to have a good potential for *in vivo* investigation of tissue mostly owing to a significant back-scattering of the forward generated CARS signals.^[31]

CARS investigation of the fingerprint region (800–1800 cm^{-1}) has been typically avoided due to the presence of multiple, overlapping peaks from different molecular groups in biological tissue within the region. This congestion of the spectra compounded by the fact that, in CARS, different spectral signatures interfere with each other and with the non-resonant background have made it difficult to utilize the information obtained without significant post-processing.^[32] However, molecules in the fingerprint region that have stronger Raman bands and found with higher concentration than the rest of the molecules in tissue or are localized in clearly definable

compartments could still be utilized as a means of contrast in CARS images. For instance, the transdermal delivery of *trans*-retinol has been assessed using CARS.^[25] Therefore, CARS seems to be able to fulfill the need for a fast, non-disruptive technique to investigate hepatic vitamin A content in intact bulk tissue.

In this contribution, the suitability and merits of CARS microscopy in assessing the vitamin A content of thick liver tissue, by probing a vibrational peak in Raman spectra of retinol, is examined. The intralobular distribution of vitamin A is visualized using CARS with the aid of multi-photon excited auto-fluorescence (MPEF) and second harmonic generation (SHG) imaging to identify the rest of the background tissue structure.

Methods

Sample Preparation

Animal Samples

The liver of a mouse was sampled in accordance with German legislation on protection of animals and with notification to the regional animal welfare committee of Thuringia. Liver was sampled from a 12 week old male C57Bl/6 J wild-type mouse (Charles River, Germany). The mouse was sacrificed by cervical dislocation prior to liver sampling. The liver was sampled freshly on the day of the CARS measurements. It was transferred into a flacon containing physiological NaCl solution immediately after sampling and kept therein at 4 °C and protected from light until the start of the CARS measurements.

For the succeeding routine experiments that assess the distribution of vitamin A, commercial pig livers purchased from a nearby supermarket were used. Tissue blocks, with sizes 2 mm × 8 mm × 8 mm on average, were excised from the samples immediately upon arrival to the laboratory. Water was pipetted on the tissue slices before placing a cover slip to keep them from drying. The imaging commenced shortly thereafter. The sample processing was deliberately kept as minimal as possible to make future transitions into *in vivo* imaging feasible.

Chemical Samples

Pure retinoid molecular species (retinol synthetic, retinyl palmitate and all-*trans*-retinal) (Sigma-Aldrich Chemie GmbH, Germany) were used for obtaining reference CARS spectra.

Image Processing and Analysis of Data

The processing of the acquired raw images, including the pseudo-coloring in the composite multi-modal images, was performed using *ImageJ*.^[33] For presentation purposes, the raw images were 4 × 4 resampled and minimal adjustments were made to their brightness and contrast.

Mechanical movement and instability in unfixed thick tissue cause mismatches when overlaying images acquired separately with different modalities. This also poses problems when examining the effect of photobleaching among a series of successive acquisitions. Here, registration of the images by just accounting for the translational shift between them using the *TemplateMatching* plugin in

ImageJ was found to be sufficient for qualitative assessment. The plugin's *Align slices* option, an implementation of the *openCV*'s template matching function, searches for a specific user-selected feature or landmark in each image in a stack and tries to maintain its position by translating the images. Large mosaic images were stitched from small tile scans using a recently developed algorithm presented in Ref. [34].

CARS spectra were extracted from a series of images obtained by varying the pump wavelength. Each bright spot in the CARS images was first segmented and its mean grey value was evaluated. The mean grey value for every spot was plotted as function of pump wavelength (wavenumber shift) after normalization using the maximum value for the spot within the series. This results in a normalized wavelength series plot for every bright spot in the CARS image. For each (wavenumber shift) point the normalized, mean grey values of different spots are grouped together to construct a box plot in Python (Python Software Foundation, U.S.A.). Such plots were then fitted to analyze the shape of the spectra and how it is influenced by the non-resonant background. This fitting procedure is adopted from a discussion reported elsewhere^[35] and the specifics are presented in the Supporting Information.

Experimental Setup

The experimental setup used for imaging retinol in bulk liver tissue is depicted in Figure 1 (detailed descriptions of the laser source and microscope were separately reported in Refs. [36] and [37], respectively). The setup is comprised of an Nd:vanadate picosecond laser source (High-Q picoTrain, High-Q Laser, Austria), generating 7.5 ps long pulses at 1064 nm with a repetition rate of 80 MHz. The laser also delivers a frequency-doubled output used for pumping an optical parametric oscillator (OPO, Levante Emerald, A.P.E, Berlin, Germany). In this study, for probing the Raman-active vibra-

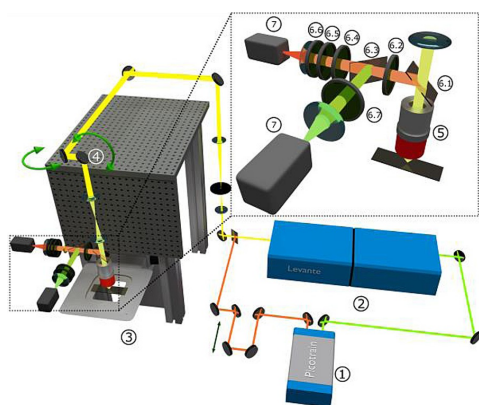


Figure 1. Experimental setup for imaging retinol in the hepatic tissue using coherent *anti*-Stokes Raman Scattering (CARS) microscopy. One output of a Nd:vanadate picosecond laser (High-Q picoTrain) (1) at 1064 nm is used as Stokes beam for the CARS process while a frequency-doubled output pumps an OPO (Levante Emerald) (2). The signal from the OPO, used as CARS pump, and the fundamental output from the Nd:vanadate laser are combined and sent directly to a laser scanning microscope (3). The galvanoscanners (4) of the microscope direct the beams, through a tube and scan lens, onto the back focal plane of a focusing objective lens (5). The generated CARS signal is epi-detected by a photomultiplier tube (7) after passing through a series of filters (6.1–6.7).

tional peak of retinol centered at 1595 cm^{-1} , the wavelength of the OPO signal is tuned to 909 nm, which together with the fundamental output from the picoTrain, results in an *anti*-Stokes radiation at 795 nm. The two excitation beams are then overlapped temporally as well as spatially, and directed to a home-built upright microscope. Two NIR focusing objectives, a $20\times$, 0.4 numerical aperture (NA) (M Plan Apo NIR 20X, Mitutoyo, Japan) and a $25\times$, 1.1 NA water immersion (CFI Apo LWD 25XW, Nikon Inc., U.S.A.), are used in this study. Unless explicitly specified, the results presented here are acquired using the $20\times$ objective that has a long working distance, making it apt for thick tissue investigations. The backward scattered light collected by the focusing objective is separated from the excitation beams using a 850 nm longpass dichroic filter (Edmund Optics, U.S.A, (6.1)) and a short-pass filter (FF01-842/SP-25, Semrock, U.S.A, (6.2)). The generated CARS signal is separated from multi-photon excited auto-fluorescence (MPEF) and second harmonic generated (SHG) signals by a dichroic mirror (FF775-Di01-25 \times 36, Semrock, U.S.A, (6.3)). The CARS beam is then filtered through a series of bandpass filters (FF01-785/62-25 (6.4), FF01-794/160-25 (6.5), FF01-731/137-25 (6.6), Semrock, U.S.A) and detected by a photomultiplier tube (PMT) (H10721-20, Hamamatsu, Japan). To obtain complementary information about the tissue, the separated MPEF and SHG signals, excited by the fundamental beam of the laser at 1064 nm, are collected by another PMT (H10721-20, Hamamatsu, Japan) after passing through a bandpass filter (for both MPEF and SHG: FF01-550/220-25, Semrock, U.S.A, for SHG only: FF01-550/88-25, Semrock, U.S.A (6.7)).

This setup can be reconfigured for lipid detection using CARS by retuning the pump wavelength to 816 nm to probe the CH_2 symmetric stretching vibration at 2845 cm^{-1} . The detection path in this case consists of a dichroic mirror (FF775-Di01-25 \times 36, Semrock, U.S.A) and two bandpass filters (FF01-661/20–25, FF01-650/150–25, Semrock, U.S.A).

Tissue images of different sizes were acquired with 2048×2048 pixel resolution and a pixel dwell time of $1\ \mu\text{s}$. 2×2 binning of the pixels to increase the signal to noise ratio results in a total acquisition time of 16 s for a single tile. Tissue damage due to linear absorption (bulk heating) is typically avoided here, as in other multi-photon microscopy applications.^[38] The combined average power of the excitation beams does not exceed 160 mW at the surface of the sample and is distributed over a large field of view ($1.2 \times 1.2\text{ mm}^2$). This results in an average illumination intensity of 11.1 W cm^{-2} which is below the reported linear tissue photodamage threshold level of 500 W cm^{-2} .^[39] Tissue damage caused by non-linear mechanisms is also not observed, as peak irradiances at the focus are limited to $17 \times 10^{12}\text{ W m}^{-2}$ for the Stokes beam; a value within the bounds of the amount tolerable by tissue which is estimated to be $750 \times 10^{12}\text{ W m}^{-2}$.^[40]

For reference purposes, TPEF, SHG and CARS images were also acquired with another non-linear, multi-modal setup (details are discussed in Ref [41]). In brief, the laser source for the reference setup is a mode-locked coherent Mira-Hp Ti:sapphire laser (Coherent, U.S.A.) that provides 3 ps long pulses at 831 nm with a pulse repetition rate of 76 MHz. This fundamental output, besides serving as a Stokes beam for the CARS process, is used to pump an optical parametric oscillator (A.P.E, Germany) that provides the CARS pump signal at 671 nm. The two beams are then recombined and sent to a commercial laser scanning microscope (LSM 510 Meta, Carl Zeiss, Germany). A $20\times$, 0.8 NA objective (Zeiss, Germany) focuses the beams, $\approx 20\text{ mW}$ each, on the sample. The forward scattered light is collected by a 0.8 NA condenser placed after the

sample and separated from the excitation beams using a shortpass filter (FF01-650/SP-25, Semrock, U.S.A). The forward generated CARS signal is then detected by a PMT (R6357, Hamamatsu, Japan) after being filtered by a shortpass and a bandpass filter (FF01-650/SP-25, FF01-550/88-25, Semrock, U.S.A). The TPEF, on the other hand, is filtered from the backward-scattered light that is collected by the focusing objective using a bandpass filter (FF01-458/64-25, Semrock, U.S.A)

2. Results and Discussion

The capability of the CARS setup in detecting vitamin A in thick tissue was first evaluated with a fresh mouse liver

sample. The images acquired show Raman resonant contribution from bright spots on a relatively dark, uniform background (Figures 2a–c). Similar Raman resonant contribution was discernible in experiments with pig liver samples (Figures 2d–f). These spots correspond to deposits of vitamin A in the liver as confirmed by the profile of the extracted CARS spectra which correlates well with that of pure retinol (Figure 2g). The CARS spectra of the pure retinol resembles a Lorentzian and exhibits the strong characteristic vibrational peak of retinol at 1595 cm^{-1} which arises from the $\text{C}=\text{C}$ stretching vibration in its conjugated polyene structure,^[25] indicating most of the contributions to the CARS signal arise from the Raman resonant part of the third-order non-linear susceptibili-

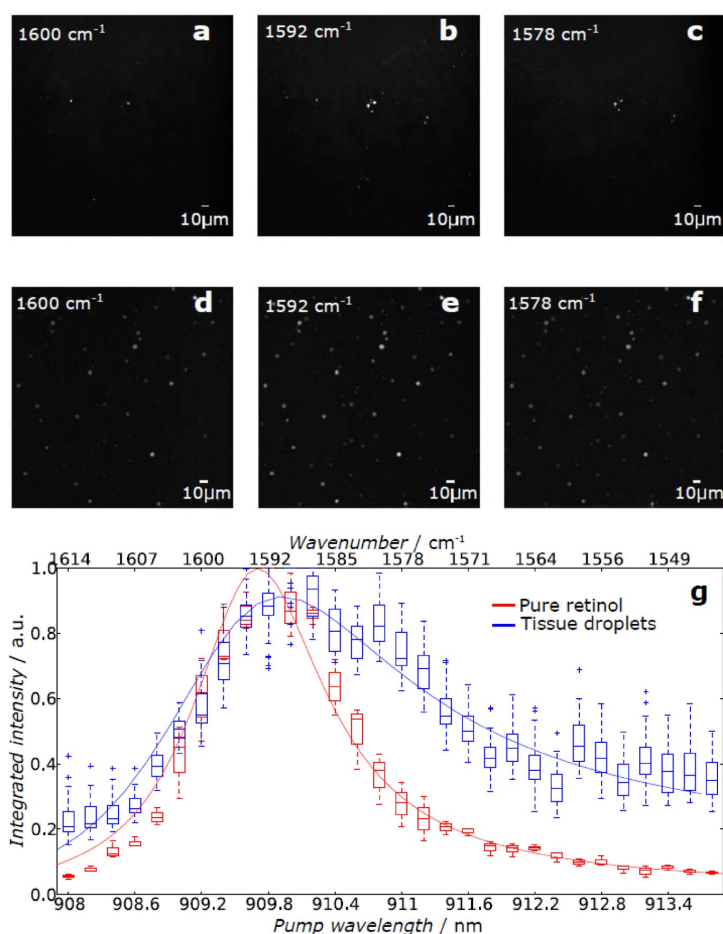


Figure 2. Vitamin A in bulk liver tissue imaged using CARS microscopy. A spectral series of CARS images from mouse liver (a–c) and pig liver (d–f) tissue. The in-resonance images (b, e) show a strong signal from the vitamin A spots forming a sharp contrast from the rest of the background. This signal fades away as we move resonance in either direction. g) CARS spectra extracted from a series of images obtained by varying the pump wavelength showing the characteristic peak of retinol. The box plot obtained from pure retinol (red) and its corresponding fit resemble a Lorentzian. In comparison, the corresponding plots extracted from the droplets in the pig liver tissue images exhibit a small red shift of the peak (in wavenumber) and an asymmetry in the peak indicating a minor contribution of the non-resonant background. These plots correspond well, in terms of peak position and width, with the SRS/CARS spectra of pure retinol recorded by Freudiger et al.^[51]

ty. On the other hand, the spectra obtained from the vitamin A droplets in liver tissue display the typical red-shift and dispersive shape introduced by interference with the non-resonant background, although the non-resonant background contribution is not significant. For the mouse and different pig tissue samples investigated the shape of the spectra remains consistent with only minor variances due to different levels of non-resonant background arising from the tissue.

To put the subsequently presented results into perspective, a schematic representation of liver architecture is depicted in Figure 3. On a microscopic level, the lobes of liver are comprised of a number of roughly hexagonal hepatic lobules that have a central vein in the middle and portal triads (tracts) at their vertices.^[42] Connective tissue surrounds these hepatic lobules and plates of hepatocytes, which are the most abundant parenchyma cells of the liver, that stretch outwards from the center of each lobule.^[43] Enlarged capillaries with fenestrated endothelium lining called liver sinusoids run from the hepatic arteries and veins of the portal triads to the central vein. The hepatic stellate cells containing vitamin A are positioned in the space of Disse between liver sinusoids and the hepatocytes.^[3,5]

Such morphological details are not apparent in the CARS images because, aside from the bright vitamin A spots, the rest of the tissue appears merely as a uniform background due to the non-resonant contribution originating from the electronic response of the sample. This hinders the assessment of the hepatic lobule vitamin A content. To that end, complementary morpho-chemical information about the investigated samples was obtained using second harmonic generation (SHG) and multi-photon excited autofluorescence (MPEF) imaging modalities. SHG is used to image non-centrosymmetric tissue

structures with large hyperpolarizability.^[44] Highly ordered anisotropic structural proteins such as collagen and elastin are typically suited for imaging with SHG.^[45] MPEF has been used to image the distribution of endogenous fluorophores such as NADH and flavin in tissue.^[46] Firstly, to independently optimize the imaging parameters, SHG and MPEF were acquired separately from CARS using only the fundamental output from the Nd:vanadate picosecond laser at 1064 nm for excitation so as not to alter the source for the setup much and realize the other modalities by just changing the detection module.

The SHG image at the surface of healthy pig liver tissue is dominated by signals from the Glisson's capsule; a network of fibrous connective tissue surrounding the liver.^[47] Within the sub-capsule region of the liver this network extends into a sheathing for the blood vessels (veins and arteries) that interconnect the portal areas of the hepatic lobules. This connective tissue surrounding the hepatic lobules is relatively abundant in pig liver, as compared to other species,^[48] and gives a decent SHG signal (Figure 4a). Consequently, the SHG contrast offers a background-free elucidation of the liver's functional subdivision into hepatic lobules analogous to the way liver vasculature is visualized using portal vein injections.

Broadening the spectral detection window to 440–660 nm allows the collection of two- or three-photon excited fluorescence, here collectively termed as MPEF, from the tissue in addition to SHG (Figure 4b). Most of the signal in the image is

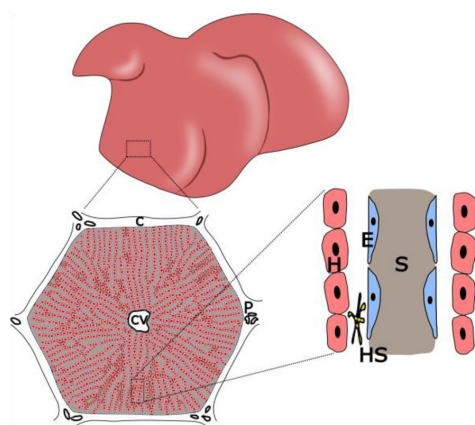


Figure 3. A schematic representation of liver architecture. The lobes of the liver are functionally subdivided into hexagonal hepatic lobules; the borders of which are outlined by a network of connective tissue (C). Each hepatic lobule of the liver has a central vein (CV) in the middle and portal triads (P) at its corners. Plates of hepatocytes (H) extend radially from the central vein to the edges of the lobule. Liver sinusoids (S), the walls of which are lined by endothelium (E), occupy the space in between the plates of hepatocytes. Hepatic stellate cells (HS) are found in the space of Disse between the liver sinusoid and the hepatocytes.

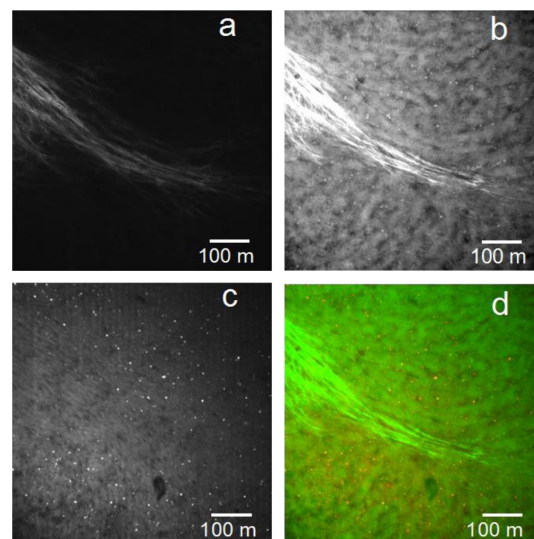


Figure 4. The use of multi-modal imaging to provide complementary information about tissue morphology. a) A second harmonic generation (SHG) image of a pig liver tissue ($\approx 15 \mu\text{m}$ below the surface) depicts mainly the connective tissue in the sample. b) Capturing multi-photon excited fluorescence (MPEF) in addition to SHG visualizes the hepatocytes and liver sinusoids. c) The CARS modality shows the vitamin A droplets laid out on an indistinct tissue background. d) A composite image formed by registering and overlaying the images in (b) and (c) shows the localization of the vitamin A droplets within the perisinusoidal space (red: retinol CARS, green: MPEF plus SHG).

likely arising from the NADH autofluorescence in the cytoplasm of hepatocytes as hypothesized elsewhere.^[22] However, in this study, as the detection is not spectrally resolved, identifying individual fluorophore contributions in the MPEF image is difficult due to the cross-talk between the broad emission spectra of different molecules. Nonetheless, the overall fluorescence intensity helps to visualize the morphology of the tissue with primary contrast formed between the bright plates of hepatocytes and the dark, blood filled sinusoids within the lobules. Although individual hepatocytes could be identified on the surface of the liver and in thin frozen cryo-section preparations (Figure 5), they are not discernible at such sub-capsule depths (starting from about 15 μm below the liver surface), with the specified imaging parameters, due to strong tissue absorption and scattering. Figure 4b also shows three-photon excited fluorescence from the droplets of vitamin A exhibited as conspicuous bright dots within the dark sinusoids of the lobule.

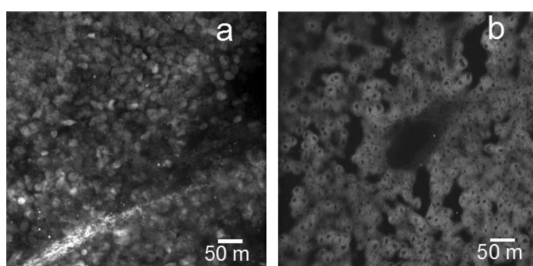


Figure 5. Identification of individual hepatocytes using MPEF. Images acquired from a) the surface of pig liver tissue and b) a cryo-section excised from a mouse liver.

A CARS image from the same region of tissue shows resonant contributions arising only from the bright vitamin A spots (Figure 4c). Registering these two image channels (Figure 4n and Figure 4c) and overlaying them with pseudo-colors demonstrates how the modalities complement each other in visualizing the vitamin A distribution within liver tissue (Figure 4d).

It has been long held that vitamin A is fat-soluble and is stored within the lipid droplets of the HSCs. Investigating the lipid droplet content of the tissue is important to further corroborate our assertion that the bright spots in the CARS images do indeed correspond to vitamin A deposits. As standard lipid staining usually fails in healthy liver tissue due to the small concentration of the droplets, the lipid imaging was performed by modifying the CARS setup to probe the CH_2 symmetric stretching vibration.

Hence, fresh pig liver tissue is first imaged with the CARS channel tuned for retinol detection (Figure 6a). A subsequently acquired complementary MPEF image of the background tissue morphology is depicted in Figure 6b. Figure 6c shows the same area of tissue scanned with the CARS modality of the setup reconfigured for lipid imaging. The composite image from the two channels (Figure 6d) reveals the expected co-lo-

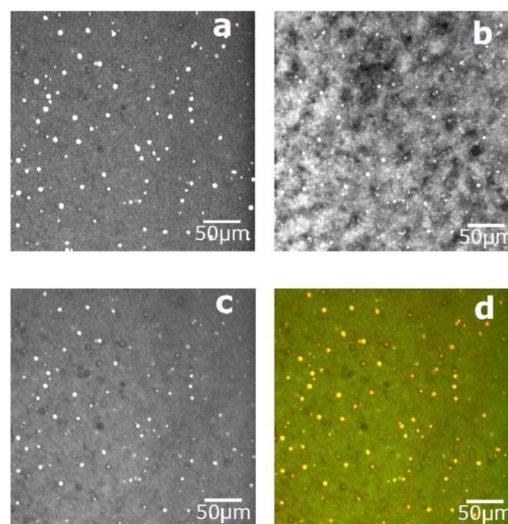


Figure 6. Multi-modal imaging employed to confirm the accumulation of vitamin A within the lipid droplets of the liver. (a) and (b) show a different region of pig liver tissue ($\approx 20 \mu\text{m}$ below the surface) imaged using the CARS (tuned for vitamin A detection) and MPEF respectively. c) The CARS channel re-configured for probing the CH_2 stretching vibration detects the lipid droplets in the tissue. d) A pseudo-colored multi-modal image (d) (retinol-CARS: red, lipid-CARS: green) shows the co-localization of the bright spots from both modalities confirming the accumulation of vitamin A in the lipid droplets.

calization of the bright vitamin A spots with the lipid droplets of the liver lobule.

Large mosaic images allow the visualization of the extended hepatic structure with a high resolution (Figure 7). A nearly complete structure of a hepatic lobule and some of the features introduced in the schematic representation of the liver are recognizable in the stitched MPEF mosaic shown in Figure 7a. In comparison, the parallel CARS image, Figure 7b, is a very specific indicator of the vitamin A distribution within the liver. In Figure 7a, some of the spots are situated very close to each other possibly indicating a pair of droplets contained within a single stellate cell. Most of the dark patches (shadows) in the CARS image are coherent imaging artefacts that arise due to the interference between the resonant contribution from small droplets and the non-resonant background. This is confirmed by the observed asymmetry in the CARS signal at these positions, caused by Gouy phase shift, as we laterally scan through the sample.^[49] The strong contrast in the CARS image enables a straightforward separation of the resonant contribution from the non-resonant background which in turn facilitates qualitative and quantitative assessment, regarding number and volume, of the hepatic vitamin A droplet content as in studies performed on lipids^[(29,30)]. For instance, within $10,000 \mu\text{m}^2$ in the periportal zone of pig liver tissue as many as 23 droplets could be identified with diameters reaching up to about $7 \mu\text{m}$. Diffraction-limited resolution of CARS microscopy guarantees the detection of even the small vitamin

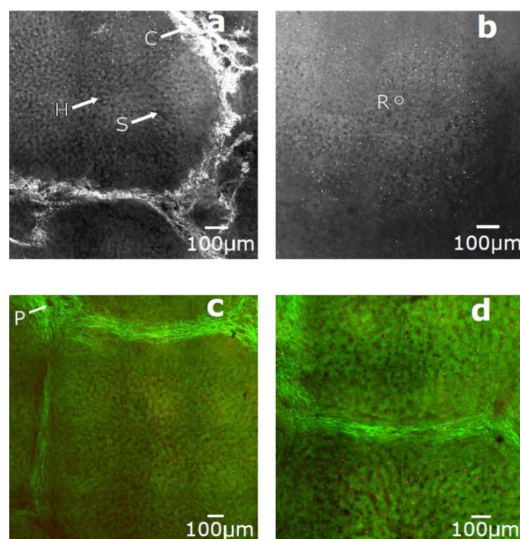


Figure 7. Representative multi-modal images of pig liver ($\approx 15 \mu\text{m}$ below the surface) portraying the intra-lobular distribution of vitamin A. (a) and (b) show sequentially acquired images. a) The multi-fluorescence from the tissue originates mostly from the hepatocytes (H) which form a clear contrast with the blood filled sinusoids of the liver (S). b) The SHG signal from the connective tissue (C) de-marks the boundaries among hepatic lobules. The CARS channel maps the distribution of the vitamin A (circled: R) throughout the lobule. (c) and (d) are multi-modal images obtained from simultaneous acquisition of the modalities partially illustrating a classic hepatic lobule and a liver acinus, respectively (retinol CARS: red, multi-photon excited fluorescence plus SHG: green, P portal tract).

A droplets in centrilobular zones of hepatic lobules, providing a more accurate description of tissue content than what is achievable with staining procedures, which often lead to underestimations.^[9] Although precise morphometric mapping of vitamin A heterogeneity is beyond the scope of this study, the zonal and regional gradients in vitamin A distribution reported in literature Ref. [9], such as relatively large droplet volumes in the periportal regions, are recognizable from qualitative assessment of the CARS images.

The increase in acquisition time needed for taking large area scans leads to complicated mismatches, among subsequently acquired modalities, which cannot simply be corrected with the registration methods described in Section 2.2. A compromise in the optimal imaging parameters of the modalities, particularly regarding the power of the fundamental beam, makes simultaneous acquisition of the modalities possible. Although simultaneous acquisition decreases the intensity of the signals acquired, especially the MPEF, it ensures perfect co-registration of the modalities. Such simultaneously acquired multi-modal images are presented in Figures 7c,d. Figure 7c illustrates the architecture of the liver from the classical hepatic lobule perspective while Figure 7d depicts the metabolic functional unit of the liver, the hepatic acinus,^[42] partially. These images show how intuitive non-linear multi-modal imaging is in providing

a clear insight into the morpho-chemical composition of a bulk tissue sample in a label-free manner.

For thick-tissue investigations, the depth of penetration achievable with the CARS setup is of particular relevance. Excitation wavelengths well into the NIR region and long-working-distance objectives were selected for this study with this consideration in mind.^[31,50] In our CARS images, we were able to get a decent contrast from the vitamin A $60 \mu\text{m}$ below the surface of bulk pig liver tissue using the $20\times$ objective. The $25\times$ objective, with its larger numerical aperture and better chromatic correction, allowed penetration depths up to $80 \mu\text{m}$ below the surface of the mouse liver tissue. These limited depths of penetration are likely due to the fact that liver is a turbid tissue containing hemoglobin that causes strong linear scattering of the excitation beams, which in turn leads to a reduction of power deep inside the tissue and prevents the formation of a tight focal spot. The reduction in power at the focus is indirectly attested by the significant amount of power the tissue is able to withstand before sample destruction could be noticed in the images. (Here, up to 500 mW of the fundamental output of the laser at 1064 nm measured at the surface of the tissue, focused using the 20×0.4 NA objective, did not cause observable damage at the focus.)

Another critical aspect of the setup, especially when imaging in the Raman fingerprint region, is spectral resolution. The estimated spectral resolution of the CARS setup ($\approx 5 \text{ cm}^{-1}$), in principle, allows the discrimination of retinol from other retinoid metabolites that might be found in healthy or pathological liver. To substantiate this claim, CARS spectra of either pure or diluted (1:10 in ethanol) forms of the molecular species placed alongside each other on a microscopic slide were acquired. The spectral peak of retinol can be clearly discriminated from that of *trans*-retinol or retinoic acid. However, retinol and retinyl palmitate have similar spectral properties, with peaks near 1594 cm^{-1} which prevents their separation with the setup. Figure 8 shows the spectral separation of pure retinol from *trans*-retinol situated within the same field of view; indicated by the appearance of two distinct intensity peaks, one coming after the other, as we change the pump wavelength to essentially probe the Raman resonance modes of retinol at

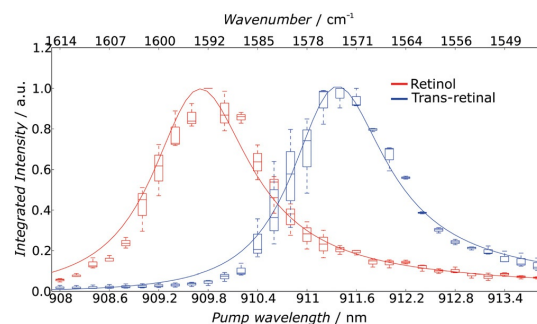


Figure 8. Result of an experiment testing the spectral resolving capabilities of the CARS setup show separation of pure retinol and *trans*-retinol placed alongside each other.

1595 cm^{-1} and all *trans*-retinal at 1572 cm^{-1} .^[18] These results anticipate the potential of CARS microscopy for investigating retinoid metabolism.

Finally, the reduction in photobleaching and tissue photo-damage when microscopically imaging vitamin A based on CARS as compared to TPEF is demonstrated by taking a time series of images with both modalities. Accordingly, a 0.5 mm thin liver tissue slice was imaged using another multimodal setup (see Section 2.3). A different multimodal setup was selected for comparison because of its suitability for operation in the visible spectrum wherein the two photon absorption maximum of retinol is located. In addition, this second setup employs shorter pulse duration sources, as compared to the main NIR setup, that result in high peak irradiance optimum for obtaining similar contrast levels from the vitamin A droplets using TPEF as in the CARS images. The TPEF image acquired, displayed in Figure 9a, exhibits the characteristic uniform distribution of patchy bright fluorescence from vitamin A in healthy liver lobule.^[22] The CARS modality of the reference setup, whose excitation wavelengths are tuned for probing the CH_2 stretching vibration at 2850 cm^{-1} , allows the visualization of vitamin A storing lipid droplets in the liver. In these multimodal images the bright auto-fluorescence from vitamin A fades away almost completely after 60 scans (acquired over

the course of 5 minutes), leaving behind the encapsulating lipid droplets and causing evident tissue damage (Figure 9b). In comparison, the vitamin A spots in a similar time series image of the tissue acquired by the CARS setup with NIR excitation wavelengths with a MPEF background, Figure 9c and Figure 9d, show no apparent decay in intensity after 100 scans. The characteristics of the excitation sources used and the nature of the molecular mechanism probed for CARS imaging led to less photo-bleaching of the sample though more average power was present at the surface of the sample as compared to the TPEF setup.

3. Conclusions

The results obtained and discussed in this contribution illustrate the feasibility of coherent *anti*-Stokes scattering (CARS) microscopy for thick tissue probing of a vibrational band in the fingerprint region. CARS microscopy was demonstrated to be a label-free, non-disruptive and fast alternative to conventional methods of assessing hepatic vitamin A content. Complementary morpho-chemical information about the tissue obtained using second harmonic generation and multi-photon excited fluorescence (MPEF) provided a contextual background to help evaluate the distribution of vitamin A within the hepatic lobules of the liver. This multi-modal approach can be employed to quantitatively analyze liver heterogeneity with regards to vitamin A storage in a label-free manner. It could also potentially be used to track the effects of hepatic diseases progression on the distribution of vitamin A *in vivo*.

Acknowledgements

Financial support by the Carl-Zeiss foundation, the DFG via the research group FOR 1738 "Heme and heme degradation products" and the BMBF (FKZ 01EO1502, Integrated Research and Treatment Center "Center for Sepsis Control and Care") is greatly acknowledged.

Keywords: coherent *anti*-Stokes Raman scattering • fluorescence imaging • hepatic stellate cells • vibrational spectroscopy • vitamin A

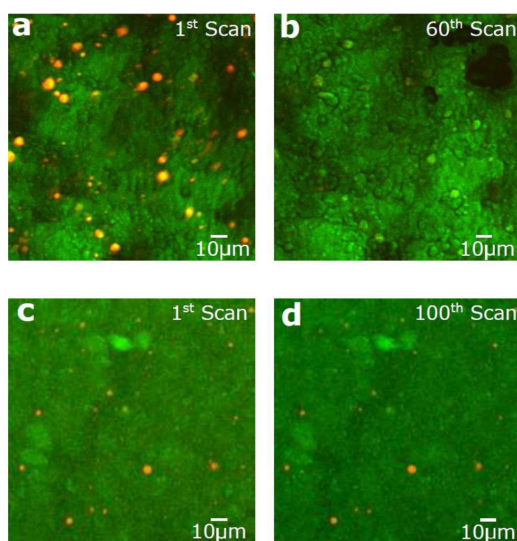


Figure 9. Assessing the photobleaching reduction merit of CARS over two-photon excited fluorescence (TPEF) in imaging vitamin A inside liver tissue. Images (a) and (b) were acquired using a multimodal setup which integrates TPEF (shown in red) and lipid-CARS (shown in green) modalities. For imaging TPEF from vitamin A this setup is better suited than the main NIR setup because it employs shorter wavelength (671 nm) pulses with shorter (3 ps) durations. These images show the complete depletion of vitamin A (bleaching of the bright spots in the TPEF images) after 60 scans. Images (c) and (d), on the other hand, were taken using our main NIR CARS setup wherein the red denotes CARS signal from the vitamin A droplets and the green is for multi-fluorescence from the rest of the liver tissue. Taking 100 successive scans using this NIR CARS setup does not lead to a reduction in the vitamin A CARS signal.

- [1] S. A. Ross, P. J. McCaffery, U. C. Drager, L. M. De Luca, *Physiol. Rev.* **2000**, *80*, 1021–1054.
- [2] X.-H. Tang, L. J. Gudas, *Annu. Rev. Pathol.* **2011**, *6*, 345–364.
- [3] W. S. Blaner, S. M. O'Byrne, N. Wongsiriroj, J. Kluwe, D. M. D'Ambrosio, H. Jiang, R. F. Schwabe, E. M. Hillman, R. Piantadosi, J. Libien, *Biochim. Biophys. Acta Mol. Cell Biol. Lipids* **2009**, *1791*, 467–473.
- [4] M. Suematsu, M. Oda, H. Suzuki, H. Kaneko, N. Watanabe, T. Furusho, S. Masushige, M. Tsuchiya, *Microvasc. Res.* **1993**, *46*, 28–42.
- [5] H. Senoo, K. Yoshikawa, M. Morii, M. Miura, K. Imai, Y. Mezaki, *Cell Biol. Int.* **2010**, *34*, 1247–1272.
- [6] S. L. Friedman, *J. Biol. Chem.* **2000**, *275*, 2247–2250.
- [7] K. Wake, *Am. J. Anat.* **1971**, *132*, 429–461.
- [8] N. Higashi, H. Senoo, *Anat. Rec. Part A* **2003**, *271*, 240–248.
- [9] Z. Zou, W. Ekataksin, K. Wake, *Hepatology* **1998**, *27*, 1098–1108.
- [10] H. Popper, *Physiol. Rev.* **1944**, *24*, 205–224.
- [11] B. Vollmar, S. Siegmund, M. D. Menger, *Hepatology* **1998**, *27*, 1544–1553.

- [12] A. Downes, A. Elfick, *Sensors* **2010**, *10*, 1871–1889.
- [13] M. Schmitt, J. Popp, *J. Raman Spectrosc.* **2006**, *37*, 20–28.
- [14] C. Krafft, D. Codrich, G. Pelizzo, V. Sergio, *J. Biophotonics* **2008**, *1*, 154–169.
- [15] A. Walter, S. Erdmann, T. Bocklitz, E. Jung, N. Vogler, D. Akimov, B. Dietzek, P. Rösch, E. Kothe, J. Popp, *Analyst* **2010**, *135*, 908–917.
- [16] K. Galler, F. Schleser, E. Fröhlich, R. P. Requardt, A. Kortgen, M. Bauer, J. Popp, U. Neugebauer, *Integr. Biol.* **2014**, *6*, 946–956.
- [17] K. Galler, R. P. Requardt, U. Glaser, R. Markwart, T. Bocklitz, M. Bauer, J. Popp, U. Neugebauer, *Sci. Rep.* **2016**, *6*, 24155.
- [18] K. Kochan, K. Marzec, E. Maslak, S. Chlopicki, M. Baranska, *Analyst* **2015**, *140*, 2074–2079.
- [19] M. Oheim, D. J. Michael, M. Geisbauer, D. Madsen, R. H. Chow, *Adv. Drug Delivery Rev.* **2006**, *58*, 788–808.
- [20] X. Nan, E. Potma, X. Xie, *Biophys. J.* **2006**, *91*, 728–735.
- [21] J. Cheng, Y. Jia, G. Zheng, X. Xie, *Biophys. J.* **2002**, *83*, 502–509.
- [22] H. Wang, X. Liang, Y. H. Mohammed, J. A. Thomas, K. R. Bridle, C. A. Thorling, J. E. Grice, Z. P. Xu, X. Liu, D. H. Crawford, M. S. Roberts, *Biomed. Opt. Express* **2015**, *6*, 780–792.
- [23] W. Denk, J. H. Strickler, W. W. Webb, *Science* **1990**, *248*, 73–76.
- [24] G. H. Patterson, D. W. Piston, *Biophys. J.* **2000**, *78*, 2159–2162.
- [25] C. L. Evans, X. S. Xie, *Annu. Rev. Anal. Chem.* **2008**, *1*, 883–909.
- [26] X. Nan, W. Y. Yang, X. S. Xie, *Biophotonics International* **2004**, *11*, 44–47.
- [27] X. Nan, J.-X. Cheng, X. S. Xie, *J. Lipid Res.* **2003**, *44*, 2202–2208.
- [28] C. Evans, X. Xu, S. Kesari, X. Xie, S. Wong, G. Young, *Opt. Express* **2007**, *15*, 12076–12087.
- [29] Y.-M. Wu, H.-C. Chen, W.-T. Chang, J.-W. Jhan, H.-L. Lin, I. Liau, *Anal. Chem.* **2009**, *81*, 1496–1504.
- [30] T. T. Le, A. Ziembra, Y. Urasaki, S. Brotman, G. Pizzorno, *PLoS one* **2012**, *7*, e51092.
- [31] C. Evans, E. Potma, M. Puoris' haag, D. Côté, C. Lin, X. Xie, *Proc. Natl. Acad. Sci. USA* **2005**, *102*, 16807.
- [32] E. M. Vartiainen, H. A. Rinia, M. MRller, M. Bonn, *Opt. Express* **2006**, *14*, 3622–3630.
- [33] C. A. Schneider, W. S. Rasband, K. W. Eliceiri, *Nat. Methods* **2012**, *9*, 671–675.
- [34] F. Legesse, O. Chernavskaia, S. Heuke, T. Bocklitz, T. Meyer, J. Popp, R. Heintzmann, *J. Microsc.* **2015**, *258*, 223–232.
- [35] T. Meyer, M. Chemnitz, M. Baumgartl, T. Gottschall, T. Pascher, C. Matthaus, B. F. Romeike, B. R. Brehm, J. Limpert, A. Tunnermann, M. Schmitt, B. Dietzek, J. Popp, *Anal. Chem.* **2013**, *85*, 6703–6715.
- [36] A. Lukic, S. Dochow, O. Chernavskaia, I. Latka, C. Matthäus, A. Schwuchow, M. Schmitt, J. Popp, *J. Biophotonics* **2015**, *9*, 138–143.
- [37] T. Meyer, M. Baumgartl, T. Gottschall, T. Pascher, A. Wuttig, C. Matthäus, B. F. Romeike, B. R. Brehm, J. Limpert, A. Tunnermann, O. Guntinas-Lichius, M. Schmitt, B. Dietzek, J. Popp, *Analyst (Cambridge, UK)* **2013**, *138*, 4048–4057.
- [38] A. Schönle, S. W. Hell, *Opt. Lett.* **1998**, *23*, 325–327.
- [39] M. Rajadhyaksha, R. R. Anderson, R. H. Webb, *Appl. Opt.* **1999**, *38*, 2105–2115.
- [40] A. Hopt, E. Neher, *Biophys. J.* **2001**, *80*, 2029–2036.
- [41] T. Meyer, D. Akimov, N. Tarcea, S. Chatzipapadopoulos, G. Muschiolik, J. Kobow, M. Schmitt, J. Popp, *J. Phys. Chem. B* **2008**, *112*, 1420–1426.
- [42] A. Rappaport, Z. Borowy, W. Lougheed, W. Lotto, *Anat. Rec.* **1954**, *119*, 11–33.
- [43] H. Ishibashi, M. Nakamura, A. Komori, K. Migita, S. Shimoda, *Semin. Immunopathol.* **2009**, *31*, 399–409.
- [44] S. Fine, W. Hansen, *Appl. Opt.* **1971**, *10*, 2350–2353.
- [45] W. Mohler, A. C. Millard, P. J. Campagnola, *Nat. Methods* **2003**, *29*, 97–109.
- [46] W. R. Zipfel, R. M. Williams, R. Christie, A. Y. Nikitin, B. T. Hyman, W. W. Webb, *Proc. Natl. Acad. Sci. USA* **2003**, *100*, 7075–7080.
- [47] S. G. Stanciu, S. Xu, Q. Peng, J. Yan, G. A. Stanciu, R. E. Welsch, P. T. So, G. Csucs, H. Yu, *Sci. Rep.* **2014**, *4*.
- [48] W. Ekataksin, K. Wake, *Am. J. Anat.* **1991**, *191*, 113–153.
- [49] K. Popov, A. Pegoraro, A. Stolow, L. Ramunno, *Opt. Express* **2011**, *19*, 5902–5911.
- [50] H. Wang, Y. Fu, P. Zickmund, R. Shi, J.-X. Cheng, *Biophys. J.* **2005**, *89*, 581–591.
- [51] C. W. Freudiger, W. Min, B. G. Saar, S. Lu, G. R. Holtom, C. He, J. C. Tsai, J. X. Kang, X. S. Xie, *Science* **2008**, *322*, 1857–1861.
- [52] W. M. Tolles, J. Nibler, J. McDonald, A. Harvey, *Appl. Spectrosc.* **1977**, *31*, 253–271.

Manuscript received: August 23, 2016
Accepted Article published: October 26, 2016
Final Article published: November 3, 2016

CHEMPHYSICHEM

Supporting Information

Hepatic Vitamin A Content Investigation Using Coherent *Anti-Stokes* Raman Scattering Microscopy

Fisseha Bekele Legesse,^[a, b] Sandro Heuke,^[a, b] Kerstin Galler,^[b, c] Patrick Hoffmann,^[b, c]
Michael Schmitt,^[a] Ute Neugebauer,^[a, b, c] Michael Bauer,^[c, d] and Jürgen Popp*^[a, b, c]

cphc_201600929_sm_miscellaneous_information.pdf

CARS spectra fitting

The anti-Stokes signal intensity is generally given by :[52]

$$I_{AS} \propto |\chi^{(3)}|^2 I_p^2 I_s \cdot L^2 \text{sinc}^2\left(\frac{\Delta k L}{2}\right) \quad (1)$$

where $k = n\omega/c$ is the wavevector, Δk is the wavevector mismatch computed as $\Delta k = k_{as} - (2k_p - k_s)$ for the case $k_{pr} = k_p$, and L is the interaction length. The frequency dependence of the intensity is given by the resonant contribution to the third order non-linear susceptibility which is the Lorentzian function approximation of the solution to a damped harmonic oscillator formulation of the frequency dependence :[25]

$$\chi_R^{(3)} = \frac{A_R}{\Delta - i\Gamma} \quad (2)$$

where A_R is the normalized vibrational mode strength, Δ is the detuning frequency given by $\Delta = \omega_{vib} - (\omega_p - \omega_s)$ in which ω_{vib} is the vibrational frequency, and Γ denotes the band width of the Raman line. With the additional non-resonant contribution to the third order non-linear susceptibility which arises as a result of electronic contributions to the polarization the third order non-linear susceptibility can stated as:

$$\chi^{(3)} = \chi_R^{(3)} + \chi_{NR}^{(3)}. \quad (3)$$

Inserting this into (1) gives:

$$I_{AS}(\Delta) \propto |\chi_{NR}^{(3)}|^2 + |\chi_R^{(3)}(\Delta)|^2 + 2\chi_{NR}^{(3)} \text{Re}\{\chi_R^{(3)}(\Delta)\}. \quad (4)$$

Equation 2 can be inserted into the above equation to result in:

$$I_{AS}(\Delta) \propto \chi_{NR}^{(3)2} + \frac{A_R^2}{\Delta^2 + \Gamma^2} + \frac{2\chi_{NR}^{(3)} A_R \Delta}{\Delta^2 + \Gamma^2}. \quad (5)$$

The CARS spectra were then fitted using this model with the unknown parameters, ω_{vib} , Γ , A_R and $\chi_{NR}^{(3)}$ using a least square model in Python.

6.3 Investigation of microalgal carotenoid content using coherent anti-Stokes Raman scattering (CARS) microscopy and spontaneous Raman spectroscopy

Documentation of Authorship

Fisseha Bekele Legesse*	Acquisition and analysis of images, preparation of the manuscript
Jan Ruger*	Acquisition and analysis of images, preparation of the manuscript
Tobias Meyer	Discussion of results
Christoph Krafft	Project coordination and supervision, discussion of results
Michael Schmitt	Project coordination and supervision, discussion of results
Jurgen Popp	Project coordination and supervision, discussion of results

All authors revised, edited and proof read the final manuscript.

*Both authors share first authorship of this manuscript.

Reprinted with kind permission from the Wiley publishing house.

[FBL3] F. B. Legesse, J. Ruger, T. Meyer, C. Krafft, M. Schmitt, and J. Popp, "Investigation of microalgal carotenoid content using Coherent anti-Stokes Raman scattering (CARS) microscopy and Spontaneous Raman Spectroscopy," *ChemPhysChem Accepted*, (2018).

Author	Fisseha Bekele Legesse
Suggested equivalent of publications	1.0

Investigation of microalgal carotenoid content using Coherent anti-Stokes Raman scattering (CARS) microscopy and Spontaneous Raman Spectroscopy

Fisseha Bekele Legesse,^{1,2,*} Jan Ruger,^{1,2,*} Tobias Meyer,^{1,2}
Christoph Krafft,^{1,2} Michael Schmitt,¹ and Jurgen Popp^{1,2,†}

¹*Institute of Physical Chemistry and Abbe Center of Photonics,*

Friedrich-Schiller University Jena, Helmholtzweg 4, 07743 Jena, Germany

²*Leibniz Institute of Photonic Technology (IPHT) Jena e.v., Albert-Einstein-Str. 9, 07745 Jena, Germany*

compiled: January 22, 2018

The yield of high-value products such as pigments that could be extracted from microalgae is affected by various nutritional and physical factors. Consequently, there is a need for fast visualization techniques that investigate the responses of individual microalgal cells to changing environmental conditions without introducing perturbations. Here we apply CARS microscopy to map the distribution of pigments in the diatoms *Ditylum brightwellii* and *Stephanopyxis turris* and report their relative change in response to varying light cycles using a marker based watershed analysis of the acquired images. Simultaneously, the underlying specific pigment composition alterations are revealed using Raman microspectroscopy at 785 nm excitation. In regards to assessing the chemical content of microalgae, these methods present themselves as viable alternatives to the standard techniques currently in use because of their non-disruptive nature and the wealth of complementary information that could be obtained from them.

Keywords: CARS(Coherent Anti-Stokes Raman Scattering), Medical and biological imaging, Algae, Vibrational spectroscopy, Carotenoids.

1. Introduction

There is an ever increasing interest in harvesting microalgae mainly driven by production of biofuels [1]. In parallel to this development, the extraction of other value added co-products from microalgae is considerably gaining traction. In this regard, microalgae are being regarded as viable, renewable and abundant sources of various biomolecules [2]. Carotenoids extracted from algae have found diverse applications in pharmaceutical, food and cosmetic industries [3]. For instance, fucoxanthin (Fx), a xanthophyll naturally found in brown algae and diatoms has been demonstrated to have anti-oxidant anti-inflammatory, and anti-cancer properties [4]. This has led to the growing volume of research invested in understanding the intra-cellular mechanisms employed by microalgae in synthesizing and storing these biomolecules. Therefore, there is a need for fast and reliable techniques that help assess the influence of different environmental factors such as nutrient availability or light conditions on the pigment content and metabolic response of microalgae.

Typically, analytic approaches such as High pressured liquid chromatography (HPLC) and mass spectrometry

are used to investigate the chemical content of microalgae. However, extensive sample preparation and bulk sample volumes are required for these techniques. Vibrational spectroscopic methods, on the other hand, can focus on single cell levels and identify changes in molecular signatures in the algae that are caused by the different external factors. Fourier transform infrared (FT-IR) spectroscopy is one such technique that has been applied to investigate the effects of environmental growth factors on microalgal response [5–7]. Nonetheless, FT-IR spectroscopy is perturbed by strong IR absorption of water and thus requires the samples to be dried for investigation.

Raman spectroscopy presents itself as a non-destructive alternative for investigating intact single cells *in vivo* at a higher resolution than FT-IR spectroscopy. Accordingly, the capability of Raman microspectroscopy in identifying chemical fingerprints has been previously used to investigate the distribution of lipids, and pigments in microalgae [8, 9]. However, Raman cross-sections of typical molecules found in living cells are quite low necessitating longer acquisition times. The increase in scattering intensities achievable when using resonance Raman has been employed to examine metabolites and pigments on and in the vicinity of algal surfaces [10]. However, photodegradation or photobleaching and strong fluorescent background due to UV-Vis excitation wavelengths in resonance with electronic

* Both authors share first authorship of this manuscript

† Corresponding author: juergen.popp@ipht-jena.de

excited states limits its applicability for imaging pigment distribution inside diatoms.

These drawbacks can be alleviated by using Coherent anti-Stokes Raman scattering (CARS), a four-wave mixing, non-linear technique that is able to extract similar information as spontaneous Raman scattering but provides signals that are much stronger. In the CARS process a pump (ω_p) and a Stokes (ω_s) beam interact in the sample and coherently drive Raman active vibrations at their difference frequency ($\omega_p - \omega_s$). The in-elastic scattering of a third probe (ω_p) beam off this vibration results in an anti-Stokes signal $\omega_{as} = 2\omega_p - \omega_s$. CARS allows label-free, video-rate imaging of samples and avoids the problem of one-photon fluorescence as the anti-Stokes signal is blue-shifted from the excitation beams [11]. This is particularly advantageous for algae investigations as spontaneous Raman scattering encounters problems with the strong chlorophyll fluorescence [12]. The large portion of CARS studies on algae have particularly focused on examining the metabolism of lipids as they provide strong signals due to the abundance of the CH_2 symmetric stretching vibration [13–15]. There have also been studies employing CARS as a means of mapping the distribution of carotenoids in specific strains of microalgae [16, 17].

Here we employ CARS microscopy and Raman spectroscopy to investigate the effect of different light cycles on pigment accumulation in the uni-cellular, photo-synthetic, autotrophs *Ditylum brightwellii* and *Stephanopyxis turris*. These diatoms store carotenoids, mainly Fx, in their chloroplasts as accessory pigments. These carotenoids play photo-synthetic as well as anti-oxidative roles in the diatoms. For CARS imaging, we focus on the prominent bands of carotenoids found in the molecular fingerprint region. CARS microscopy was used to show the relative intensity and morphology changes observed among batches as the conditions are varied. CARS microscopy reveals information about the spatial distribution of the carotenoids within the uni-cellular structure of the diatoms. It also permits rapid entire-cell imaging of several diatoms for monitoring comprehensive, specific pigment concentration changes within the limited measurement times available, a feat that is un-realizable by Spontaneous Raman spectroscopy. On the other-hand, Raman spectra from selected points within the diatoms were acquired concurrently to help identify differences in the molecular fingerprints of the cells that correlate with the change of light cycles.

Consequently, an increase in carotenoid content and a corresponding, relative change in pigment contributions were observed with cells kept longer in the dark than the normal 12:12 hours light cycle. In general, we demonstrate CARS and spontaneous Raman to be complementary and potent techniques for thorough investigation of the influence of metabolic factors on the pigment accumulation capabilities of diatoms.

2. Experiment

2.A. Cell culture and sample preparation

D. brightwellii and *S. turris* cultures were both isolated from the North Sea and kept in 50 mL culture flasks (Greiner) with artificial seawater medium prepared as described in [18]. Three batches with varying light cycles (light:dark), 20:4 h, 12:12 h and 4:20 h, were prepared and the measurements were performed for three consecutive days. All batches were grown in a homebuilt cultivation chamber at a constant temperature of 18 °C and an illuminance of approximately 1000 lx with fluorescent tubes (Osram T5 36W 640). In order to achieve varying light cycles, batches with light exposure periods shorter than 20 h were transferred to a light-excluding box at the appropriate time every day. After onset of the corresponding light period, cells were allowed to acclimate for at least 3 hours before spectroscopic measurements were performed. Cell densities were controlled using a Fuchs-Rosenthal hemocytometer. Over the course of the three-day experiments all cultures were in the stationary growth phase. For obtaining reference CARS spectra pure β -carotene and Fx, purchased from Sigma-Aldrich, Germany, were utilized.

2.B. CARS measurements

The setup used for acquiring CARS images of the diatoms has already been described in its entirety in ([19]) and detailed descriptions of the source and microscope could be found elsewhere ([20] and [21] respectively). To emphasize the specifics relevant to the discussion here, the Stokes beam for the CARS process is generated by an 80MHz repetition rate Nd:vanadate picosecond laser source (High Q picoTrain, High Q Laser, Austria) and the pump (and probe) beam is produced by an OPO (Levante Emerald, A.P.E, Berlin, Germany). In a previous study, the band assignments of Raman spectra acquired from the specific strain of diatoms investigated here attributed the prominent peak located around 1528 cm^{-1} to the carotenoid pigments in the diatoms [22]. For investigating this particular Raman active vibrational peak using CARS microscopy, the fundamental output of the pico-train at 1064 nm (7.5ps) is combined with the OPO signal tuned to 915 nm(5ps). This study was conducted using a 25 \times , 1.1 NA water immersion objective (CFI Apo LWD 25XW, Nikon Inc., U.S.A) fitted on a home built nonlinear upright microscope. In order to avoid the cells from moving around during the acquisition period poly-L-lysine was applied on glass bottom petri-dishes before the cells were deposited. After the diatoms are pipetted, a cover slip is then placed on the top for examination under a water immersion objective with a cover slip correction.

An 850 nm long pass dichroic filter (Edmund Optics, U.S.A) separates the CARS signal from the back-scattered light collected by the focusing objective. The beam is further filtered by a short pass filter (FF01-842/SP-25, Semrock, U.S.A) and a series of band-pass filters (FF01-794/160-25, FF02-809/81-25, Sem-

rock, U.S.A) before being detected by a photomultiplier tube (PMT) (H10721-20, Hamamatsu, Japan). Two-photon excited auto-fluorescence (TPEF) of the diatoms was also investigated to obtain complementary information that could be used as a reference for the CARS images. For acquiring this modality, just the pump beam was used for excitation and in the detection module the bandpass filters were removed.

The 2 μ s pixel dwell time of the setup scales to a total acquisition time of 8 s for a single CARS image tile considering a 1024×1024 pixel resolution and $2 \times$ averaging employed to improve the SNR. The maximum combined average power of the excitation beams used is 125 mW (80 mW pump and 35 mW Stokes) before the objective and does not lead to observable photo-damage and photo-bleaching of the diatoms during the image acquisition period. This is evident from consistencies in the CARS intensity measured and by afterwards microscopically monitoring the morphological intactness of the cells investigated for a time series of CARS image acquisitions. Axial image stacks were acquired by using the motorized piezo scanner (PIFOC P-725.4CD, PI, Germany) on which the objective is mounted.

In the CARS experiments the field of view is typically zoomed-in to an area covering $\approx 200 \times 200 \mu\text{m}^2$ which can contain upto 5 diatoms. 15 images were taken from each batch and this resulted in a variability of the number of cells investigated due to difference in the cell density among the batches and the particular region on the slides investigated. The number of cells investigated using CARS microscopy for each experiment is summarized in Table 1.

Table 1. The number of *D. brightwellii* and *S. turris* cells investigated using CARS microscopy.

	<i>D. brightwellii</i>			<i>S. turris</i>		
	20:4	12:12	4:20	20:4	12:12	4:20
Day 1	52	44	31	53	56	48
Day 2	50	27	34	49	49	64
Day 3	19	30	25	64	50	39

2.C. Processing and Analysis of CARS images

Individual cells are manually selected from CARS image acquisitions in *ImageJ* ([23]) using the *Polygon Selection Tool* to prepare the cell database presented in Table 1. The segmentation and analysis of the acquired CARS images was carried out in MATLAB (The MathWorks, MA, USA). In order to segment the chloroplasts that encapsulate the carotenoids in the diatoms a marker based watershed approach was followed [24]. In this method, a grey-level image is regarded as a topographical terrain wherein the regional maxima represent catchment basins and the gradients in the image serve as watersheds that segment filled basins. Accordingly, a gradient image is first computed using the *sobel* operator to serve as the input to the watershed segmentation function. Foreground and background markers are used in order

to avoid over-segmentation. The foreground markers are computed by first cleaning up the image by a series of grey-level morphological operations and determining regional maxima with the *imregionalmax* function. The background marker applied here is the morphological skeleton of the thresholded and inverted image. The algorithm eventually results in labelled segmented regions in the images. These are then used as masks for computing the mean intensity of the carotenoid areas in the original image. The aforementioned image analysis procedure as applied to a sample image is presented in the supplementary material (section A).

2.D. Raman measurements

Spontaneous Raman spectroscopic measurements were performed using a commercial Raman microscope setup (Holoprobe, Kaiser Optical System, USA) equipped with a multi-mode diode laser at 785 nm emission and previously described in more detail in [22]. Raman scattered light was collected by a 60 x, 1.0 NA water immersion objective lens (Nikon). Samples were placed on CaF₂ slides that have been surface-modified with poly-L-lysine beforehand. From each batch 40 individual cells were investigated by taking 10 spectra along the main axis of the elongated cells with an exposure time of 0.5 s. During the measurements the automated cosmic spike removal option of the built-in software (Holograms, Kaiser Optical System, USA) was active. The laser power at the sample plane was limited to 30 mW in order to prevent photo-damage of cells as monitored by microscopic inspection. Before starting the measurements a calibration lamp (Kaiser Optical System, USA) was used for intensity and wavelength calibration of the spectrometer.

2.E. Preprocessing and analysis of Raman spectra

Raw spectra were preprocessed and analysed in R using the *hyperSpec* package [25]. The analysis was confined to the spectral range from 700 to 1800 cm^{-1} . Small variances in the wavenumber channels of spectra acquired on different days were corrected applying spectral smoothing and interpolation with the *spc.loess* function. Background correction was accomplished following an EMSC approach as implemented in the *cbmodels* package [26]. 10 spectra of each individual cell were averaged and the resulting mean spectra were area-normalized relative to the whole spectral range of interest. Subsequently performed classification was realized with the help of the *plsllda* function from *cbmodels*.

3. Results and discussion

3.A. CARS microscopy results

Representative images of the diatoms taken using the CARS microscopic setup are presented in Figure 1. Figure 1a depicts multi-modal images of the diatom *D. brightwellii*. The red channel in the images is the CARS modality while a subsequently taken reference two photon fluorescence image is co-displayed in the green chan-

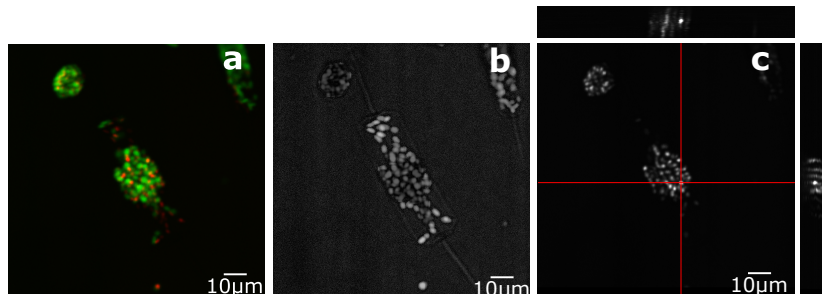


Fig. 1. Nonlinear microscopic images of single *D. brightwellii*. (a) Composite image of the diatom *D. brightwellii* with the modalities epi-collected CARS at 1528 cm^{-1} (red) and TPEF from chlorophyll (green). (b) Contrast adjusted CARS image of the diatom to enhance the non-resonant contributions so that the entire cellular structure is apparent. (c) Depth profile of *D. brightwellii* constructed from 60 CARS images taken in $1\ \mu\text{m}$ axial steps demonstrate the potential of the setup for optical sectioning and subsequent three dimensional reconstruction with sub-micron resolution.

nel. The CARS channel, here tuned to probe the Raman active vibration at 1528 cm^{-1} , shows a resonant contribution from chloroplasts containing carotenoid pigments that forms a very strong contrast with the rest of the cell background. The stretching vibrations arising from conjugated double bonds (C=C) in the carotenoids are responsible for the strong CARS signal observed. In particular, the main contribution of this CARS signal is from the carotenoid Fx (this point is elaborated in the later part of this section). Although the fingerprint spectral region ($800\text{--}1800\text{ cm}^{-1}$) is typically congested by the overlapping peaks from different bio-molecules, here the main contribution from the carotenoids forms an un-contested contrast in the images. The fluorescence channel, mostly filled with signal from the chlorophyll shows how these areas are situated relative to the structure of the entire cell. Accordingly, the carotenoids are found to be localized within the chloroplasts of the diatom. Two photon auto fluorescence from chloroplasts of the diatoms does not cause apparent perturbation or leak through to the CARS channels in these measurements as in the case of lipid investigations. In the test we performed by tuning to the CH_2 stretching vibration (data not shown) the background fluorescence is too high to allow significant analysis to be carried out. Consequently, for examining lipid accumulations in microalgae, modulated ([15]) or time-gated detection ([14]) approaches might be needed. The fluorescence background-free detection of the carotenoids here is possible due to reduced fluorescence from the NIR excitation wavelengths utilized ([27]) and the large gap between the anti-Stokes signal detected at 802 nm and the peak of the fluorescence from chlorophyll centred around 680 nm [28]. In *D. brightwellii*, the area of the carotenoid-containing chloroplasts, as determined from these CARS acquisitions, is between 1 to $5\ \mu\text{m}^2$. Following an approach similar to Cavonius *et al.* ([14]),

the outline of the complete uni-cellular structure can be traced by adjusting the contrast of the CARS image so that the low-intensity parts of the image are also readily visible as presented in Figure 1b. In this image, the long spines extruding from the triangular valves at both ends of the diatom are identifiable. The diatoms appear in different sizes and shapes in the CARS images acquired but are on average $130\ \mu\text{m}$ in length and $25\ \mu\text{m}$ in diameter. One of the inherent advantages on non-linear microscopic methods such as CARS is optical sectioning possible due to the fact that signal generation is limited to a tight focal spot. The lateral depth stack acquisitions presented in Figure 1c serve to show these capabilities with regards to imaging the entire volume of the cells and the carotenoids in particular. The depth of penetration achievable with the microscopic setup, which can extend to $80\ \mu\text{m}$ for turbid tissue samples, is sufficient to cover the complete axial diameter of the diatoms.

Analogously, images of the diatom *S. turris* taken with the CARS microscopic setup are presented in Figure 2. In Figure 2a, the Raman-resonant CARS channel in red maps the distribution of the carotenoids with background fluorescence shown in green. The chloroplast containing the carotenoids in *S. turris* are arranged around the periphery of the cell, as such the boundaries of the cell are already demarked by the two modalities. The sizes of chloroplasts in *S. turris* are smaller than those in *D. brightwellii* and are in the range between 0.7 and $3\ \mu\text{m}^2$. Orthogonal slices extracted from axial stack acquisitions of the diatom near large carotenoid deposits are shown in Figure 2b.

The microscopic setup used for CARS imaging evidently did not lead to photo-bleaching of the signals or destruction of the cells as inferred from preliminary tests done by taking time series images of the diatoms. If the power of the excitation beams is increased significantly from the level stipulated in the section 2.B, the diatoms

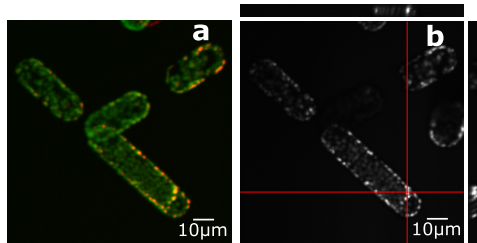


Fig. 2. *S. turris* cells imaged with the non-linear microscopic setup. (a) CARS at 1528 cm^{-1} (red) and TPEF from chlorophyll (green) elucidating how the carotenoids are distributed throughout the cells. (b) *S. turris* orthogonal slices constructed from 50 CARS axial stack acquisitions taken in steps of $1\ \mu\text{m}$.

will exhibit clear damage as the pigments morphological disintegrate in the image acquisitions.

To validate that the observed high-intensity areas in the resonant CARS images are actually from carotenoids, CARS images acquired at different spectral positions are displayed in Figure 3. Figure 3b shows sample on-resonance images of the diatom *D. brightwellii*. These strong resonant signals around 1528 cm^{-1} are from the carotenoids in the algae. This signal fades away in the corresponding off-resonance images in figures 3a and 3c as the difference frequency is shifted from the resonance in either direction. For constructing CARS spectra, images of the cells were acquired as the pump wavelength was varied from 912-918 nm in steps of 0.2 nm, thereby covering Raman wavenumbers in the range of $1495\text{-}1566\text{ cm}^{-1}$.

The extracted mean intensity of the carotenoids as the pump wavelength is varied is first normalized to the maximum value within the series and then averaged for a cell. The spectra of 5 cells is presented as box plot as shown in Figure 3d. Similar spectra computed from CARS microscopic images of pure Fx and β -carotene are co-plotted in the graph for reference purposes. The CARS spectra of the pure β -carotene and Fx correlate well with the respective Raman spectra and what is reported in literature [10, 29]. Similarly, the observed CARS spectra of the diatoms resembles a Lorentzian indicating an overwhelming contribution from Raman-resonant component of the third order non-linear susceptibility. Various pigments in diatoms that have prominent peaks in the proximity ($1510\text{-}1530\text{ cm}^{-1}$) could contribute to the CARS spectra of the diatoms [30]. For instance, from reference Raman spectra of such pigments, it is observed that the major pigment in the diatom, Fx has a peak at 1531 cm^{-1} while the peak of another commonly occurring microalgal pigment diadinoxanthin (Ddx) is found at 1521 cm^{-1} . As the Raman-resonant contribution to the CARS intensity

quadratically increases with increasing concentration of the molecules being probed, the relative concentrations with which these pigments are co-localized in the diatoms will affect the shape of the total CARS spectra. In the CARS spectra of the diatoms it could be observed that the dominating carotenoid in these particular diatom strains is Fx.

This carotenoid imaging potential of the CARS setup is then employed to examine the effect of varying the light regimen on the amount of pigment accumulated in the diatoms. For these investigations, the CARS images of the diatoms acquired at a single optimal axial focus level where the signals were deemed the strongest were analysed. The differences observed are explained using sample images from the different light-dark cycles are presented in Figure 4. Cells kept under longer dark cycles (4:20) contained chloroplasts that provided relatively stronger CARS signal intensity and were bigger than those kept under (20:4) light dark cycles. This implies that the prolongation of the dark cycle resulted in accumulation of more pigments.

Following the approach discussed in section 2.C the mean carotenoid intensity of the diatoms in different light cycles is evaluated from the CARS images and the results found are summarized in Figure 5. The bar graphs present the median CARS intensity of the segmented regions for the three light cycles in the three days of experiments. Although there is considerable variability in the CARS intensity even for the cells kept under the same conditions, there is an overlaying trend of increasing CARS intensity as the cells are kept in the dark for longer times indicating an increase in the accumulation of pigments. It is a well established fact that, in addition to nutritional factors, physical factors such as light intensity affect the pigment composition in microalgae [31]. Depending on the particular strain of algae investigated changing the light regime or photo-period has a particular effect on the carotenoid content. In the case of *D. brightwellii* longer dark times seem to favour the production of carotenoids. This relatively strong trend is observable in all the three days of experiments as depicted in Figure 5a. The *S. turris* also exhibits this trend in the first two days (Figure 5b). On day 3 of the experiments, at which time point the cells are stressed the most, the CARS intensity does not follow the increasing trend for the last two light cycles and exhibits a lot of variability (see overlapping error bars).

As demonstrated, CARS microscopy is a practical technique for fast, disruption-free investigation of microalgal responses to changing environmental factors enabling the imaging of a large number of cells. The analysis incorporates information about the spatial distribution of the pigments within each of the cells with diffraction limited resolution. However, possible relative pigment contribution changes that accompany these responses cannot be extracted from such single-band CARS measurements. For these purposes, concurrent Raman Spectroscopic measurements of the diatoms were

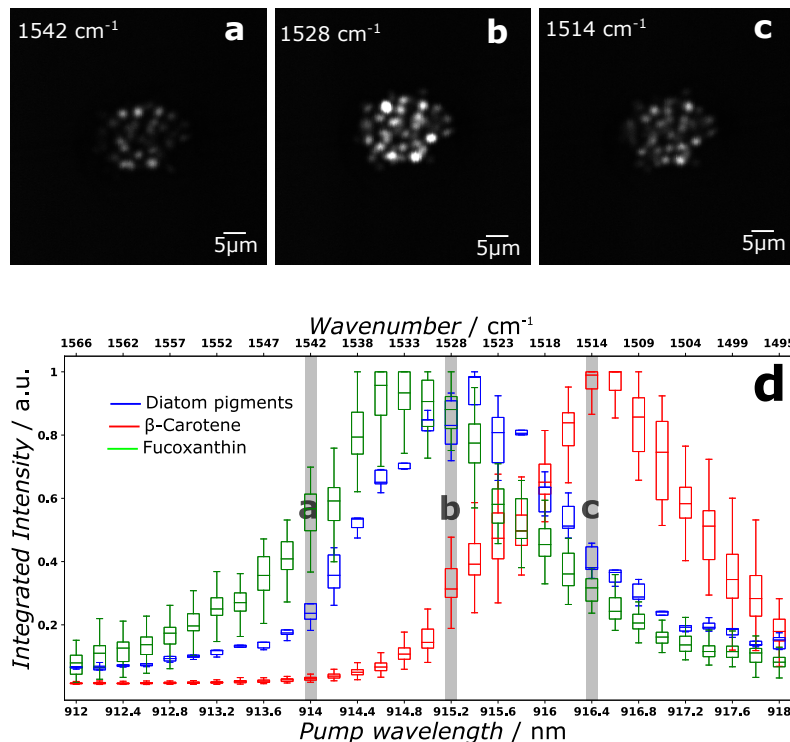


Fig. 3. CARS spectral characteristics of carotenoids in the diatoms. A spectral series of CARS images of the diatom *D. brightwellii* (a-c). The in-resonance image (b) shows a strong signal from the carotenoids forming a sharp contrast to the rest of the background. This contrast decreases with off-resonance measurements on either side of the resonance (a,c). (d) CARS spectra extracted from a series of images of *D. brightwellii* (in blue) exhibit the peak arising from the conjugated double bond (C=C) structure. Similarly acquired CARS spectra of pure fucoxanthin and β -carotene (in red) show slightly shifted peaks. For details see text.

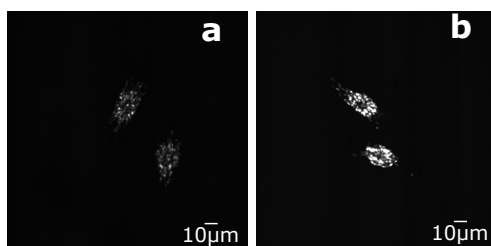


Fig. 4. Example images showing the effect of different light cycles on the accumulation of pigments in *D. brightwellii* (a) under 20:4 light:dark cycle (b) under 4:20 light:dark cycle

performed as the light regimen was varied. In these Raman measurements presented in the following section

only 10 spectra were taken per cell, as it would be impossible to obtain spectroscopic information from each point in the cell and build carotenoid distribution maps as shown in Figure 1a and 2a using spontaneous Raman scattering considering the long acquisition times required for Raman imaging and the number of cells evaluated.

3.B. Raman Spectroscopy results

Detailed information about the biomolecular composition of the cells can be extracted from Raman microscopy as it probes several molecular vibrations simultaneously in contrast to the single-band CARS microscopy. Raman spectra of living diatoms are dominated by spectral contributions arising from the photosynthetic as well as photoprotective pigments due to resonance enhancement effects. In Figure 6a a mean Raman spectrum of all investigated diatom cells is shown along with labels for the prominent bands. Minor Ra-

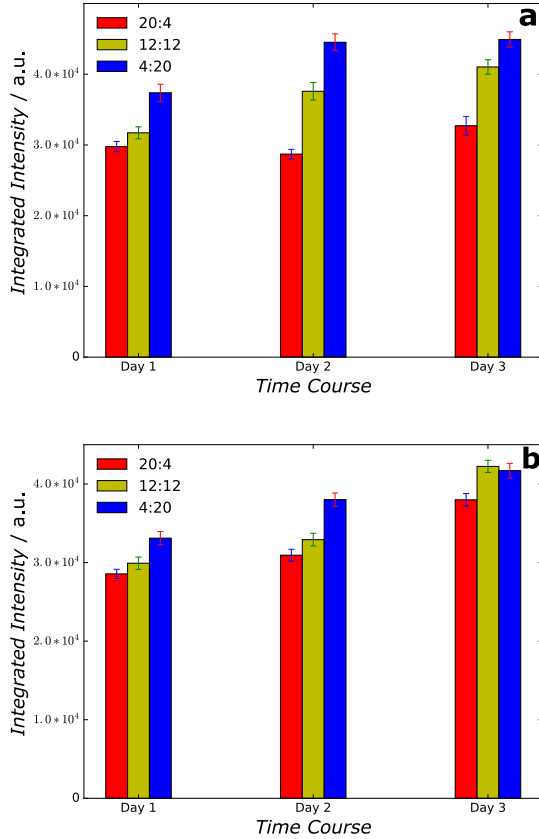


Fig. 5. Mean CARS intensity of segmented regions in (a) *D. brightwellii* (b) *S. turris* cells kept under different light cycles for three consecutive days of measurements. The CARS intensities, in general, show an increasing trend with the prolongation of the dark period within the light cycle.

man bands at 746, 988 and 1328 cm^{-1} can be assigned to vibrations from chlorophyll *a* (Chl *a*) whereas most of the remaining bands, especially those at 1162 and 1528 cm^{-1} originate from carotenoid species, above all the photosynthetic Fx. Despite their lower abundances, the photoprotective pigments diadinoxanthin and diatoxanthin (Ddx/Dtx) play a crucial role in the delicate control mechanism of photosynthesis in diatom cells leading to distinct changes in relative amounts upon environmental impacts [32].

In our experiment of varying light-dark cycles we also collected Raman spectra of individual *D. brightwellii* and *S. turris* cells in order to test the modality's suitability for monitoring changes in the pigmentary pool. The applied area-normalization results in Raman spectra that are normalized relative to the carotenoid con-

tent. Observable spectral variations can therefore be regarded as relative changes in pigment composition with respect to Fx. During the experiment Raman spectra of 40 individual cells per light-dark cycle were measured on the three consecutive days resulting in 360 spectra for each species. In a 100 times repeated procedure PLS-LDA classification models were trained with random subsamples of half the dataset whereas the rest was used for model validation. Corresponding model coefficients with mean and standard deviation are shown in Figure 6a for *D. brightwellii* (above) and *S. turris* (below), respectively. To visualize classification performances, the scores plots of one randomly chosen iteration step are also depicted in Figure 6b. Herein, two independent score layers are combined. In one layer, colored hexagons represent a two-dimensional histogram of the training data in linear discriminant (LD) subspace. On the second layer a scatter plot with circles, squares and triangles shows the respective model projections of the test dataset. In both cases the majority of predicted objects are correctly assigned to their appropriate class. Taking into consideration the relative position of each class in LD subspace allows for spectroscopic interpretation of model coefficients.

In models trained with spectra from *D. brightwellii* characteristic patterns in coefficients arise at around 1162 cm^{-1} for LD1 and 1528 cm^{-1} for LD2. These wavenumbers reflect solely contributions from carotenoid molecules. The corresponding scores plot indicates a correlation between spectra from 4:20 light cycle and positive coefficients on both axes. On the contrary, spectra from cells at 20:4 light cycle correlate with negative coefficients. A strikingly similar coefficient pattern has been observed in a previous Raman study on the growth phases of *D. brightwellii* cultures [22]. From the chemometric model it could be deduced that during the transition from exponential to declining phase cells tend to accumulate photoprotective pigments Ddx/Dtx due to nutrient limitation. This reallocation in pigment composition is favored over de novo biosynthesis of Chl *a* and Fx. Accordingly, the exposure of *D. brightwellii* cells to high light conditions triggers a similar control mechanism to protect light-harvesting molecules from photodamage. Cells kept under ambient light conditions (12:12 light cycle) are in this regard projected in between these two classes. Coefficients of LD1 in models of *S. turris* exhibit an analogous pattern at 1162 cm^{-1} that leads to a distinct separation of cell spectra from high light conditions from the two other classes. Moreover, positive coefficients at 1048 and 1328 cm^{-1} indicate spectral variations that can be assigned to Chl *a* molecules and correlate with cell spectra from ambient and low light conditions, respectively. The interpretation that the relative Chl *a* content is higher in the latter two is hampered by the fact that other prominent Raman bands of Chl *a* are not represented in the coefficients. LD2 clearly discriminates cells under ambient conditions from those at low light. Overall, it can be

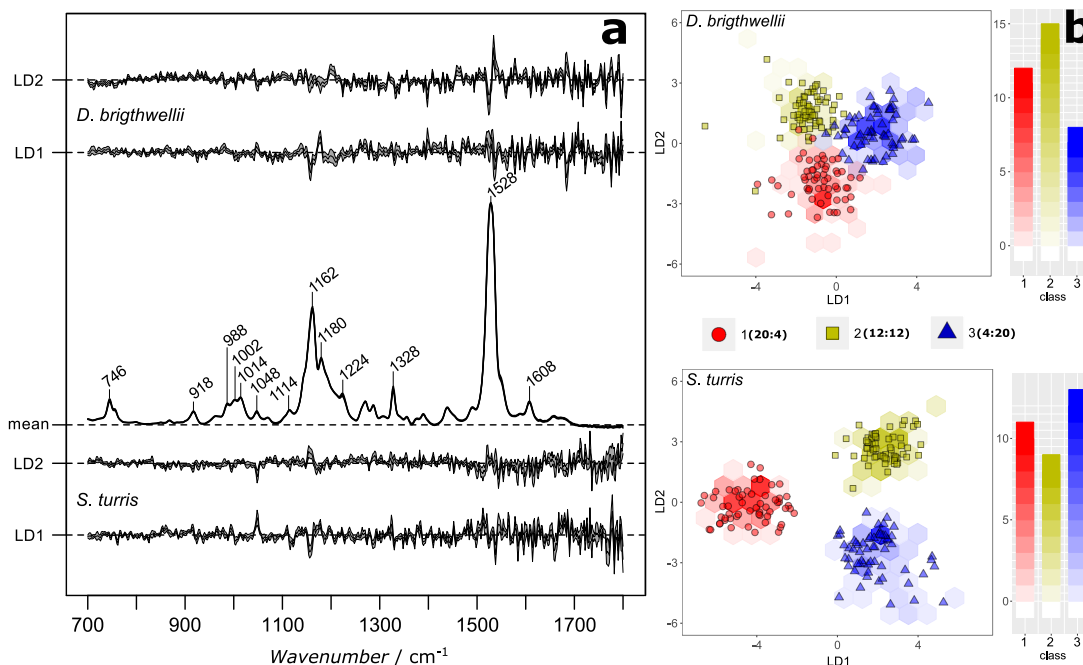


Fig. 6. Acquisition and analysis of spontaneous Raman spectra from the diatoms *D. brighwellii* and *S. turris*. (a) Linear discriminant (LD) coefficients (mean and standard deviation) are displayed in comparison with a mean Raman spectrum of all investigated cells. Chemometric models were established using 50 % of the spectral dataset as training data whereas 50 % was hold out for validation. This process was iterated 100 times. (b) Scores plots are shown for one randomly chosen iteration step and contain two different layers. One of them represents a 2-dimensional histogram (hexagons) for the distribution of projected training data into LD subspace. Points as the second layer indicate the projections of the corresponding test data that was left out from modelling.

deduced that the same control mechanism leading to an accumulation of Ddx/Dtx under high light conditions is present in *S. turris* as well. Raman spectroscopy thereby proves to be a valuable and sensitive tool for probing changes in the pigment pool of microalgae.

4. Conclusion

The study emphasizes the viability of CARS microscopy to investigate microalgal pigments exhibiting strong bands in the fingerprint region. As can be witnessed from the images the resonant contributions are so strong that the rest of the cell structures are not visible unless the contrast has been deliberately adjusted or other modalities are co-registered. Here we capitalized on this capability by performing relative intensity comparisons to uncover a hypothesized increase in pigment accumulation as the diatoms are kept in extended dark-light cycles. The faster image acquisition rate of CARS microscopy as compared to spontaneous Raman microscopy allowed the whole-cell imaging of a large number of diatoms, which is particularly relevant con-

sidering the limited time window between successive measurement cycles. This introduces spatial distribution information into the pigment analysis procedure via the wealth of image processing algorithms available, among which a marker based watershed algorithm was employed here. The comparative changes among the different diatom pigments, that can not be monitored from single band CARS microscopy images, could alternatively be accessed by Raman spectroscopic measurements of selected points within the diatoms. In this regard, chemometric models based on concurrent Raman spectroscopic measurements revealed relative changes in the carotenoid pool. Higher light conditions lead to a distinct increase in the ratio of light-protecting pigments Ddx/Dtx regarding to the accessory pigment Fx. Such investigations have potential bearings on strategies to be adopted for increasing the production of high-value products from microalgae. This study also re-iterates the importance of using different modalities and the interplay of information between them.

Acknowledgments

This work was supported by the Deutsche Forschungsgemeinschaft DFG (KR4387/1-1 and SFB 1127 ChemBioSys). We thank Prof. Pohnert (University of Jena) for providing the culture medium.

References

- [1] T. M. Mata, A. A. Martins, and N. S. Caetano, "Microalgae for biodiesel production and other applications: a review," *Renewable and sustainable energy reviews* **14**, 217–232 (2010).
- [2] P. M. Foley, E. S. Beach, and J. B. Zimmerman, "Algae as a source of renewable chemicals: opportunities and challenges," *Green Chemistry* **13**, 1399–1405 (2011).
- [3] A. C. Guedes, H. M. Amaro, and F. X. Malcata, "Microalgae as sources of carotenoids," *Marine drugs* **9**, 625–644 (2011).
- [4] J. Peng, J.-P. Yuan, C.-F. Wu, and J.-H. Wang, "Fucoxanthin, a marine carotenoid present in brown seaweeds and diatoms: metabolism and bioactivities relevant to human health," *Marine drugs* **9**, 1806–1828 (2011).
- [5] K. Stehfest, J. Toepel, and C. Wilhelm, "The application of micro-FTIR spectroscopy to analyze nutrient stress-related changes in biomass composition of phytoplankton algae," *Plant Physiology and Biochemistry* **43**, 717–726 (2005).
- [6] S. A. Patel, F. Currie, N. Thakker, and R. Goodacre, "Spatial metabolic fingerprinting using FT-IR spectroscopy: investigating abiotic stresses on microorganisms," *Analyst* **133**, 1707–1713 (2008).
- [7] C. J. Hirschmugl, Z.-E. Bayarri, M. Bunta, J. B. Holt, and M. Giordano, "Analysis of the nutritional status of algae by Fourier transform infrared chemical imaging," *Infrared physics & technology* **49**, 57–63 (2006).
- [8] N. D. Parab and V. Tomar, "Raman spectroscopy of algae: a review," *J. Nanomed. Nanotechnol* **3**, 24 (2012).
- [9] P. Heraud, J. Beardall, D. McNaughton, and B. R. Wood, "In vivo prediction of the nutrient status of individual microalgal cells using Raman microspectroscopy," *FEMS microbiology letters* **275**, 24–30 (2007).
- [10] K. Grosser, L. Zedler, M. Schmitt, B. Dietzek, J. Popp, and G. Pohnert, "Disruption-free imaging by Raman spectroscopy reveals a chemical sphere with antifouling metabolites around macroalgae," *Biofouling* **28**, 687–696 (2012).
- [11] C. L. Evans and X. S. Xie, "Coherent anti-Stokes Raman scattering microscopy: chemical imaging for biology and medicine," *Annu. Rev. Anal. Chem.* **1**, 883–909 (2008).
- [12] J.-X. Cheng and X. S. Xie, *Coherent Raman scattering microscopy* (CRC press, 2016).
- [13] X. He, J. Allen, P. Black, T. Baldacchini, X. Huang, H. Huang, L. Jiang, and Y. Lu, "Coherent anti-Stokes Raman scattering and spontaneous Raman spectroscopy and microscopy of microalgae with nitrogen depletion," *Biomedical optics express* **3**, 2896–2906 (2012).
- [14] L. Cavonius, H. Fink, J. Kiskis, E. Albers, I. Undeland, and A. Enejder, "Imaging of lipids in microalgae with coherent anti-Stokes Raman scattering microscopy," *Plant physiology* **167**, 603–616 (2015).
- [15] D. Jaeger, C. Pilger, H. Hachmeister, E. Oberländer, R. Wördenweber, J. Wichmann, J. H. Mussnug, T. Huser, and O. Kruse, "Label-free in vivo analysis of intracellular lipid droplets in the oleaginous microalga *monoraphidium neglectum* by coherent raman scattering microscopy," *Scientific reports* **6**, 35340 (2016).
- [16] A. Dementjev and J. Kostkevičienė, "Applying the method of coherent anti-Stokes Raman microscopy for imaging of carotenoids in microalgae and cyanobacteria," *Journal of Raman Spectroscopy* **44**, 973–979 (2013).
- [17] A. M. Barlow, A. D. Slepko, A. Ridsdale, P. J. McGinn, and A. Stolow, "Label-free hyperspectral nonlinear optical microscopy of the biofuel micro-algae *haematococcus pluvialis*," *Biomedical optics express* **5**, 3391–3402 (2014).
- [18] I. Maier and M. Calenberg, "Effect of extracellular Ca^{2+} and Ca^{2+} -Antagonists on the movement and chemoorientation of male gametes of *ectocarpus siliculosus* (phaeophyceae)," *Plant Biology* **107**, 451–460 (1994).
- [19] F. B. Legesse, S. Heuke, K. Galler, P. Hoffmann, M. Schmitt, U. Neugebauer, M. Bauer, and J. Popp, "Hepatic vitamin a content investigation using coherent anti-Stokes Raman scattering microscopy," *ChemPhysChem* **17**, 4043–4051 (2016).
- [20] A. Lukić, S. Dochow, O. Chernavskaia, I. Latka, C. Matthäus, A. Schwuchow, M. Schmitt, and J. Popp, "Fiber probe for nonlinear imaging applications," *Journal of biophotonics* (2015).
- [21] T. Meyer, M. Baumgartl, T. Gottschall, T. Pascher, A. Wuttig, C. Matthäus, B. F. Romeike, B. R. Brehm, J. Limpert, A. Tünnermann *et al.*, "A compact microscope setup for multimodal nonlinear imaging in clinics and its application to disease diagnostics," *Analyst* **138**, 4048–4057 (2013).
- [22] J. Rüger, N. Unger, I. W. Schie, E. Brunner, J. Popp, and C. Krafft, "Assessment of growth phases of the diatom *ditylum brightwellii* by FT-IR and Raman spectroscopy," *Algal Research* **19**, 246–252 (2016).
- [23] C. A. Schneider, W. S. Rasband, K. W. Eliceiri, J. Schindelin, I. Arganda-Carreras, E. Frise, V. Kaynig, M. Longair, T. Pietzsch, S. Preibisch *et al.*, "671 nih image to imagej: 25 years of image analysis," *Nat. Methods* **9** (2012).
- [24] F. Meyer, "Topographic distance and watershed lines," *Signal processing* **38**, 113–125 (1994).
- [25] C. Beleites, R. Salzer, and V. Sergio, "Validation of soft classification models using partial class memberships: An extended concept of sensitivity & co. applied to grading of astrocytoma tissues," *Chemometrics and Intelligent Laboratory Systems* **122**, 12–22 (2013).
- [26] C. Beleites, "cbmodels: Collection of combined models: Pca-lda, pls-lda, pls-lr as well as emsc," R package version 0.5-20150729 (2015).
- [27] B. Schrader, H. Klump, K. Schenzel, and H. Schulz, "Non-destructive NIR FT Raman analysis of plants," *Journal of Molecular Structure* **509**, 201–212 (1999).
- [28] G. Krause and E. Weis, "Chlorophyll fluorescence and photosynthesis: the basics," *Annual review of plant biology* **42**, 313–349 (1991).
- [29] C. Brackmann, A. Bengtsson, M. L. Alming, U. Svanberg, and A. Enejder, "Visualization of β -carotene and starch granules in plant cells using CARS and SHG microscopy," *Journal of Raman Spectroscopy* **42**, 586–592 (2011).
- [30] P. Kuczynska, M. Jemiola-Rzeminska, and K. Strzalka, "Photosynthetic pigments in diatoms," *Marine drugs*

- 13, 5847–5881 (2015).
- [31] J. R. Benavente-Valdés, C. Aguilar, J. C. Contreras-Esquivel, A. Méndez-Zavala, and J. Montañez, “Strategies to enhance the production of photosynthetic pigments and lipids in chlorophyceae species,” *Biotechnology Reports* **10**, 117–125 (2016).
- [32] J. Lavaud, B. Rousseau, and A.-L. Etienne, “Enrichment of the light-harvesting complex in diadinoxanthin and implications for the nonphotochemical fluorescence quenching in diatoms.” *Biochemistry* **42**, 5802–5808 (2003).

Appendix A: Supplementary material

In order to help elaborate the image processing procedure followed, figure A.1a shows a CARS image taken on the second day of experiments from diatoms kept under Light Cycle 3 (4:20) conditions. Each cell was independently extracted in *ImageJ* for analysis (A.1b). The gradient image, on the basis of which the watershed segmentation is performed, is depicted in Figure A.1c. The regional maxima in the images (Figure A.1d) serve as foreground markers, while the skeleton of the image (Figure A.1e) is used as background marker wherein the ‘flooding’ process in the watershed segmentation is initiated. From the final result depicted in Figure A.1f it can be seen that even touching chloroplasts in the cells are segmented well and there is no severe over-segmentation.

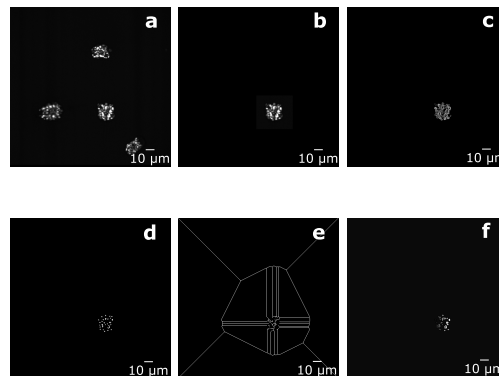


Fig. A.1. The image processing work flow used for the analysis of CARS images. (a) An overview image containing 4 cells (b) A cell singled out using *Imagej* (c) A gradient image of the cell (d) Regional maxima identified in the images. (e) A morphological skeleton image of the cell. (f) The result of the watershed segmentation process.

Investigation of microalgal carotenoid content using coherent anti-Stokes Raman scattering (CARS) microscopy and spontaneous Raman spectroscopy (print version)

Investigation of Microalgal Carotenoid Content Using Coherent Anti-Stokes Raman Scattering (CARS) Microscopy and Spontaneous Raman Spectroscopy

Fisseha Bekele Legesse^{+, [a, b]}, Jan Rüger^{+, [a, b]}, Tobias Meyer^{+, [a, b]}, Christoph Krafft^{+, [a, b]}, Michael Schmitt^[a] and Jürgen Popp^{*, [a, b]}

The yield of high-value products, such as pigments that could be extracted from microalgae, is affected by various nutritional and physical factors. Consequently, there is a need for fast visualization techniques that investigate the responses of individual microalgal cells to changing environmental conditions without introducing perturbations. Here, we apply CARS microscopy to map the distribution of pigments in the diatoms *Ditylum brightwellii* and *Stephanopyxis turris* and report their relative change in response to varying light cycles using a

marker-based watershed analysis of the acquired images. Simultaneously, the underlying specific pigment composition alterations are revealed using Raman microspectroscopy at 785 nm excitation. In regards to assessing the chemical content of microalgae, these methods present themselves as viable alternatives to the standard techniques currently in use because of their non-disruptive nature and the wealth of complementary information that could be obtained from them.

1. Introduction

There is an ever-increasing interest in harvesting microalgae, mainly driven by the production of biofuels.^[1] In parallel to this development, the extraction of other value-added co-products from microalgae is considerably gaining attention. In this regard, microalgae are being regarded as viable, renewable and abundant sources of various biomolecules.^[2] Carotenoids extracted from algae have found diverse applications in pharmaceutical, food and cosmetic industries.^[3] For instance, fucoxanthin (Fx), a xanthophyll naturally found in brown algae and diatoms has been demonstrated to have anti-oxidant, anti-inflammatory, and anti-cancer properties.^[4] This has led to the growing volume of research invested in understanding the intra-cellular mechanisms employed by microalgae in synthesizing and storing these biomolecules. Therefore, there is a need for fast and reliable techniques that help assess the influence of different environmental factors, such as nutrient availability or light conditions, on the pigment content and metabolic response of microalgae.

Typically, analytic approaches such as high-pressure liquid chromatography (HPLC) and mass spectrometry are used to in-

vestigate the chemical content of microalgae. However, extensive sample preparation and bulk sample volumes are required for these techniques. Vibrational spectroscopic methods, on the other hand, can focus on single-cell levels and identify changes in molecular signatures in the algae that are caused by the different external factors. Fourier-transform infrared (FT-IR) spectroscopy is one such technique that has been applied to investigate the effects of environmental growth factors on microalgal response.^[5-7] Nonetheless, FT-IR spectroscopy is perturbed by strong IR absorption of water and thus requires the samples to be dried for investigation.


Raman spectroscopy presents itself as a non-destructive alternative for investigating intact single cells in vivo at a higher resolution than FT-IR spectroscopy. Accordingly, the capability of Raman micro-spectroscopy in identifying chemical fingerprints has been previously used to investigate the distribution of lipids, and pigments in microalgae.^[8,9] However, Raman cross-sections of typical molecules found in living cells are quite low necessitating longer acquisition times. The increase in scattering intensities achievable when using resonance Raman has been employed to examine metabolites and pigments on and in the vicinity of algal surfaces.^[10] However, photodegradation or photo-bleaching and strong fluorescent background due to UV/Vis excitation wavelengths in resonance with electronic excited states limits its applicability for imaging pigment distribution inside diatoms.

These drawbacks can be alleviated by using coherent anti-Stokes Raman scattering (CARS), a four-wave mixing, non-linear technique that is able to extract similar information as spontaneous Raman scattering but provides signals that are much stronger. In the CARS process a pump (ω_p) and a Stokes (ω_s) beam interact in the sample and coherently drive Raman

[a] F. B. Legesse,⁺ J. Rüger,⁺ Dr. T. Meyer, Dr. C. Krafft, Prof. Dr. M. Schmitt, Prof. Dr. J. Popp
Institute of Physical Chemistry and Abbe Center of Photonics
Friedrich-Schiller University Jena, Helmholtzweg 4
07743 Jena (Germany)
E-mail: juergen.popp@uni-jena.de

[b] F. B. Legesse,⁺ J. Rüger,⁺ Dr. T. Meyer, Dr. C. Krafft, Prof. Dr. J. Popp
Leibniz Institute of Photonic Technology (IPHT) Jena e.v.
Albert-Einstein-Str. 9, 07745 Jena (Germany)

[*] These authors contributed equally to this work.

 Supporting Information for this article can be found under:
<https://doi.org/10.1002/cphc.201701298>.

active vibrations at their difference frequency ($\omega_p - \omega_s$). The inelastic scattering of a third probe (ω_p) beam off this vibration results in an anti-Stokes signal $\omega_{as} = 2\omega_p - \omega_s$. CARS allows label-free, video-rate imaging of samples and avoids the problem of one-photon fluorescence as the anti-Stokes signal is blue-shifted from the excitation beams.^[11] This is particularly advantageous for algae investigations as spontaneous Raman scattering encounters problems with the strong chlorophyll fluorescence.^[12] The large portion of CARS studies on algae have particularly focused on examining the metabolism of lipids as they provide strong signals due to the abundance of the CH_2 symmetric stretching vibration.^[13–15] There have also been studies employing CARS as a means of mapping the distribution of carotenoids in specific strains of microalgae.^[16,17]

Here, we employ CARS microscopy and Raman spectroscopy to investigate the effect of different light cycles on pigment accumulation in the uni-cellular, photosynthetic, autotrophs *Ditylum brightwellii* and *Stephanopyxis turris*. These diatoms store carotenoids, mainly Fx, in their chloroplasts as accessory pigments. These carotenoids play photosynthetic as well as anti-oxidative roles in the diatoms. For CARS imaging, we focus on the prominent bands of carotenoids found in the molecular fingerprint region. CARS microscopy was used to show the relative intensity and morphology changes observed among batches as the conditions are varied. CARS microscopy reveals information about the spatial distribution of the carotenoids within the uni-cellular structure of the diatoms. It also permits rapid entire-cell imaging of several diatoms for monitoring comprehensive, specific pigment concentration changes within the limited measurement times available, a feat that is un-realizable by spontaneous Raman spectroscopy. On the other hand, Raman spectra from selected points within the diatoms were acquired concurrently to help identify differences in the molecular fingerprints of the cells that correlate with the change of light cycles.

Consequently, an increase in carotenoid content and a corresponding, relative change in pigment contributions were observed with cells kept longer in the dark than the normal 12:12 hours light cycle. In general, we demonstrate CARS and spontaneous Raman to be complementary and potent techniques for thorough investigation of the influence of metabolic factors on the pigment accumulation capabilities of diatoms.

2. Experimental Section

2.1. Cell Culture and Sample Preparation

D. brightwellii and *S. turris* cultures were both isolated from the North Sea and kept in 50 mL culture flasks (Greiner) with artificial seawater medium prepared as described in Ref. [18]. Three batches with varying light cycles (light:dark), 20:4 h, 12:12 h and 4:20 h, were prepared and the measurements were performed for three consecutive days. All batches were grown in a homebuilt cultivation chamber at a constant temperature of 18 °C and an illuminance of approximately 1000 lx with fluorescent tubes (Osram T5 36W 640). To achieve varying light cycles, batches with light exposure periods shorter than 20 h were transferred to a light-excluding box at the appropriate time every day. After onset of the corre-

sponding light period, cells were allowed to acclimate for at least three hours before spectroscopic measurements were performed. Cell densities were controlled using a Fuchs–Rosenthal hemocytometer. Over the course of the three-day experiments all cultures were in the stationary growth phase. For obtaining reference CARS spectra, pure β -carotene and Fx, purchased from Sigma–Aldrich, Germany, were utilized.

2.2. CARS Measurements

The setup used for acquiring CARS images of the diatoms has already been described in its entirety in Ref. [19], and detailed descriptions of the source and microscope can be found elsewhere (Refs. [20] and [21], respectively). To emphasize the specifics relevant to the discussion here, the Stokes beam for the CARS process is generated by an 80 MHz repetition rate Nd:vanadate picosecond laser source (High Q picoTrain, High Q Laser, Austria) and the pump (and probe) beam is produced by an OPO (Levante Emerald, A.P.E. Berlin, Germany). In a previous study, the band assignments of Raman spectra acquired from the specific strain of diatoms investigated here attributed the prominent peak located around 1528 cm^{-1} to the carotenoid pigments in the diatoms.^[22] For investigating this particular Raman-active vibrational peak using CARS microscopy, the fundamental output of the pico-train at 1064 nm (7.5 ps) is combined with the OPO signal tuned to 915 nm (5 ps). This study was conducted using a 25 \times , 1.1 NA water immersion objective (CFI Apo LWD 25XW, Nikon Inc., U.S.A) fitted on a home built nonlinear upright microscope. To avoid the cells from moving around during the acquisition period, poly-L-lysine was applied on glass bottom petri-dishes before the cells were deposited. After the diatoms are pipetted, a cover slip is then placed on the top for examination under a water immersion objective with a cover slip correction.

An 850 nm long pass dichroic filter (Edmund Optics, U.S.A) separates the CARS signal from the back-scattered light collected by the focusing objective. The beam is further filtered by a short pass filter (FF01-842/SP-25, Semrock, U.S.A) and a series of bandpass filters (FF01-794/160-25, FF02-809/81-25, Semrock, U.S.A) before being detected by a photomultiplier tube (PMT) (H10721-20, Hamamatsu, Japan). Two-photon excited auto-fluorescence (TPEF) of the diatoms was also investigated to obtain complementary information that could be used as a reference for the CARS images. For acquiring this modality, just the pump beam was used for excitation and in the detection module the bandpass filters were removed.

The 2 μs pixel dwell time of the setup scales to a total acquisition time of 8 s for a single CARS image tile considering a 1024 \times 1024 pixel resolution and 2 \times averaging employed to improve the SNR. The maximum combined average power of the excitation beams used is 115 mW (80 mW pump and 35 mW Stokes) before the objective and does not lead to observable photo-damage and photo-bleaching of the diatoms during the image acquisition period. This is evident from consistencies in the CARS intensity measured and by afterwards microscopically monitoring the morphological intactness of the cells investigated for a time series of CARS image acquisitions. Axial image stacks were acquired by using the motorized piezo scanner (PIFOC P-725.4CD, PI, Germany) on which the objective is mounted.

In the CARS experiments, the field of view is typically zoomed-in to an area covering $\approx 200 \times 200 \mu\text{m}^2$, which can contain up to five diatoms. 15 images were taken from each batch and this resulted in a variability of the number of cells investigated due to difference in

Table 1. The number of *D. brightwellii* and *S. turris* cells investigated using CARS microscopy.

	<i>D. brightwellii</i>			<i>S. turris</i>		
	20:4	12:12	4:20	20:4	12:12	4:20
Day 1	52	44	31	53	56	48
Day 2	50	27	34	49	49	64
Day 3	19	30	25	64	50	39

the cell density among the batches and the particular region on the slides investigated. The number of cells investigated using CARS microscopy for each experiment is summarized in Table 1.

2.3. Processing and Analysis of CARS Images

Individual cells are manually selected from CARS image acquisitions in *ImageJ*^[23] using the *Polygon Selection Tool* to prepare the cell database presented in Table 1. The segmentation and analysis of the acquired CARS images was carried out in MATLAB (The MathWorks, MA, USA). To segment the chloroplasts that encapsulate the carotenoids in the diatoms a marker based watershed approach was followed.^[24] In this method, a grey-level image is regarded as a topographical terrain wherein the regional maxima represent catchment basins and the gradients in the image serve as watersheds that segment filled basins. Accordingly, a gradient image is first computed using the *sobel* operator to serve as the input to the watershed segmentation function. Foreground and background markers are used in order to avoid over-segmentation. The foreground markers are computed by first cleaning up the image by a series of grey-level morphological operations and determining regional maxima with the *imregionalmax* function. The background marker applied here is the morphological skeleton of the thresholded and inverted image. The algorithm eventually results in labelled segmented regions in the images. These are then used as masks for computing the mean intensity of the carotenoid areas in the original image. The aforementioned image analysis procedure as applied to a sample image is presented in the Supporting Information.

2.4. Raman Measurements

Spontaneous Raman spectroscopic measurements were performed using a commercial Raman microscope setup (Holoprobe, Kaiser Optical System, USA) equipped with a multi-mode diode laser at

785 nm emission and previously described in more detail in.^[22] Raman scattered light was collected by a 60 \times , 1.0 NA water immersion objective lens (Nikon). Samples were placed on CaF₂ slides that have been surface-modified with poly-L-lysine beforehand. From each batch 40 individual cells were investigated by taking ten spectra along the main axis of the elongated cells with an exposure time of 0.5 s. During the measurements the automated cosmic spike removal option of the built-in software (Holograms, Kaiser Optical System, USA) was active. The laser power at the sample plane was limited to 30 mW to prevent photo-damage of cells as monitored by microscopic inspection. Before starting the measurements, a calibration lamp (Kaiser Optical System, USA) was used for intensity and wavelength calibration of the spectrometer.

2.5. Preprocessing and Analysis of Raman Spectra

Raw spectra were preprocessed and analysed in R using the hyper-Spec package.^[25] The analysis was confined to the spectral range from 700 to 1800 cm⁻¹. Small variances in the wavenumber channels of spectra acquired on different days were corrected applying spectral smoothing and interpolation with the *spc.loess* function. Background correction was accomplished following an EMSC approach as implemented in the *cbmodels* package.^[26] 10 spectra of each individual cell were averaged and the resulting mean spectra were area-normalized relative to the whole spectral range of interest. Subsequently performed classification was realized with the help of the *plslda* function from *cbmodels*.

3. Results and Discussion

3.1. CARS Microscopy Results

Representative images of the diatoms taken using the CARS microscopic setup are presented in Figure 1. Figure 1a depicts multi-modal images of the diatom *D. brightwellii*. The red channel in the images is the CARS modality while a subsequently taken reference two photon fluorescence image is co-displayed in the green channel. The CARS channel, here tuned to probe the Raman active vibration at 1528 cm⁻¹, shows a resonant contribution from chloroplasts containing carotenoid pigments that forms a very strong contrast with the rest of the cell background. The stretching vibrations arising from conjugated double bonds (C=C) in the carotenoids are responsible for the strong CARS signal observed. In particular, the main contribu-

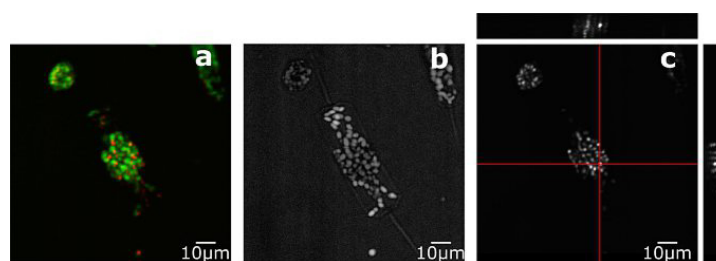


Figure 1. Nonlinear microscopic images of single *D. brightwellii*. a) Composite image of the diatom *D. brightwellii* with the modalities epi-collected CARS at 1528 cm⁻¹ (red) and TPEF from chlorophyll (green). b) Contrast-adjusted CARS image of the diatom to enhance the non-resonant contributions so that the entire cellular structure is apparent. c) Depth profile of *D. brightwellii* constructed from 60 CARS images taken in 1 μ m axial steps demonstrate the potential of the setup for optical sectioning and subsequent three dimensional reconstruction with sub-micron resolution.

tion of this CARS signal is from the carotenoid Fx (this point is elaborated in the later part of this section). Although the fingerprint spectral region ($800\text{--}1800\text{ cm}^{-1}$) is typically congested by the overlapping peaks from different bio-molecules, here the main contribution from the carotenoids forms an un-contested contrast in the images. The fluorescence channel, mostly filled with signal from the chlorophyll shows how these areas are situated relative to the structure of the entire cell. Accordingly, the carotenoids are found to be localized within the chloroplasts of the diatom. Two photon auto fluorescence from chloroplasts of the diatoms does not cause apparent perturbation or leak through to the CARS channels in these measurements as in the case of lipid investigations. In the test we performed by tuning to the CH_2 stretching vibration (data not shown) the background fluorescence is too high to allow significant analysis to be carried out. Consequently, for examining lipid accumulations in microalgae, modulated^[15] or time-gated detection^[14] approaches might be needed. The fluorescence background-free detection of the carotenoids here is possible due to reduced fluorescence from the NIR excitation wavelengths utilized^[27] and the large gap between the anti-Stokes signal detected at 802 nm and the peak of the fluorescence from chlorophyll centred around 680 nm .^[28] In *D. brightwellii*, the area of the carotenoid-containing chloroplasts, as determined from these CARS acquisitions, is between 1 to $5\ \mu\text{m}^2$. Following an approach similar to Cavonius et al.,^[14] the outline of the complete uni-cellular structure can be traced by adjusting the contrast of the CARS image so that the low-intensity parts of the image are also readily visible as presented in Figure 1 b. In this image, the long spines extruding from the triangular valves at both ends of the diatom are identifiable. The diatoms appear in different sizes and shapes in the CARS images acquired but are on average $130\ \mu\text{m}$ in length and $25\ \mu\text{m}$ in diameter. One of the inherent advantages on non-linear microscopic methods such as CARS is optical sectioning possible due to the fact that signal generation is limited to a tight focal spot. The lateral depth stack acquisitions presented in Figure 1 c serve to show these capabilities with regards to imaging the entire volume of the cells and the carotenoids in particular. The depth of penetration achievable with the microscopic setup, which can extend to $80\ \mu\text{m}$ for turbid tissue samples, is sufficient to cover the complete axial diameter of the diatoms.

Analogously, images of the diatom *S. turris* taken with the CARS microscopic setup are presented in Figure 2. In Figure 2 a, the Raman-resonant CARS channel in red maps the distribution of the carotenoids with background fluorescence shown in green. The chloroplast containing the carotenoids in *S. turris* are arranged around the periphery of the cell, as such the boundaries of the cell are already demarked by the two modalities. The sizes of chloroplasts in *S. turris* are smaller than those in *D. brightwellii* and are in the range between 0.7 and $3\ \mu\text{m}^2$. Orthogonal slices extracted from axial stack acquisitions of the diatom near large carotenoid deposits are shown in Figure 2 b.

The microscopic setup used for CARS imaging evidently did not lead to photo-bleaching of the signals or destruction of

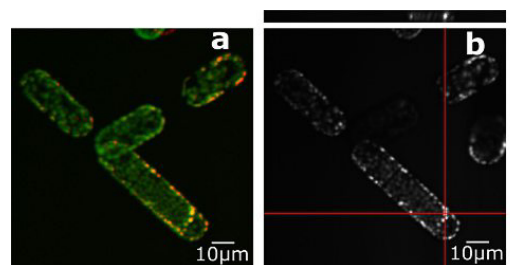


Figure 2. *S. turris* cells imaged with the non-linear microscopic setup. a) CARS at 1528 cm^{-1} (red) and TPEF from chlorophyll (green) elucidating how the carotenoids are distributed throughout the cells. b) *S. turris* orthogonal slices constructed from 50 CARS axial stack acquisitions taken in steps of $1\ \mu\text{m}$.

the cells as inferred from preliminary tests done by taking time series images of the diatoms. If the power of the excitation beams is increased significantly from the level stipulated in the section 2.2, the diatoms will exhibit clear damage as the pigments morphological disintegrate in the image acquisitions.

To validate that the observed high-intensity areas in the resonant CARS images are actually from carotenoids, CARS images acquired at different spectral positions are displayed in Figure 3. Figure 3 b shows sample on-resonance images of the diatom *D. brightwellii*. These strong resonant signals around 1528 cm^{-1} are from the carotenoids in the algae. This signal fades away in the corresponding off-resonance images in Figures 3 a and 3 c as the difference frequency is shifted from the resonance in either direction. For constructing CARS spectra, images of the cells were acquired as the pump wavelength was varied from $912\text{--}918\text{ nm}$ in steps of 0.2 nm , thereby covering Raman wavenumbers in the range of $1495\text{--}1566\text{ cm}^{-1}$.

The extracted mean intensity of the carotenoids as the pump wavelength is varied is first normalized to the maximum value within the series and then averaged for a cell. The spectra of five cells is presented as box plot as shown in Figure 3 d. Similar spectra computed from CARS microscopic images of pure Fx and β -carotene are co-plotted in the graph for reference purposes. The CARS spectra of the pure β -carotene and Fx correlate well with the respective Raman spectra and what is reported in literature.^[29,10] Similarly, the observed CARS spectra of the diatoms resembles a Lorentzian indicating an overwhelming contribution from Raman-resonant component of the third order non-linear susceptibility. Various pigments in diatoms that have prominent peaks in the proximity ($1510\text{--}1530\text{ cm}^{-1}$) could contribute to the CARS spectra of the diatoms.^[30] For instance, from reference Raman spectra of such pigments, it is observed that the major pigment in the diatom, Fx has a peak at 1531 cm^{-1} while the peak of another commonly occurring microalgal pigment diadinoxanthin (Ddx) is found at 1521 cm^{-1} . As the Raman-resonant contribution to the CARS intensity quadratically increases with increasing concentration of the molecules being probed, the relative concentrations with which these pigments are co-localized in the diatoms will affect the shape of the total CARS spectra. In the

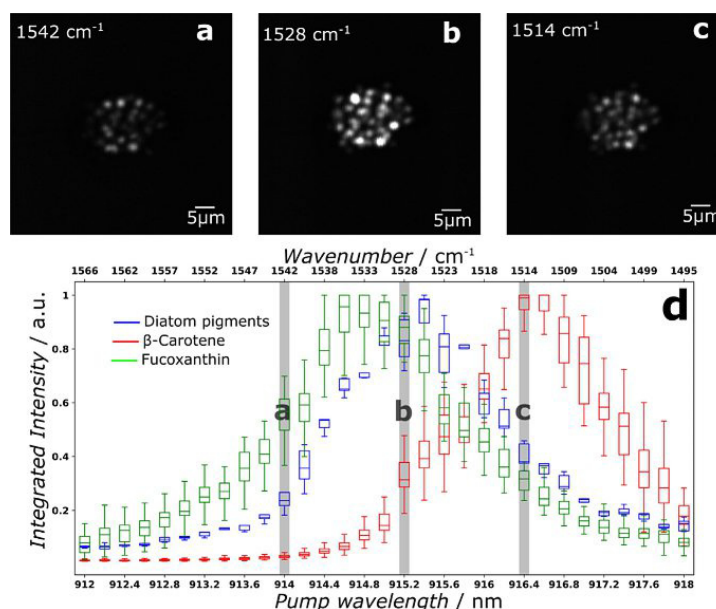


Figure 3. CARS spectral characteristics of carotenoids in the diatoms. A spectral series of CARS images of the diatom *D. brightwellii* (a–c). The in-resonance image (b) shows a strong signal from the carotenoids forming a sharp contrast to the rest of the background. This contrast decreases with off-resonance measurements on either side of the resonance (a,c). d) CARS spectra extracted from a series of images of *D. brightwellii* (in blue) exhibit the peak arising from the conjugated double bond (C=C) structure. Similarly acquired CARS spectra of pure fucoxanthin and β -carotene (in red) show slightly shifted peaks. For details see text.

CARS spectra of the diatoms it could be observed that the dominating carotenoid in these particular diatom strains is Fx.

This carotenoid imaging potential of the CARS setup is then employed to examine the effect of varying the light regimen on the amount of pigment accumulated in the diatoms. For these investigations, the CARS images of the diatoms acquired at a single optimal axial focus level where the signals were deemed the strongest were analysed. The differences observed are explained using sample images from the different light-dark cycles are presented in Figure 4. Cells kept under longer dark cycles (4:20) contained chloroplasts that provided relatively stronger CARS signal intensity and were bigger than those kept under (20:4) light dark cycles. This implies that the pro-

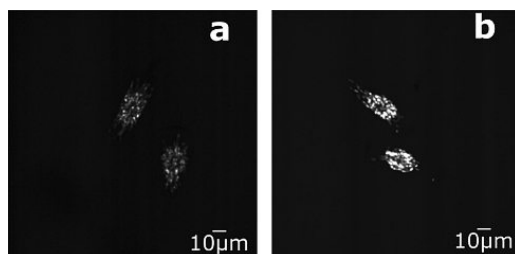


Figure 4. Example images showing the effect of different light cycles on the accumulation of pigments in *D. brightwellii*: a) under 20:4 light:dark cycle and b) under 4:20 light:dark cycle.

longation of the dark cycle resulted in accumulation of more pigments.

Following the approach discussed in Section 2.3 the mean carotenoid intensity of the diatoms in different light cycles is evaluated from the CARS images and the results found are summarized in Figure 5. The bar graphs present the median CARS intensity of the segmented regions for the three light cycles in the three days of experiments. Although there is considerable variability in the CARS intensity even for the cells kept under the same conditions, there is an overlaying trend of increasing CARS intensity as the cells are kept in the dark for longer times indicating an increase in the accumulation of pigments.

It is a well-established fact that in addition to nutritional factors, physical factors such as light intensity affect the pigment composition in microalgae.^[31] Depending on the particular strain of algae investigated, changing the light regime or photo-period has a particular effect on the carotenoid content. In the case of *D. brightwellii* longer dark times seem to favour the production of carotenoids. This relatively strong trend is observable in all the three days of experiments, as depicted in Figure 5a. The *S. turris* also exhibits this trend in the first two days (Figure 5b). On day three of the experiments, at which time point the cells are stressed the most, the CARS intensity does not follow the increasing trend for the last two light cycles and exhibits a lot of variability (see overlapping error bars).

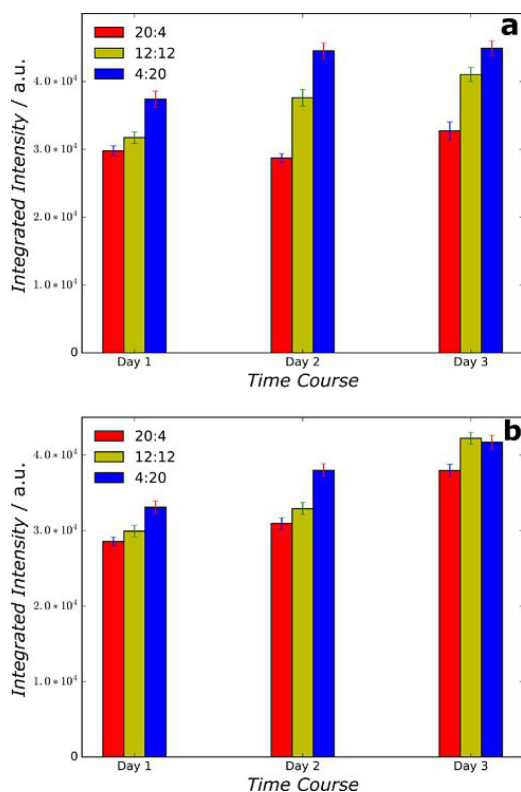


Figure 5. Mean CARS intensity of segmented regions in: a) *D. brightwellii* and b) *S. turris* cells kept under different light cycles for three consecutive days of measurements. The CARS intensities, in general, show an increasing trend with the prolongation of the dark period within the light cycle.

As demonstrated, CARS microscopy is a practical technique for fast, disruption-free investigation of microalgal responses to changing environmental factors, enabling the imaging of a large number of cells. The analysis incorporates information about the spatial distribution of the pigments within each of the cells with diffraction-limited resolution. However, possible relative pigment contribution changes that accompany these responses cannot be extracted from such single-band CARS measurements. For these purposes, concurrent Raman Spectroscopic measurements of the diatoms were performed as the light regimen was varied. In these Raman measurements presented in the following section, only ten spectra were taken per cell, as it would be impossible to obtain spectroscopic information from each point in the cell and build carotenoid distribution maps as shown in Figures 1 and 2a using spontaneous Raman scattering considering the long acquisition times required for Raman imaging and the number of cells evaluated.

3.2. Raman Spectroscopy Results

Detailed information about the biomolecular composition of the cells can be extracted from Raman microspectroscopy as it probes several molecular vibrations simultaneously in contrast to the single-band CARS microscopy. Raman spectra of living diatoms are dominated by spectral contributions arising from the photosynthetic as well as photoprotective pigments due to resonance enhancement effects. In Figure 6a a mean Raman spectrum of all investigated diatom cells is shown along with labels for the prominent bands. Minor Raman bands at 746, 988 and 1328 cm^{-1} can be assigned to vibrations from chlorophyll *a* (Chl *a*) whereas most of the remaining bands, especially those at 1162 and 1528 cm^{-1} originate from

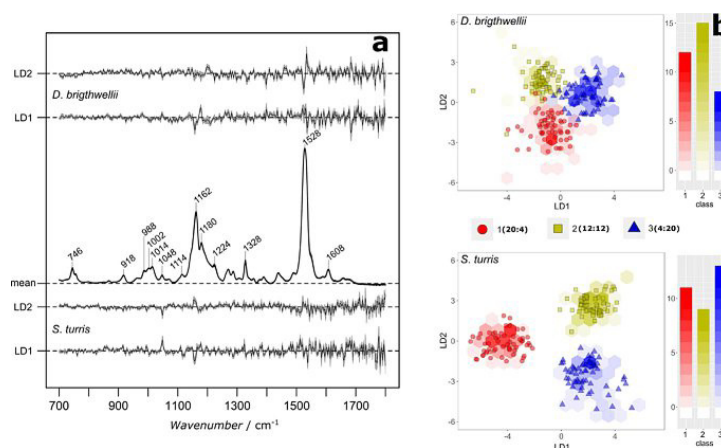


Figure 6. Acquisition and analysis of spontaneous Raman spectra from the diatoms *D. brightwellii* and *S. turris*. a) Linear discriminant (LD) coefficients (mean and standard deviation) are displayed in comparison with a mean Raman spectrum of all investigated cells. Chemometric models were established using 50% of the spectral dataset as training data whereas 50% was held out for validation. This process was iterated 100 times. b) Scores plots are shown for one randomly chosen iteration step and contain two different layers. One of them represents a two-dimensional histogram (hexagons) for the distribution of projected training data into LD subspace. Points as the second layer indicate the projections of the corresponding test data that was left out from modelling.

carotenoid species, above all the photosynthetic Fx. Despite their lower abundances, the photoprotective pigments diadinoxanthin and diatoxanthin (Ddx/Dtx) play a crucial role in the delicate control mechanism of photosynthesis in diatom cells leading to distinct changes in relative amounts upon environmental impacts.^[32]

In our experiment of varying light–dark cycles, we also collected Raman spectra of individual *D. brightwellii* and *S. turris* cells to test the modality's suitability for monitoring changes in the pigmentary pool. The applied area-normalization results in Raman spectra that are normalized relative to the carotenoid content. Observable spectral variations can therefore be regarded as relative changes in pigment composition with respect to Fx. During the experiment Raman spectra of 40 individual cells per light–dark cycle were measured on the three consecutive days resulting in 360 spectra for each species. In a 100 times repeated procedure PLS-LDA classification models were trained with random subsamples of half the dataset whereas the rest was used for model validation. Corresponding model coefficients with mean and standard deviation are shown in Figure 6a for *D. brightwellii* (above) and *S. turris* (below), respectively. To visualize classification performances, the scores plots of one randomly chosen iteration step are also depicted in Figure 6b. Herein, two independent score layers are combined. In one layer, colored hexagons represent a two-dimensional histogram of the training data in linear discriminant (LD) subspace. On the second layer a scatter plot with circles, squares and triangles shows the respective model projections of the test dataset. In both cases the majority of predicted objects are correctly assigned to their appropriate class. Taking into consideration the relative position of each class in LD subspace allows for spectroscopic interpretation of model coefficients.

In models trained with spectra from *D. brightwellii*, characteristic patterns in coefficients arise at around 1162 cm^{-1} for LD1 and 1528 cm^{-1} for LD2. These wavenumbers reflect solely contributions from carotenoid molecules. The corresponding scores plot indicates a correlation between spectra from 4:20 light cycle and positive coefficients on both axes. On the contrary, spectra from cells at 20:4 light cycle correlate with negative coefficients. A strikingly similar coefficient pattern has been observed in a previous Raman study on the growth phases of *D. brightwellii* cultures.^[22] From the chemometric model it could be deduced that during the transition from exponential to declining phase cells tend to accumulate photoprotective pigments Ddx/Dtx due to nutrient limitation. This reallocation in pigment composition is favored over de novo biosynthesis of Chl a and Fx. Accordingly, the exposure of *D. brightwellii* cells to high light conditions triggers a similar control mechanism to protect light-harvesting molecules from photodamage. Cells kept under ambient light conditions (12:12 light cycle) are in this regard projected in between these two classes. Coefficients of LD1 in models of *S. turris* exhibit an analogous pattern at 1162 cm^{-1} that leads to a distinct separation of cell spectra from high light conditions from the two other classes. Moreover, positive coefficients at 1048 and 1328 cm^{-1} indicate spectral variations that can be assigned to

Chl a molecules and correlate with cell spectra from ambient and low light conditions, respectively. The interpretation that the relative Chl a content is higher in the latter two is hampered by the fact that other prominent Raman bands of Chl a are not represented in the coefficients. LD2 clearly discriminates cells under ambient conditions from those at low light. Overall, it can be deduced that the same control mechanism leading to an accumulation of Ddx/Dtx under high light conditions is present in *S. turris* as well. Raman spectroscopy thereby proves to be a valuable and sensitive tool for probing changes in the pigment pool of microalgae.

4. Conclusions

The study emphasizes the viability of CARS microscopy to investigate microalgal pigments exhibiting strong bands in the fingerprint region. As can be witnessed from the images, the resonant contributions are so strong that the rest of the cell structures are not visible unless the contrast has been deliberately adjusted or other modalities are co-registered. Here, we capitalized on this capability by performing relative intensity comparisons to uncover a hypothesized increase in pigment accumulation as the diatoms are kept in extended dark–light cycles. The faster image acquisition rate of CARS microscopy as compared to spontaneous Raman micro-spectroscopy allowed the whole-cell imaging of a large number of diatoms, which is particularly relevant considering the limited time window between successive measurement cycles. This introduces spatial distribution information into the pigment analysis procedure via the wealth of image processing algorithms available, among which a marker based watershed algorithm was employed here. The comparative changes among the different diatom pigments, that can not be monitored from single band CARS microscopy images, could alternatively be accessed by Raman spectroscopic measurements of selected points within the diatoms. In this regard, chemometric models based on concurrent Raman spectroscopic measurements revealed relative changes in the carotenoid pool. Higher light conditions lead to a distinct increase in the ratio of light-protecting pigments Ddx/Dtx regarding to the accessory pigment Fx. Such investigations have potential bearings on strategies to be adopted for increasing the production of high-value products from microalgae. This study also re-iterates the importance of using different modalities and the interplay of information between them.

Acknowledgements

This work was supported by the Deutsche Forschungsgemeinschaft DFG (KR4387/1-1 and SFB 1127 ChemBioSys). We thank Prof. Pohnert (University of Jena) for providing the culture medium.

Conflict of interest

The authors declare no conflict of interest.

Keywords: algae · carotenoids · coherent anti-Stokes Raman scattering · medical and biological imaging · vibrational spectroscopy

- [1] T. M. Mata, A. A. Martins, N. S. Caetano, *Renewable Sustainable Energy Rev.* **2010**, *14*, 217–232.
- [2] P. M. Foley, E. S. Beach, J. B. Zimmerman, *Green Chem.* **2011**, *13*, 1399–1405.
- [3] A. C. Guedes, H. M. Amaro, F. X. Malcata, *Mar. Drugs* **2011**, *9*, 625–644.
- [4] J. Peng, J.-P. Yuan, C.-F. Wu, J.-H. Wang, *Mar. Drugs* **2011**, *9*, 1806–1828.
- [5] K. Stehfest, J. Toepel, C. Wilhelm, *Plant Physiol. Biochem.* **2005**, *43*, 717–726.
- [6] S. A. Patel, F. Currie, N. Thakker, R. Goodacre, *Analyst* **2008**, *133*, 1707–1713.
- [7] C. J. Hirschmugl, Z.-E. Bayarri, M. Bunta, J. B. Holt, M. Giordano, *Infrared Phys. Technol.* **2006**, *49*, 57–63.
- [8] N. D. Parab, V. Tomar, *J. Nanomed. Nanotechnol.* **2012**, *3*, 24.
- [9] P. Heraud, J. Beardall, D. McNaughton, B. R. Wood, *FEMS Microbiol. Lett.* **2007**, *275*, 24–30.
- [10] K. Grosser, L. Zedler, M. Schmitt, B. Dietzek, J. Popp, G. Pohnert, *Biofouling* **2012**, *28*, 687–696.
- [11] C. L. Evans, X. S. Xie, *Annu. Rev. Anal. Chem.* **2008**, *1*, 883–909.
- [12] J.-X. Cheng, X. S. Xie, *Coherent Raman scattering microscopy*, CRC, Boca Raton, **2016**.
- [13] X. He, J. Allen, P. Black, T. Baldacchini, X. Huang, H. Huang, L. Jiang, Y. Lu, *Biomed. Opt. Express* **2012**, *3*, 2896–2906.
- [14] L. Cavonius, H. Fink, J. Kiskis, E. Albers, I. Undeland, A. Enejder, *Plant Physiol.* **2015**, *167*, 603–616.
- [15] D. Jaeger, C. Pilger, H. Hachmeister, E. Oberländer, R. Würdenweber, J. Wichmann, J. H. Mussnug, T. Huser, O. Kruse, *Sci. Rep.* **2016**, *6*, 35340.
- [16] A. Dementjev, J. Kostkeviciene, *J. Raman Spectrosc.* **2013**, *44*, 973–979.
- [17] A. M. Barlow, A. D. Slepko, A. Ridsdale, P. J. McGinn, A. Stolow, *Biomed. Opt. Express* **2014**, *5*, 3391–3402.
- [18] I. Maier, M. Calenberg, *Plant Biol.* **1994**, *107*, 451–460.
- [19] F. B. Legesse, S. Heuke, K. Galler, P. Hoffmann, M. Schmitt, U. Neugebauer, M. Bauer, J. Popp, *ChemPhysChem* **2016**, *17*, 4043–4051.
- [20] A. Lukić, S. Dochow, O. Chernavskaia, I. Latka, C. Matthäus, A. Schwuchow, M. Schmitt, J. Popp, *J. Biophotonics* **2016**, *9*, 138–143.
- [21] T. Meyer, M. Baumgartl, T. Gottschall, T. Pascher, A. Wuttig, C. Matthäus, B. F. Romeike, B. R. Brehm, J. Limpert, A. Tünnermann, O. Guntinas-Lichius, M. Schmitt, B. Dietzek, J. Popp, *Analyst* **2013**, *138*, 4048–4057.
- [22] J. Rüger, N. Unger, I. W. Schie, E. Brunner, J. Popp, C. Krafft, *Algal Res.* **2016**, *19*, 246–252.
- [23] C. A. Schneider, W. S. Rasband, K. W. Eliceiri, *Nat. Methods* **2012**, *9*, 671–675.
- [24] F. Meyer, *Signal Processing* **1994**, *38*, 113–125.
- [25] C. Beleites, R. Salzer, V. Sergo, *Chemom. Intell. Lab. Syst.* **2013**, *122*, 12–22.
- [26] C. Beleites, R package version 0.5-20150729, **2015**.
- [27] B. Schrader, H. Klump, K. Schenzel, H. Schulz, *J. Mol. Struct.* **1999**, *509*, 201–212.
- [28] G. Krause, E. Weis, *Annu. Rev. Plant Biol.* **1991**, *42*, 313–349.
- [29] C. Brackmann, A. Bengtsson, M. L. Alminger, U. Svanberg, A. Enejder, *J. Raman Spectrosc.* **2011**, *42*, 586–592.
- [30] P. Kuczynska, M. Jemiola-Rzeminska, K. Strzalka, *Mar. Drugs* **2015**, *13*, 5847–5881.
- [31] J. R. Benavente-Valdés, C. Aguilar, J. C. Contreras-Esquivel, A. Méndez-Zavala, J. Montañez, *Biotechnol. Rep.* **2016**, *10*, 117–125.
- [32] J. Lavaud, B. Rousseau, A.-L. Etienne, *Biochemistry* **2003**, *42*, 5802–5808.

Manuscript received: December 1, 2017
Accepted manuscript online: January 22, 2018
Version of record online: February 16, 2018

6.4 Fiber-based dual-focus time-demultiplexed second harmonic generation microscopy

Documentation of Authorship

Sandro Heuke*	Design of concept, acquisition and analysis of SHG images, preparation of the manuscript
Fisseha Bekele Legesse*	Acquisition and analysis of SHG images
Adrian Lorenz	Building of a fiber amplifier
Torbjörn Pascher	Reconfiguration of the electronics and software of the laser scanning microscope
Denis Akimov	Discussion of results
Matthias Jäger	Project coordination and supervision, discussion of results
Michael Schmitt	Project coordination and supervision, discussion of results
Jürgen Popp	Project coordination and supervision, discussion of results

All authors revised, edited and proof read the final manuscript.

*Both authors share first authorship of this manuscript.

Reprinted with kind permission from the OSA publishing group.

[FBL4] S. Heuke, F. B. Legesse, A. Lorenz, T. Pascher, D. Akimov, M. Jäger, M. Schmitt, and J. Popp, “Fiber-based dual-focus time-demultiplexed second harmonic generation microscopy,” *Optics letters* **40**, 2505–2508 (2015).

Author	S. Heuke	Fisseha Bekele Legesse
Suggested equivalent of publications	1.0	1.0

Fiber-based dual-focus time-demultiplexed second harmonic generation microscopy

Sandro Heuke,¹ Fisseha Bekele Legesse,¹ Adrian Lorenz,¹ Torbjörn Pascher,^{2,3} Denis Akimov,¹ Matthias Jäger,¹ Michael Schmitt,^{1,4} and Jürgen Popp^{1,4,*}

¹Leibniz Institute of Photonic Technology (IPHT) Jena e.v., Albert-Einstein-Str. 9, 07745 Jena, Germany

²Pascher Instruments AB, Stora Rabybyaväg 24, 22478 Lund, Sweden

³Department of Chemical Physics Lund University, Kemicentrum, Getingevägen 60, 22241 Lund, Sweden

⁴Institute of Physical Chemistry and Abbe Center of Photonics, Friedrich-Schiller University Jena, Helmholtzweg 4, 07743 Jena, Germany

*Corresponding author: Jürgen.Popp@ipht-jena.de

Received April 1, 2015; accepted April 25, 2015;
posted April 30, 2015 (Doc. ID 237299); published May 20, 2015

We present a dual-focus second harmonic generation (SHG) microscopy approach based on stable, compact, and inexpensive fiber technology. One-tenth of the fiber laser output is coupled into a 100 m (± 500 ns) long single-mode fiber and further amplified to achieve two separately guided beams with time-alternating pulse trains. SHG detection is performed sequentially, generating two individual images in one scan. Thus, the configuration allows for imaging of distinct areas within the field of view at twice the repetition rate of the fiber laser but is readily extended to a multiple of the repetition rate with tens of foci. © 2015 Optical Society of America

OCIS codes: (170.0180) Microscopy; (190.2620) Harmonic generation and mixing; (110.2350) Fiber optics imaging; (060.3735) Fiber Bragg gratings; (170.3880) Medical and biological imaging.
<http://dx.doi.org/10.1364/OL.40.002505>

Laser scanning second harmonic generation (SHG) microscopy is a versatile tool for the investigation of non-centrosymmetric organic and inorganic matter [1–4]. Among the former, collagen SHG imaging emerged to a valuable diagnostic technique providing insight to aging, healing, or tumor progression processes [5]. Use of SHG microscopy for medical purposes, however, is still in its infancy. The delay of technology transfer into the clinics can be attributed to a limited imaging speed especially for deep tissue examination of collagen's microstructure, among other reasons. Depending on the average and pulse peak power, the SHG image acquisition rate is limited by the tissue's damage threshold [6]. One possibility to avoid tissue damage caused by overheating is to increase the scanning speed of the laser scanning mirrors by replacing nonresonant with resonant galvo scanners or polygonal mirrors. Resonant scanners, however, can be only driven at one velocity while the performance of polygonal mirrors is compromised by pyramidal errors that result in beam fluctuations [1]. Besides increasing the SHG imaging speed by implementing novel scanning technologies, numerous multifocus approaches were proposed. Among the latter, microlens arrays [7], passive beam splitters [8], and beam splitters relying on the etalon effect [9] were implemented. Since all these configurations utilize cameras as detecting elements, intervoxel SHG cross talk occurs in particular for thick samples due to scattering of the SHG radiation. The image quality is further compromised by coherence artifacts if simultaneous illumination of the sample is applied, i.e., if the laser pulses interact isochronally with each focal position. Coherence artifacts can be avoided by delaying laser pulses for different foci in time, also referred to as time multiplexing [10]. To remove the intervoxel cross talk for strongly scattering samples the detection has to be either confocal [11], thereby intrinsically losing the majority of the generated photons, or time demultiplexed. The latter was achieved using photomultiplier tubes together with a solid state laser

source with up to six foci [12]. This illumination and detection layout by Sheetz *et al.* [12] is ideal for deep tissue investigation, since it minimizes artifacts and tissue damage, but still allows the adjustment of the scanning velocity. For routine clinical applications, however, the ideal experimental implementation also has to be compact and stable, rendering the majority of bulk solid state laser sources unsuitable in favor of fiber technology. A one-to-one transition of conventionally applied femtosecond (fs) solid state lasers at repetition rates of 70–80 MHz to fiber laser and fiber pulse guidance is complicated by linear and nonlinear dispersion leading to a severe loss of peak irradiance of spectrally broad fs-pulses. To avoid laborious pulse pre- or postcompression, it is beneficial to utilize spectrally narrow picosecond pulses and to reduce the laser's repetition rate to 1–10 MHz to maintain high peak irradiances [13]. If single element detectors, such as photomultiplier tubes (PMTs), are employed for time demultiplexing, low repetition rates also allow the free choice of the number of foci to implement. State of the art PMTs possess rise and transit times on the order of a few tens of nanoseconds, which puts a constraint on the pulse to pulse time slice for all foci combined to avoid interfocal cross talk.

With these considerations in mind, we selected a 1 MHz fiber laser at 1032 nm with a temporal and spectral pulse (FWHM) width of 75 ps and 0.8 nm, respectively, to prove the concept of a fiber-based dual-focus SHG microscope. A schematic sketch of the experimental setup is displayed in Fig. 1. Technical details concerning the basic optical layout, detection, and control of the microscope can be found elsewhere [14].

The fiber laser output of 90 mW is split 10:1 (NDC-100S-4M, Thorlabs). The minor beam part is coupled into a 100 m single-mode fiber (SM800, Thorlabs) using aspheric fiber couplers (PAF-X-18-PC-B, Thorlabs) to delay the pulses by half of the repetition rate. For amplification, the single-mode fiber is spliced to 1.5 m of a Yb

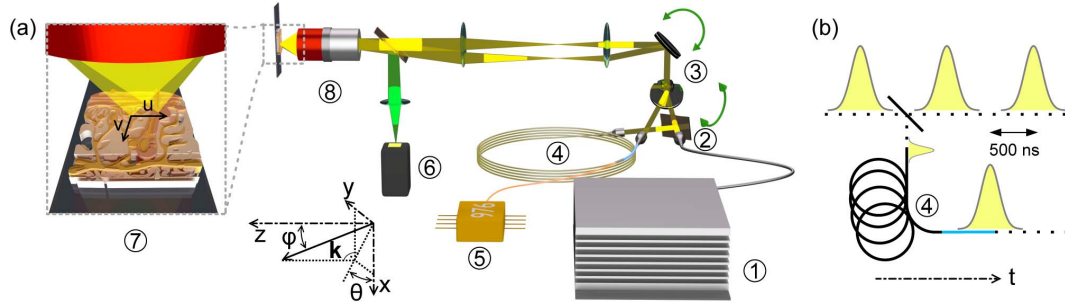


Fig. 1. Experimental setup and time multiplexing: (a) the fiber laser emits pulses at 1032 nm of 75 ps (FWHM) with a repetition rate of 1 MHz. The output is split 10:1 by a reflective filter wheel. The minor beam part is coupled into a 100 m long single-mode fiber to delay the pulses by half of the repetition period of the fiber laser and further amplified. Both beams are centered on the laser scanning mirrors and imaged to the back focal plane of the objective lens. Due to the angle shift, both beams are focused at distinct positions at the sample. A triggered PMT demultiplexes the SHG signals from both beams. (b) Schematic of time multiplexing. ① fiber laser; ② beam splitter; ③ laser scanning mirrors; ④ 100 m single-mode fiber spliced to 1.5 m of a Yb fiber; ⑤ pump laser diode at 976 nm; ⑥ PMT; ⑦ sliced skin section; and ⑧ objective lens.

fiber (LAS-YB-07-01, CorActive) that is core-pumped at 976 nm. As a result, 80 mW average power at 1032 nm with a spectral width of only 2.5 nm (FWHM) and a pulse length of 56 ps determined by autocorrelation are obtained. Both beams, i.e., fiber-delayed and amplified as well as the nonfiber-delayed part, are centered on the first laser scanning mirror with a distinct angle of incidence. The scanning mirror is imaged onto the back aperture of a 25 \times water immersion objective (CFI Apo LWD 25XW, Nikon) via tube and scan lens (MPM-SL, Thorlabs) and further focused onto the sample with an average power of 15 mW per beam. Depending on the difference in their angles of incidence, both beams are focused at different lateral positions, which is readily shown for a scalar approximation. The incoming wave is given via

$$E_i(x, y, z) = E_0 \exp[ik(x \sin \theta \cos \varphi + y \sin \theta \sin \varphi + z \cos \theta)], \quad (1)$$

where E_0 is a constant amplitude factor and $k = 2\pi/\lambda$ is the absolute value of the wave vector of the incoming beam. Dropping constants, the intensity distribution in the back focal plane is given by [15]

$$I_f(u, v) = \left\| \iint E_i \exp[-i2\pi(f_x x + f_y y)] dx dy \right\|^2 = \|\mathcal{F}[E_i]\|^2, \quad (2)$$

where f is the focal length of the objective lens; u, v denote the Cartesian coordinates at the back focal plane; and $f_x = u/(\lambda f)$, $f_y = v/(\lambda f)$ are the input Fourier components. Inserting Eq. (1) into Eq. (2) and dropping E_0 yields

$$I_f(u, v) = \delta(u - f \sin \theta \cos \varphi, v - f \sin \theta \sin \varphi). \quad (3)$$

Thus, changing the incoupling angles θ and φ of both beams at the objective's back aperture allows for tuning the relative position of the foci at the sample. The generated SHG radiation is collected in the backward direction,

separated from the fundamental beam by a dichroic mirror (SEM-FF775-Di01-25x3, Semrock) and filtered by short- and bandpass filters ($1 \times$ FF01-525/45-25, $1 \times$ FF01-750/SP-2, Semrock). A PMT (H10721-20, Hamamatsu) is used for detection. To demultiplex the SHG signal, a fiber laser internal photodiode generates 80 ns-long voltage pulses that are temporally delayed (9520 Digital Delay Pulse Generator, Quantum Composers) and further used to gate the PMT output by the SHG signal integrator. Compared to a single focus approach, the gated PMT readout, therefore, also halves the impact of system specific external noise sources such as ambient light. For demonstration of a clinically relevant application, Fig. 2 displays in-plane dual-focus SHG images of a 20 μ m-thick section of human skin arising from tumor surgery. The two foci are displaced horizontally by approximately 100 μ m. The total acquisition time for both SHG images of each 4096 pixels \times 4096 pixels was 16 s, with an effective pixel dwell time of 0.48 μ s collecting single shots. To reduce noise, the SHG images were binned 4 by 4, corresponding to a pixel dwell time of 7.6 μ s. The image alignment was adjusted manually while laser scanning by changing the angle of incidence of one beam relative to the other. Note that overlapping areas could be used in future applications for an automatic image

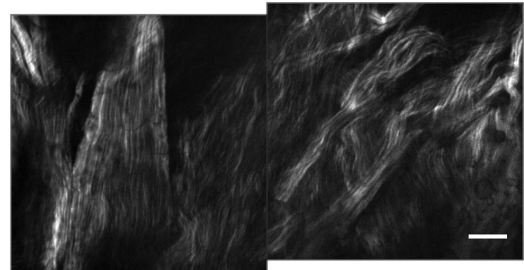


Fig. 2. In-plane dual-focus SHG microscopy images of a human skin section. Both images were acquired time multiplexed, i.e., sequentially pulse after pulse. The adjacent images were aligned manually. Scale bar: 20 μ m.

registration, e.g., by phase correlation [16], but is beyond the scope of the work presented here. The images displayed in Fig. 2 clearly prove the capability of the dual-focus approach to reveal the collagen's fibrous microstructure. No interimage cross talk is observed, though it shall be noted that saturation in one SHG image results in dimmed areas at corresponding positions in the other SHG image. The reason for this artifact is a reduced PMT sensitivity for short times after PMT saturation affecting both images. Thus, penalties for image saturation are higher than for a single focus approach and shall be avoided.

Besides splitting the field of view, several depths can be scanned simultaneously if the divergence of one beam is altered, as exemplified in Fig. 3. Figure 3(a) shows a z stack of a 100 μm -thick section of pig ear skin imaged with two foci of different axial positions. By gently changing the distance between the single-mode fiber end with respect to the output coupler the beam divergence was reduced to change the focus to higher depths in the sample. The interfocal axial distance is approximately 15 μm . SHG images of nearly corresponding z positions are displayed in Fig. 3(b). The difference within the images results from a slight axial displacement and a difference between the incident polarizations of the electric fields. The latter can be controlled by using more expensive polarization maintaining single-mode fibers to delay the pulse trains. Nevertheless, for clinical decision making the distinction between epithelium and connective tissue is of particular

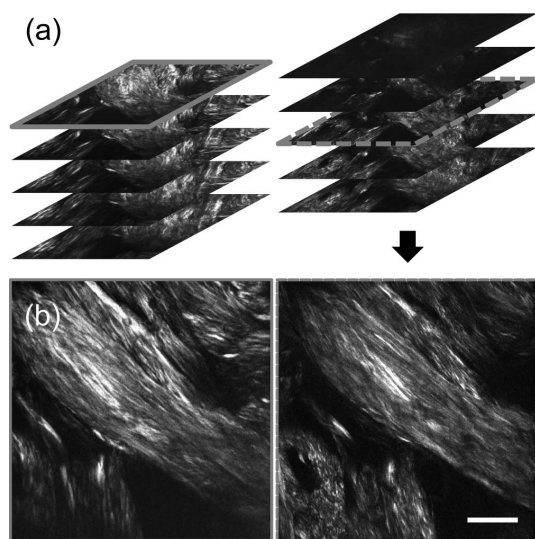


Fig. 3. z -displaced dual-focus SHG microscopy of a 100 μm -thick section of pig ear skin sliced perpendicular to the skin's surface. (a) z stacks acquired with an 8 μm step size. Little change of the beam divergence allows for z displacement of the focal positions. The foci were axially displaced by approximately 15 μm , illustrating the opportunity for simultaneous image acquisition at different tissue depths in one scan. The continuous and dashed gray boxes highlight the images detailed in (b) dual-focus SHG images acquired at similar z positions. It shall be noted that both images are also slightly displaced in the x and y direction. Scale bar: 50 μm .

importance and, therefore, an alteration of the incident polarization after the fiber is of minor impact. As a consequence of the angle shifted incoupling, both images exhibit a lateral displacement in addition to the axial offset. Reducing the angle between both images will diminish this displacement. Alternatively, a polarizing beam combiner for perpendicularly polarized beams may be exploited to avoid lateral displacement.

In conclusion, we presented a simple, stable, and inexpensive dual-focus SHG microscopy approach on the grounds of compact fiber technology that is readily transferred to clinics. The fiber laser output is split and time multiplexed as well as amplified by a combination of a 100 m single-mode and a 1.5 m Yb fiber. Recombination of the two beams with a selected angular displacement allows for splitting the field of view and, therefore, imaging at twice the rate of the corresponding single-focus approach. Furthermore, alteration of the divergence of one beam enables the imaging of different depths of bulky biomedical samples at once without interfocal cross talk. If saturation is avoided, the presented approach does not lose any advantage of a single-focus setup, i.e., it requires no redesign of the optics nor does it compromise the lateral resolution for in-plane SHG measurements like in nontime-multiplexed multifocus implementations with small interfocal distances [17]. Switching between the dual- and single-focus configuration is as simple as removing a beam splitter. Moreover, the presented approach can be scaled up until the combined repetition rate of all foci is equal to the PMT's readout rate (10–100 s of foci) if the output power of the fiber laser is increased accordingly. We consider the latter as our current limitation though increasing power is noncritical considering the recent development of high-power fiber laser systems [18]. An upscaling of the fiber laser source with an in-built fiber splitter spliced to time multiplexing single-mode fibers will create an alignment-free system that minimizes coupling losses. Furthermore, the approach may be extended to other kinds of clinically relevant coherent nonlinear microscopy techniques including third harmonic generation and coherent anti-Stokes Raman scattering. Among these, the latter is part of our current work.

This work was financially supported by the Federal Ministry of Education and Research, Germany (Project Fiber Health Probe FKZ: 13N1225, 3N12526), and the Carl-Zeiss-Stiftung.

References

1. F. S. Pavone and P. J. Campagnola, eds., *Second Harmonic Generation Imaging*, Series in Cellular and Clinical Imaging (CRC Press, 2013).
2. R. Cicchi, E. Baria, C. Matthäus, M. Lange, A. Lattermann, B. R. Brehm, J. Popp, and F. S. Pavone, *J. Biophotonics* **8**, 347 (2015).
3. R. Kumar, K. M. Grønhaug, E. I. Romijn, A. Finnøy, C. L. Davies, J. O. Drogset, and M. B. Lilledahl, "Polarization second harmonic generation microscopy provides quantitative enhanced molecular specificity for tissue diagnostics," *J. Biophotonics*, doi: 10.1002/jbio.201400086 (to be published).
4. A. M. Raja, S. Xu, S. Zhuo, D. C. Tai, W. Sun, P. T. So, R. E. Welsch, C.-S. Chen, and H. Yu, "Differential remodeling of extracellular matrices by breast cancer initiating cells," *J. Biophotonics*, doi: 10.1002/jbio.201400079 (to be published).

2508 OPTICS LETTERS / Vol. 40, No. 11 / June 1, 2015

5. R. Cicchi, N. Vogler, D. Kapsokalyvas, B. Dietzek, J. Popp, and F. S. Pavone, *J. Biophotonics* **6**, 129 (2012).
6. F. Fischer, B. Volkmer, S. Puschmann, R. Greinert, W. Breitbart, J. Kiefer, and R. Wepf, *J. Biomed. Opt.* **13**, 041320 (2008).
7. M. Kobayashi, K. Fujita, T. Kaneko, T. Takamatsu, O. Nakamura, and S. Kawata, *Opt. Lett.* **27**, 1324 (2002).
8. N. Ji, J. C. Magee, and E. Betzig, *Nat. Methods* **5**, 197 (2008).
9. D. N. Fittinghoff, P. W. Wiseman, and J. A. Squier, *Opt. Express* **7**, 273 (2000).
10. V. Andresen, A. Egner, and S. W. Hell, *Opt. Lett.* **26**, 75 (2001).
11. J. Martini, V. Andresen, and D. Anselmetti, *J. Biomed. Opt.* **12**, 034010 (2007).
12. K. E. Sheetz, E. E. Hoover, R. Carriles, D. Kleinfeld, and J. A. Squier, *Opt. Express* **16**, 17574 (2008).
13. M. Baumgartl, T. Gottschall, J. Abreu-Afonso, A. Dez, T. Meyer, B. Dietzek, M. Rothhardt, J. Popp, J. Limpert, and A. Tünnermann, *Opt. Express* **20**, 21010 (2012).
14. T. Meyer, M. Baumgartl, T. Gottschall, T. Pascher, A. Wuttig, C. Matthäus, B. F. M. Romeike, B. R. Brehm, J. Limpert, A. Tünnermann, O. Guntinas-Lichius, B. Dietzek, M. Schmitt, and J. Popp, *Analyst* **138**, 4048 (2013).
15. J. W. Goodman, *Introduction to Fourier Optics* (Roberts & Company, 2005).
16. C. D. Kuglin and D. C. Hines, in *Proc. IEEE Conference on Cybernetics and Society* (IEEE, 1975), pp. 163–165.
17. J. Bewersdorf, A. Egner, and S. W. Hell, *Handbook of Biological Confocal Microscopy*, J. Pawley, ed. (2005), Chap. 29, pp. 550–560.
18. C. Jauregui, J. Limpert, and A. Tünnermann, *Nat. Photonics* **7**, 861 (2013).

6.5 Dual-focus coherent anti-Stokes Raman scattering microscopy using a compact two-beam fiber laser source

Documentation of Authorship

Fisseha Bekele Legesse	Acquisition and analysis of images, preparation of the manuscript
Tobias Meyer	Acquisition and analysis of images, Discussion of results
Sandro Heuke	Discussion of results
Thomas Gottschall	Setting up of laser source
Torbjörn Pascher	Reconfiguration of the electronics and software of the laser scanning microscope
Jens Limpert	Project coordination and supervision, discussion of results
Andreas Tünnermann	Project coordination and supervision, discussion of results
Michael Schmitt	Project coordination and supervision, discussion of results
Jürgen Popp	Project coordination and supervision, discussion of results

All authors revised, edited and proof read the final manuscript.
Reprinted with kind permission from the OSA publishing group.

[FBL5] F. B. Legesse, T. Meyer, S. Heuke, T. Gottschall, T. Pascher, J. Limpert, A. Tünnermann, M. Schmitt, and J. Popp, “Dual-focus coherent anti-Stokes Raman scattering microscopy using a compact two-beam fiber laser source,” *Optics letters* **42**, 183–186 (2017).

Author	Fisseha Bekele Legesse
Suggested equivalent of publications	1.0

Optics Letters

Dual-focus coherent anti-Stokes Raman scattering microscopy using a compact two-beam fiber laser source

FISSEHA BEKELE LEGESSE,^{1,2} TOBIAS MEYER,^{1,2} SANDRO HEUKE,^{1,2} THOMAS GOTTSCHALL,³
TORBJÖRN PASCHER,^{4,5} JENS LIMPERT,³ ANDREAS TÜNNERMANN,^{3,6} MICHAEL SCHMITT,¹ AND JÜRGEN POPP^{1,2,*}

¹Institute of Physical Chemistry and Abbe Center of Photonics, Friedrich-Schiller University Jena, Helmholtzweg 4, 07743 Jena, Germany

²Leibniz Institute of Photonic Technology (IPHT) Jena e.v., Albert-Einstein-Str. 9, 07745 Jena, Germany

³Institute of Applied Physics, Abbe Center of Photonics, Friedrich-Schiller University Jena, Albert-Einstein-Str. 15, 07745 Jena, Germany

⁴Pascher Instruments AB, Stora Rabybyväg 24, 22478 Lund, Sweden

⁵Department of Chemical Physics Lund University, Kemicentrum, Getingevägen 60, 22241 Lund, Sweden

⁶Fraunhofer Institute for Applied Optics and Precision Engineering, Albert-Einstein-Str. 7, 07745 Jena, Germany

*Corresponding author: juergen.popp@ipht-jena.de

Received 18 October 2016; revised 2 December 2016; accepted 6 December 2016; posted 7 December 2016 (Doc. ID 278345); published 6 January 2017

We have developed a dual-focus coherent anti-Stokes Raman scattering (CARS) microscope based on a dual output, compact fiber laser source. The underlying concepts of time-multiplexed, two-beam scanning and demultiplexed detection that we already employed for second-harmonic generation are here naturally extended for CARS microscopy. The layout of a robust, all-fiber laser source was re-configured to provide two outputs, each containing the two colors necessary for the CARS process. The utilization of the design for simultaneously imaging two laterally or axially separated fields of view and, thus, inherently speeding up the image acquisition process, is demonstrated on human artery tissue samples. © 2017 Optical Society of America

OCIS codes: (300.6230) Spectroscopy, coherent anti-Stokes Raman scattering; (060.2350) Fiber optics imaging; (170.3880) Medical and biological imaging; (060.3510) Lasers, fiber; (180.0180) Microscopy.

<https://doi.org/10.1364/OL.42.000183>

Coherent anti-Stokes Raman scattering (CARS) is a third-order, nonlinear Raman spectroscopic technique that provides a coherent, high-intensity signal [1,2]. The great benefit of CARS is its vibrational contrast mechanism which is similar to spontaneous Raman scattering, but is orders of magnitude stronger, thus leading to smaller image acquisition times [3]. After a significant development by the introduction of tight focusing to relax phase matching requirements, the technique was subsequently integrated into standard laser scanning microscopes that use fast galvo-scanners [4,5]. CARS microscopy has since then been increasingly employed to investigate cells and tissues in a label-free manner by providing a chemical contrast. Concurrently, diagnostically relevant information has been

extracted from CARS images of tissues, demonstrating its potential applicability for clinical purposes [6,7].

The bulk of the research employing CARS for biomedical purposes has been so far limited to case studies investigating a small number of tissue samples. In order to make the analysis of the images more robust, increase the validity of the results, and cope with inter-patient variance that is normally encountered with routine clinical diagnostics, a large volume of tissue samples has to be imaged within a reasonable time scale. In addition, imaging dynamic processes in cells and tissues requires high-speed acquisition [8]. Hence, increasing the image acquisition rate of CARS microscopes is crucial for such applications.

Both single and multi-focus approaches have been proposed to speed up the image acquisition rate of nonlinear microscopes in general. Single focus approaches increase the image acquisition rate by employing faster scanning methods. The reduction in pixel dwell times inherent with faster scanning necessitates the simultaneous increase of excitation powers to maintain decent signal-to-noise ratios (SNRs). Unfortunately, linear and nonlinear tissue damage pose a constraint on the amount of average and peak power that can be applied on the sample, respectively. With large excitation powers and spatial oversampling of the tissue area, faster scanning without giving the tissue enough cooling time between successive laser pulses also leads to linear tissue damage. Rapid scanning has been implemented with resonant galvo-scanners and polygon mirrors, both of which have drawbacks [9]. Resonant scanners can only be driven at a fixed speed in a sinusoidal pattern leading to position-dependent pixel dwell times for a constant pixel rate frame grabber. Polygonal mirrors, on the other hand, significantly complicate the optical design of the microscope and are prone to artefacts due to beam fluctuations.

The alternative route typically followed in multi-photon microscopy is to use a multi-focus setup. These methods essentially split a laser beam output into a number of beamlets,

usually using micro-lens arrays, which eventually form multiple, separated focal spots within the sample [8,10,11]. Large area detectors such as CCD cameras are then used to collectively detect the response from multiple spots at the same time. This detection scheme is prone to coherence artefacts due to the interference between the responses of different foci. This problem has been circumvented by using time multiplexing with point detection, wherein the pulses are temporally delayed from each other, e.g., using thick glass plates so that signals arriving at the detector are temporally de-multiplexed [12]. However, what still persists, especially when imaging in turbid media, is inter-focus crosstalk. In addition, these approaches are vulnerable to intensity inhomogeneities among the beamlets, and much of the laser light generated is wasted. Bulk laser source designs with multiple outputs mitigate some of these drawbacks, but have the issue of scaling up [13]. More importantly, multi-focal fiber laser sources that are compact, robust, and easy to use are needed in order to adapt CARS for routine clinical use. In this regard, NIR laser sources based on four-wave mixing of a fiber oscillator output inside a photonic crystal fiber (PCF), have been successfully employed for single-focus CARS imaging [14,15].

In our previous Letter, we reported dual-focus second-harmonic generation microscopy based on such fiber laser designs [16]. We demonstrated the feasibility of using a time-multiplexed, two-beam excitation and demultiplexed detection for speeding up the imaging acquisition by a factor of 2. In this followup Letter, we extended this basic approach to CARS microscopy. The CARS process generates a strong signal that is resonantly enhanced when the difference frequency of a pump (ω_p) and a Stokes (ω_s) excitation beam matches a certain Raman band within the sample being investigated. For this purpose, the layout of a previously reported fiber laser source was redesigned to provide two temporally delayed outputs, each having the required two colors [15].

To recapitulate the characteristics of the setup pertaining to the discussion here, the original fiber laser design is based on an amplified ytterbium fiber oscillator, generating 1032 nm pulses with a duration of 40 ps, spliced into a PCF fiber after being amplified in two steps. A low repetition rate and ps duration pulses were chosen to compromise the resulting spectral resolution, nonlinear artefacts, and fiber integration ease with the

duty cycle necessary for nonlinear imaging. Optical parametric generation by degenerate four-wave mixing inside the PCF provides a synchronized second signal output at 797 nm that is inherently overlapped with the fundamental output temporally and spatially. The PCF fiber is chosen so that the frequency difference of the fundamental and the signal corresponds to the CH_2 stretching vibration at 2850 cm^{-1} .

The schematic of the modified fiber laser design is depicted in Fig. 1. In the current configuration, the pre-amplified output from the fiber oscillator is split in two before optical parametric generation. One part is delayed by half the repetition rate of the oscillator using a 100 m single-mode fiber in line with the all-single-mode fiber design of the laser. Each part is then further amplified and spliced into a PCF to generate a signal at 797 nm with 25 ps pulse duration, using four-wave mixing. Integrating the optical components for temporal multiplexing into the source itself, as compared to our previous implementation, greatly simplifies the whole scheme and makes it more robust and compact. In addition to stabilization of the outputs, the in-built splitting and splicing into a single-mode fiber reduces in-coupling losses.

Figure 2 shows how the two outputs of the source are then collimated using acromatic doublets on to the scanning mirrors of an in-house built laser scanning microscope, the specific description of which can be found elsewhere [17]. Separating the incident angles of the beams on the galvo-scanners by adjusting the in-coupling mirrors ensures the lateral separation of the laser foci on the sample. The two beams are then focused onto the back focal plane of a 0.4 NA, 20 \times objective (*M* Plan Apo NIR 20 \times , Mitutoyo) using a tube and a scan lens. At the focal plane of the objective, each beam has an average power of 25 mW. The microscope is configured for F-CARS imaging with a series of detection filters (Short Pass 750, Semrock and Bandpass 650/40 Thorlabs) for separating the signal from the excitation lasers. The generated CARS signal is ultimately detected by a photomultiplier tube (PMT) [H10721-20, Hamamatsu]. Temporal de-multiplexing is achieved by feeding the 80 ns long voltage pulse outputs of the fiber laser internal photodiode to a delay generator (9520 Digital Delay Pulse Generator, Quantum Composers) for generating the pulses that gate the PMT readout.

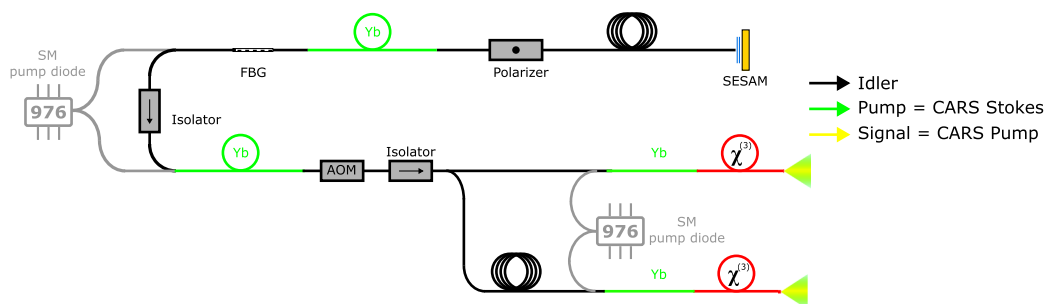


Fig. 1. Schematic for a dual output fiber laser. The basic oscillator consists of a semi-conductor saturable absorber mirror at one end and a fiber Bragg grating at the other. After pre-amplification and a reduction of the pulse repetition rate by an acousto-optical modulator, the oscillator output at 1032 nm is split into two paths. Time multiplexing is performed by fiber delaying one arm of the oscillator output. The ytterbium fundamental is further amplified, and a second color is generated using four-wave mixing in a piece of PCF. (This schematic is a modified version of the layout presented in [14].)

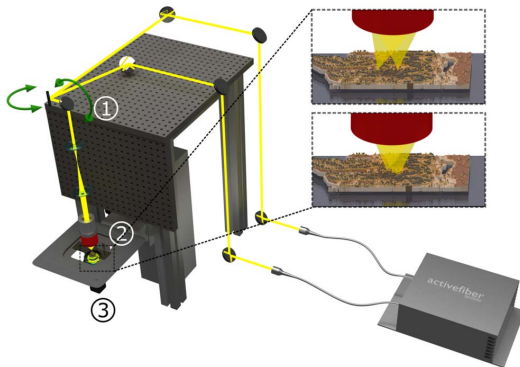


Fig. 2. Experimental setup for using the dual output laser source with the laser scanning microscope. The two outputs of the laser are guided by mirrors onto the galvo-scanners (1) of the microscope which directs the beams through a tube and scan lens onto the back plane of a focusing objective lens (2). The generated CARS signal is forward-detected by a photomultiplier tube (3).

The imaging capabilities of the whole system are demonstrated on a 20 μm thick cryosection of human perivascular tissue surrounding an artery obtained from a routine biopsy (with permission from the ethics committee for human research, from the Medical Faculty, Friedrich-Schiller-University Jena, Germany). A CARS signal generated at the sample surface could be detected after transmission through the tissue as thick as 1 mm. However, the generation of a signal at depths exceeding 200 μm would require higher excitation powers. Alternatively, for thick cryosections and bulk tissue samples, a backward detection path can be used by placing a dichroic (Beam splitter 775, Semrock) to separate the epi-directed signal from the incident radiation. In the corresponding resonant, CARS images of the lipid content of the tissue give a strong contrast due to the CH_2 stretching vibration it abundantly contains.

Figures 3(a) and 3(b) show a sample result wherein two laterally displaced in-focus CARS images of the tissue are acquired with the set-up. The fields of view of these particular images are horizontally overlapping. The custom-built acquisition software allows simultaneous viewing of the two images so that the alignment can be carried out by using the overlapping region as a reference. Each image has a resolution of 2048×2048 pixels and, with the averaging of $4\times$ chosen to improve the SNR, the total image acquisition time totals 16 s. This corresponds to a pixel dwell time of $\approx 2 \mu\text{s}$ which, in essence, equates to a doubling in image acquisition speed, compared to single-beam CARS microscopy with the same beam repetition rate and equal power at the sample.

Similarly, two focal planes can be simultaneously imaged with this approach, thereby splitting the field of view in the lateral direction, by changing the depth of focus of the beams independently. This is made possible by adjusting the distance between fiber ends and the collimating acromats so that the divergence of the two beams is different. Figure 3(c) shows an in-focus CARS image from one beam, and Fig. 3(d) depicts an image from the second beam whose focus is placed at the

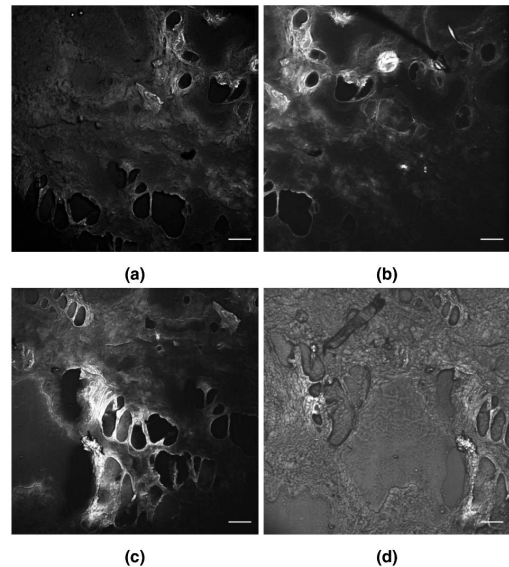


Fig. 3. Dual-focus CARS microscopy of human artery tissue showing the imaging capabilities of the setup. (a) and (b) show two laterally displaced fields of view acquired simultaneously. (c) and (d) show two axially shifted images with one being out of focus. Scale bars: 50 μm .

border between the thin tissue slice and the sample holder made of quartz glass.

The excitation parameters used for the two beam paths are similar to each other and to the basic single focus implementation. Consequently, the quality and contrast of the images acquired are comparable, and there is no apparent linear or nonlinear tissue damage observed in the images. The temporal multiplexing and demultiplexing ensured that there is no interference or crosstalk between the responses of the two foci.

In conclusion, we have developed an all-fiber, alignment-free dual output source for CARS microscopy and demonstrated its use for faster acquisition by splitting the field of view between the two foci. This is, to the best of our knowledge, the first working and scalable dual-focus CARS setup that does not require a microlens array scanner. The setup can be used to acquire other nonlinear imaging modalities as well by just changing the combination of detection filters and is a promising approach for faster image acquisition using turnkey, compact source designs. Scaling up the current approach to a larger number of foci could be accomplished by further adding similar extensions of varying delay the fiber length within the source. The number of foci to be accommodated can theoretically be increased until the time slice between two consecutive pulses approaches the temporal resolution of the detector. However, the mere use of mirrors to in-couple multiple beams on the small area scanners of the microscope objective is practically challenging and not feasible. In this regard, the design of dedicated multi-focal scanning optics as proposed by Sheetz *et al.* might be required [13]. The improvement of image acquisition rates is particularly pertinent for applications that use nonlinear multi-modal imaging for pathological

diagnosis, as it would facilitate the adaptation of the technique for clinical use. Another way to exploit this approach is to improve the SNR of the obtained images by simultaneously increasing the pixel dwell time while maintaining the total image acquisition time similar to the single focus case [8]. The configuration also presents a way to accommodate different nonlinear modalities, such as epi-CARS, without the need for adding other detection modules.

Funding. Carl-Zeiss-Stiftung; Bundesministerium für Bildung und Forschung (BMBF) (13N13805).

REFERENCES

1. J.-X. Cheng, A. Volkmer, and X. S. Xie, *J. Opt. Soc. Am. B* **19**, 1363 (2002).
2. C. L. Evans and X. S. Xie, *Annu. Rev. Anal. Chem.* **1**, 883 (2008).
3. M. D. Duncan, J. Reintjes, and T. Manuccia, *Opt. Lett.* **7**, 350 (1982).
4. A. Zumbusch, G. R. Holtom, and X. S. Xie, *Phys. Rev. Lett.* **82**, 4142 (1999).
5. J.-X. Cheng, Y. K. Jia, G. Zheng, and X. S. Xie, *Biophys. J.* **83**, 502 (2002).
6. T. Meyer, O. Guntinas-Lichius, F. von Eggeling, G. Ernst, D. Akimov, M. Schmitt, B. Dietzek, and J. Popp, *Head Neck* **35**, E280 (2013).
7. S. Heuke, N. Vogler, T. Meyer, D. Akimov, F. Kluschke, H.-J. Röwert-Huber, J. Lademann, B. Dietzek, and J. Popp, *Healthcare* **1**, 64 (2013).
8. T. Minamikawa, M. Hashimoto, K. Fujita, S. Kawata, and T. Araki, *Opt. Express* **17**, 9526 (2009).
9. C. Evans, E. Potma, M. Puoris' haag, D. Côté, C. Lin, and X. Xie, *Proc. Natl. Acad. Sci. USA* **102**, 16807 (2005).
10. J. Bewersdorf, R. Pick, and S. W. Hell, *Opt. Lett.* **23**, 655 (1998).
11. A. Buist, M. Muller, J. Squier, and G. Brakenhoff, *J. Microsc.* **192**, 217 (1998).
12. V. Andresen, A. Egner, and S. W. Hell, *Opt. Lett.* **26**, 75 (2001).
13. K. E. Sheetz, E. E. Hoover, R. Carriles, D. Kleinfeld, and J. A. Squier, *Opt. Express* **16**, 17574 (2008).
14. M. Baumgartl, T. Gottschall, J. Abreu-Afonso, A. Diez, T. Meyer, B. Dietzek, M. Rothhardt, J. Popp, J. Limpert, and A. Tünnermann, *Opt. Express* **20**, 21010 (2012).
15. T. Gottschall, M. Baumgartl, A. Sagnier, J. Rothhardt, C. Jauregui, J. Limpert, and A. Tünnermann, *Opt. Express* **20**, 12004 (2012).
16. S. Heuke, F. B. Legesse, A. Lorenz, T. Pascher, D. Akimov, M. Jäger, M. Schmitt, and J. Popp, *Opt. Lett.* **40**, 2505 (2015).
17. T. Meyer, M. Baumgartl, T. Gottschall, T. Pascher, A. Wuttig, C. Matthäus, B. F. Romeike, B. R. Brehm, J. Limpert, A. Tünnermann, O. Guntinas-Lichius, B. Dietzek, M. Schmitt, and J. Popp, *Analyst* **138**, 4048 (2013).

6.6 Bessel beam coherent anti-Stokes Raman scattering microscopy

Documentation of Authorship

Sandro Heuke*	Design of concept, implementation of Bessel beams into the CARS microscope, numerical calculations, preparation of the manuscript
Fisseha Bekele Legesse*	Acquisition of CARS images
Denis Akimov	Discussion of results
Uwe Hübner	Structuring of polymer test samples
Jan Dellith	Acquisition of scanning electron microscopy images
Michael Schmitt	Project coordination and supervision, discussion of results
Jürgen Popp	Project coordination and supervision, discussion of results

All authors revised, edited and proof read the final manuscript.

*Both authors share first authorship of this manuscript.

Reprinted with kind permission from the OSA publishing group.

[FBL6] S. Heuke, F. B. Legesse, D. Akimov, U. Hübner, J. Dellith, M. Schmitt, and J. Popp, “Bessel beam coherent anti-Stokes Raman scattering microscopy,” *JOSA B* **32**, 1773–1779 (2015).

Author	S. Heuke	Fisseha Bekele Legesse
Suggested equivalent of publications	1.0	1.0

Bessel beam coherent anti-Stokes Raman scattering microscopy

SANDRO HEUKE,^{1,†} FISSEHA BEKELE LEGESSE,^{1,†} DENIS AKIMOV,¹ UWE HÜBNER,¹ JAN DELLITH,¹ MICHAEL SCHMITT,^{1,2} AND JÜRGEN POPP^{1,2,*}

¹Leibniz Institute of Photonic Technology Jena (IPHT), Albert-Einstein-Straße 9, 07745 Jena, Germany

²Institute of Physical Chemistry and Abbe Center of Photonics, Friedrich-Schiller-University Jena, Helmholtzweg 4, 07743 Jena, Germany

*Corresponding author: Juergen.Popp@ipht-jena.de

Received 26 May 2015; accepted 26 June 2015; posted 7 July 2015 (Doc. ID 241823); published 3 August 2015

We report about laser scanning coherent anti-Stokes Raman scattering (CARS) microscopy using a Bessel beam to enhance the lateral resolution. This study covers a numerical investigation that predicts an improvement in the lateral resolution by a factor of up to 1.33, while the axial depth of view increases up to a factor of 2 for an ideal Bessel beam serving as both a pump and a probe. Further, we present a simple experimental implementation of a Bessel-like beam by adding only two axicons and a telescope to a conventional CARS laser scanning microscopy setup. The predicted resolution improvement is demonstrated for well-scattering, structured polymer samples. © 2015 Optical Society of America

OCIS codes: (180.4315) Nonlinear microscopy; (300.6230) Spectroscopy, coherent anti-Stokes Raman scattering; (350.4600) Optical engineering.

<http://dx.doi.org/10.1364/JOSAB.32.001773>

1. INTRODUCTION

In 1982, Duncan *et al.* added a high-magnifying lens to a folded-box illumination geometry utilized in coherent anti-Stokes Raman scattering (CARS) spectroscopy to obtain the first laser scanning microscopic CARS image of deuterated water in onion cells [1]. Seventeen years later, Zumbusch *et al.* noticed that, under tight-focusing conditions, phase-matching is widely relaxed, allowing for the use of collinear Gaussian beams for an efficient generation of anti-Stokes radiation [2]. Ever since, the plane-phase collinear illumination geometry has been applied mostly in CARS microscopy because of its simplicity with only a few exceptions, such as wide-field configurations [3,4]. Over the past 10 years, however, it has been increasingly recognized that the relaxed phase-matching condition permits the implementation of alternative excitation beam profiles. Since then, spatially resolved multi- or single-resonance CARS spectroscopy has been developed to an elaborated microscopy technique yielding valuable microstructural information in a label-free manner [5–11]. In particular, phase shaping of the excitation profile, known as focus engineering [8], received considerable attention for its ability to increase the sensitivity of CARS microscopy to interfaces [7,9] and to enhance the overall spatial resolution [10,11]. Similarly, amplitude shaping was performed for the anti-Stokes emission path using an annular mask to suppress low spatial frequency components [12]. Shaping of the excitation profile, however, was neglected until today, which may be attributed to critical

power losses because of, e.g., annular aperture discarding the majority of the Gaussian beam profile of low peak power ps-lasers. Here, we present an amplitude shaping approach using two axicons for lossless generation of a hollow beam [13]. The obtained thin laser ring yields a Bessel-like beam profile near the nominal focal plane. In a multiplicative focal volume approach, the Stokes beam is used as a conventional Gaussian beam overfilling the objective's back aperture to truncate the effective anti-Stokes scattering source, i.e., the anti-Stokes polarization that is predefined by the Bessel-like profile of the pump and probe beam. As a consequence, the lateral resolution is enhanced, while the axial resolution drops for the Bessel illumination as compared to the conventional Gaussian illumination scheme.

The subsequent part of the paper is organized as follows. First, results from numerical simulations based on the Debye integral and Green's function are summarized. Second, the experimental setup is presented, and the Bessel beam CARS microscopy images of polymer samples are discussed.

2. ANALYTICAL AND NUMERICAL CALCULATIONS

For the experimental realization of conventional laser scanning CARS microscopy, a narrow Gaussian beam is magnified by a tube and scan lens to overfill the back aperture of high NA objective lenses [14]. Here, an increase of the misalignment

insensitivity and an improvement of spatial resolution have to be balanced against power losses for extending this overfilling. For the following comparison with the Bessel illumination, we consider the best spatial resolution that is achieved by utilizing a plane-phase Gaussian beam profile, i.e., the infinite overfilling of the objective's back aperture. In scalar approximation, the lateral intensity profile near the nominal focal plane is described by the Airy disc, which is given by $I = I_0 \cdot [2J_1(ka \sin \alpha) / (ka \sin \alpha)]^2$, where $k = 2\pi/\lambda$ is the magnitude of the wave vector, a denotes the radius of the aperture, α is the angle of observation with respect to the optical axis and J_m , and $m = 0, 1, 2$ is the m th-order Bessel function. Compared to the best Gaussian illumination, the lateral intensity profile of an ideal Bessel beam is characterized by a zeroth-order Bessel function, i.e., $I = I_0 \cdot [J_0(ka \sin \alpha)]^2$. Figure 1(a) shows that the Bessel beam displays a narrower central lobe than the Airy disc. For linear microscopy, the side lobes of the Bessel illumination lead to a reduction in spatial resolution, unless they are filtered out, e.g., by truncation of the image that is acquired perpendicular to the excitation direction [15]. In nonlinear microscopy, artifacts arising from the side lobes are readily removed by utilizing the multiplicative nature of the CARS process. Here, inspired by the principle of stimulated emission depletion (STED) [16], we use the Bessel beam as a pump and probe beam, while for the Stokes beam, we still use a Gaussian beam overfilling the back aperture of the objective. As a result, the squared absolute value of the anti-Stokes polarization, which can be regarded as the effective source of radiation, $\|P_{as}^{(3)}\|^2 \propto I_p^2 I_S$, is narrowed by a factor of 1.33 as compared to an overfilling of the back aperture (see Fig. 1(b)).

The generation of an ideal Bessel beam would require an infinite amount of energy and, therefore, is not possible. In practice, a beam profile with reasonably similar properties to a Bessel beam can be obtained by focusing a thin laser ring using, e.g., an annular aperture in the excitation path [17]. For visualization, the x -polarized, complex amplitude distributions of the pump and Stokes beams near the nominal focus were calculated employing the Debye integral (see Appendix A), assuming an excitation wavelength of 797 and

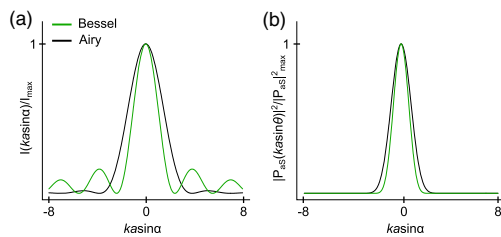


Fig. 1. Lateral intensity profiles of the illumination and anti-Stokes polarization near the nominal focus. (a) Lateral intensity profile for the best conventional Gaussian illumination (Airy, black) and Bessel illumination (green). (b) Lateral intensity profile of the anti-Stokes polarization generated by the conventional illumination (black) or a Bessel beam used as pump and probe, in combination with a Gaussian beam serving as Stokes (green). For simplicity, the wavelengths of the pump and Stokes beams were assumed to be equal.

1032 nm, respectively. For modeling the pump Bessel beam, the incident angles were restricted between $\theta_{p,min} = 39^\circ$ and $\theta_{p,max} = 48^\circ$, while the incident angle for the Stokes Gaussian beam was set to a range between $\theta_{s,min} = 0^\circ$ and $\theta_{s,max} = 48^\circ$, corresponding to a numerical aperture (NA) of 0.75 (air immersion). Figure 2 displays the focal intensity plots of the pump, Stokes, and anti-Stokes polarization for Bessel and best Gaussian beam illumination. Figure 2 clearly highlights that the anti-Stokes polarization under Bessel illumination is axially more elongated and laterally slimmer than under Gaussian illumination. Figure 3 provides a scheme about the reshaping of the anti-Stokes polarization, as well as the reduction of the peak power of the pump beam as a function of the minimum incident angle of the pump beam $\theta_{p,min}$. Note that the experimentally accessible ratio of the laser ring width d and laser ring diameter D is related to the incident angles via $(\sin \theta_{p,max} - \sin \theta_{p,min}) / (2 \sin \theta_{p,max}) = d/D$; see also Fig. 7.

For $\theta_{p,min} \rightarrow \theta_{p,max}$, the lateral full width at half-maximum (FWHM) of the squared absolute value of anti-Stokes polarization drops by a factor of 1.33, while the axial FWHM increases by a factor of 2. In reality, $\theta_{p,min}/\theta_{p,max} = 1$ ($d = 0$) transfers no light toward the focus and, therefore, yields no CARS signal, but a ratio of $\theta_{p,min}/\theta_{p,max} = 0.8$ is readily achieved using the experimental configuration presented in the following section. Thus, a lateral resolution enhancement

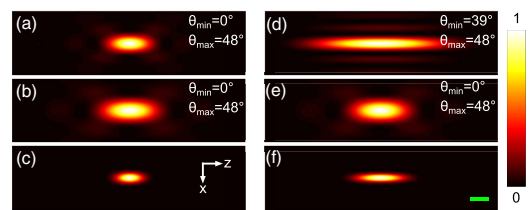


Fig. 2. Intensity plots of (a), (d) pump and (b), (e) Stokes beams, as well as (c), (f) anti-Stokes polarization near the nominal focus in the xz plane for (a)–(c) best Gaussian illumination and (d)–(f) Bessel illumination. Note that the intensity distribution of the anti-Stokes polarization for Bessel illumination is elongated in the axial direction, but narrowed in the lateral direction, as compared to its counterpart for the Gaussian illumination. The green bar equals 1 μm .

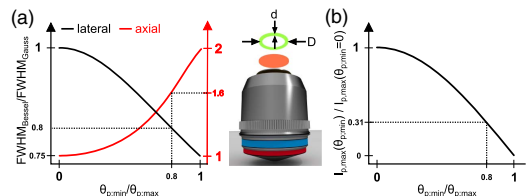


Fig. 3. Change in resolution and reduction of peak power as a function of the ratio $\theta_{p,min}/\theta_{p,max}$. (a) The plot shows the ratio of the FWHM of the intensity distributions of the anti-Stokes polarization displayed in Figs. 2(c) and 2(e). (b) The intensity drop of the pump beam is plotted as a function of the minimum incident angle $\theta_{p,min}$, assuming equal incident power at the objective's back aperture.

beyond the best Gaussian illumination by a factor of 1.25 is considered here to be realistic for the applied laser scanning CARS experiment utilizing Bessel beams. To determine the best signal collection geometry and to estimate the strength of the overall observed anti-Stokes radiation, we calculated the radiation pattern for various excitation and sample geometries (see Appendix A for details of the numerical implementation). Figures 4(a) and 4(b) compare the radiation patterns of a homogeneous sample under Gaussian and Bessel illumination, respectively.

The transparent dark cones in Fig. 4 indicate the maximum excitation angle at $\theta_{\max} = 48^\circ$ as a reference. As is evident from Fig. 4(a), the anti-Stokes radiation of a homogeneous sample under Gaussian illumination is mostly forward directed. In contrast, the strongest radiation under Bessel illumination is observed for higher angles than the largest excitation angle. As a consequence, it is beneficial for the collection efficiency to use optics with larger NA in a forward direction to collect the light than was used for excitation. For calculation, the incident power on the back focal plane of the objective lens was normalized. With the same total power at the sample, anti-Stokes generation under Gaussian illumination is about 21 fold more efficient than under Bessel illumination which has to be attributed partially to peak power reduction of the pump, as visualized in Fig. 3(b). Furthermore, the difference in the radiation pattern between Gaussian and Bessel illumination will have an impact on the image contrast obtained. It is well known that small scattering objects display a scattering pattern that is less directed. If the NAs of the excitation and collection objective lenses are similar, a higher signal of small objects is collected under Bessel illumination, while a lower signal is obtained under Gaussian illumination, as is evident from Figs. 4(c) and 4(d), where the radiation patterns of spheres with a radius of 400 nm are presented. Consequently, structures with high spatial frequency components, such as edges, will be

pronounced in Bessel illumination, if a suitable collection geometry is selected. Note that a similar conclusion was drawn for CARS microscopy using Laguerre–Gaussian beams [7].

3. EXPERIMENTAL SETUP

The experimental setup is based on a fiber laser [18] and a homebuilt laser scanning microscope that was presented elsewhere [19]. A schematic of the experimental configuration is depicted in Fig. 5. The fiber laser generates two collinear propagating colors at a repetition rate of 1 MHz. Serving as a Stokes beam, 90 mW of average power at 1032 nm (± 0.8 nm FWHM) is generated with a temporal pulsewidth of 75 ps (FWHM). A 9 mW pump beam is generated at 797 nm (± 3 nm FWHM) and 20 ps (FWHM). The energy difference between 1032 and 797 nm corresponds to the CH_2 -stretching vibration at 2850 cm^{-1} .

The pump beam is reshaped to a hollow beam of narrow width by means of two axicons (1-APX-2-G254, Altechna; X50-200 FPX, Asphericon) and further reduced in size by a Keplerian telescope (ACA254-030-B and AC508-150-B-ML; Thorlabs). Both beams, i.e., pump and Stokes, are temporally and spatially overlapped and scanned via a tube and scan lens (MPM-SL, Thorlabs), as well as the objective lens (CFI Plan Apo Lambda 20X, Nikon) over the sample. The combined average power of the pump and Stokes beams at the sample did not exceed 15 mW. Anti-Stokes radiation is collected in a forward direction by a 25 \times water immersion objective lens (CFI Apo LWD 25XW, Nikon). It shall be noted that Bessel beams are sensitive to aberrations and misalignment [20]. Thus, the quality of the laser ring generation and, therefore, of the Bessel beam formation was evaluated and adjusted by

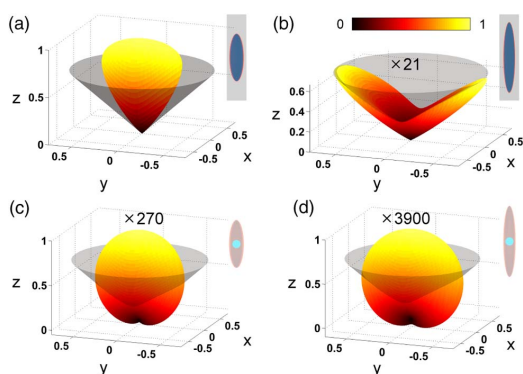


Fig. 4. Far-field anti-Stokes radiation pattern. (a) and (c) display the radiation pattern under Gaussian illumination. (b) and (d) show the corresponding radiation pattern under Bessel illumination. For (a) and (b), a homogeneous sample was assumed, while, for (c) and (d), spherical samples of a diameter of 400 nm were considered. The transparent dark cones indicate the maximum incident angle of $\theta_{\max} = 48^\circ$. The images were normalized to the maximum intensity of (a).

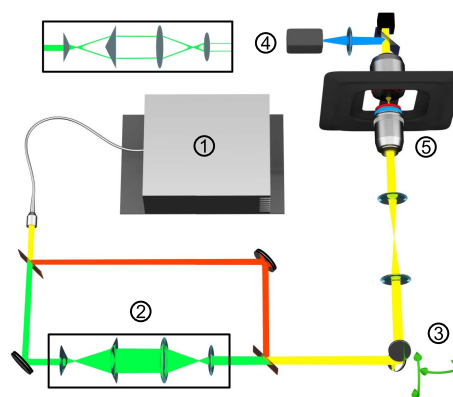


Fig. 5. Experimental setup: a fiber laser generates the pump and Stokes beams at 797 and 1032 nm, respectively. The pump beam is separated from the Stokes beam using a dichromatic beamsplitter and is reshaped into a narrow hollow beam by two axicons, in combination with a Keplerian telescope. Pump and Stokes beams are recombined and scanned over the sample by Galvo scanners. CARS radiation is collected in a forward direction and detected by a photomultiplier tube (PMT). 1, fiber laser; 2, two axicons and telescope creating a hollow beam; 3, scanning mirrors; 4, PMT; 5, objective lenses, sample and translational stage.

replacing both objective lenses with a single weak lens (AC254-200-B-ML, Thorlabs). The weakly focused Bessel beam is monitored by a camera (DCC1645C, Thorlabs) that is placed at the back focal plane. For demonstration purposes, we used microstructured test samples, namely, polyethylene (PE) beads (Cospheric LLC, USA) or cyclic olefin copolymer (COC). The microstructured COC samples were produced in-house by electron beam lithography and plasma etching. CARS images of a size of 4096×4096 pixels were acquired with a dwell time of $4 \mu\text{s}$ per pixel, averaging over four laser shots.

4. EXPERIMENTAL RESULTS AND DISCUSSION

For demonstration of the expected properties of Bessel beams, Fig. 6 presents CARS images of polymer samples. Figures 6(a) and 6(b) display PE beads under conventional Gaussian and Bessel illumination. The blue boxes magnify three PE beads, highlighting the change of the lateral resolution. In Fig. 6(c), the intensity profile outlined by the green dashed lines in Figs. 6(a) and 6(b) is shown. The black curve corresponds to the Bessel illumination, while the blue curve shows the intensity profile for Gaussian illumination. The black curve indicates a better separation of the two beads under Bessel illumination than under Gaussian illumination. Our laser scanners introduce a jitter that depends on the scanning speed and size of the area selected. This jitter displaces individual image lines in a sweep direction by up to 200 nm for the blue boxes shown in Figs. 6(a) and 6(b), thereby putting a constraint on the ability to quantify the resolution improvement. This problem can be overcome by using laser scanners with better precision and reproducibility. To mitigate the effect of the jitter (i.e., the artifact), we have selected for quantification 30 corresponding lines for all three beads and each illumination type. Each profile

was fitted by a Gaussian function. On average, the FWHM of each bead under Bessel illumination is 82 nm smaller than under Gaussian illumination. For the Gaussian illumination experiment, we used a gentle overfilling of the objective's back aperture for the pump and Stokes beams corresponding to the filling factors of $f_0 = 0.88$ (20% truncation of the beam) and $f_0 = 0.96$ (40% truncation of the beam); see Appendix A for the implementation and definition of the filling factor.

The corresponding numerically calculated FWHM of the anti-Stokes polarization in a lateral direction is $\text{FWHM}_{P_{as}}^{\text{Gauss}} = 587 \text{ nm}$. For the Bessel illumination, we assumed an overfilling factor of $f_0 = \infty$ and $f_0 = 0.96$ for the pump and Stokes beams, respectively, resulting in an FWHM of the anti-Stokes polarization of $\text{FWHM}_{P_{as}}^{\text{Bessel}} = 416 \text{ nm}$. For simplicity, we assumed here that the sample scatter profile $N(\mathbf{r})$, as well as the amplitude of the anti-Stokes polarization $P_{as}(\mathbf{r})$, can be approximated by a Gaussian function. Further, we assume a negligible nonresonant background and relaxed phase-matching so that the observed anti-Stokes intensity scales quadratically with the number of coherently oscillating scatterers. The size of each PE bead in the laser scanning CARS image is given by the square of the convolution (*) of the anti-Stokes polarization with the sample profile $I_{as} = \|P_{as} * N\|^2$. The corresponding FWHM of the PE bead in the CARS image can be calculated by $(\sqrt{2} \cdot \text{FWHM}_{I_{as}})^2 = \text{FWHM}_N^2 + \text{FWHM}_{P_{as}}^2$. For a bead size of $\text{FWHM}_N = 500 \text{ nm}$, corresponding well to the size of the beads investigated, the difference of the image bead sizes $\text{FWHM}_{I_{as}}^{\text{Bessel}} - \text{FWHM}_{I_{as}}^{\text{Gauss}} = 85 \text{ nm}$ agrees nicely with the experimentally observed difference of 82 nm . Thus, the theoretical prediction of a lateral resolution enhancement of a Bessel beam CARS illumination geometry has been experimentally confirmed. Note that edge or point-like samples will benefit more from the resolution enhancement because of a negligible size of FWHM_N .

Figures 6(d) and 6(e) compare a microstructured COC sample under Bessel and Gaussian illumination, respectively. As a reference, Fig. 6(f) displays a scanning electron microscopy (SEM) image of a similar area revealing the sample to be composed of variously bent columns of approximately $1 \mu\text{m}$ in width and $3 \mu\text{m}$ in height. The columns in Fig. 6(d) appear narrower and sharper than those in Fig. 6(e)—compare structures in the dotted green boxes—providing further evidence for the lateral resolution enhancement under Bessel illumination, as well as modification of the image contrast under Bessel illumination, which favors higher spatial sample frequencies; see Figs. 4(c) and 4(d), as well as the corresponding discussion. Furthermore, Figs. 6(d) and 6(e) provide evidence for the elongation of the anti-Stokes polarization, as outlined exemplarily by dotted yellow boxes. Apparently, some columns appear dark under Gaussian illumination, but still appear bright under Bessel illumination; this may be attributed to the difference in height of the COC columns. Thus, the reduced axial resolution for the Bessel illumination can be exploited as an extension of the depth of view for suitable applications.

Finally, it shall be noted that there are advantages that have not been discussed yet, making the implementation of CARS microscopy with Bessel beams even more attractive. Because of

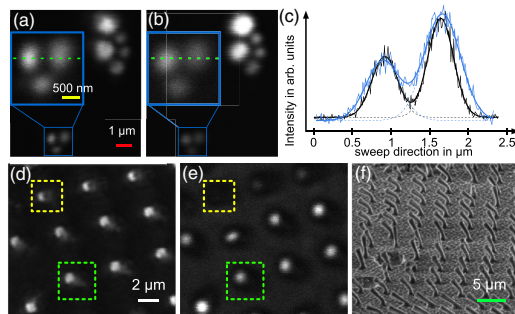


Fig. 6. Experimental results: (a) and (b) display Bessel and Gaussian illuminated CARS images of PE beads, respectively. The plot in (c) compares the lateral intensity profiles in a laser scanner sweep direction indicated by dashed green lines in (a) and (b). The blue and the black curves in (c) correspond to the Gaussian and Bessel illumination, respectively. Dashed lines delineate the results of Gaussian fitting. (d) and (e) show CARS images under Bessel and Gaussian illumination of a structured cyclic olefin copolymer (COC) sample, respectively. A secondary electron micrograph (SEM) image of the corresponding area is displayed in (f). The surface of the sample was tilted by 60° with respect to the incident electrons. The yellow, red, white, and green scale bars equal 500 nm , $1 \mu\text{m}$, $2 \mu\text{m}$, and $5 \mu\text{m}$, respectively.

an elongation of the excitation profile, the overlap of the pump and Stokes beams will be guaranteed, even in the presence of strong chromatic aberrations. Thus, a reduction of the anti-Stokes generation because of the mismatch of axial focus positions for different colors while varying the imaging depth will become less pronounced. Furthermore, Bessel beams are also expected to maintain the lateral resolution for higher penetration depths. For investigations at high penetration depths, the optical path length increases with the illumination angle θ . Consequently, on-axis rays are less attenuated by scattering and absorption than off-axis rays, leading to a reduction of the effective NA of the objective lens [21]. Since the optical path length for all illumination angles θ under Bessel illumination displays only a minimal variation, the reduction of resolution with increasing penetration depth is minimized.

5. CONCLUSION

We compared laser scanning CARS microscopy under the conventional Gaussian scheme with a Bessel illumination scheme. Analytically, it was found that an ideal Bessel beam yields a 1.33 fold lateral resolution enhancement for point-like or edge objects over a homogeneous illumination of the objective lens's back aperture. This expectation was confirmed numerically, assuming a homogeneous hollow laser ring entering the back aperture of an objective lens. Furthermore, the Bessel illumination favors sample structures with high spatial frequencies if the NA of excitation and collection is matched. For the lossless generation of a hollow laser beam, two axicons were implemented into the pump beam path of a laser scanning microscope. The resolution enhancement was demonstrated, qualitatively investigating polymer samples. In summary, we found that the combination of the nonlinearity of the CARS process and the Bessel illumination yields an easy-to-implement, intrinsically confocal microscopy technique providing a lateral resolution beyond the diffraction limit that may also serve as an extension of the depth of view. The results presented apply to all multicolor nonlinear microscopy techniques, such as sum frequency generation microscopy or dual-color, two-photon excited fluorescence.

APPENDIX A: NUMERICAL CALCULATIONS

The Debye integral is given by [22]

$$E_{p/S_x}(\rho, \phi, z) = \frac{ikf}{2} \exp(-ikf) [I_{00} + I_{02} \cos(2\phi)], \quad (\text{A1})$$

where f is the focal length of the objective lens and $\mathbf{r}(\rho, \phi, z)$ points toward the excitation position of the back focal plane in cylindrical coordinates; see also Fig. 7. I_{0m} is given by

$$I_{0m} = \int_{\theta_{\min}}^{\theta_{\max}} f_w(\theta) E_0 \sin(\theta) [\cos(\theta)]^{1/2} g_m(\theta)_{\text{m}} [k\rho \sin(\theta)] d\theta. \quad (\text{A2})$$

Here, g_m denotes $1 + \cos(\theta)$, $\sin(\theta)$, and $1 - \cos(\theta)$ for $m = 0, 1, 2$, respectively, and E_0 is a constant amplitude factor of the incoming x -polarized electrical field. θ_{\max} and θ_{\min} are the maximum and minimum incident angles of the focused laser at the sample, respectively. The ratio $(\sin \theta_{\max} - \sin \theta_{\min}) / (2 \sin \theta_{\max}) = d/D$ characterizes our Bessel geometry. d and

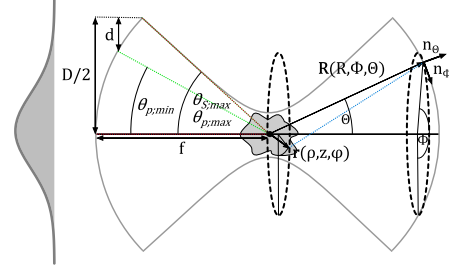


Fig. 7. Depiction of the parameters used for the numerical calculations.

D correspond to the ring width and ring diameter of the hollow laser beam, respectively; see also Fig. 3. $f_w(\theta)$ is given by

$$f_w(\theta) = \exp\left(-\frac{\sin^2 \theta}{f_0^2 \sin^2 \theta_{\max}}\right), \quad (\text{A3})$$

where f_0 is the filling factor of the objective lens's back aperture. Unless otherwise stated, f_0 was set to ∞ . The anti-Stokes polarization of an isotropic sample is given by [23]

$$P_{a_s}^{(3)}(\mathbf{r}) = 3\chi_{xxxx}^{(3)}(\mathbf{r}) E_{p_x}^2 E_{s_x}^*, \quad (\text{A4})$$

where χ_{xxxx} is the anti-Stokes susceptibility. Note that, even for high NA objective lenses with a $\theta_{\max} \leq 60^\circ$ electrical field, components polarized along the y and z axes can be neglected for the anti-Stokes generation because of the nonlinearity of the CARS process. Verification of this statement is provided in the following section.

The far-field anti-Stokes radiation is given by

$$\begin{aligned} \begin{bmatrix} E_{a_s, \Theta}(R, \Theta, \Phi) \\ E_{a_s, \Phi}(R, \Theta, \Phi) \end{bmatrix} &= -\frac{\omega_{a_s}^2 \exp(ik_{a_s} R)}{c^2 |R|} \\ &\times \iiint_{-\infty}^{\infty} \rho d\rho d\phi dz \frac{\exp(ik_{a_s} \mathbf{r} \mathbf{R})}{|R|} \\ &\times \begin{bmatrix} \cos(\Theta) \cos(\Phi) P_{a_s, x}^{(3)}(\mathbf{r}) \\ -\sin(\Phi) P_{a_s, x}^{(3)}(\mathbf{r}) \end{bmatrix}, \end{aligned} \quad (\text{A5})$$

where $\mathbf{R}(R, \Theta, \Phi)$ denotes the detection position in spherical coordinates. The corresponding measurable anti-Stokes intensity is given by

$$I_{a_s, \text{far}}(R, \Theta, \Phi) = \|E_{a_s, \Theta}\|^2 + \|E_{a_s, \Phi}\|^2. \quad (\text{A6})$$

APPENDIX B: CONTRIBUTION OF y AND z POLARIZATIONS

It was noticed earlier that, even under tight-focusing conditions, only the x -polarized field components of the pump, probe, and Stokes beams contribute to the anti-Stokes radiation [23]. In our Bessel illumination, the back aperture of the objective lens is not filled, but illuminated by a hollow laser beam of narrow width. As a consequence, the y - and z -polarized field components of the pump and probe beam, E_{p_y} and E_{p_z} , are more pronounced, as compared to the conventionally performed filling or overfilling of the objective lens's back aperture.

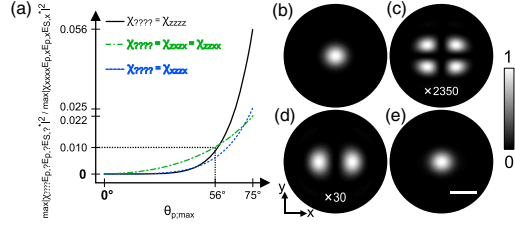


Fig. 8. Evaluation of the impact of non- x -polarized field and polarization density components. (a) Four strongest polarization density elements normalized by contribution of $\chi_{xxxx}^{(3)}$ as a function of the incident angle. (b) Squared absolute values of the sum of all seven nonzero anti-Stokes polarization density elements that are polarized in the x direction $\|\sum P_{aS,x}^{(3)}\|^2$. The distribution is displayed near the nominal focus, i.e., at $z = 0$. (c)–(e) Corresponding plots for $\|\sum P_{aS,y}^{(3)}\|^2$, $\|\sum P_{aS,z}^{(3)}\|^2$, and $\|\sum P_{aS,x}^{(3)}\|^2 + \|\sum P_{aS,y}^{(3)}\|^2 + \|\sum P_{aS,z}^{(3)}\|^2$. The maximum and minimum incident angles of the pump beam were set to $\theta_{max} = 56^\circ$ and $\theta_{min} = 45^\circ$, matching a water immersion objective of NA 1.1 and $d/D = 1/13$. Note that the scaling was changed in (c) and (d) as compared to (b). The white scale bar equals 500 nm.

Thus, a reevaluation is required for the approximation that neglects the non- x -polarized field components.

As an extension of Eq. (A1), the angular spectrum representation of a focused field, including y and z components, is given by [22,24]

$$\begin{bmatrix} E_x(\rho, \phi, z) \\ E_y(\rho, \phi, z) \\ E_z(\rho, \phi, z) \end{bmatrix} = \frac{ikf}{2} \exp(-ikf) \begin{bmatrix} I_{00} + I_{02} \cos(2\phi) \\ I_{02} \sin(2\phi) \\ -i2I_{01} \cos(\phi) \end{bmatrix}. \quad (\text{B1})$$

The superposition of the pump, probe, and Stokes fields, and multiplication with the anti-Stokes susceptibility tensor, yields the polarization density. Contributions to the polarization density by single elements of the anti-Stokes susceptibility are given as

$$P_{aS,l}^{(3)}(r) = 3\chi_{lmmo}^{(3)}(r)E_{p,m}E_{p,n}E_{S,o}^* \quad (\text{B2})$$

where l , m , n , and o correspond to x , y , or z . Under the assumption of an isotropic medium, only 21 of 81 $\chi_{lmmo}^{(3)}(r)$ elements are nonzero [5]. In Fig. 8(a), the four most important contributions of anti-Stokes susceptibility elements are displayed as a function of the maximum incident angle $\theta_{p,max}$, where the index p indicates the pump or probe pulse. Apparently, the impact of components other than x -polarized field components rises significantly with an increasing incident angle $\theta_{p,max}$. For the incident angle $\theta_{p,max} = 56^\circ$ (NA 1.1, water immersion), the squared absolute values of the sum of all seven nonzero anti-Stokes polarization density elements that are polarized in the x direction $\|\sum P_{aS,x}^{(3)}\|^2$ are visualized in Fig. 8(b). Corresponding plots for $\|\sum P_{aS,y}^{(3)}\|^2$, $\|\sum P_{aS,z}^{(3)}\|^2$, and $\|\sum P_{aS,x}^{(3)}\|^2 + \|\sum P_{aS,y}^{(3)}\|^2 + \|\sum P_{aS,z}^{(3)}\|^2$ are given in Figs. 8(c)–8(e). As is evident from Figs. 8(a) and 8(d), the z -polarized anti-Stokes polarization density reduces the resolution only if very high NA objective lenses are used,

e.g., NA = 0.95 (air immersion). Thus, we confirmed that contributions other than $\chi_{xxxx}^{(3)}$ are negligible for the generation of anti-Stokes radiation with the soft condition $\theta_{p,max} \leq 60^\circ$.
†These authors contributed equally to this work.

Funding. Bundesministerium für Bildung und Forschung (Federal Ministry of Education and Research) (13N1225, 13N12526); Carl-Zeiss-Stiftung (Carl Zeiss Foundation).

REFERENCES

1. M. D. Duncan, J. Reintjes, and T. J. Manuccia, "Scanning coherent anti-Stokes Raman microscope," *Opt. Lett.* **7**, 350–352 (1982).
2. A. Zumbusch, G. R. Holtom, and X. S. Xie, "Three-dimensional vibrational imaging by coherent anti-Stokes Raman scattering," *Phys. Rev. Lett.* **82**, 4142–4145 (1999).
3. C. Heinrich, S. Bernet, and M. Ritsch-Marte, "Wide-field coherent anti-Stokes Raman scattering microscopy," *Appl. Phys. Lett.* **84**, 816–818 (2004).
4. P. Berto, A. Jesacher, C. Roeder, S. Monneret, H. Rigneault, and M. Ritsch-Marte, "Wide-field vibrational phase imaging in an extremely folded box-CARS geometry," *Opt. Lett.* **38**, 709–711 (2013).
5. J.-X. Cheng and X. S. Xie, eds., *Coherent Raman Scattering Microscopy*, Series in Cellular and Clinical Imaging (CRC Press, 2012), pp. 30–276.
6. A. Volkmer, J.-X. Cheng, and X. S. Xie, "Vibrational imaging with high sensitivity via epidetected coherent anti-Stokes Raman scattering microscopy," *Phys. Rev. Lett.* **87**, 023901 (2001).
7. L. Cheng and D. Y. Kim, "Differential imaging in coherent anti-Stokes Raman scattering microscopy with Laguerre–Gaussian excitation beams," *Opt. Express* **15**, 10123–10134 (2007).
8. V. V. Krishnamachari and E. O. Potma, "Focus-engineered coherent anti-Stokes Raman scattering microscopy: a numerical investigation," *J. Opt. Soc. Am. A* **24**, 1138–1147 (2007).
9. V. V. Krishnamachari and E. O. Potma, "Multi-dimensional differential imaging with FE-CARS microscopy," *Vib. Spectrosc.* **50**, 10–14 (2009).
10. V. Raghunathan and E. O. Potma, "Multiplicative and subtractive focal volume engineering in coherent Raman microscopy," *J. Opt. Soc. Am. A* **27**, 2365–2374 (2010).
11. H. Kim, G. W. Bryant, and S. J. Stranick, "Superresolution four-wave mixing microscopy," *Opt. Express* **20**, 6042–6051 (2012).
12. J. Lin, F. Lu, H. Wang, W. Zheng, C. J. Sheppard, and Z. Huang, "Improved contrast radially polarized coherent anti-Stokes Raman scattering microscopy using annular aperture detection," *Appl. Phys. Lett.* **95**, 133703 (2009).
13. S. Heuke, J. Zheng, D. Akimov, R. Heintzmann, M. Schmitt, and J. Popp, "Bessel beam CARS of axially structured samples," *Sci. Rep.* **5**, 10991 (2015).
14. T. Meyer, M. Schmitt, B. Dietzek, and J. Popp, "Accumulating advantages, reducing limitations: multimodal nonlinear imaging in biomedical sciences—the synergy of multiple contrast mechanisms," *J. Biophotonics* **6**, 887–904 (2013).
15. F. O. Fahrbach and A. Rohrbach, "Propagation stability of self-reconstructing Bessel beams enables contrast-enhanced imaging in thick media," *Nat. Commun.* **3**, 632–638 (2012).
16. S. W. Hell and J. Wichmann, "Breaking the diffraction resolution limit by stimulated emission: stimulated-emission-depletion fluorescence microscopy," *Opt. Lett.* **19**, 780–782 (1994).
17. A. M. Mahmoud, M. Y. Shalaby, and D. Khalil, "Propagation of Bessel beams generated using finite-width Durbin ring," *Appl. Opt.* **52**, 256–263 (2013).
18. M. Baumgartl, T. Gottschall, J. Abreu-Afonso, A. Diez, T. Meyer, B. Dietzek, M. Rothhardt, J. Popp, J. Limpert, and A. Tünnermann, "Alignment-free, all-spliced fiber laser source for CARS microscopy based on four-wave-mixing," *Opt. Express* **20**, 21010–21018 (2012).
19. T. Meyer, M. Baumgartl, T. Gottschall, T. Pascher, A. Wuttig, C. Matthaus, B. F. M. Romeike, B. R. Brehm, J. Limpert, A. Tünnermann, O. Guntinas-Lichius, B. Dietzek, M. Schmitt, and J. Popp, "A compact microscope setup for multimodal nonlinear imaging

- in clinics and its application to disease diagnostics," *Analyst* **138**, 4048–4057 (2013).
20. R. Arimoto, C. Saloma, T. Tanaka, and S. Kawata, "Imaging properties of axicon in a scanning optical system," *Appl. Opt.* **31**, 6653–6657 (1992).
21. C. K. Hayakawa, V. Venugopalan, V. V. Krishnamachari, and E. O. Potma, "Amplitude and phase of tightly focused laser beams in turbid media," *Phys. Rev. Lett.* **103**, 043903 (2009).
22. L. Novotny and B. Hecht, *Principles of Nano-Optics* (Cambridge University, 2012).
23. J.-X. Cheng, A. Volkmer, and X. S. Xie, "Theoretical and experimental characterization of coherent anti-Stokes Raman scattering microscopy," *J. Opt. Soc. Am. B* **19**, 1363–1375 (2002).
24. B. Richards and E. Wolf, "Electromagnetic diffraction in optical systems. II. Structure of the image field in an aplanatic system," *Proc. R. Soc. London* **253**, 358–379 (1959).

Own Publications

- [FBL1] S. Heuke, O. Chernavskaia, T. Bocklitz, F. B. Legesse, T. Meyer, D. Akimov, O. Dirsch, G. Ernst, F. von Eggeling, I. Petersen, M. Schmitt, and J. Popp, “Multimodal nonlinear microscopy of head and neck carcinoma – toward surgery assisting frozen section analysis,” *Head & neck* **38**, 1545–1552 (2016).
- [FBL2] F. B. Legesse, S. Heuke, K. Galler, P. Hoffmann, M. Schmitt, U. Neugebauer, M. Bauer, and J. Popp, “Hepatic Vitamin A Content Investigation Using Coherent Anti-Stokes Raman Scattering Microscopy,” *ChemPhysChem* **17**, 4043–4051 (2016).
- [FBL3] F. B. Legesse, J. Rüger, T. Meyer, C. Krafft, M. Schmitt, and J. Popp, “Investigation of microalgal carotenoid content using Coherent anti-Stokes Raman scattering (CARS) microscopy and Spontaneous Raman Spectroscopy,” *ChemPhysChem* **Accepted**, (2018).
- [FBL4] S. Heuke, F. B. Legesse, A. Lorenz, T. Pascher, D. Akimov, M. Jäger, M. Schmitt, and J. Popp, “Fiber-based dual-focus time-demultiplexed second harmonic generation microscopy,” *Optics letters* **40**, 2505–2508 (2015).
- [FBL5] F. B. Legesse, T. Meyer, S. Heuke, T. Gottschall, T. Pascher, J. Limpert, A. Tünnermann, M. Schmitt, and J. Popp, “Dual-focus Coherent anti-Stokes Raman scattering microscopy using a compact two-beam fiber laser source,” *Optics letters* **42**, 183–186 (2017).
- [FBL6] S. Heuke, F. B. Legesse, D. Akimov, U. Hübner, J. Dellith, M. Schmitt, and J. Popp, “Bessel beam Coherent anti-Stokes Raman scattering microscopy,” *JOSA B* **32**, 1773–1779 (2015).

-
- [FBL7] F. B. Legesse, O. Chernavskaia, S. Heuke, T. Bocklitz, T. Meyer, J. Popp, and R. Heintzmann, “Seamless stitching of tile scan microscope images,” *Journal of microscopy* **258**, 223–232 (2015).
- [FBL8] F. B. Legesse, A. Medyukhina, S. Heuke, and J. Popp, “Texture analysis and classification in Coherent anti-Stokes Raman scattering (cars) microscopy images for automated detection of skin cancer,” *Computerized Medical Imaging and Graphics* **43**, 36–43 (2015).
- [FBL9] J. Popp, R. Geitner, F.-B. Legesse, N. Kuhl, T. Meyer, T. Bocklitz, S. Zechel, J. Vitz, M. Hager, U. S. Schubert *et al.*, “Do you get what you see? understanding molecular self-healing,” *Chemistry-A European Journal* (2017).

Poster

- [P1] F. B. Legesse, T. Meyer, S. Heuke, T. Gottschall, T. Pascher, J. Limpert, A. Tünnermann, M. Schmitt, and J. Popp, “European Conference on Non-linear Optical Spectroscopy,” in European Conference on Non-linear Optical Spectroscopy (ECONOS), (2017).

Curriculum Vitae

Personal Data

Name	Fisseha Bekele Legesse
Birthday	22.11.1988
Birthplace	Addis Ababa, Ethiopia

Education

10/2005-07/2009	Bachelor of Science in Electrical Engineering at the Bahir Dar University, Bahir Dar, Ethiopia
10/2011-04/2014	Master of Science in Photonics at the Abbe School of Photonics, Friedrich-Schiller-University Jena, Germany

Work Experience

10/2009-09/2011	Software Engineer, System Developer at the Information and Network Security Agency, Addis Ababa, Ethiopia
08/2012-10/2012	Intern at the Carl Zeiss AG, Oberkochen, Germany

Fisseha Bekele Legesse: Jena

Acknowledgement

I would like to express my sincere gratitude to the following people who have contributed to this work. First, I would like to thank Prof. Dr. Jürgen Popp for giving me the opportunity to work on my thesis in the molecular imaging group under his supervision. This work would not have been possible without his support and the autonomy he has afforded me. I would also like to thank apl. Prof. Dr. Michael Schmitt for his immediate and invaluable mentor-ship. I am also grateful for our collaboration partners in the clinic Prof. Dr. Michael Bauer, Prof. Dr. Ute Neugebauer, for the fruitful discussions and feedbacks.

I am indebted to Dr. Tobias Meyer and Dr. Sandro Heuke for their massive contribution to this thesis with regards to imparting their knowledge on the subject matter and giving me constructive comments. I would also like to acknowledge, Dr. Thomas Bocklitz, Dr. Olga Matrosova, Dr. Anna Medyukhina, and Dr. Nadine Vogler for their collaborative efforts in the analysis of multi-modal images. I thank Dr. Denis Akimov and Aleksandar Lukic for sharing their technical expertise on the optical setups. I thank my collaborators in the liver experiments Dr. Kerstin Galler and Patrick Hoffmann, and in the algae studies, Dr. Christoph Krafft and Jan Rüger for providing samples and discussing the results obtained. My gratitude also extends to the other members of the molecular imaging group Ines Latka, Susanne Pfeifenbring, Karl-Benjamin Suttner, Hyeonsoo Bae and Marko Rodewald for the conducive working environment they have created.

Lastly I want to thank my family, Selam, and all my friends for their unwavering support. Thank you for lending me your ears and your helping hands which saw me through the ups and downs.

Erklärung

Erklärung zu den Eigenanteilen des Promovenden/der Promovendin sowie der weiteren Doktoranden/Doktorandinnen als Koautoren an den Publikationen und Zweitpublikationsrechten bei einer kumulativen Dissertation

Für alle in dieser kumulativen Dissertation verwendeten Manuskripte liegen die notwendigen Genehmigungen der Verlage (“Reprint permissions”) für die Zweitpublikation vor.

Die Koautoren der in dieser kumulativen Dissertation verwendeten Manuskripte sind sowohl über die Nutzung, als auch über die oben angegebenen Eigenanteile informiert und stimmen dem zu.

Fisseha Bekele Legesse: Jena,

Ich bin mit der Abfassung der Dissertation als publikationsbasiert, d.h. kumulativ, einverstanden und bestätige die vorstehenden Angaben. Eine entsprechend begründete Befürwortung mit Angabe des wissenschaftlichen Anteils des Doktoranden/der Doktorandin an den verwendeten Publikationen werde ich parallel an den Rat der Fakultät der Chemisch-Geowissenschaftlichen Fakultät richten.

Prof. Dr. Jürgen Popp: Jena,

Anlage zur Erklärung zu den Eigenanteilen des Promovenden sowie der weiteren Doktoranden/ Doktorandinnen als Koautoren an den Publikationen und Zweitpublikationsrechten bei einer kumulativen Dissertation

Publikation [FBL1] S. Heuke, O. Chernavskaia, T. Bocklitz, F. B. Legesse, T. Meyer, D. Akimov, O. Dirsch, G. Ernst, F. von Eggeling, I. Petersen, M. Schmitt, and J. Popp, “Multimodal nonlinear microscopy of head and neck carcinoma – toward surgery assisting frozen section analysis,” *Head & neck* **38**, 1545–1552 (2016).

Beteiligt an (Zutreffendes ankreuzen)	S. Heuke	Fisseha Bekele Legesse
Konzeption des Forschungsansatzes	×	
Planung der Untersuchungen	×	
Datenerhebung	×	
Datenanalyse und interpretation	×	×
Schreiben des Manuskripts	×	
Vorschlag Anrechnung Publikationsäquivalente	1.0	0.5

Publikation [FBL2] F. B. Legesse, S. Heuke, K. Galler, P. Hoffmann, M. Schmitt, U. Neugebauer, M. Bauer, and J. Popp, “Hepatic Vitamin A Content Investigation Using Coherent Anti-Stokes Raman Scattering Microscopy,” *ChemPhysChem* **17**, 4043–4051 (2016).

Beteiligt an (Zutreffendes ankreuzen)		Fisseha Bekele Legesse
Konzeption des Forschungsansatzes		×
Planung der Untersuchungen		×
Datenerhebung		×
Datenanalyse und interpretation		×
Schreiben des Manuskripts		×
Vorschlag Anrechnung Publikationsäquivalente		1.0

Publikation [FBL3] F. B. Legesse, J. Rüger, T. Meyer, C. Krafft, M. Schmitt, and J. Popp, “Investigation of microalgal carotenoid content using Coherent anti-Stokes Raman scattering (CARS) microscopy and Spontaneous Raman Spectroscopy,” ChemPhysChem **Accepted**, (2018).

Beteiligt an (Zutreffendes ankreuzen)	Fisseha Bekele Legesse	
Konzeption des Forschungsansatzes	×	
Planung der Untersuchungen	×	
Datenerhebung	×	
Datenanalyse und interpretation	×	
Schreiben des Manuskripts	×	
Vorschlag Anrechnung Publikation- säquivalente	1.0	

Publikation[FBL4] S. Heuke, F. B. Legesse, A. Lorenz, T. Pascher, D. Akimov, M. Jäger, M. Schmitt, and J. Popp, “Fiber-based dual-focus time-demultiplexed second harmonic generation microscopy,” Optics letters **40**, 2505–2508 (2015).

Beteiligt an (Zutreffendes ankreuzen)	S. Heuke	Fisseha Bekele Legesse
Konzeption des Forschungsansatzes	×	
Planung der Untersuchungen	×	
Datenerhebung	×	×
Datenanalyse und interpretation	×	×
Schreiben des Manuskripts	×	
Vorschlag Anrechnung Publikation- säquivalente	1.0	1.0

Publikation [FBL5] F. B. Legesse, T. Meyer, S. Heuke, T. Gottschall, T. Pascher, J. Limpert, A. Tünnermann, M. Schmitt, and J. Popp, “Dual-focus coherent anti-Stokes Raman scattering microscopy using a compact two-beam fiber laser source,” Optics letters **42**, 183–186 (2017).

Beteiligt an (Zutreffendes ankreuzen)	Fisseha Bekele Legesse	
Konzeption des Forschungsansatzes	×	
Planung der Untersuchungen	×	
Datenerhebung	×	
Datenanalyse und interpretation	×	
Schreiben des Manuskripts	×	
Vorschlag Anrechnung Publikation- säquivalente	1.0	

Publikation [FBL6] S. Heuke, F. B. Legesse, D. Akimov, U. Hübner, J. Dellith, M. Schmitt, and J. Popp, “Bessel beam coherent anti-Stokes Raman scattering microscopy,” *JOSA B* **32**, 1773–1779 (2015).

Beteiligt an (Zutreffendes ankreuzen)	S. Heuke	Fisseha Bekele Legesse
Konzeption des Forschungsansatzes	×	
Planung der Untersuchungen	×	
Datenerhebung	×	×
Datenanalyse und interpretation	×	
Schreiben des Manuskripts	×	
Vorschlag Anrechnung Publikation- säquivalente	1.0	1.0

Selbstständigkeitserklärung

Ich erkläre, dass ich die vorliegende Arbeit selbständig und unter Verwendung der angegebenen Hilfsmittel, persönlichen Mitteilungen und Quellen angefertigt habe.

Fisseha Bekele Legesse: Jena,